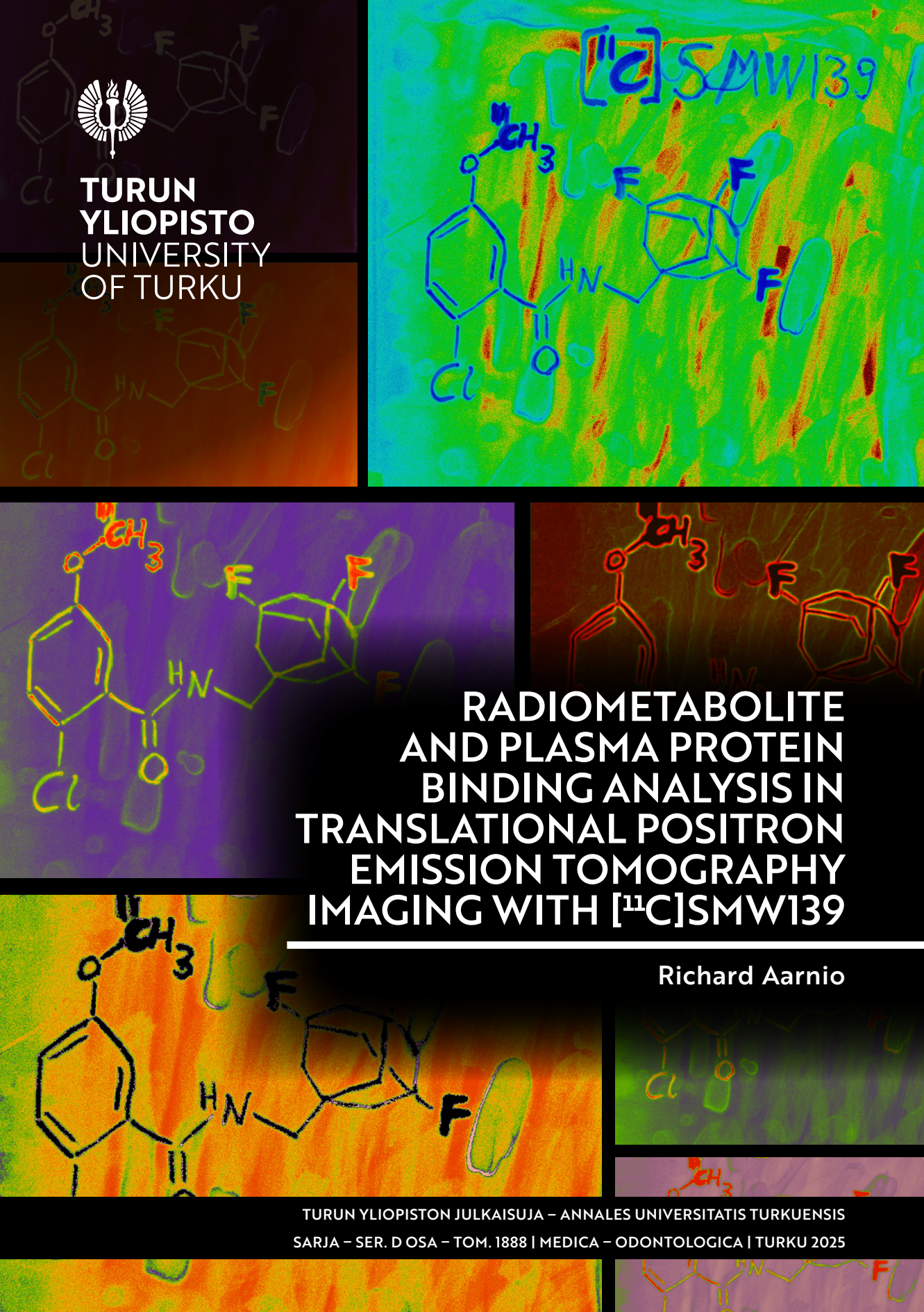

TURUN YLIOPISTO
UNIVERSITY OF TURKU

RADIOMETABOLITE AND PLASMA PROTEIN BINDING ANALYSIS IN TRANSLATIONAL POSITRON EMISSION TOMOGRAPHY IMAGING WITH [^{11}C]SMW139

Richard Aarnio

TURUN YLIOPISTON JULKAISUJA – ANNALES UNIVERSITATIS TURKUENSIS
SARJA – SER. D OSA – TOM. 1888 | MEDICA – ODONTOLOGICA | TURKU 2025

TURUN
YLIOPISTO
UNIVERSITY
OF TURKU

RADIOMETABOLITE AND PLASMA PROTEIN BINDING ANALYSIS IN TRANSLATIONAL POSITRON EMISSION TOMOGRAPHY IMAGING WITH [^{11}C]SMW139

Richard Aarnio

TURUN YLIOPISTON JULKAISUJA – ANNALES UNIVERSITATIS TURKUENSIS
SARJA – SER. D OSA – TOM. 1888 | MEDICA – ODONTOLOGICA | TURKU 2025

University of Turku

Faculty of Medicine
Department of Clinical Medicine
Clinical Physiology and Nuclear Medicine
Drug Research Doctoral Programme
Turku PET Centre

Supervised by

Adjunct Professor
Merja Haaparanta-Solin, PhD
Turku PET Centre
University of Turku
Turku, Finland

Adjunct Professor
Sarita Forsback, PhD
Turku PET Centre
University of Turku
Turku, Finland

Reviewed by

Assoc. Prof. Mag. Cécile Philippe, PhD
Department of Biomedical Imaging and
Image-guided Therapy
Medical University of Vienna
Vienna, Austria

Assistant Prof. Pedro Brugarolas, PhD
Department of Radiology
Massachusetts General Hospital and
Harvard Medical School
Boston, Massachusetts

Opponent

Prof. Olof Eriksson, PhD
Department of Medicinal Chemistry
Uppsala Universitet
Uppsala, Sweden

The originality of this publication has been checked in accordance with the University of Turku quality assurance system using the Turnitin OriginalityCheck service.

Cover Image: Richard Aarnio

ISBN 978-952-02-0223-1 (PRINT)
ISBN 978-952-02-0224-8 (PDF)
ISSN 0355-9483 (Print)
ISSN 2343-3213 (Online)
Painosalama, Turku, Finland 2025

To my family, friends, and colleagues around the world. Thank you for your unwavering support and encouragement through all these years.

UNIVERSITY OF TURKU
Faculty of Medicine
Department of Clinical Medicine
Clinical Physiology and Nuclear Medicine
Turku PET Centre
RICHARD AARNIO: Radiometabolite and Plasma Protein Binding Analysis in Translational Positron Emission Tomography Imaging with [^{11}C]SMW139
Doctoral Dissertation, 191 pp.
Drug Research Doctoral Programme
March 2025

ABSTRACT

Positron emission tomography (PET) is a highly sensitive, non-invasive, imaging technique used for quantification of biological targets. The accuracy of quantification is influenced by the tracer metabolism and plasma protein binding (PPB). This thesis focuses on the development of novel methodologies for radiometabolite analysis (RMA) and PPB assessment of the P2X7 receptor binding PET tracer [^{11}C]SMW139 in both preclinical and clinical research.

Key challenges in PET imaging include the rapid metabolism of tracers, which generates radiometabolites that may have altered binding properties and biodistribution. These radiometabolites can accumulate in tissues in critical quantification areas, affecting PET signal quantification and interpretation. To address this, robust thin-layer chromatography (TLC), high-performance TLC (HPTLC), and high-performance liquid chromatography (HPLC) methods were developed and optimised for quantification of the unchanged tracer and its radiometabolites in plasma and brain tissue. Additionally, an ultrafiltration PPB analysis method was developed to simultaneously determine the plasma protein-free fraction of [^{11}C]SMW139 and of its radiometabolites. The free fraction of the radiometabolites had not been analysed before.

The results demonstrate that [^{11}C]SMW139 undergoes rapid metabolism in both mouse and human plasma, the parent and its radiometabolites are able to penetrate the blood-brain-barrier (BBB). However, suitable compartment modelling with corrections for BBB penetrating radiometabolites enabled robust quantification. Moreover, [^{11}C]SMW139 was found to be highly bound to plasma proteins, while the radiometabolites had a much higher free fraction enhancing their abundant penetration through the BBB. The findings provide essential insights into the pharmacokinetics of [^{11}C]SMW139 and its radiometabolites, enabling improved PET data interpretation and tracer evaluation for brain imaging. Standardisation of RMA and PPB analysis methodologies and especially their detailed reporting are recommended for enhancing the reliability of RMA and PPB studies in future studies.

KEYWORDS: Radiometabolite analysis, plasma protein binding analysis, translational PET research, [^{11}C]SMW139.

TURUN YLIOPISTO
Lääketieteellinen tiedekunta
Kliininen laitos
Kliininen fysiologia ja isotooppilääketiede
Turun PET-keskus
RICHARD AARNIO: [^{11}C]SMW139 merkkiaineen radiometaboliitti- ja plasman proteiinisitoutumisanalyysit translaationaalisessa positroniemissiotomografia-kuvantamisessa
Väitöskirja, 191 s.
Lääketutkimuksen tohtoriohjelma
Maaliskuu 2025

TIIVISTELMÄ

Positroniemissiotomografia (PET) on herkkä ja kajoamaton kuvantamismenetelmä, jota käytetään biologisten kohteiden kvantitatiiviseen tutkimiseen. PET-merkkiaineen metaboloituminen ja plasman proteiineihin sitoutuminen (PPB) vaikuttavat sen tarkkuuteen. Tämä väitöskirja keskittyy PET-merkkiaineen [^{11}C]SMW139:n radiometaboliittianalyysi- (RMA) ja PPB-analyysimenetelmien kehittämiseen prekliinisissä ja kliinisissä tutkimuksissa.

PET-kuvantamisen haasteisiin kuuluu merkkiaineiden nopea metaboloituminen, joka tuottaa radiometaboliitteja, joilla voi olla erilaiset sitoutumis- ja jakautumisominaisuudet kuin alkuperäisellä merkkiaineella. Erityisesti radiometaboliittien kertyminen kudoksiin kvantitointialueilla voi vääristää signaalin analyysiä. Tätä varten kehitettiin ja optimoitiin ohutlevykromatografia (TLC), korkean erotuskyvyn ohutlevykromatografia (HPTLC), ja korkean suorituskyvyn nestekromatografia (HPLC)-menetelmiä. Näiden avulla määritettiin merkkiaineen ja sen radiometaboliittien pitoisuudet plasmassa ja aivokudoksessa. Lisäksi kehitettiin ultrasuodatusmenetelmä PPB-analyysiin, jotta voitiin [^{11}C]SMW139:n ja sen radiometaboliittien vapaat fraktiot plasmassa määrittää samanaikaisesti. Radiometaboliittien vapaata fraktiota ei ole aiemmin analysoitu.

Tutkimuksen tulokset osoittivat, että [^{11}C]SMW139 metaboloituu nopeasti sekä hiiren että ihmisen plasmassa, ja muuttumaton merkkiaine ja sen radiometaboliitit pystyvät läpäisemään veri-aivoesteen (BBB). Kuitenkin, BBB-läpäisevillä radiometaboliiteilla korjattu lokeromallimallinnus mahdollisti luotettavan kvantitoinnin. [^{11}C]SMW139 sitoutuu voimakkaasti plasman proteiineihin, kun taas sen radiometaboliiteilla on huomattavasti suurempi vapaa fraktio, edistäen niiden BBB-läpäisyä. Nämä löydökset tarjoavat arvokasta tietoa [^{11}C]SMW139:n ja sen radiometaboliittien farmakokinetiikasta, mikä parantaa PET-kuvantamisen tulosten tulkinnan ja merkkiaineen arviointia. Lisäksi tutkimus korostaa RMA- ja PPB-analyysimenetelmien standardointia ja yksityiskohtaisen raportoinnin merkitystä PET-tutkimusten luotettavuuden parantamiseksi.

AVAINSANAT: Radiometaboliittianalyysi, plasma proteiinisitoutumisanalyysi, translationaalinen PET-tutkimus, [^{11}C]SMW139.

Table of Contents

Abbreviations

3R	Replacement, reduction, and refinement
^{11}C	Carbon-11
^{18}F	Fluorine-18
^{68}Ga	Gallium-68
[^{11}C]SMW139	2-chloro-5-[^{11}C]methoxy-N-((3,5,7-trifluoroadamantan-1-yl)methyl)benzamide
[^{18}F]FDG	2-deoxy-2-[^{18}F]fluoroglucose
[^{18}F]FDOPA	6-[^{18}F]fluoro-L-DOPA
@EOS	At the end of synthesis
@injection	At the time of injection
%IA/g	Percentage of injected activity per gram of tissue
λ	Decay constant
A_m	Molar activity
A_m(max)	Maximum molar activity in theory
AADC	Aromatic L-amino acid decarboxylase
ACN	Acetonitrile
ADME	Absorption, distribution, metabolism, and excretion
AFOV	Axial field-of-view
AIC	Akaike information criterion
AIF	Arterial input function
β^+	Beta$^+$ decay
BBB	Blood-brain barrier
BGO	Bismuth germanate
BP	Binding potential
BP_{ND}	Non-displaceable binding potential
CBV	Cerebral blood volume
c_P	Radioactivity concentration of plasma
CT	Computer tomography
EAE	Experimental autoimmune encephalomyelitis
ED	Equilibrium dialysis
$E_{max}(\beta^+)$	Maximum positron energy

$E_{mean}(\beta^+)$	Mean positron energy
f_M	Radiometabolite plasma protein-free fraction
f_P	Parent plasma protein-free fraction
$f_{M/A}$	Fraction of plasma protein free radiometabolite radioactivity over all radioactivity
$f_{M/M}$	Fraction of plasma protein free radiometabolite radioactivity over total radiometabolite radioactivity
$f_{P/A}$	Fraction of plasma protein free parent radioactivity over all radioactivity
$f_{P/P}$	Fraction of plasma protein free parent radioactivity over total parent radioactivity
GC	Gas chromatography
HC	Healthy controls
HPLC	High-performance liquid chromatography
HPTLC	High-performance thin-layer chromatography
HSA	Human serum albumin
ICLAS	International Council of Laboratory Animal Science
IDIF	Image derived input function
i.v.	Intravenous
k_1	Rate of tracer transfer from plasma to tissue
k_2	Rate of tracer clearance from tissue back to plasma
k_3	Rate of the tracer binding to the target receptor
k_4	Rate of tracer dissociation from the target receptor
K_i	Net influx rate
LAFOV	Long-axial field-of-view
LC	Liquid chromatography
LC-MS	Liquid chromatography-mass spectrometry
LC-MS/MS	Liquid chromatography with tandem mass spectrometry
LogP	Logarithmic of the partition coefficient of a solute between octanol and water
LYSO	Lutetium yttrium orthosilicate
MEPS	Microextraction by packed sorbent
MLC	Micellar liquid chromatography
MRI	Magnetic resonance imaging
MS	Multiple sclerosis
MSNA	Molecular spherical nucleic acids
NaI(Tl)	Thallium-doped sodium-iodine
NMR	Nuclear magnetic resonance
p.i.	Post-injection
PET	Positron emission tomography

Ph. Eur.	European Pharmacopoeia
PMS	Progressive multiple sclerosis
PMT	Photomultiplier tube
PPB	Plasma protein binding
PPBA	Plasma protein binding analysis
PSL	Photostimulated luminescence
RCP	Radiochemical purity
RED	Rapid equilibrium dialysis
RMA	Radiometabolite analysis
RMS	Relapsing multiple sclerosis
ROI	Region of interest
R_t	Retention time
TAC	Time-activity curve
TFA	Trifluoroacetic acid
SAFOV	Short-axial field-of-view
SiPM	Silicon photomultiplier
SLS-MEPS	Semi-automated lead shielded microextraction by packed sorbents
SPE	Solid-phase extraction
SPME	Solid-phase microextraction
SD	Standard deviation
STUK	Radiation and Nuclear Safety Authority in Finland
TB	Total-body
TBV	Total blood volume
TLC	Thin-layer chromatography
TOF	Time-of-flight
TSPO	Translocator protein
UF	Ultrafiltration
V_B	Blood volume parameter
V_T	Volume of distribution

List of original publications

This dissertation is based on the following original publications, which are referred to in the text by their Roman numerals:

I Obada M. Alzghool, **Richard Aarnio**, Jatta S. Helin, Saara Wahlroos, Thomas Keller, Markus Matilainen, Junel Solis, Jonathan J. Danon, Michael Kassiou, Anniina Snellman, Olof Solin, Juha O. Rinne & Merja Haaparanta-Solin. Glial reactivity in a mouse model of beta-amyloid deposition assessed by PET imaging of P2X7 receptor and TSPO using [^{11}C]SMW139 and [^{18}F]F-DPA. *EJNMMI Research* 2024, 14, 25.

II **Richard Aarnio**, Obada M. Alzghool, Saara Wahlroos, James O'Brien-Brown, Michael Kassiou, Olof Solin, Juha O. Rinne, Sarita Forsback, Merja Haaparanta-Solin. Novel plasma protein binding analysis method for a PET tracer and its radiometabolites: A case study with [^{11}C]SMW139 to explain the high uptake of radiometabolites in mouse brain. *Journal of Pharmaceutical and Biomedical Analysis*, 2022; 219:114860.

III Joachim Brumberg, **Richard Aarnio**, Anton Forsberg, Päivi Marjamäki, Vera Kerstens, Mohammad M. Moein, Sangram Nag, Saara Wahlroos, Michael Kassiou, Albert D Windhorst, Christer Halldin, Merja Haaparanta-Solin, Patrik Fazio, Vesa Oikonen, Juha O Rinne, Andrea Varrone. Quantification of the purinergic $P2X_7$ receptor with [^{11}C]SMW139 improves through correction for brain-penetrating radiometabolites. *Journal of Cerebral Blood Flow & Metabolism*, 2023; 43(2):258-268.

IV Jussi Lehto, **Richard Aarnio**, Jouni Tuisku, Marcus Sucksdorff, Esa Mikko Koivumäki, Marjo Nylund, Semi Helin, Johan Rajander, Jonathan J. Danon, Jayson Gilchrist, Michael Kassiou, Vesa Oikonen, Laura Airas. P2X7-receptor binding in new-onset and secondary progressive MS – a [^{11}C]SMW139 PET study. *EJNMMI research*, 2024; 14(1), 123.

1 Introduction

Positron emission tomography (PET) is a non-invasive and quantitative molecular imaging modality, which enables the localization of positron emitting radionuclides *in vivo* with the aid of a PET scanner. PET images can be combined with other imaging modalities, such as magnetic resonance imaging (MRI) or computer tomography (CT) to obtain high-resolution anatomical references for localizing the exact source of the PET signal. PET imaging was first used for clinical imaging in 1953 by Drs Brownell and Aronov (Jones & Townsend, 2017). Since then this technique has developed immensely and inspired researchers to develop new ways to utilize this technology in medical imaging and drug development. Various PET tracers for different targets have been developed, such as the most famous PET tracer, 2-deoxy-2-[^{18}F]fluoroglucose ([^{18}F]FDG). PET tracers are radiolabelled with positron emitting radionuclides, each having their unique advantages for different applications.

Often PET tracers are built upon molecules that are not naturally found in the human body. By nature, the human body strives to protect itself by excreting such molecules, which do not belong in the body, and usually hastens up excretion by metabolizing the molecule to a more suitable form for a speedy excretion if possible. Tracers can also be based on molecules that are already found in the body by isotopically labelling them. Depending on the molecule, these too can be directly excreted, or take part in biological processes occurring in the body resulting in further metabolism of the molecule so that the body can utilize parts of the molecule it needs for example, as building blocks in *de novo* synthesis and energy production.

When the tracer undergoes any change and forms radiometabolites, the new positron emitting molecules have altered key properties such as new possible binding targets and altered affinity. Enzymatic activity in the bloodstream, in organs or in the target tissue also plays an important role in enabling the metabolic pathways and affecting the rate of metabolism. The *in vivo* stability of the tracer can vary in different subject groups depending on age, sex, metabolic status, medication etc. Depending on the new structure of the radiometabolite and therefore the affinity properties and ability to penetrate any membranes, which often depends on the molecular weight, charge and lipophilicity of the radiometabolites, the

radiometabolites can accumulate to new targets or circulate without specific binding, contributing to increased tissue background radioactivity.

The overall metabolism of tracers and its rate can be influenced by additional factors, including the concentration of proteins in the bloodstream, the presence and progression of diseases, and the use of anaesthetics (Ramos-Torres *et al.*, 2024). In addition, the extent to which a tracer binds to intermediate carriers, such as human serum albumin (HSA), other plasma proteins, or are taken into erythrocytes, can affect its metabolism. Drug metabolites can potentially exhibit toxic properties; fortunately, the trace level injection of PET tracers usually prevents this from causing any adverse effects as trace level doses are intendedly used so that the tracer or its metabolites will not induce any significant pharmacological effect in the body.

The radiometabolites can hamper PET imaging data collection and analysis in many ways. As it is not possible to determine from the PET data alone whether the signal originates from the parent tracer or its radiometabolites (Ghosh *et al*., 2020), any metabolism, i.e. alterations of the tracer structure, must be studied using blood and tissue samples. This is essential for understanding the true ratio of the original parent tracer and its radiometabolites contributing to the observed signal. The increased background radioactivity in the region of interest (ROI) affects negatively the signal-to-noise ratio. When using reference tissue modelling, it is assumed that the reference tissue has the same radioactivity concentration of non-specifically bound radiometabolites than in the ROI and that it does not have any specific binding sites for the tracer. In reality, radiometabolites might be accumulating in different amounts into the different regions and cause bias to the results. For quantification of the target, by for example, compartment-modelling using arterial input function (AIF), the radiometabolites must be corrected from the plasma time-activity curve (TAC). Also, tracers that undergo rapid metabolism have a limited time for the uptake of the original tracer and it should be considered to limit the time frames for quantification to times shortly after the injection. As *in vivo* sampling during PET studies from human subjects is limited to blood and urine samples, and human post mortem and other *in vitro* studies do not provide all the information needed, preclinical studies are essential to provide an understanding of the metabolism in addition to the biodistribution of the radiometabolites of the parent tracer.

Metabolism of PET tracers have been studied mainly by using various chromatographical methods such as high-performance liquid chromatography (HPLC) and thin-layer chromatography (TLC). Separating different molecules from each other from a mixture of molecules using such chromatographical methods is based on affinity differences between the different radiometabolites and the parent tracer to the stationary phase, combined with the effect of the strength of the eluent to displace their reversible binding to the stationary phase. It usually requires significant effort to develop and validate effective separation methods.

In addition, other corrections to plasma TAC should be considered, like the effect of the tracers' protein-free fraction in plasma. Plasma protein binding (PPB) is an important part of PET tracer characterization, as the PPB of the tracer and its radiometabolites can hugely affect the kinetics of the tracer. Understanding these characteristics can aid in improving the modelling of the PET data. As with radiometabolite analysis (RMA), the PPB analysing methods and the ways in which these methods and results are reported, are diverse. More standardization should be established in these fields through detailed reporting of materials and methods and acquired data.

Utilizing the emitted particles or photons from radioactive decay of the PET tracer and its radiometabolites enormously enhances the capabilities to accurately quantify their trace level concentrations. RMA and PPB analysis requires highly sensitive radiodetectors or phosphorimagers to enable the analysis of late time point samples. The sensitivity of these radiodetectors is often a limiting factor for these studies.

The aim of this thesis is to provide new angles of approach, novel methods and increased understanding to the field of RMA and PPB analysis by developing such methods for the P2X7 receptor targeting PET tracer 2-chloro-5-[^{11}C]methoxy-N-((3,5,7-trifluoroadamantan-1-yl)methyl)benzamide ([^{11}C]SMW139, Figure 1) and assessing the results in preclinical and clinical studies. The outline of the Studies I–IV is shown in Table 1.

Table 1. Outline of the Studies.

	Study I	**Study II**	**Study III**	**Study IV**
PET tracer	[^{11}C]SMW139			
Study subjects	Mice (APP/PS1-21 TG and C57BL/6J WT)	Mice (C57BL/6J)	Humans (HC), Mice (C57BL/6J)	Humans (MS and HC)
Developed methods	HPTLC and TLC RMA	UF PPBA	HPLC RMA	UF PPBA refined for humans

Abbreviations: HC = healthy controls, MS = multiple sclerosis, HPLC = high-performance liquid chromatography, HPTLC = high-performance thin-layer chromatography, PPBA = plasma protein binding analysis, RMA = radiometabolite analysis, TLC = thin-layer chromatography, UF = ultrafiltration.

2 Review of the literature

2.1 Positron emission tomography

2.1.1 Radioactivity and its detection

The unstable nature of matter i.e. radioactive decay is the fundamental phenomena underlying PET imaging. PET tracers contain positron-emitting radionuclides that decay via β^+ decay, emitting a positron (the antimatter counterpart of an electron) that subsequently annihilates with an electron, producing two 511 keV gamma photons that travel 180 ± 0.25° in the opposite directions according to the law conservation of energy and momentum (Belcari *et al.*, 2024). The positron-emitting radionuclides are produced mainly with particle accelerators, mostly cyclotrons, by colliding high-energy protons with suitable stable target nuclei. In the subsequent nuclear reactions proton rich (neutron poor) nuclei, such as fluorine-18 (^{18}F) and carbon-11 (^{11}C), are formed. If these nuclei have an energetically unfavourable proton-to-neutron ratio, they will spontaneously decay either via positron emission or electron capture.

The probability of the spontaneous radioactive decay is characteristic for each radionuclide, leading to a well-defined decay constant (λ) and half-life. The half-life is the time it takes for half of the amount of radionuclides to decay.

Ernest Lawrence and his co-workers invented the first cyclotron in 1930 (Wagner, 1998). Frédéric Joliot and Irène Curie were the first to publish about artificially produced radioactivity in 1934 (Joliot & Curie, 1934; Guerra *et al.* 2012).

2.1.2 Positron energy and range

The maximum positron energy ($E_{max}(\beta^+)$) of emitted positrons affects their travel distance before annihilation, influencing spatial resolution in PET imaging. The mean positron energy ($E_{mean}(\beta^+)$) is roughly one third of the $E_{max}(\beta^+)$. High-energy positrons, such as those from gallium-68 (^{68}Ga, $E_{max}(\beta^+)$ = 1.9 MeV, $E_{mean}(\beta^+)$ = 0.74 MeV, half-life 68.3 min), travel further before annihilation, leading to image blurring, while lower-energy positrons from carbon-11 (^{11}C, $E_{max}(\beta^+)$ = 0.96 MeV, $E_{mean}(\beta^+)$ = 0.385 MeV, half-life 20.4 min) provide better resolution. Fluorine-18

(^{18}F, $E_{max}(\beta^+)$ = 0.635 MeV, $E_{mean}(\beta^+)$ = 0.242 MeV, half-life 109.8 min) has the shortest positron range among these, offering high spatial resolution (Cherry *et al.*, 2012). Other commonly used PET isotopes are oxygen-15 (^{15}O, $E_{max}(\beta^+)$ = 1.73 MeV, $E_{mean}(\beta^+)$ = 0.735 MeV, half-life 2.03 min) and zirconium-89 (^{89}Zr, $E_{max}(\beta^+)$ = 0.902 MeV, $E_{mean}(\beta^+)$ = 0.395 MeV, half-life 78.41 h) (Kuchar & Mamat, 2015). The balance between radionuclide availability, image resolution and radiochemistry realities must be considered in PET tracer development planning.

2.1.3 Overview of PET imaging

PET is a powerful imaging modality that enables non-invasive visualization and quantification of metabolic and physiological processes *in vivo*. PET imaging was first used for clinical imaging in 1953 by Dr. Brownell and Dr. Aronov (Jones & Townsend, 2017) at Massachusetts General Hospital in Boston, USA. PET has since evolved into a widely used tool in medical diagnostics and research, particularly in oncology, neurology, and cardiology (Wagner, 1998; Cherry *et al.*, 2012). PET provides high-sensitivity functional imaging by detecting the pairs of gamma photons by PET scanner detectors. This allows image reconstruction of the tracer's distribution in the body in millimetre precision.

The concept of PET scanners has developed immensely since the first adaptation of the PET principle into scanners. The clinical PET scanners were significantly improved in the following decades with the introduction of time-of-flight (TOF) technology (Cherry *et al.*, 2012; Surti, 2015).

Recent advances in PET scanners include the development of more efficient radiodetectors. Zatcepin & Ziegler (2023) published an overview, highlighting two main types: scintillation and semiconductor detectors. Scintillation detectors, using photomultiplier tubes (PMTs) with materials like thallium-doped sodium-iodine (NaI(Tl)), lutetium yttrium orthosilicate (LYSO), and bismuth germanate (BGO), provide high light yield and fast response, making them suitable for TOF-PET and improving image quality. Semiconductor detectors, particularly silicon photomultiplier (SiPM) based ones, have superior spatial resolution (Moehrs *et al.*, 2006). The modern trend toward SiPMs in newer PET systems improves time resolution and imaging accuracy. The combination of detector materials and technologies to improve system performance aim to optimise energy resolution, spatial resolution, and sensitivity for more precise PET imaging (Zatcepin & Ziegler, 2023).

2.1.4 Combining PET with CT or MRI

PET is often combined with anatomical imaging techniques such as CT or MRI to form a hybrid imaging system i.e. multimodal imaging system for improved accuracy and clinical applicability by enabling the combination of the PET signal with an accurate anatomical reference (Ehman *et al.*, 2017). PET/CT is a far more common combination due to cheaper purchase and running costs, superior bone contrast, and is often established as the golden standard for tumour detection due to the better resolution. In addition, CT provides better attenuation correction, and better compatibility with the PET detector types with less artefact issues. CT is also faster (Ehman *et al.*, 2017). However, the MRI modality has advantages when better soft tissue contrast is needed, for example, in brain imaging. In some cases, PET/MRI has been shown to even outperform PET/CT in oncology (Singnurkar *et al.*, 2024; Zhang *et al.*, 2023). Modern high-end standalone MRI systems for human brain imaging can go up to 11.7 T, which can offer superior resolution (Boulant *et al.*, 2024). When combined with PET, a 9.4 T for preclinical PET/MRI has been developed, while the commercially available clinical PET/MRI go only up to 3 T, which compromises the MRI resolution (Perera Molligoda Arachchige, 2023). Non-commercial PET inserts have been developed to increase the clinical scanner magnetic field (Bogdanovic *et al*., 2022).

2.1.5 Development of total-body PET imaging

Total-body (TB) PET imaging represents a transformative leap in nuclear medicine, enabling the simultaneous imaging of the entire human body with high sensitivity and spatial resolution. Traditional PET systems have been limited by their restricted axial field-of-view (AFOV; typically 15–30 cm) (Chen *et al.*, 2024), requiring multiple consecutive scans at different bed positions to cover the entire body, making the scans much more time consuming. TB PET and long-axial field-of-view (LAFOV) systems, however, utilize extended AFOV detectors, allowing for whole-body imaging in a single bed position (Alberts *et al.*, 2023; Godinez *et al.*, 2024).

The concept of TB PET imaging was first proposed in the early 2000s, with researchers recognizing the potential benefits of increased sensitivity and reduced scan times (Cherry *et al.*, 2017; Cherry *et al.*, 2018). The first TB scanner, with an AFOV of 194 cm, was constructed in 2018. The system achieved a 40-fold increase in sensitivity, and faster scan times, in addition to enabling lower doses of radioactivity, and TB images with high resolution compared to conventional PET scanners. This enabled novel dynamic imaging of radiotracer kinetics simultaneously across the entire body (Badawi *et al.*, 2019). However, the introduction of LAFOV systems that image from head-to-thigh (vertex-to-thigh), that have an AFOV just over 100 cm, are much more affordable and have similar

extended capabilities compared to traditional short-axial field-of-view (SAFOV) scanners.

A very recent review by Mingels *et al.* (2025) explained some of the challenges and opportunities associated with TB PET/CT. Key challenges include the high cost of system development, the need for advanced reconstruction algorithms to handle the massive amount of data, and the optimisation of imaging protocols for clinical use. In addition, other practical challenges have been discussed, such as the increased noise (Daube-Witherspoon *et al.*, 2022), and much longer tubing for blood sampling and the consequential increased dispersion (Gu & Wu, 2023). A key challenge when combining LAFOV PET and RMA is the significantly decreased radioactivity concentration in plasma, due to reduced injected dose, which severely hampers the ability to perform RMA. To our knowledge, this issue has not been properly brought up in any publications. However, the opportunities are vast, including the ability to study systemic diseases in ways previously not possible. Mingels *et al.* (2025) also emphasized the potential for low-dose imaging, short acquisition times, delayed imaging, and dual-tracer protocols, which are now feasible with LAFOV and TB PET systems.

Other advantages, such as clinically relevant applications in TB PET have been discussed by Chen *et al.* (2024). These include, for example, improved detection of metastatic disease and better quantification and staging of tumours in oncology, short scan times while maintaining image quality, better accuracy for radiation dosimetry, and the lower dose, which improves staff and patient safety while reducing noise in images. In addition, simultaneous imaging of the brain and peripheral organs enable studies of the systemic interactions, for example, brain-gut interplays for Parkinson's disease research (Chen *et al.*, 2024).

2.2 PET tracers

2.2.1 PET tracers

PET imaging is based on PET tracers, which are synthesized and radiolabelled with a suitable positron emitting radionuclide often produced using a cyclotron. Some β^+-emitting radionuclides are produced using generators, such as ^{68}Ge/^{68}Ga generators in the case of ^{68}Ga (Dash & Chakravarty, 2019; Velikyan, 2015). The PET tracers are designed to bind to specific molecular targets to enable quantification and detecting of biological processes. They could target, for example, metabolic processes and reveal the metabolic status, such as with [^{18}F]FDG – a glucose analogue depicting glucose metabolism (Pauwels *et al.*, 1998). Alternatively, PET tracers could target specific ligands, antigens, receptors, and neurotransmitters in the body, to enable studying receptor availability, neurological, and psychiatric

disorders, and even to detect cancer (Pike, 1995; Trotter *et al.*, 2023; Nakamoto *et al.*, 2024). PET tracers can be also used for enzyme targets, neuroinflammation (Kreisl *et al.*, 2020), and immune activation, for example, in autoimmune conditions (Besson *et al.*, 2024). Also hypoxia can be studied with tracers, such as, [^{18}F]EF5 and [^{18}F]F-DPA (Saha *et al.*, 2024). Cardiac, and other perfusion imaging targets can be studied with [^{15}O]H_2O (Nesterov *et al.*, 2009; Maaniitty *et al.*, 2020; Knuuti *et al.*, 2023).

The most widely known and utilized PET tracer is [^{18}F]FDG, a glucose analogue that can be used to surrogate glucose metabolism. [^{18}F]FDG PET imaging has been the cornerstone in oncology for tumour detection, staging, and monitoring therapeutic responses, as cancer cells often express elevated glucose uptake. Also, [^{18}F]FDG is used in neurology for assessing cerebral glucose metabolism, and in cardiology for evaluating myocardial conditions, in addition to many other applications.

As an example of another PET tracer, [^{18}F]F-DPA targets the translocator protein (TSPO) associated with neuroinflammation (Keller *et al.*, 2018). By binding to TSPO, [^{18}F]F-DPA enables the assessment of microglial activation in rodents, and quantification of inflammatory cells in humans (Nutma *et al*., 2023).

The development of new PET tracers continues to enhance the ability to expand the applications and possibilities of PET imaging to study diverse biological processes *in vivo*, enabling improved diagnosis, drug research, and understanding of various diseases.

2.2.2 [^{11}C]SMW139 as a P2X7 receptor targeting PET tracer for microglial activation and neuroinflammation

The P2X7 receptor is a trimeric, adenosine triphosphate (ATP) gated cation channel belonging to the P2X receptor family, which forms one branch of the purinergic P2 receptor family (Sluyter, 2017). Purinergic signalling, first proposed by Geoffrey Burnstock in the 1960s, describes the role of extracellular nucleotides such as ATP in cell communication (Burnstock, 1972; Burnstock, 2014; Shmidt *et al.*, 2023). The P2 receptor family includes seven P2X receptors, which are ligand-gated ion channels. The P2X7 forms non-selective macropores that can permit the passage of molecules up to 900 Da (Shmidt *et al.*, 2023).

The P2X7 receptor is primarily expressed in all innate and adaptive immune system cells, including macrophages, monocytes, dendritic cells, and microglia, astrocytes, oligodendrocytes, and Schwann cells, and plays an important role in health and disease (Cai *et al.*, 2021; Ren *et al.*, 2021; Shmidt *et al.*, 2023). The P2X7 is critical for its antigen presentation characteristics affecting the immune system (Acuña-Castillo *et al.*, 2024). The P2X7 receptor is connected to numerous

pathological processes, including neurodegenerative diseases, chronic pain, autoimmune conditions such as rheumatoid arthritis, and cancer. The polymorphisms can alter receptor function, with some associated with either gain or loss of function, affecting disease susceptibility and treatment response (Shmidt *et al.*, 2023). Species differences must be considered in translational research, as the human, rat, and mouse P2X7 receptors differ significantly in ligand affinity (Hibell *et al.*, 2000).

Wilkinson *et al.* (2017) synthesised a group of benzamides, from which SMW139 showed to have good characteristics as an allosteric P2X7 receptor antagonist. This molecule stemmed from the work of Baxter *et al.* (2003), who developed potent adamant amide antagonists targeting the P2X7. The ^{11}C-labelled SMW139 tracer, [^{11}C]SMW139 (Figure 1), has emerged from this as a promising tool for PET imaging of microglial activation and neuroinflammation, particularly due to its affinity to the P2X7 receptor. Janssen *et al.* (2018) demonstrated its potential as a PET tracer for microglial activation in a rat model. The study validated [^{11}C]SMW139's specificity to human post mortem P2X7 receptor *in vitro*, although it had trouble showing differences in binding between the healthy control and Alzheimer's disease subject brain tissues (Janssen *et al.*, 2018). This study showed [^{11}C]SMW139 as a potential tracer for imaging neuroinflammatory processes, particularly in diseases like Alzheimer's disease and multiple sclerosis (MS).

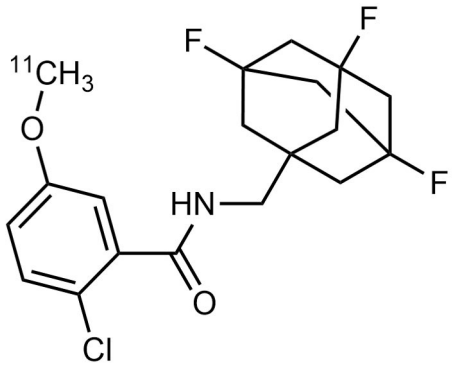

Figure 1. The molecular structure of 2-chloro-5-[^{11}C]methoxy-N-((3,5,7-trifluoroadamantan-1-yl)methyl)benzamide ([^{11}C]SMW139). *Created using Chemdraw 19.0. Modified from Study II.*

Hagens *et al.* (2020) conducted the first-in-human study of [^{11}C]SMW139 in active relapsing multiple sclerosis (RMS) and healthy controls (HC). The study reported higher [^{11}C]SMW139 uptake in RMS subjects compared to HCs, demonstrating its ability to detect neuroinflammation *in vivo*. This work provided

evidence for the utility of [^{11}C]SMW139 in clinical neuroimaging and its potential for staging MS progression (Hagens *et al.*, 2020).

Further validation was shown by Beaino *et al.* (2020), who used [^{11}C]SMW139 in the experimental autoimmune encephalomyelitis model of MS in Lewis rats. The study confirmed increased P2X7 receptor expression in pro-inflammatory microglia and specificity to P2X7 receptor through blocking studies with JNJ-47965567 (Beaino *et al.*, 2020).

Other PET tracers targeting the P2X7 receptor have also been developed, such as ^{11}C-GSK1482160 (Territo *et al.*, 2017), ^{18}F-PTTP (Fu *et al.*, 2019), and [^{18}F]JNJ-4413739 (Berdyyeva *et al.*, 2019).

2.3 Metabolite analysis

2.3.1 Metabolism of drugs

The metabolism of drugs in biological systems is a biologically vital and natural process. It is a critical component affecting the pharmacokinetics, being a part of the drug's absorption, distribution, metabolism, and excretion (ADME) properties. Understanding the metabolic pathways and their impact on ADME is essential for predicting and understanding drug behaviour, efficacy, and safety.

Drug metabolism reactions are generally categorized into two phases:

Phase I reactions concerns mainly functionalization reactions. These involve chemical modifications such as oxidation, reduction, and hydrolysis, bringing in new, changing existing, or uncovering functional groups to increase the molecule's polarity. The cytochrome P450 enzyme family, particularly CYP3A4, plays a significant role in these reactions (Zhao *et al.*, 2021a; Waller & Sampson, 2018).

Phase II reactions, also known as conjugation reactions. In this phase, the drug or its Phase I metabolites undergo conjugation with endogenous substrates like glucuronic acid, sulphate, or glutathione, resulting in more hydrophilic compounds that are easier to excrete (Ibrahim *et al.*, 2023; Waller & Sampson, 2018).

As metabolism alters the drug's lipophilicity, it affects the distribution of the drug's components in the body. Metabolites with increased polarity are less likely to cross cell membranes, potentially limiting their distribution to certain tissues (Yang & Hinner, 2015).

The specific impact of metabolism on the drug's ADME properties is critical. The first-pass metabolism, occurring for example, in the liver and intestines, can reduce the availability of orally administered drugs affecting the absorption. PET tracers are mainly administered intravenously (i.v.), but, for example, intramuscular injection, inhalation, and oral administrations are also used (Kapoor & Kasi, 2022; Wang *et al.*, 2022; Schimochi *et al.*, 2024). The mode of administration affects the

rate of availability in the blood circulation. Due to the strict time constrains and to limit gastrointestinal metabolism, i.v. injection is preferred. Also, intracranial injections are sometimes used in preclinical studies when drugs do not sufficiently penetrate the BBB, an example of such in a recent use of intracerebroventricular injections is published by Yang *et al.* (2025).

Drug metabolism can be characterized by the rate, extent, and individual metabolite profiles, which can vary significantly among individuals. This variability may be due to differences in enzyme quantity and activity, for example, of the cytochrome P450 family enzymes (Zanger & Schwab, 2013). Genetic polymorphisms can lead to enzyme catalysis or inhibition, resulting in altered drug metabolism (Ingelman-Sundberg, 2005). Impaired metabolism can lead to the accumulation of active drugs or toxic metabolites (Dreisbach & Lertora, 2008). Also, in drug pharmacokinetic studies it is important to understand the role of competing substrates, such as additional drugs that the individual is taking that share the same enzymes, transporters, receptors, plasma protein binding sites and endogenous substrates. Therefore, different individuals may experience variations in drug efficacy and differences in adverse effects.

The excretion abilities of drugs heavily depends on the increased polarity that metabolism enables in the administered drugs. Polar metabolites are typically excreted via the renal route (Waller & Sampson, 2018).

The metabolism of drugs can be substantially manipulated, enabling higher bioavailability of the drug to the target by inhibiting the metabolism pathways. One example of this is the use of carbidopa, an aromatic L-amino acid decarboxylase (AADC) inhibitor (Muranova & Shanina, 2023) to inhibit 6-[^{18}F]fluoro-L-DOPA ([^{18}F]FDOPA) metabolism (Melega *et al.*, 1990; Melega *et al.*, 1991; Tuomela *et al.*, 2013; Walker *et al.*, 2013). The dopaminergic system targeting PET tracer [^{18}F]FDOPA is used to study, for example, neuropsychiatric diseases, movement disorders, brain malignancies (Pretze *et al.*, 2014), and even malignancies of the pancreas (Kalliokoski *et al.*, 2014). [^{18}F]FDOPA has a substantial rate of metabolism, resulting in a reduction in its availability for brain uptake. However, when inhibitors, such as carbidopa is administered as an AADC inhibitor, it significantly reduces the peripheral metabolism of the parent tracer. This effect has been demonstrated in multiple species, including mice, rats, monkeys, and humans (Melega *et al.*, 1990; Tuomela *et al.*, 2013). The studies found that carbidopa pretreatment restricted [^{18}F]FDOPA metabolism predominantly to the formation of [^{18}F]3-OMFD. Consequently, the increased plasma levels of intact [^{18}F]FDOPA allowed for greater cerebellum uptake (Melega *et al.*, 1990; Tuomela *et al.*, 2013).

The ability to affect drug metabolism through co-administration of inhibitors, such as carbidopa, is particularly valuable in PET imaging, where the metabolic stability is crucial for sufficient uptake and signal-to-noise ratio, leading to accurate

quantification of tracer uptake in target tissues. As for reference tissue modelling for example, the radiometabolites need to be minimal (Salinas *et al.*, 2015). Reducing the interference from radiometabolites can enable more accurate reference tissue modelling. If such reference region is not obtainable due to a too high radiometabolite presence, then a radiometabolite-corrected AIF is usually needed (Ghosh *et al.*, 2020; van der Weijden *et al.*, 2023).

Drug metabolism has also been modified by deuterating the hydrogens in the tracer (Gant, 2014). Deuterium is a stable and nontoxic hydrogen isotope that, when incorporated into drug molecules, can enhance pharmacokinetic properties. By substituting conventional carbon–hydrogen (C–H) bonds with the stronger carbon–deuterium (C–D) bonds, deuterated drugs require more energy to reach the transition state. This improves their metabolic stability, especially against defluorination (Cargnin *et al.*, 2019; Liao *et al.*, 2025; Kuchar & Mamat, 2015). Such approaches have been used, for example, for the type 1 cannabinoid receptor agonist PET tracer [^{18}F]FMPEP-d_2 (Takkinen *et al.*, 2018; Ghosh *et al.*, 2020), and for the 18kDa translocator protein targeting [^{18}F]D_2-LW223, where its stability in plasma was compared to the non-deuterated version (Liao *et al.*, 2025). Deuterating the C–H does not in every case lead to altered metabolism of the drug. Sun *et al.* (2023) identified that deuterating the C–H increases the stability of the molecule mainly when applied to aliphatic chain parts of the molecule and not when the C–H hydrogens are substituted with deuterium in aromatic structures, as was the case with a demyelination tracer [^{18}F]3F4AP (Sun *et al.*, 2023).

2.3.2 Radiometabolite analysis (RMA) of PET tracers

Most PET tracers undergo the same natural metabolic processes as any other drug once administered into the body, resulting in radiometabolites circulating in plasma soon after its administration (Pike, 2009; Pike, 2016). These processes can rapidly decrease the fraction of the original PET tracer over all radioactivity in the blood. Some PET tracers are reported not to have any radiometabolites present in the brain, and good stability in plasma. For example, two recently developed TSPO binding tracers, [^{11}C]DPA-813 and [^{18}F]DPA-814, have shown 99% stability up to 45 min post injection in the brain (Beaino *et al.*, 2025). An example of a tracer with good stability in plasma is [^{18}F]FAZA, a PET tracer for imaging hypoxia. Its parent fraction was over 91% up to 40 min p.i. (Li *et al.*, 2020). The metabolism of the tracer, in addition to the efflux out of the bloodstream, decreases the concentration of the PET tracer in plasma, making it harder to analyse if the metabolism is fast. RMA is usually performed from plasma samples, but it is equally important to analyse the most critical tissue samples to understand for example, BBB penetration of the parent tracer and its radiometabolites (Ghosh *et al.*, 2020; Price *et al.*, 2001).

In addition, the radiometabolites interfere with interpretation of PET imaging data. This makes it essential to study the metabolism of PET tracers in the blood and tissues to understand their pharmacokinetics and correct for them. Radiometabolites formed during this process may have specific binding patterns and can accumulate in tissues or organs, leading to misinterpretation of PET data if they cannot be quantified and corrected for. Understanding the radiometabolite profile is therefore crucial for accurate PET quantification and for understanding the biological characteristics of the tracer (Ghosh *et al.*, 2020; Price *et al.*, 2001; Moein *et al.*, 2020). In addition to RMA of blood and tissue samples, radiometabolites often accumulate in urine at relatively high concentrations. Urine is easily collected, and its matrix is relatively clean, enabling RMA with minimal sample preparation. This makes it an accessible and informative sample type for assessing radiometabolites. Although this data is not required for the AIF, it provides valuable insight into the route of excretion and can help determine whether additional radiometabolites are formed during urinary excretion. An example of RMA from urine samples and it's correlation to plasma parent fraction was discussed by Chitneni *et al.* (2008).

Several methodologies and their variations are utilized in the various steps of PET RMA. These include radioHPLC (Rokka *et al.*, 2017; Declercq *et al.*, 2017; Luoto *et al.*, 2010), liquid chromatography-mass spectrometry (LC-MS; Varrone *et al.*, 2022, Ghosh *et al.*, 2020; Hashimoto *et al.*, 2015; Qiu *et al.*, 2024), radioTLC (Haaparanta *et al.*, 2006; Li *et al.*, 2020), micellar liquid chromatography (MLC; Schröder *et al.*, 2015), mixed MLC (Nakao *et al.*, 2013), semi-automated lead shielded microextraction by packed sorbents (SLS-MEPS; Moein *et al.* 2020), turbulent flow chromatography (Malherbe *et al.*, 2019), column-switching radioHPLC (Brugarolas *et al.*, 2022; Hilton *et al.*, 2000; Vasdev & Collier, 2016; Yu *et al.*, 1997; Werkhoven-Goewie *et al.*, 1983), SepPak columns for the polar fraction (Wang *et al.*, 1997; Golla *et al.*, 2015; Hagens *et al.*, 2020; Beaino *et al.*, 2025; Shields *et al.*, 2005), and ultracentrifugation (Ustsinau *et al.*, 2023). Also, techniques to quantify radiometabolites from exhaled gases, such as $[^{11}C]CO_2$, have been reported (Shields *et al.*, 1992). These techniques aim to provide both qualitative and quantifiable information about the radiometabolites, and to offer insights into their chemical properties.

Despite the long list of possible methodologies to assess the parent fraction, radioHPLC remains as one of the most commonly used methods. Having the HPLC effluent travel through a radioactivity detector, such as a flow-through scintillation counting radiodetector, radioHPLC can provide high-resolution separation and high-sensitivity radioactivity detection. The application of LC-MS adds specificity by allowing the identification of the mass-to-charge ratio of the radiometabolites, which further enables elucidating the structures of the radiometabolites (Ghosh *et al.*, 2020; Qiu *et al.*, 2024).

Ghosh *et al.* (2020) reviews and summarizes several RMA methodologies and presents some of the advantages and disadvantages of the methods that have been published by others. Ghosh states that while TLC is fast, inexpensive and can detect everything deposited on the plate, it has been mainly a qualitative method with limitations like accuracy, resolution and reproducibility and would not be suitable for RMA (Ghosh *et al.*, 2020; Malherbe *et al.*, 2019). However, many other studies have not seen these claims too limiting to exclude radioTLC method options and have successfully proven radioTLC to be an accurate method (Li *et al.*, 2020; Aarnio *et al.*, 2024). Autoradiography, which is sensitive and has a linear PSL response over a wide radioactivity range, enables quantifiable radioTLC analysis (Haaparanta *et al.*, 2006).

LC-MS, particularly with tandem mass spectrometry (LC-MS/MS) (Varrone *et al.*, 2022), has become increasingly popular in identifying radiometabolites, enabling greater accuracy. The pharmaceutical industry has also invested significant resources in using LC-MS to identify drug metabolites (Korfmacher, 2005; Ma *et al.*, 2010; Ludwig *et al.*, 2018).

LC-MS and LC-MS/MS-based methods offer a powerful tool for identifying metabolites by utilizing fragmentation patterns. In addition to revealing the mass-to-charge ratio of the molecule, its sensitivity is improved by the non-radiolabelled in addition to the radiolabelled fractions that are detectable using this method, increasing the concentrations of the detectable substances in the sample (Shetty *et al.*, 2013). Additionally, integrating MS with nuclear magnetic resonance (NMR) data can further aid in elucidating complex radiometabolite structures, providing valuable information for further tracer development (Qiu *et al.*, 2018; Ghosh *et al.*, 2020). Often, it is necessary to synthesise the expected metabolites separately or apply *in vitro* methods to obtain sufficient quantities for successful analysis (Amini *et al.*, 2013; Ludwig *et al.,* 2018).

Despite the vast progress in RMA methodologies, there are notable gaps in the literature regarding fully reporting the used methods. The lack of standardized protocols and detailed method reporting practices hampers the ability to validate the findings across laboratories, and limits comparability between studies. For example, many publications do not fully report the specific details, such as specific column, mobile phase gradients, and flow rate, making replication difficult. In addition, publishing sufficient exemplary radiochromatograms and reporting the exact way of interpretation and analysing the results is vital as the analysis can be performed in many different ways (Aarnio *et al.*, 2024).

2.3.3 Radiometabolite analysis (RMA) of [^{11}C]SMW139

The [^{11}C]SMW139 tracer was initially published by Janssen *et al.* (2018). Three other similar analogues were assessed in this work. The study included RMA in rats, revealing that [^{11}C]SMW139 undergoes metabolism, producing brain-penetrating radiometabolites. However, [^{11}C]SMW139 was the most stable of the four analogues and therefore selected for further studies. For RMA a tC18 SepPak (Waters, Milford, MA, USA) was used to elute first the polar fraction with water, and then with methanol and water to gain the non-polar fraction. The non-polar fractions were separated using HPLC and the collected fractions were measured using a gamma counter (Wizard 1470 or 2480, Wallac/PerkinElmer, Waltham, MA, USA). In plasma, there was 42 ± 2% of intact tracer remaining at 45 min post-injection (p.i.), while in brain the corresponding value was 66 ± 2%. Janssen *et al.* used MetaPrint2D-React metabolite predictor to predict the possible metabolites to be formed by hydroxylation of the aromatic ring or cleavage at the amide bond (Janssen *et al.*, 2018).

As the utility for imaging targets in the brain is highly dependent on the *in vivo* stability of [^{11}C]SMW139, each published study has involved RMA. In addition, the BBB penetration abilities of [^{11}C]SMW139 and its radiometabolites play a crucial role for understanding the modelling approach, so each study using [^{11}C]SMW139 have implemented RMA for plasma and brain samples, excluding Moein *et al.* who performed RMA only for the plasma samples (Janssen *et al.*, 2018; Hagens *et al.*, 2020; Beaino *et al.*, 2020; Moein *et al.*, 2020). Wilkinson *et al.* (2017) had initially performed *in vitro* stability experiments with rat liver microsomes on non-radiolabelled SMW139 and found significant increased plasma stability, compared to the same compound without the fluorine additions (Figure 1).

In the first-in-human study with [^{11}C]SMW139, Hagens *et al.* referenced a RMA method previously used for [^{18}F]DPA-714, published in the supplementary materials by Golla *et al.* (2015). However, the referenced method described by Golla *et al.* differed from that employed by Janssen *et al.*, as it involved direct radio-HPLC analysis of plasma samples without prior separation of polar and non-polar fractions using Sep-Pak extraction. In contrast, Hagens *et al.* briefly described a different procedure to have been used which aligns with the method reported by Janssen *et al.* Based on personal correspondence with the authors, it was clarified that they had used the method as described by Janssen *et al.* While Hagens *et al.* provided a comprehensive account of their kinetic modelling approach, the RMA results were neither presented nor discussed in the publication.

Beaino *et al.* (2020) investigated [^{11}C]SMW139 in the experimental autoimmune encephalomyelitis (EAE) model of MS in Lewis rats (*SsNHsd)*. The used RMA method was well described in the methods section. The method was identical as already published in the supplemental materials of Janssen *et al.* (2018). In plasma,

the unchanged fraction was 47 ± 10% at 45 min p.i, while in brain the corresponding value was 66 ± 11% (Beaino *et al.*, 2020).

Moein *et al.* (2020) developed a new method for [^{11}C]SMW139 RMA using SLS-MEPS. The study included comparing the SLS-MEPS to a protein precipitation RMA method with rat plasma samples. Both methods utilized radioHPLC. The protein precipitation method could only analyse up to 30 min, while the SLS-MEPS managed to enable analysis up to 60 min time point. The parent fraction in rat plasma with the SLS-MEPS method was 58.7 and 27.1 at 30 and 60 min time points, respectively. However, the protein precipitation method yielded a much lower value, 33.2%, at the 30 min time point (Moein *et al.*, 2020).

2.4 Sample preparation for RMA

Some literature on sample preparation techniques for the analysis of PET tracer radiometabolites exists, where various methodologies for improving the accuracy of PET imaging are explored (Moein *et al.*, 2019). However, reviews of the development of the techniques have not recently been published.

Effective sample preparation techniques are essential for clearing up the sample matrix, enabling better chromatographical separation. In addition, sample preparation can be used to concentrate the sample, for example, by using a capture column (Hilton *et al.*, 2000) in order to increase the signal-to-noise ratio. Some studies report to manage without or with minimal sample preparation for RMA (Malherbe *et al.*, 2019; Ustsinau *et al.*, 2023). Defining an absolute border between the sample preparation and the actual RMA method can be difficult. For example, the column-switching method (Hilton *et al.*, 2000) has integrated the sample matrix clean up and concentrating steps into the radioHPLC RMA method. Some interpret column-switching with the initial capture column, cartridge or solid-phase extraction (SPE) column or such being part of the RMA and not a sample preparation step as Ghosh *et al.* (2020) interpreted when column-switching was listed in a table of RMA methods and their need of sample preparation. Also, Nakao & Halldin (2013) reported of a simplified SPE method using a micellar medium for rapid determination of different PET tracers in plasma. The sample preparation is automated into the system through online SPE and offered lower backpressure. In this approach, plasma samples are mixed with a micellar eluent containing an anionic surfactant, such as sodium dodecyl sulphate, and loaded onto a SPE cartridge. The parent tracer is retained on the cartridge, while polar metabolites are eluted with the micellar medium. This technique allows for quick separation with minimal preparation time, making it suitable for even high-throughput RMA (Nakao & Halldin, 2013). Definition-wise, any step that for example, simplifies the sample matrix before the final separation could be considered as sample preparation even if

it is automated and built into a HPLC system. However, it is not easy to draw a definite border here.

The sample preparation for RMA of tissue samples often necessitates mechanical disruption to effectively and rapidly release the radiotracer and its radiometabolites into the supernatant. Common techniques include homogenization using a pestle, blade homogenizers, or sonication. However, care must be taken to prevent chemical alterations of the analytes during the process. Additionally, emulsions formed during tissue disruption can complicate subsequent analyses (Moein *et al.*, 2019; Ghosh *et al.*, 2020).

Protein removal by precipitation and centrifugation is a widely used technique to separate the dissolved proteins from plasma samples and to prepare the sample for chromatographic separation methods (Nakao *et al.*, 2013; Moein & Halldin, 2020). Protein remnants generally interfere with separation, and for example, may deteriorate or even clog HPLC columns (Moein *et al.,* 2019; Li *et al.*, 2020; Ghosh *et al.*, 2020), and cause unwanted secondary interactions, causing broader peaks and altered retention. A deteriorated column contributes to non-reproducible separation and decreasing the lifetime of a column, and it might not be recoverable even with extensive washing (Raval & Patel, 2020). Precipitation with organic solvents also disrupt the binding between the analytes and the proteins, increasing the extraction efficiency. Typically, an organic solvent such as acetonitrile (ACN) or acid such as trichloroacetic acid is added to the plasma, causing proteins to precipitate (Polson *et al.*, 2003). After centrifugation, the supernatant containing the extracted radiotracer and its radiometabolites is collected for further analysis. This method is straightforward and efficient for preparing samples prior to chromatographic separation (Ghosh *et al.*, 2020). The sufficient ratio of precipitation solvent-to-sample is crucial to achieve adequate protein removal. This depends on the precipitation solvent, temperature and sample being precipitated (Polson *et al.*, 2003). In addition to sufficient degree of protein precipitation, filtering the supernatant along with using, and frequent changing of guard columns are commonly advised preventative means to keep the HPLC column in good condition (Raval & Patel, 2020).

Other methods such as SPE, microextraction by packed sorbent (MEPS), and solid-phase microextraction (SPME; Reyes-Garcés *et al.*, 2017) have been compared for RMA and their sample preparation aspects (Moein *et al.*, 2019). These techniques offer advantages in handling small sample volumes and simplifying the extraction process (Moein *et al.*, 2015).

MEPS is a miniaturised form of SPE that integrates the extraction process in a syringe. In MEPS, a small amount of sorbent material, approximately 2–4 mg, is packed into the syringe (Moein *et al.*, 2015; Moein *et al.*, 2019). This configuration

allows for the direct extraction of analytes from various sample matrices, including biological fluids like urine and plasma.

The MEPS method involves several steps. Firstly, the sorbent is conditioned and activated using appropriate solvents to prepare it for analyte retention. Secondly, the sample is drawn into the syringe, allowing analytes to interact with and bind to the sorbent. Thirdly, the matrix components, usually the polar components, are eluted using a washing solvent through the sorbent. Finally, the retained analytes are eluted or desorbed using a small volume of a stronger elution solvent (Moein *et al.*, 2019).

The MEPS technique offers several advantages over traditional SPE. The technique is faster than SPE (1–4 min instead of 10–15 min), requires normally minimal amounts of solvents and sample volumes (10–100 µL), making it more environmentally friendly and cost-effective (Moein *et al.*, 2015). In addition, MEPS can be automated and coupled online with analytical instruments such as gas chromatography (GC) and liquid chromatography (LC) (Silva *et al.*, 2014; Yang *et al.*, 2017). The sorbent bed in MEPS can be reused tens or up to hundreds of times without significant loss of performance (Abdel-Rehim & Abdel Rehim, 2013; Moein *et al.*, 2015).

The MEPS technique is versatile and has been successfully applied in various fields, including pharmaceutical, environmental, and food analysis. Its ability to handle small sample volumes and integrate seamlessly with analytical instruments makes it a valuable tool in modern analytical laboratories (Yang *et al.*, 2017; Moein *et al.*, 2019; Moein *et al.*, 2015). Although it has some limitations. The syringe can be easily clogged, so dilution or protein precipitation with ACN or methanol prior to loading may be needed. Also, sample volumes only up to 500 µL can usually be used, and a limited range of sorbents for the right selectivity are available (Moein *et al.*, 2015).

On the other hand, also SPME, which was first introduced already in 1989 (Belardi & Pawliszyn, 1989), offers versatile sample preparation options and has been shown to be robust (Zhou *et al.*, 2008). However, the needed amount of sample volume (0.5–20 mL) and processing time is higher (10–20min) compared to MEPS, making it harder to use for short-lived radiotracers. In general, the SPME is based on biocompatible coated fibres that absorb or adsorb the analytes. They are consequently desorbed by gas in GC or liquid in LC. The SPME stationary phase is similarly reusable up to around 100 times (Reyes-Garcés *et al.*, 2017).

Out of these three versions, SPE is the most common as a sample preparation technique. It also offers efficient isolation and purification of radiolabelled compounds from complex biological matrices. Its application enhances the accuracy of RMA by ensuring cleaner sample matrix and the ability to concentrate the sample, enhancing the separation and detection possibilities (Pawelke, 2005). SPE methods

are based on cartridges packed with a stationary phase with various sorbent possibilities (Fontanals *et al.*, 2019).

In a study by Chitneni *et al.* (2008), an on-line SPE method was developed for the purification and analysis of various PET radiotracers. In addition, the same setup was utilized as an on-line sample preparation method for the RMA of cell homogenate, plasma, and urine samples. Utilizing gamma counting of the fractions separated by HPLC with an SPE Oasis HLB cartridge, the approach allowed for the effective separation of radiotracers from their radiometabolites without prior protein precipitation. The method demonstrated high recovery rates (>91%) (Chitneni *et al.*, 2008).

SPE, especially online SPE, SPME and MEPS remain as useful techniques, although they are not that often seen as the sample preparation method of choice in the latest PET tracer RMA publications. However, recent trends and development can be seen when reading publications from other fields, such as for SPME by Kataoka *et al.* (2024) and online SPE by Šrámková *et al.* (2022).

Sample preparation can be a rather lengthy process. For PET tracers, the race is against the radioactive decay. As SPE is not usually set as an online method, it can be time consuming as a multi-step process. Therefore, the method length ought to be an important factor when assessing the right method, and automation may save a considerable amount of time (Chitneni *et al.*, 2008; Ghosh *et al.*, 2020). Another important factor to consider in addition to the effects on preparation time, hence to the percentage decayed, is the influence to the analytes and recovery of the radioactivity (Pawelke, 2005).

Pawelke (2005) summarized the sample preparation techniques for *in vitro* RMA. As it is important to study both the radiometabolites excreted into the medium and the lysate (contents of the cells) to reveal the metabolism inside the cells, specialized sample preparation needs to be considered for both methods. Usually, the liquid phase is separated from the solid cell fraction. Pawelke mentions protein precipitation with different organic solvents or strong acidification, followed by reconditioning of the sample matrix to be suitable, for example, for HPLC. To separate the lysate centrifugation or suction of solvents are proposed (Pawelke, 2005).

In summary, various sample preparation techniques are employed in PET RMA, each with its advantages and limitations. The choice of method depends on factors such as the nature of the biological matrix, the properties of the radiotracer and its radiometabolites, and the specific requirements of the study. In addition, the initial amount of radioactivity and the used radionuclide and its characteristic half-life determines the amount of decay time that can be tolerated.

2.5 Extraction efficiency

The extraction efficiency in RMA is a crucial parameter to consider for accurate parent fraction analysis, consequently affecting the AIF. This is also true in any field of analytical chemistry where sample preparation is needed for quantitative analysis (Steiner *et al.*, 2020). Poor extraction efficiency can cause significant errors. In most RMA methods, sample preparation is essential. Usually this means that only part of the original sample is carried over into the final analysis phase. This poses a risk that part of the radiolabelled analytes are not analysed. So, the sample recovery rate, which encompasses all of the steps from start to finish, should be examined.

However, when only the fractions of radioactivity are needed, complete recovery may not be necessary as long as the following two conditions are met: (1) the radioactivity in the remainder part has the same radiolabelled molecules in the same fractions, and (2) the signal-to-noise ratio remains sufficient. These conditions are not always fully met, so the extraction efficiency needs to be measured. The extraction efficiency is defined as the fraction of radioactivity extracted, for example, from the plasma sample into the supernatant. The extraction efficiency is a subcomponent of the sample recovery rate. Sample preparation methods that do not lose any radiolabelled analytes such as presented by Ustsinau *et al.* (2023) should be preferred as long as they are sufficient in enabling robust RMA methods. Otherwise, the measuring of the sample recovery rate and extraction efficiency and appropriate corrections should be performed, as demonstrated by Finnema *et al.* (2018).

Sometimes only maximizing the extraction efficiency is not the optimal aim, as it might require an impractically large solvent volumes or time-consuming steps. The radioactivity concentration might be decreased dramatically due to the large solvent volume and radioactive decay. Instead, the radioactivity concentration should be considered during sample preparation optimisation, as discussed by Aarnio *et al.* (2024).

One method to increase the extraction efficiency is by extracting the same sample in two phases as was done by Ueberham *et al.* (2023). In a study with [^{18}F]LUZ5-d_8 targeting the cannabinoid receptor type 2, they extracted the plasma and brain sample in consecutive extractions. In short, after the first supernatant was collected, the precipitate was re-dissolved in a small volume (100 µL) of extraction solvent, and the extraction procedure was repeated and the supernatants were combined. One reason for this system working well is that the supernatant was concentrated under 70 °C argon stream, increasing the radioactivity concentration. The overall extraction efficiencies when using methanol:water (9:1, *v/v*) and ACN:water (9:1, *v/v*) were 94% and 89%, respectively. However, the effect of this second round of extraction was not reported, and further studies are needed to quantify its impact.

Most studies do not report the actual extraction efficiency values. Reporting them would be a valuable addition for assessing the credibility of the used methods. Lee *et al.* (2020) showed the reproducibility of the extraction efficiency measurements of 10 subjects with 10 samples from each and including another set of retest measurements. The reported extraction efficiency was 79.6(6.4)% for the first set and 82.5(5.7)% for the retest, showing no significant differences between the two ($p>0.10$).

Moein *et al.* (2020) optimised their SLS-MEPS RMA sample preparation method for [^{11}C]SMW139 according to the extraction efficiency and radiodetector response. They concluded that a certain speed for the plunger and volume of the organic solvent had the optimal combination for these two. The method was automated to reduce the variation due to manual operations (Moein *et al.*, 2020).

In the first in *in vivo* rat study of [^{11}C]SMW139, Janssen *et al.* (2018) evaluated the extraction efficiency for brain samples. Janssen *et al.* concluded that despite optimising the method, the extraction efficiency from brain homogenates was only 62(3)%. The extraction efficiency for plasma samples was not discussed.

The effect of the extraction efficiency to the plasma TAC in cases where, for example, liquid-liquid extractions are used to extract the components is discussed by Ma *et al.* (2010). The parent and radiometabolite fractions that are left in the phase, which is not analysed, might be different from what was in the analysed fraction leaving some potential for errors. Typically, plasma radioactivity is measured directly from the initial plasma sample and multiplied with the parent fraction to gain the plasma TAC (van der Weijden *et al.*, 2023).

2.6 Plasma protein binding (PPB)

2.6.1 Human serum albumin (HSA)

HSA is a very thoroughly studied protein found in the human blood. It is the most abundant protein in human plasma, with a reference concentration of 35–50 g/L and a molecular weight of 66,348 Da. It primarily functions as a carrier protein for endogenous and exogenous substances, including peptides, fatty acids, hormones, amino acids, drugs, nutrients, metal ions, steroids, and fatty acids, while also contributing to plasma oncotic pressure, stabilising extracellular fluid volume and regulating the pH of the blood (Mishra & Heath, 2021; Siddiqui *et al.*, 2019; Siddiqui *et al.*, 2021).

The primary binding sites for lipophilic drugs in HSA are hydrophobic cavities within subdomains IIA (site I), IIIA (site II), and IB (site III) (Siddiqui *et al.*, 2021; Ghuman *et al.*, 2005).

Serum albumin plays a crucial role in drug pharmacokinetics by affecting drug ADME. In circulation, drugs exist in bound and unbound forms, where only the free fraction is metabolised and excreted and can pass through membranes (Otagiri, 2005; Otagiri, 2009). The bound portion acts as a reservoir, prolonging drug half-life, while the unbound drugs can interact with therapeutic targets (Tesseromatis & Alevizou, 2008).

The binding affinity of drugs to HSA significantly influences their pharmacological properties. Strong binding prolongs drug biological half-life and may lead to unwanted effects, such as the need for elevated drug total concentration to reach the desired effective concentration of the free drug, slower distribution to the desired sites, and it may take longer to eliminate from the body. However, too weak binding may affect drug delivery to target sites negatively by allowing the drug to aggregate or remain less soluble in the biological matrix. Therefore, optimal binding affinity is necessary for achieving therapeutic efficacy (Ghuman *et al.*, 2005).

The study of HSA-drug interactions can be performed with various techniques, including UV–visible spectroscopy, fluorescence spectroscopy, and synchronous fluorescence. Other advanced methods like isothermal titration calorimetry, and Fourier transform infrared spectroscopy, and Förster resonance energy transfer can be used in characterising HSA-drug interactions. Additionally, *in silico* (computational) approaches such as molecular docking and molecular dynamics simulations provide valuable insights into binding mechanisms (Siddiqui *et al.*, 2021).

2.6.2 Plasma protein binding analysis (PPBA) in drug research

PPB is a critical parameter in drug research, as it influences the pharmacokinetics and pharmacodynamics of the drug. Likewise, it affects PET radiotracer development. PPB refers to the fraction of a drug or radiotracer bound to plasma proteins (e.g., HSA, transthyretin, α1-acid glycoprotein). The drug-PPB is often reported as the plasma free fraction, f_P, which represents the fraction of unbound, biologically active drug fraction available for tissue uptake. Accurate measurement of PPB of the parent tracer is essential for interpreting PET data and developing accurate quantitative kinetic models (Moein *et al.*, 2019; Vuignier *et al.*, 2010; Amini *et al.*, 2014; Pike, 2009). As a note, some references use f_P to mean plasma free fraction, especially in non-PET related drug studies. However, in some sources, especially PET related, and in this thesis, the P in f_P is used to emphasize the parent free fraction, as especially in this thesis it needs to be separated from the radiometabolite free fraction (f_M).

Several methods have been developed for analysing PPB in drug research (Moein & Halldin, 2020; Vuignier *et al.*, 2010). These include, for example, ultrafiltration (UF) (Castiaux *et al.*, 2018; Kratzer *et al.*, 2016; Patt *et al.*, 2014; Lee *et al.*, 2020; Zoghbi *et al.*, 2006), ultracentrifugation (Dimitrijevic *et al.*, 2023), microdialysis (Sun *et al.*, 2014), equilibrium gel filtration (Isbell et. al, 2018), LC-MS (Atcheson *et al.*, 2003), affinity microcolumns in high-performance frontal analysis (Amini *et al.*, 2014; Anguizola *et al.*, 2013; Matsuda *et al.*, 2015; Zhang & Hage, 2019), and rapid equilibrium dialysis (RED) (Dimitrijevic *et al.*, 2023; Wiltschko *et al.*, 2023; Waters *et al.*, 2008; Ye *et al.*, 2017; Shave *et al.*, 2020; Thermo Fisher Scientific, (21.1.2025)). Among these, equilibrium dialysis (ED) (Gunn *et al.*, 2012; Srivastava *et al.*, 2021) being one of the most common methods, is considered the golden standard in most traditional drug research fields (Barton *et al.*, 2007). ED has been used for PPB studies related to PET tracers, though only with *in vitro* samples and with non-radiolabelled compounds and analysed using LC-MS/MS (Gunn *et al.*, 2012). However, the ED technique has its drawback too. The use of ED for plasma protein binding analysis (PPBA) especially for *in vivo* samples when using short-lived radioisotopes is not feasible. This is due to the very long equilibrium formation times (Lindberg *et al.*, 2023) causing too much radioactive decay and as the tracer and radiolabelled free parent tracer concentrations in plasma are already extremely low – in the range of picomoles per millilitre. When PET radioisotopes are used that have a longer half-life, like zirconium-89, the minimum total time for running the samples is not that critical. Although, the compound needs to be stable in the ED buffer when using this method. Even for the rapid version of ED, RED, the equilibrium time according to the manufacturer is at minimum 3-5 hours (Waters *et al.*, 2008; Thermo Fisher Scientific, (21.1.2025)). When using ^{11}C or ^{18}F-radioisotopes, a 4 h protocol results in having only 0.03% or 22%, respectively, of the original radioactivity left in the sample. In addition, for many tested compounds the equilibrium time is found to be much longer (Wiltschko *et al.*, 2023). The ED devices take even longer to analyse the sample with a minimum of 16 hours.

Other shortcomings of the ED are non-specific binding of the semipermeable membrane, buffer volume shifts due to the oncotic pressure, or colloid osmotic pressure difference that relates to the different amounts of large particles, like proteins on the different sides of the membrane, in addition to the Donnan effect due to the ionic differences (Vuignier *et al.*, 2010). Some of these effects can be minimized and corrected for (Srivastava *et al.*, 2021). However, the accumulation of error sources add up to make this technique more prone for errors and include complicated correction protocols (Barton *et al.*, 2007).

UF is a widely used technique to determine the PPB of PET tracers in plasma. Sometimes it is called ultracentrifugation (Patt *et al.*, 2014), probably by mistake.

Ultracentrifugation is a different principle where filtration devices are not used. The differences between UF and ultracentrifugation techniques are explained by Dimitrijevic *et al.* (2023). The ultrafiltration method involves separating the free unbound tracer from the protein-bound tracer using a semipermeable membrane, traditionally under centrifugal force. The concentration of the free tracer in the filtrate is then measured to calculate the f_P by dividing it with its original concentration in the plasma (Castiaux *et al.*, 2018).

The non-specific binding to membranes have been acknowledged to have an effect on results that utilize semipermeable membranes (Srivastava *et al.*, 2021). Only the hydrophilic substances are expected to have lower binding to traditional membranes compared to less hydrophilic substances. However, there are exceptions to these (Dimitrijevic *et al.*, 2023).

Patt *et al.* (2014) utilized UF to evaluate the PPB of (-)-[^{18}F]Flubatine, a PET tracer targeting the nicotinic acetylcholine α4β2 receptor (Sabri *et al.*, 2015). Possible membrane correction was not reported. Their findings indicated that 15(2)% (mean(SD)) of the tracer was bound to plasma proteins, which can be considered a very low level of PPB. Also, the tracer was very stable in plasma. This low binding profile with low metabolism rate is advantageous for PET imaging as it ensures that a sufficient part of the initially injected tracer is in the free form and is available for the target (Patt *et al.*, 2014).

Especially, for intravenously injected PET tracers that target the brain, a high f_P is important as only the free fraction can penetrate into the brain. There are many additional factors that influence the BBB penetration too, such as low molecular weight and high lipophilicity (partition coefficient (logP) = 2–3.5) are favoured. However, high lipophilicity often goes hand-in-hand with low f_P. For example, the widely used [^{11}C]PK11195 suffers from several limiting properties, such as low f_P (Sokias *et al.*, 2025; Salerno *et al.*, 2024). In addition, charged molecules have decreased ability to passively diffuse due to their decreased solubility to the BBB's lipid bilayer. Also, the hydrogen bonding ability, especially as a donor, limits the BBB penetration capability (Gunn *et al.*, 2012; Lindberg *et al.*, 2023; Pike, 2009; Waterhouse, 2003).

Other recently developed PET tracers have also reported to suffer from low f_P. In the case of molecular spherical nucleic acids (MSNA), Auchynnikava *et al.* (2025) reported low f_P hindering the analysis of RMA of the developed MSNA tracers.

Analysing PPB with exactness can be very challenging as multiple sources of error are present in each technique (Nilsson, 2013). Therefore, when the fraction of PPB is lower than 0.01, then even small errors have significant impact in the availability outcome. In 2017, Di *et al.* pointed out how regulatory agencies mandate the assessment of PPB in drug-drug interaction studies. To ensure conservative estimates, regulatory agencies recommend using a lowest limit of 0.01 for the

unbound fraction in highly bound compounds, regardless of actual measurements. While this approach reduces false negatives, it may lead to excessive false positives, resulting in unnecessary clinical trials, stricter inclusion criteria, and increased costs and delays in drug development. The review by Di *et al.* examines current PPB measurement methods and key factors influencing their accuracy and precision. They concluded that accurate PPB values below 0.01 could be reliably measured using appropriate PPB methods. Ongoing efforts aim to refine PPB measurement techniques, which in turn can aid also in improved drug-drug interaction predictions (Di *et al.*, 2017). Other researchers (Riccardi *et al.*, 2015) have pointed out similar criticisms.

For separative PPB methods, such UF, that rely on separating the plasma water and the free analytes it contains from the proteins, the depletion of analytes and its effect on the delicate equilibrium should be taken into account (Theodoridis, 2006; Jiao *et al.*, 2018). Theodoridis *et al.* (2006) explains the benefits of SPME as a non-depleting method which maintains the equilibrium during analysis. UF can be considered as only negligibly or non-depleting if only a small fraction of filtrate is filtered.

To our knowledge, the PPB of radiometabolites has not been measured or discussed earlier in PET related literature. However, at least one study has reported an *in vitro* PPB analysis of non-radiolabelled metabolites of verinurad via ultracentrifugation (Gopaul *et al.*, 2021). Additionally, to our knowledge, the PPB of [^{11}C]SMW139 has not been previously reported.

2.7 Modelling PET data

Quantitative PET imaging data analysis relies on an accurate AIF, which is typically derived from manual arterial plasma measurements or as an image derived input function (IDIF) from the PET image, to quantify biological processes. The measured signal in PET reflects both the parent radiotracer and its radiometabolites, which makes interpretation impossible without understanding the metabolism and their biodistribution (van der Weijden *et al.*, 2023). In addition, analysing the extent of PPB helps understanding the kinetics better which may aid in choosing the correct modelling approach.

Usually, the primary aim of using PET tracers and PET data modelling is to extract physiologically meaningful parameters such as the net rate of influx (K_i), binding potential (BP) and volume of distribution (V_T) to quantify the target of the PET tracer (van der Weijden *et al.*, 2023). For example, the [^{11}C]SMW139 tracer is used to quantify P2X7 receptors expression *in vivo* (Hagens *et al.*, 2020).

The non-displaceable binding potential (BP_{ND}) represents the ratio of specifically bound radiotracer to its free concentration in tissue (k_3/k_4) (Hagens *et al.*, 2020). The

V_T, on the other hand, reflects the equilibrium ratio of tracer concentration in tissue to plasma (Mansoor & Mahabadi, 2023).

To estimate these parameters accurately, compartmental modelling and reference tissue modelling are used. The compartmental models use a radiometabolite-corrected plasma input function to describe tracer kinetics, yielding V_T, whereas reference tissue models bypass arterial sampling by using a reference region which does not have specific binding of the tracer (Tonietto *et al.*, 2015; van der Weijden *et al.*, 2023; Salinas *et al.*, 2015). When using subjects with potentially disrupted BBB, such as in MS, it hinders the use of a reference region. Likewise, using the reference tissue modelling is impossible, if the whole brain area has the target present, and no reference region can be found (van der Weijden *et al.*, 2023), as it is the case of P2X7 in the brain (Hagens *et al.*, 2020). For using full kinetic modelling, such as compartment modelling or graphical methods like Logan and Gjedde-Patlak plots, the correction for radiometabolites is essential to ensure reliable quantification of the PET signal (Ghosh *et al.*, 2020; Zhou *et al.*, 2010).

Hagens *et al.* (2020) compared different kinetic modelling approaches to identify the optimal model for [^{11}C]SMW139. Single-tissue and two-tissue compartment models were used to model the tissue time-activity curves. The Akaike information criterion (AIC) was used to estimate the best fit to the models (Akaike, 1974). The best model from these options was the reversible two-tissue compartment model, using the blood volume parameter (V_B) and the dissociation rate (k_4) fixed to the whole-brain value (Hagens *et al.*, 2020).

In a typical two-tissue compartment model, the radiotracer's behaviour is described by the free tracer in tissue and the tracer specifically bound to the target receptor. The kinetic processes are described by the following rate constants: k_1 is the rate of tracer transfer from plasma to tissue, k_2 is the rate of tracer clearance from tissue back to plasma, k_3 is the rate of the tracer binding to the target receptor, and k_4 is the rate of tracer dissociation from the target receptor (Gunn *et al.*, 2012; Salinas *et al.*, 2015). In the case of [^{11}C]SMW139, the k_4 represents the rate that the [^{11}C]SMW139 returns from the bound state in the brain back to the unbound state in the brain, which was needed by Hagens *et al.* (2020).

3 Aims

The purpose of this thesis was to develop robust and novel methods for analysing samples from study subjects to characterise the behaviour of the PET radiotracer [^{11}C]SMW139 *in vivo*. Specifically, the aim was to take into account the various corrections to plasma TACs, by considering the radiometabolites and plasma protein-free fraction of [^{11}C]SMW139, thereby ensuring more precise quantification of the tracer pharmacokinetics.
The main specific objectives for each studies were:

Study I To develop fast and reproducible sample preparation and RMA methods for [^{11}C]SMW139. The methods were used for mouse plasma and brain samples to enable parent fraction corrections for plasma and brain time-activity curves (TACs). Additionally, the study aimed to enhance the understanding of [^{11}C]SMW139 tracer kinetics in the APP/PS1-21 mouse model of Alzheimer's disease.

Study II To study the high flux of [^{11}C]SMW139 radiometabolites through the BBB by developing a rapid and robust method to analyse the parent fraction and plasma protein-free fractions simultaneously from the parent tracer and its radiometabolites by further applying the methods developed in Study I. The developed method is used to study PPB from mice injected with [^{11}C]SMW139.

Study III To develop RMA methods and further utilise the plasma and brain RMA preclinical and clinical findings of the [^{11}C]SMW139 tracer and its radiometabolites to explain the accumulation of radiometabolites into the human brain. The aim was to improve the approach of modelling of the PET data of human subjects'.

Study IV To study the usability of [^{11}C]SMW139 in analysing differences between MS and HC subjects by utilizing parent fraction data in addition to parent and radiometabolite free fraction analysis data to accurately quantify the differences in the tracer uptake.

4 Materials and methods

All work with radioactivity complied with the regulations of the Radiation and Nuclear Safety Authority (STUK) in Finland.

4.1 PET tracer [^{11}C]SMW139

In this thesis, all the studies (Studies I–IV) included the PET tracer [^{11}C]SMW139. In Study I, [^{18}F]F-DPA was also used, but this thesis focuses only on the RMA and PPBA aspects of the [^{11}C]SMW139 tracer.

4.1.1 [^{11}C]SMW139 synthesis method

The [^{11}C]SMW139 was synthesized in the Radiopharmaceutical Chemistry Laboratory of Turku PET Centre for all the studies performed in Turku. For the Study III the subjects imaged in Karolinska Institutet received the tracer batch from their radiochemistry site. Shortly, the method used in Turku: [^{11}C]CO_2 was produced via the ^{14}N(p,α)^{11}C reaction using nitrogen with 0.2% oxygen and 17.5 MeV protons (ACSI TR19, Advanced Cyclotron Systems, Inc., Richmond, BC, Canada). [^{11}C]CO_2 was reduced to [^{11}C]CH_4 by H_2/Ni at 370 °C, trapped on Carbosphere at −196 °C, and released by heating. It was mixed with iodine vapour at 100 °C, followed by a radical reaction at 720 °C to form [^{11}C]CH_3I, which was trapped on Porapak Q and released at 190 °C. [^{11}C]CH_3I was reacted with 0.5 mg desmethyl-SMW139 precursor (School of Chemistry, The University of Sydney, Australia) in DMSO/NaOH. The mixture was purified by HPLC (Phenomenex Luna C18 (10 µm, 250 × 10 mm), ACN:0.1% trifluoroacetic acid (TFA), 50:50, 5 mL/min). [^{11}C]SMW139 was collected (SepPak C18 light, Waters, Milford, MA, USA), washed with water, eluted with ethanol, and formulated with phosphate buffer and propylene glycol before sterile filtration (0.22 µm Millex® GV filter, Millipore).

The full synthesis method description used in Turku can be found from the supplemental materials in Study II. Likewise, the method used in Karolinska Institutet can be found from the supplemental materials in Study III.

4.1.2 Tracer synthesis quality control and molar activity determination

The tracer quality control and molar activity (A_m) determination methods used in Turku site are described in the supplemental materials of Study II. In short, the radiochemical purity, radiochemical identity, tracer stability and the A_m was analysed using a radioHPLC. The analytical method used was as follows: SymmetryShield RP18 column (5 µm, 150 × 3.0 mm) with 1 mL/min flow using an isocratic gradient of 43% ACN and 57% ammonium phosphate (0.01 M, pH 2.5).

The non-radioactive SMW139 reference was used to determine the retention time (R_t; 7.34 min) and the A_m was calculated as the radioactivity of the [^{11}C]SMW139 in GBq divided by the amount of the carrier substance in µmol.

The corresponding analyses for the batches produced in Karolinska have minor differences to the method described above. They are found in the supplemental materials of Study III.

4.2 Study subjects

4.2.1 Preclinical studies (Studies I–III)

In the preclinical Studies I–III using [^{11}C]SMW139, C57BL/6J mice were used as the study subjects. In Studies I and II, in accordance to the replacement, reduction, and refinement (3R) principle, all data collected from the subjects were utilized across multiple studies where applicable.

In Studies I and II, a total of 73 mice (43 females and 30 males; weight: 31.7 ± 5.5 g, n = 45 wild type and n = 28 transgenic) were used. In addition, in Study III, 11 mice were used (all female and transgenic; weight: 34 ± 4 g; age: 8.7 ± 1.9 months).

All animals were bred and maintained in the Central Animal Laboratory of University of Turku according to the guidelines of the International Council of Laboratory Animal Science (ICLAS). The studies were performed in accordance with the European Ethics Committee (decree 86/609/CEE).

The animal studies were approved by the Project Authorization Board in Finland and the Regional State Administrative Agency for Southern Finland (license numbers: ESAVI/16273/2019 and ESAVI/16273/2019) and they were performed in accordance with the EU Directive 2010/63/EU on the protection of animals used for scientific purposes. The current ARRIVE guidelines (Kilkenny *et al.*, 2010; Percie du Sert *et al.*, 2020) of the time of the study were followed.

4.2.2 Clinical studies (Study III–IV)

All participants provided written informed consent before undergoing study procedures. The studies were approved by the Ethics Committee of the Hospital District of Southwest Finland and the Scientific Project Group of the Turku PET Centre. The studies were conducted according to the principles of the Declaration of Helsinki, including its later amendments.

The Study III was registered as a clinical trial in the EudraCT database (2017-001585-19).

Demographics and the related human study subject information from Studies III and IV are shown in section 5.2.

4.3 Radiometabolite analysis

The RMA i.e. the parent fraction analysis was performed in order to assess the metabolic rate of [^{11}C]SMW139, and to enable quantification of the true input function to the target. Various analytical methods were tested and developed during the studies. The following sections introduce these methods and presents the studies in which they were applied.

4.3.1 Blood sampling and sample preparation

For the clinical studies (Studies III and IV), about 2 mL of arterial blood was drawn via a catheter placed in the radial artery and collected into lithium-heparin tubes (Vacutainer, Becton, Dickinson and Company, Franklin Lakes, NJ). For the preclinical studies (Studies I–III) a volume of 200–500 µL of arterial blood was drawn via cardiac puncture under deep isoflurane anaesthesia and collected into heparin-gel tubes (Microtainer, Becton, Dickinson and Company).

To analyse radiometabolites using radioTLC or radioHPLC, the sample matrix was simplified by separating plasma from the red blood cells through centrifugation. Preclinical samples were centrifuged at 12,100 × g for 90 s at room temperature, while clinical samples were centrifuged at 3,100 × g for 5 min at +4 °C.

The post injection sample collection time points were optimised separately for each study.

The plasma proteins were removed by protein precipitation with the addition of ACN with the plasma to ACN ratio of 1:1.4 for the HPTLC and radioHPLC methods, and 1:2 (*v/v*) for the TLC method. The mixture was then vortexed and centrifuged (3,370 × g for 3 min for the clinical samples analysed with radioHPLC, and 12,100 × g for 90 s for preclinical samples analysed using HPTLC or TLC). The resulting plasma supernatant was used in the HPTLC, TLC or radioHPLC analysis as described in the following sections.

4.3.2 Sample preparation of mouse brain samples

The parent fraction of [^{11}C]SMW139 from mouse brain tissue homogenates was analysed in Studies I–III using HPTLC, TLC and radioHPLC. The methods for brain tissue RMA were developed during the studies for the plasma RMA.

Brain samples were obtained from saline-perfused mice and processed as follows: When whole brain slice autoradiography was needed, only a small piece of the cortex was used. In cases where the brain was not sliced for autoradiography, a larger, more representative cross section of the whole brain was used.

The brain sample was placed into a glass homogenizer with tweezers. The tissue was first ground without adding any solvent. Then the homogenizing solvent (Studies I and II: eluent, and Study III: ACN:water solution (9:1, *v/v*)) was added by small increments and the mixture was homogenized until 50-100 µL of the sample could be transferred into an Eppendorf tube. The tube was centrifuged to separate the solids, and the resulting clear supernatant was collected for RMA.

4.3.3 HPTLC

In Study I, the initial method for analysing the parent fraction of [^{11}C]SMW139 used a high-performance thin-layer chromatography plate (HPTLC, silica gel 60 RP-18, art. No. 1.05914.0001, Merck KGaA, Darmstadt, Germany). On the application line a [^{11}C]SMW139 standard sample, plasma supernatants (maximum 8 µL), and brain homogenate supernatants (maximum 8+8 µL with a short drying period between the 8 µL increments) were applied onto the same plate.

The mobile phase consisted of ACN, water, and TFA in a volumetric ratio of 75:25:0.1 (*v/v/v*). Chromatographic separation was performed in a 10 × 10 cm Twin Trough Chamber (Camag, Muttenz, Switzerland), with 5 mL of the mobile phase in each compartment. The elution time for a 4 cm solvent migration distance took 35-50 min. After elution, the corners of the application line and solvent front were marked with a few microliters of radioactive standard to enable retardation factor calculations. The distribution of radioactivity on the HPTLC plate was digitized using autoradiography as explained in Section 4.3.5.

4.3.4 TLC

During Study I, the RMA method was improved as a faster method with better resolution was developed. This new TLC method was also used in Study II RMA, and in Studies II and IV to separate the non-protein-bound (protein-free fractions) parent and radiometabolites from each other in the ultrafiltrate. The steps of the RMA method are the same as used in HPTLC, with the following changes: A TLC plate with a larger particle size (Silica Gel 60 RP-18, Merck KGaA, art. No.

1.05559.0001) was used as the stationary phase. The maximum application volume for plasma and brain was 16 µL and the mobile phase was ACN:water:TFA (65:35:0.1, *v/v/v*). A larger volume of the brain sample could have been applied in small batches, but the amount of radioactivity was high enough in this study already with this volume. The elution time for a 4 cm solvent migration distance was 6 min.

4.3.5 Autoradiography for quantification of radioactivity in TLC and HPTLC plates

When autoradiography was used in Studies I–III to convert radioactivity in the TLC or HPTLC plates into quantifiable digital data, then the following procedure was followed:

BAS-TR2025 autoradiography imaging plates (Fuji Photo Film Co., Ltd., Tokyo, Japan) were used. To eliminate background signal accumulation, the plates were erased immediately before use with a storage phosphor screen eraser (BAS-1000, Fuji Photo Film Co.). The rapidly blow-dried TLC or HPTLC plate was fixed in an exposure cassette, and the freshly erased imaging plate was placed onto the sample with the blue coloured side against the radioactive sample.

The imaging plate was exposed in a lead shielded environment for the duration of at least two half-lives (40 min for ^{11}C-labelled compound). If the sample had low radioactivity levels, then the exposure time was extended up to 1.5 h to maximize the signal transferred onto the imaging plate without increasing the background radioactivity too significantly or allowing the fading process to affect too much.

The energy stored on the imaging plate was released and digitized using a phosphorimager device (BAS-5000, Fuji Photo Film Co.) with 100-µm resolution, L4 dynamic range and S1000 laser energy. These parameters ensured optimal signal-to-noise ratio for the samples analysed in these studies.

The acquired data were background corrected. In the TLC analysis, the results were calculated as photostimulated luminescence (PSL) from the integrated area of the unchanged [^{11}C]SMW139 peak divided by the total PSL area of the sample to gain the parent fraction of the sample. Autoradiography images were analysed using Aida Image analyzer v.4.22 (Elysia-Raytest, GmbH, Straubenhardt, Germany).

4.3.6 RadioHPLC

A radioHPLC method for parent fraction analysis from plasma was developed for Study III to enable the RMA analysis from larger sample volumes of human plasma supernatants that had lower radioactivity concentrations compared to the preclinical samples. Additionally, radioHPLC was used to analyse mouse plasma and brain

supernatant samples in Study III, enabling a comparison of the R_ts of the radiometabolites between mouse and human samples.

The radioHPLC consisted of a Merck Hitachi L-7100 gradient pump system, 1 mL injection loop in a Rheodyne 7725i Manual Sample Injector (IDEX Health & Science, LLC) coupled with a Radiomatic 150TR (Packard, USA) radiodetector.

The degassed mobile phases were ACN and 0.1 % TFA in distilled H_2O. The gradient method is presented in Table 2.

Table 2. RadioHPLC mobile phase gradient used in Study III and IV. The gradient was initially described in Study III.

TIME (MIN)	A (ACN)	B (0.1% TFA)	FLOW (ML/MIN)
0	30	70	5
8	90	10	5
9	90	10	5
10	30	70	5
12	30	70	5

Abbreviations: ACN = acetonitrile, TFA = trifluoroacetic acid, min = minutes.

A Phenomenex Luna C18(2) (5µm, 250 × 10 mm) column was used. The injection volume was adjusted by the radioactivity of the sample to prevent radiodetector saturation and ensure measurements in the quantifiable range.

To limit the ACN content and residuals of previous injections in the sample loop, the loop was rinsed several times with 1 mL of ACN:H_2O solution (50:50, *v/v*), and then with pure H_2O.

A [^{11}C]SMW139 standard was injected on each study day to validate the method, and to confirm the R_t of the parent compound. On human study days, the radioactive standard was prepared into the plasma supernatant of the same study subject collected prior to the radiotracer administration. On preclinical study days, it was prepared by spiking ACN:H_2O (65:35, *v/v*) solvent mixture and injecting it into the radioHPLC.

The resulting radiochromatograms were analysed using the radioHPLC's software (Merck Hitachi D-7000 HSM, Merck). The peaks were decay corrected to the start of the analysis, integrated and the parent fraction was calculated as the fraction of unchanged [^{11}C]SMW139 over all radioactivity in the sample.

4.3.7 Extraction efficiency

In Study II, the extraction efficiency of the RMA plasma sample preparation step was analysed. This efficiency was defined as the percentage of radioactivity extracted from the plasma into the resulting supernatant. The residual supernatant in the pellet was accounted for by measuring the mass of the proteins in the plasma sample and deducting radioactivity relating to the fraction of the remaining supernatant.

4.3.8 *In vitro* mouse brain RMA

A parent fraction analysis study with mouse brain homogenate was performed. The transcardially saline perfused brain was dissected and homogenized (Ultra-Turrax T8, IKA, Staufen, Germany) into 4 mL of phosphate-buffered saline solution. After adding 1 MBq of [^{11}C]SMW139, the mixture was vortexed for 1 minute and incubated for 45 min in 36 °C. Aliquots of the mixed incubate were analysed at 10, 30 and 45 minute using the radioTLC and radioHPLC methods described in earlier sections. An identically prepared sham sample was prepared and incubated to study if [^{11}C]SMW139 remains intact throughout the sample preparation and incubation steps.

4.4 Plasma protein binding analysis (PPBA)

4.4.1 PPBA methods in preclinical studies

To determine the fraction of plasma protein-free parent radioactivity over all radioactivity ($f_{P/A}$), and similarly the radiometabolite plasma protein-free fraction over all radioactivity ($f_{M/A}$), the radioactivity concentration in the *in vivo* plasma sample (c_P) was measured by applying a known volume of plasma (for example, 3 µL) in duplicate onto a TLC plate (Silica gel 60 RP-18, Art. No. 1.05559.0001, Merck KGaA) (Figure 2). Autoradiographic quantification was used to quantify the PSL/volume radioactivity concentration. The parent fraction analysis was used to calculate the concentrations of the parent tracer and its radiometabolites in the plasma sample.

Protein-free [^{11}C]SMW139 and its protein-free radiometabolites were separated from protein-bound fractions using UF (Microcon-10 kDa, Merck KGaA). A minimum of 80 µL of plasma (p+, meaning plasma that still contains its natural proteins) was required. P+ was centrifuged (14,100 × g, 4 min and 3 min in two parts) to obtain at least 40 µL of filtrate (p-). This p- was then transferred to a second UF device after both centrifugations and centrifuged for an additional 3 min to obtain twice filtered filtrate (p--) that was centrifuged the same amount of time as the p-.

Simultaneously, the original plasma (p+) was ultrafiltered (14,100 × g, total of 7 min) to yield additional p- filtrate. Samples, including a radioactive standard, plasma, brain supernatants, and both filtrates (10 µL each), were applied onto the same TLC plate application line (Figure 2), developed, imaged using autoradiography, and analysed as outlined in Sections 4.3.4 and 4.3.5.

The membrane correction factor for the parent tracer was determined by calculating the concentration ratio (PSL/applied volume) between once filtered filtrate (p-) and twice-filtered filtrate (p--). Dividing the parent tracer concentration in the filtrate (p-) by this correction factor provided the true free parent concentration that would have been present if the membrane would not retain any of the parent compound. The corrected concentration in filtrate (p-) was divided by total radioactivity in plasma (p+) to determine $f_{P/A}$. For radiometabolites, the membrane correction factor and filtrate (p-) concentration were calculated similarly, with the true protein-free radiometabolite radioactivity concentration yielding $f_{M/A}$.

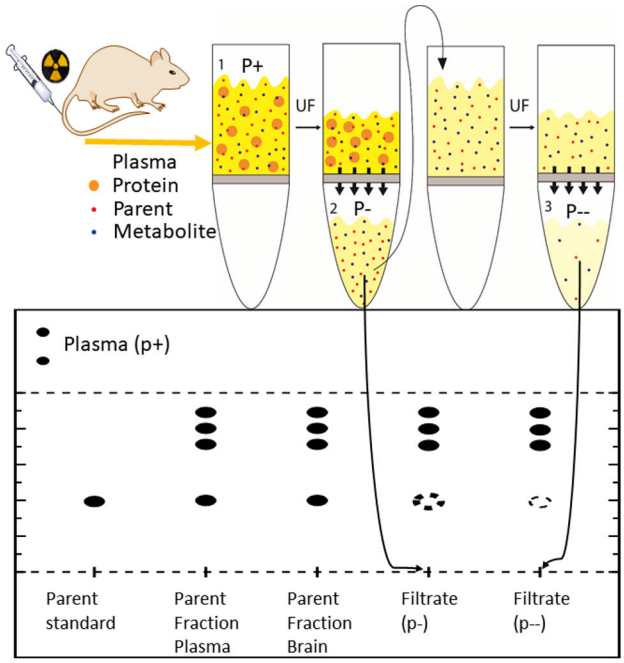

Figure 2. The schematic diagram of the ultrafiltration (UF) process shows how the plasma is ultrafiltered twice and how the proteins, and protein-bound and protein-free [^{11}C]SMW139 (parent) and radiometabolites behave in the filtration processes. Aliquots of the once (p-) and twice filtered (p - -) plasma are applied onto the TLC plate's application line (lower dashed line) and the parent and radiometabolites separated along with the standard, and plasma and brain supernatants when eluted. The original plasma sample (p+) is applied to the top of the plate to determine the total radioactivity concentration. Results are used to calculate the parent fraction in plasma and brain, the protein-free fractions of the parent and radiometabolites (f_P and f_M), and filter membrane correction factors simultaneously. *Figure modified from Study II.*

4.4.2 Development of the PPBA method for human plasma (Study IV)

In Study IV, the PPBA method was further developed to adapt to the lower radioactivity concentrations in human plasma. In order to collect comprehensive data, an *in vitro* approach by spiking the time point 0 plasma collected prior to [^{11}C]SMW139 injection was used in addition to the 20-minute p.i. plasma sample for direct *in vivo* analysis of the native parent and radiometabolite protein-bound and protein-free fractions. To assess if freezing the plasma sample affected the *in vitro* results, a 1.5 mL aliquot of the time point 0 plasma was frozen in -80 °C for later duplicate analysis.

In vitro analysis of the time point 0 plasma sample: Before [^{11}C]SMW139 injection, 4 mL of arterial blood was collected and the plasma was separated by centrifugation (4 °C, 2,118 × g, 5 min). An aliquot of 1.5 mL plasma was spiked with 50–200 kBq of [^{11}C]SMW139, vortexed, and incubated in +36 °C for 1 min (p+). After incubation, the plasma was re-vortexed and divided into three Microcon UF devices, 400 µL in each. One UF device was centrifuged for 8 min to obtain the once-filtered plasma. The other two were centrifuged for 4 min, after which their filtrates were transferred into a fourth UF device and all three were centrifuged for another 4 min. Next, the filtrates from the first two devices were pipetted into the fourth UF device again, and all were centrifuged once more. This ensured that the fourth UF device underwent a total of 8 min of ultrafiltration, yielding twice-ultrafiltered plasma filtrate (p--), corresponding to the same ultrafiltration time as for the once-ultrafiltered plasma (p-). The *in vitro* analysis did not require any TLC elution as there was only the parent [^{11}C]SMW139 present in these samples. From these samples, three 5.0 µL applications of p+, two spots of p-, and two of p-- sample spots were spotted on the TLC plate. The plate was dried, and analysed using autoradiography as explained in the Section 4.3.5. Frozen *in vitro* plasma samples were analysed identically as the fresh samples in one analysis day.

In vivo analysis of the 20-minute plasma sample: The protocol was identical to the *in vitro* time point 0 sample, excluding the spiking it with extra [^{11}C]SMW139 and incubation. In addition, from these samples, three 5.0-µL applications of p+ were placed to the top edge of the TLC plate, which area would not be eluted. A radioactive standard, a plasma supernatant sample for RMA, a p-, and a p-- sample were spotted on the TLC plate application line and eluted in identical conditions as in the radioTLC method, and analysed using autoradiography (Section 4.3.5). The frozen *in vitro* samples were analysed identically as the fresh samples. To concentrate the samples, up to 45 µL of p- and p-- filtrates were acquired by UF and spotted onto TLC plate in 10-µL increments while drying the spot in between into a small area.

Calculation of the membrane correction factor: The membrane correction factor was determined by calculating the amount of radioactivity in p-- over the amount of radioactivity in p- for both the parent and radiometabolites.

5 Results

5.1 [^{11}C]SMW139 synthesis and tracer injection key indicators

The full details of the tracer quality and injection information are listed in Table 3.

Table 3. [^{11}C]SMW139 tracer quality and injection information from Studies I–IV. The results are expressed as mean and standard deviation (SD).

	STUDY I PRECLINICAL	STUDY II PRECLINICAL	STUDY III PRECLINICAL	STUDY III* CLINICAL	STUDY IV CLINICAL
NUMBER OF BATCHES	32	27	5	7	26
RCP (%)	98.3(0.5)	98.3(0.5)	98.3(0.3)	98.3(0.3)	98.0(0.3)
A_M (@EOS; GBq/µmol)		110(49)	102.4(47.5)	152.0(131.5)	
A_M (@injection; GBq/µmol)	33.0(21.0)	37(27)	42.2(24.1)	85.9(73.8)	95(88)
INJECTED ACTIVITY (MBq)	9.5(0.5)	14.5(5.8)	17.9(6.2)	424.0(54.8)	402.9(11.5)
INJECTED MASS (µg)	0.18(0.17)	0.25(0.20)	0.21(0.12)	1.91(1.31)	2.7(1.7)

*The Study III clinical batch information is only from the subjects imaged in Turku.
Abbreviations: RCP = radiochemical purity, A_M = molar activity, @EOS = at the end of synthesis, @injection = at the time of injection, GBq = gigabecquerel, µmol = micromoles, MBq = megabequerel, µg = microgram.

5.2 Clinical subject demographics (Studies III–IV)

In Study III, only HC subjects were included in this sub study concerning the modelling aspects of [^{11}C]SMW139. Seven subjects in the Turku PET Centre and five in Karolinska Institutet were recruited. The inclusion criteria were: age 45–80 years, good health according to medical and psychiatric history, physical examination, cognitive assessment (Mini-Mental State Examination $\geq$28),

laboratory tests, electrocardiogram, and unremarkable MRI of the brain. For the included subjects in Turku, the mean (standard deviation (SD)): age was 68.4(8.4) years, and body mass index was 26.2(4.8).

In Study IV, for the parent fraction analysis, 10 HCs, and 15 subjects with MS (six RMS, and nine progressive multiple sclerosis (PMS)) were analysed. The PPB was successfully analysed from a subset of 11 subjects. All of the Study IV subjects were imaged and laboratory work performed in the Turku PET Centre.

In Study IV, all MS subjects were required to have a confirmed diagnosis based on the 2017 McDonald criteria. Additionally, eligibility criteria included at least one Gd^+ lesion (min 0.5 cm), in addition to a clinical diagnosis of secondary progression for individuals in the RMS and PMS groups. Participants were excluded if they were pregnant, claustrophobic, or had other significant central nervous system disorders unrelated to MS. Before imaging, all MS subjects underwent neurological assessments, MRI, and [^{11}C]SMW139 PET scans. The HC group consisted of age-matched individuals for comparison.

The subject demographics and other baseline characteristics in Study IV: A total of 26 subjects participated in the study, with the final analysis including 15 subjects with MS (6 RMS, 9 PMS) and 9 HCs; 2 subjects (1 PMS, 1 HC) were excluded due to technical issues during PET imaging. RMS subjects were enrolled within 0.5 years of diagnosis (mean 0.12 years) and imaged approximately 4 months later, while PMS subjects were imaged over 10 years post-diagnosis (mean 16.9 years). HCs and MS subjects were of similar age (mean 47.5 vs. 49.6 years, p=0.479), but PMS subjects had significantly higher EDSS scores than RMS subjects (mean 5.1 vs. 2.5, p=0.005). The two MS cohorts were also of comparable age (mean 49.2 vs. 45.0 years). The male-to-female ratio varied across groups: 6/3 (33% F) in HCs, 9/6 (40% F) in MS, 4/5 (56% F) in PMS, and 5/1 (17% F) in RMS. At the time of PET imaging, treatments in the RMS cohort included natalizumab (n = 2), ocrelizumab (n = 1), and rituximab (n = 3), while PMS subjects were treated with rituximab (n = 3), natalizumab (n = 1), and fingolimod (n = 1).

5.3 RMA method development

In the preclinical studies I–III, the RMA method was further developed during the studies, and the best method developed so far to answer the question in focus was used.

The HPTLC method showed sufficient resolution to analyse the parent fraction in most cases. However, the method was not robust and it was delicate regarding the applied volume as the plate capacity was easily overloaded, especially with the plasma supernatant sample. The boundary of how much could be applied was not definite and varied both with the plasma and brain sample. Therefore, it was

necessary to establish a safe limit for the application volume to avoid producing a chromatogram that would be too complex or even impossible to analyse, as demonstrated in Figures 3 and 5. The inconsistent amount of plasma supernatant able to be applied onto the plate before overloading the plate is seen well in Figure 5. When using the HPTLC method, applying multiple application spots with various volumes was often a wise decision that resulted in at least one or two successful radiochromatograms of the samples and gave a better understanding of the characteristics of the method in use.

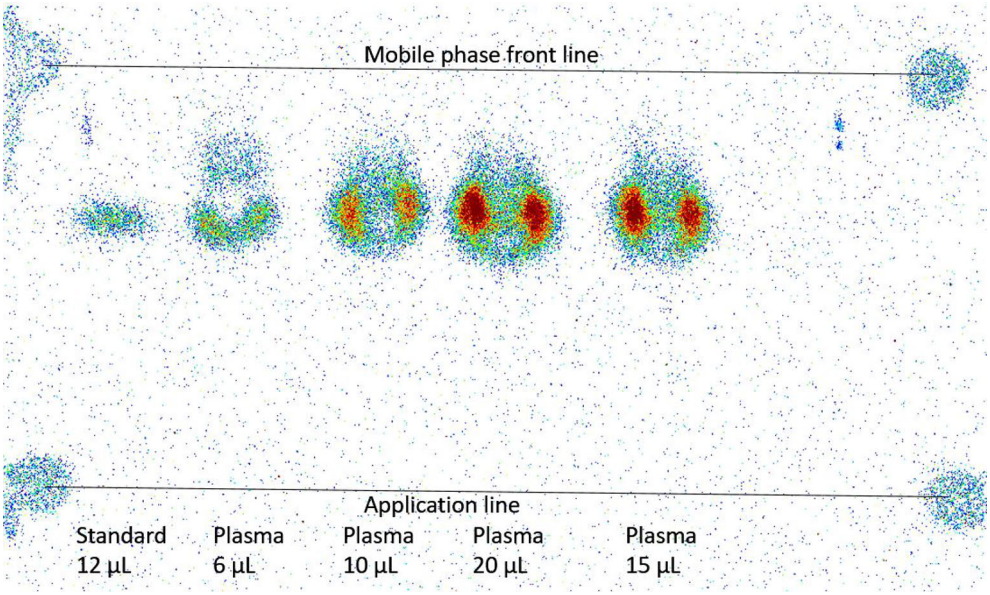

Figure 3. The autoradiography image of a HPTLC plate containing from left to right: standard and four applications of plasma supernatant with various application volumes to demonstrate the HPTLC plate capacity overloading. The plasma supernatant samples were from a single mouse from the 10-min time point. *Created using AIDA Image Analyzer 4.22.*

The difference of the parent fraction curves calculated from all of the mice in Studies I and II that were analysed either using the HPTLC and TLC methods is shown in Figure 4.

Table 4. The parent fractions from the mice plasma and brain samples that were analysed using both TLC and HPTLC methods simultaneously in Study I. The results are expressed as the mean and standard deviation in percentages.

Method		Plasma 10 min	Brain 10 min	Plasma 30 min	Brain 30 min	Plasma 45 min	Brain 45 min
TLC	M	72.5	78.2	42.9	35.3	34.6	28.5
	SD	8.9	8.8	1.3	4.0	5.0	4.5
	n	10	5	2	2	3	3
HPTLC	M	73.9	79.1	43.1	34.5	32.6	28.4
	SD	8.8	6.5	1.0	2.7	4.9	2.8
	n	10	5	2	2	3	3

Abbreviations: M = mean, SD = standard deviation, n = amount of subjects, min = minutes.

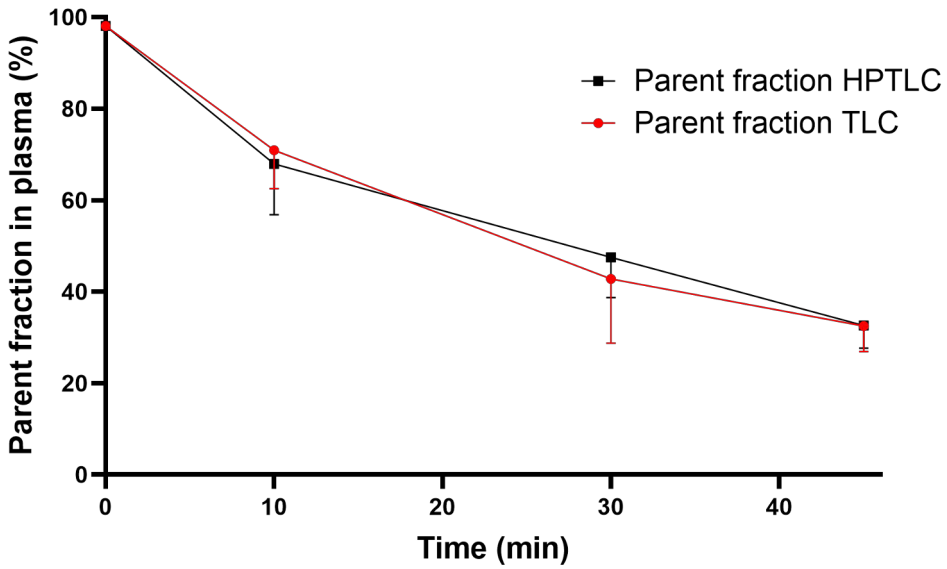

Figure 4. The mean and standard deviation (SD) of the parent fraction results of all of the mice that were analysed using HPTLC or TLC methods in Studies I and II. n = 22, 5, and 3 for HPTLC and n = 19, 14, and 13 for TLC methods for 10, 30, and 45-min time points, respectively. *Created using GraphPad Prism 9.*

The low deviation of the means and SDs as presented in Table 4 along with the Figure 4 show how both the HPTLC and TLC methods give comparable data. Although the Table 4 demonstrates small differences in the mean and SD between the two different TLC methods, the resulting change in the fractions is negligible.

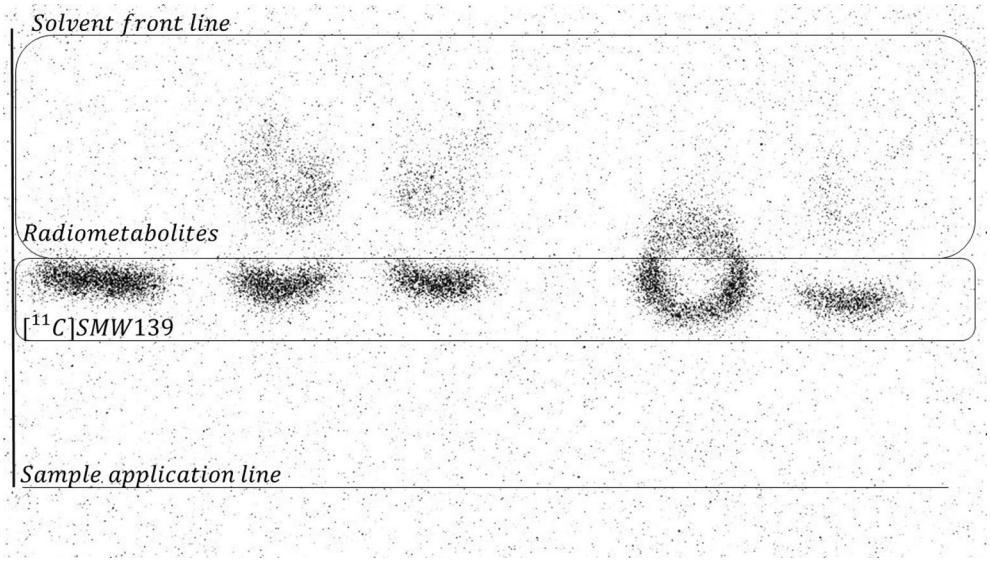

Figure 5. An exemplary autoradiography image from a HPTLC plate with the following samples from left to right: Standard, plasma supernatant from mouse1 (20 µL); brain from mouse1 (20 µL); plasma supernatant from mouse2 (20 µL); brain from mouse2 (20 µL). The more hydrophilic radiometabolites travel further than the [^{11}C]SMW139. All of the samples were from the 30-min time point. *Created using AIDA Image Analyzer 4.22.*

The TLC method was sufficient to provide a good signal-to-noise ratio and resolution even up to 45 min time point for parent fraction analysis in the preclinical mouse studies as shown in the autoradiography images and their corresponding radiochromatograms in Figure 6. The differences between the HPTLC method and TLC method are explained in Sections 4.3.3 and 4.3.4.

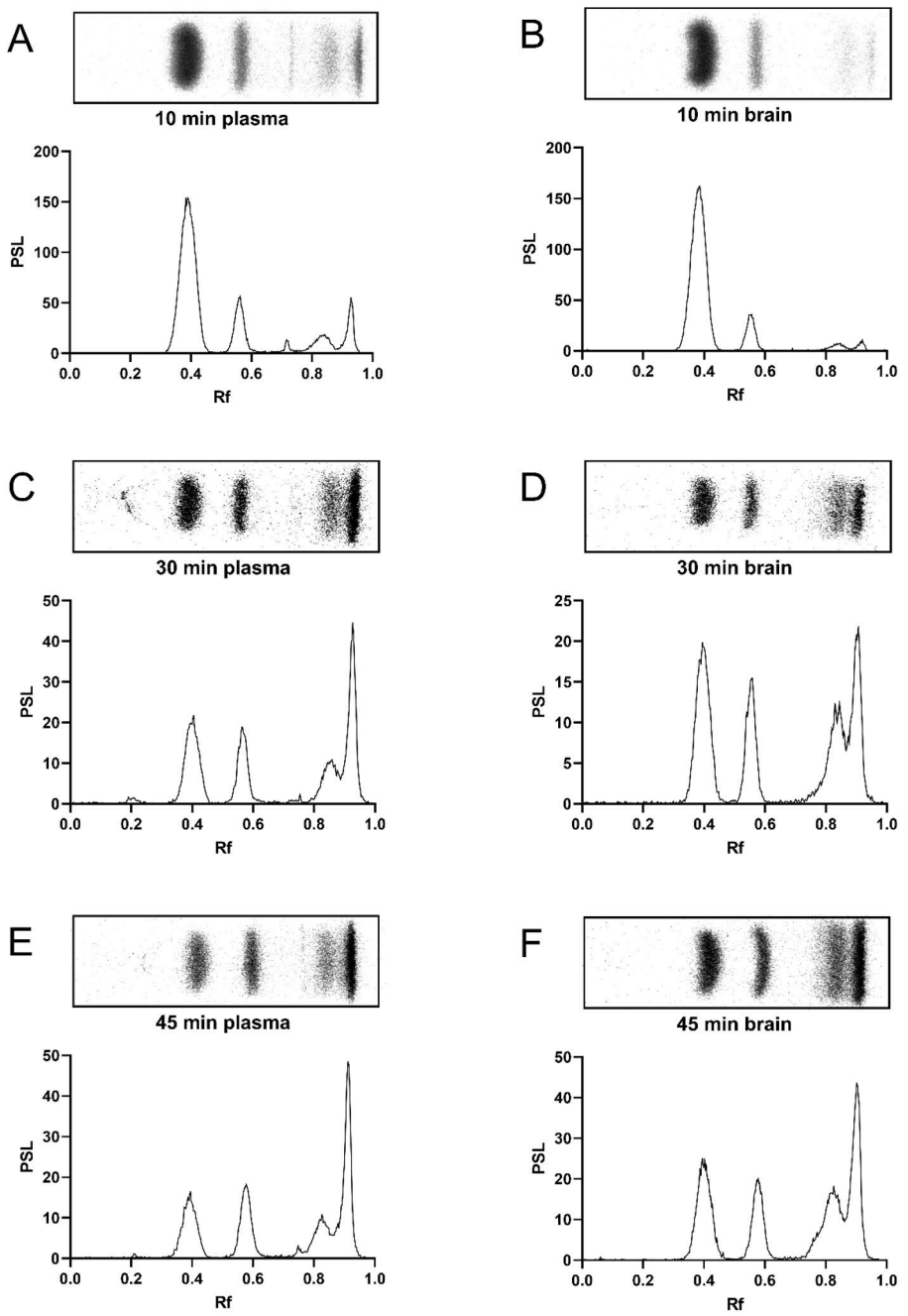

Figure 6. Representative digital autoradiographs and their chromatograms of parent tracer and its radiometabolites from (A) 10-min plasma, (B) 10-min brain, (C) 30-min plasma, (D) 30-min brain, (E) 45-min plasma, and (F) 45-min brain. The standard sample confirmed the retardation factor (R_f) for the parent tracer to be 0.4. The chromatograms are presented as the photostimulated luminescence (PSL) as a function of the Rf. *Originally created using GraphPad Prism 9 and AIDA image Analyzer 4.22. Published in Study II.*

As the TLC method was not able to provide sufficient signal-to-noise ratio from clinical study subjects in the Study III in the latest time points, a radioHPLC method was successfully developed that enabled the accurate analysis of the parent and the different radiometabolite fractions even up to the 90-minute time point. The radiometabolites were numbered 1–3 according to the order of appearance (increasing R_t) in the radiochromatogram, which reflects the decreasing polarity or increasing lipophilicity of the eluted analyte. Figure 7 demonstrates the sufficient signal-to-noise ratio for the different radiometabolite and parent compound peaks. For the limit of quantification, a ratio of three is mostly set as the minimum. With the radioHPLC a ratio of 14 for radiometabolite 1, 4 for radiometabolite 2, 7 for radiometabolite 3, and 26 for the parent tracer could be often achieved. Most importantly, a baseline separation was achieved between the radiometabolites and the parent peaks. The peaks were divided into wider peak areas to take into account the possible smaller peaks and possible minor shifts in the R_t. This approach only enhanced the accuracy of the method as the radiochromatogram is background corrected and the wide peak areas even out the steady fluctuation of the background better than a narrow peak could.

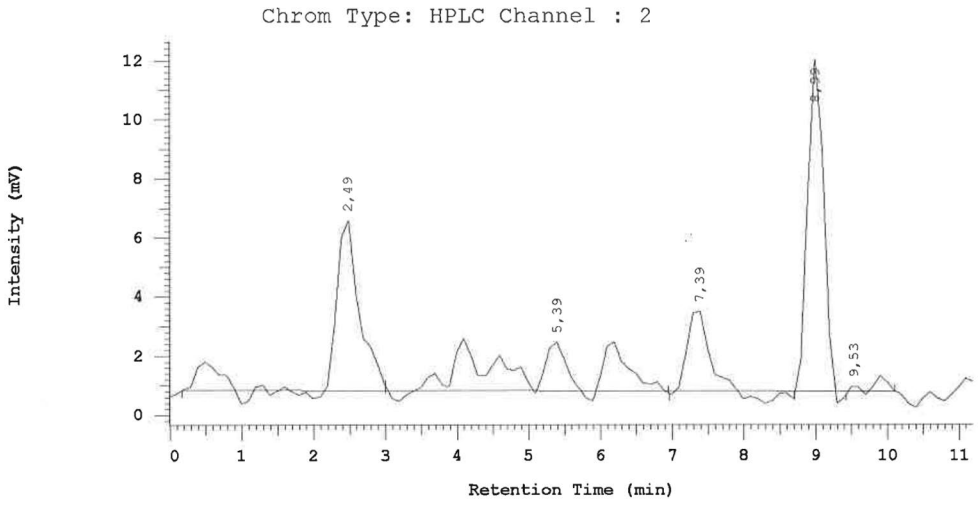

Figure 7. An exemplary radiochromatogram to demonstrate the adequate signal-to-noise ratio in a 90-min time point human plasma supernatant sample. The peak regions extend from 0–3 min for radiometabolite 1, 3–7 min for radiometabolite 2, 7–8.7 min for radiometabolite 3, and from 8.7–9.4 min for the unchanged [^{11}C]SMW139. The numbers above the highest peak in the peak region denotes the retention time of the highest point of the peak. *Created using HSM version 3.1 (Merck Hitachi, England).*

The sample preparation method was slightly updated so that the ACN to plasma ratio was changed from 1.4 to 2 when updating from HPTLC to the TLC method.

The extraction efficiency was measured in triplicate using the ACN:plasma mixture (2:1; *v/v*). The remaining radioactivity corresponding to the remaining supernatant in the pellet was taken into account and the extraction efficiency was 99% for the plasma samples.

5.4 RMA in the preclinical studies (Studies I–III)

5.4.1 The parent fraction and RMA

The percentage of the unmetabolized [^{11}C]SMW139 i.e. the parent fraction values as presented in Figures 4 and 8 (A and B) and in Table 5 illustrate the rapid metabolism of the parent tracer in mice. The fraction of radiometabolites in plasma and the dissected brain supersedes the fraction of the unchanged tracer already before the 30-min time point post [^{11}C]SMW139 injection. The effect of the age, sex and strain of the mouse on the parent fraction value is reported in more detail in the following sections.

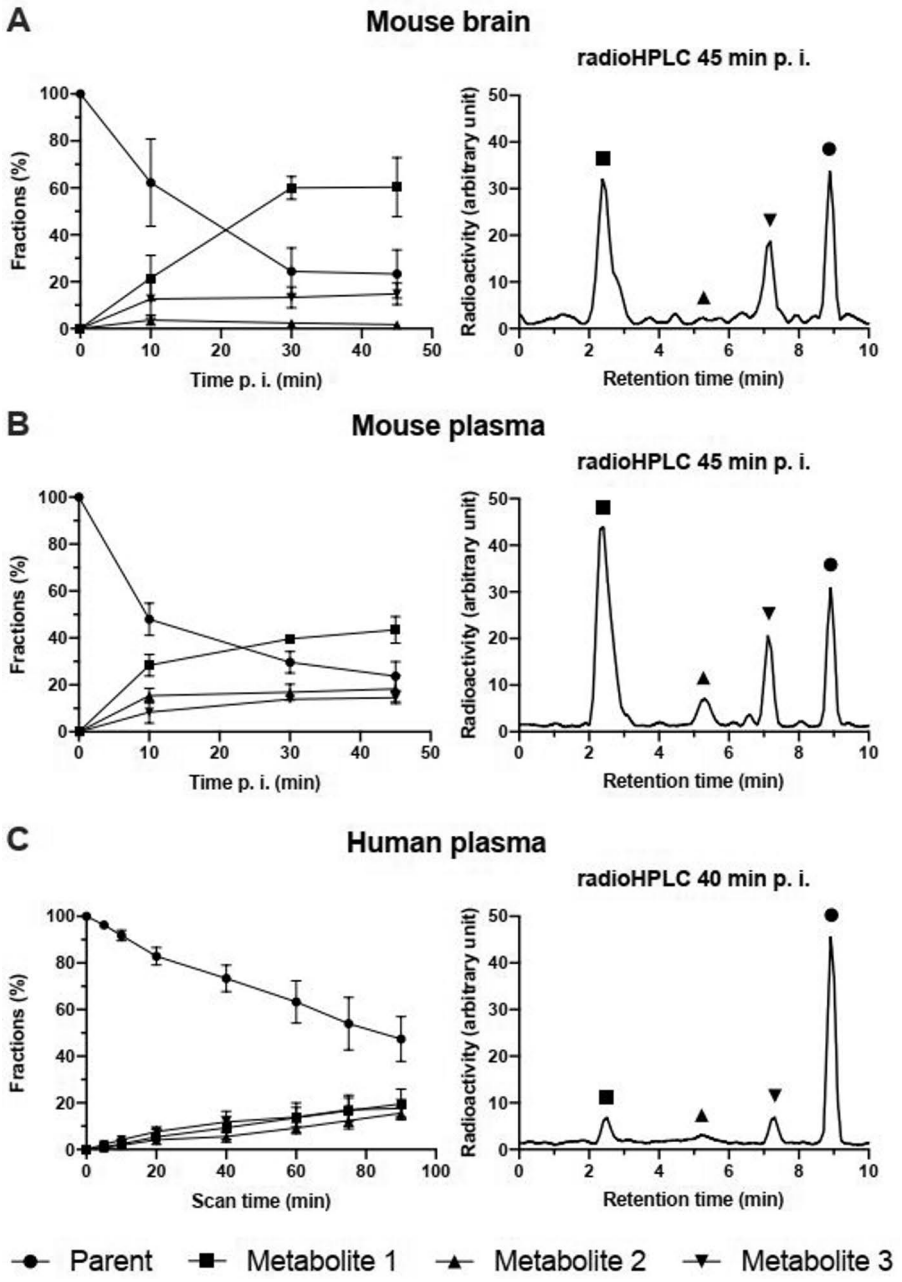

Figure 8. [^{11}C]SMW139 radiometabolite analysis from Study III. The left panels show the mean fraction of the whole radioactivity in the sample and its standard deviation of [^{11}C]SMW139 and of the different radiometabolites in (A) mouse brain, and (B) mouse plasma supernatant (n = 4, 3, and 4, at 10, 30, and 45 min, respectively), and (C) human plasma (n = 10). The right panels show exemplary radioHPLC chromatograms from (A) mouse brain, (B) mouse plasma, and (C) human plasma. *Published in Study III.*

Table 5. Mean and standard deviation of the mean for plasma parent fraction, and parent and radiometabolite free fractions. Measured from the same mice that had both data collected from them in Study II. At the 10, 30, 38, and 45-min time points, respectively: n = 3, 4, 2, and 4. *Modified from original publication (Study II).*

Time point (min)		Plasma parent fraction	$f_{P/A}$, Free parent/ all radio-activity	$f_{P/P}$, Free parent/ all parent	$f_{M/A}$, Free metab/ all radio-activity	$f_{M/M}$ Free metab/ all metab	Free parent/ all free radio-activity	Free radio-activity/ all radio-activity
10	*M*	0.567	0.032	0.057	0.368	0.835	0.085	0.399
	SD	0.098	0.000	0.009	0.113	0.119	0.019	0.113
30	*M*	0.347	0.012	0.034	0.508	0.760	0.023	0.520
	SD	0.077	0.005	0.007	0.083	0.092	0.011	0.081
38	*M*	0.336	0.010	0.031	0.520	0.778	0.019	0.530
	SD	0.050	0.001	0.008	0.076	0.056	0.000	0.077
45	*M*	0.323	0.007	0.021	0.350	0.518	0.019	0.356
	SD	0.043	0.002	0.006	0.017	0.035	0.006	0.019

Abbreviations: $f_{P/A}$ = protein-free parent radioactivity over all radioactivity, $f_{P/P}$ = protein-free parent radioactivity over all parent radioactivity, $f_{M/A}$ = protein-free radiometabolite radioactivity over all radioactivity, $f_{M/M}$ = protein-free radiometabolite radioactivity over all radiometabolite radioactivity, M = mean, metab = radiometabolites, SD = standard deviation, min = minutes.

In Studies I and II, radioTLC was used. In Study III, the preclinical RMA was performed using radioHPLC. The separation of different radiometabolites from each other was more reliable and consistent using the radioHPLC method. Separating the radiometabolites from each other was crucial in this study, as the radiometabolite 2 fraction was required to enable more advanced modelling that took into account the fraction that did not enter into the mouse brain. The RMA of human subjects was performed with the same radioHPLC instrument and method to enable better translation of conclusions from the mouse RMA to human RMA and PET data modelling. At least three distinct radiometabolites can be separated from each other using the radioHPLC method as seen in the radiochromatograms in Figure 8. With the radioTLC method, the number of radiometabolites was up to four as seen in Figure 6. However, usually only up to three were seen.

The results in Study III analysed with radioHPLC showed similarly a rapid metabolism of [^{11}C]SMW139 in mouse plasma and brain as shown in Figure 8 panels A and B. When comparing to the subject group analysed using the TLC or HPTLC methods (Figure 4) in Studies I and II, the metabolism rate was slightly faster in the subjects analysed with the radioHPLC (Figure 8). The parent fraction analysed using the radioHPLC method showed a rapid decline in the unchanged fraction of [^{11}C]SMW139 as at the 10-min time point the mean parent fraction value was 47.9(6.8)% in the plasma supernatant and 62.2(18.6)% in the brain supernatant. The

Figure 8 shows how the parent fraction plateaus in brain by 30 min at around 24.3(10.0)% while the plasma parent fraction value still decreases slightly from 29.6(4.6)% at 30 min to 23.7(6.2)% at 45 min post injection.

When comparing the plasma and brain supernatant radiometabolite profiles with each other, an important difference stands out. Radiometabolite 2 is present only at low levels in the mouse brain homogenate supernatant, with mean(SD) percentages of 3.7(2.2), 2.4(1.0), and 1.7(0.5) at the 10-, 30-, and 45-minute time points, respectively. In contrast, it is abundantly present in the plasma supernatant, with significantly higher mean(SD) percentages of 15.4(3.2), 16.9(3.2), and 18.3(5.6) at the same time points. The ratios of the fraction of radiometabolite 2 in brain over the corresponding fraction in plasma were 0.24, 0.14, and 0.09 at 10, 30 and 45-min time points, respectively. At the same time, the corresponding ratios for the radiometabolite 1 were 0.76, 1.51, and 1.39 and for the radiometabolite 3 1.51, 0.96, and 1.02 at 10, 30 and 45-min time points, respectively, as shown in Figure 9.

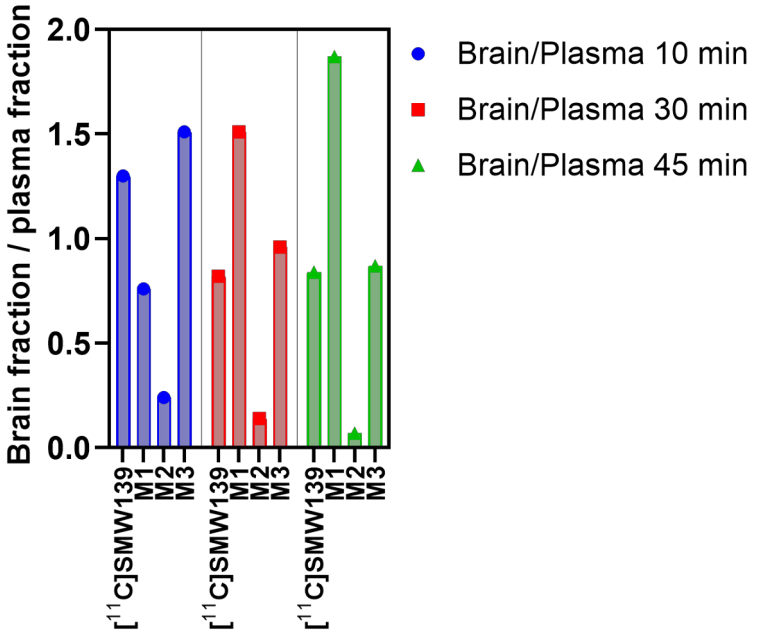

Figure 9. The mean relative fraction of the parent tracer [^{11}C]SMW139 and the different radiometabolites 1–3 as a ratio of the fraction in brain over fraction in plasma (n = 4, 3, and 4 for 10, 30, and 45-min time points, respectively). *Created using GraphPad Prism 9.*

According to the *in vitro* mouse brain homogenate study in Study II, no radiometabolites were found from the incubated brain homogenate. Therefore, the radiometabolites do not form directly in the brain, but they cross the blood-brain

barrier (BBB) from the blood compartment. If reference tissue modelling could be used, the effective BBB crossing would cause problems as the total radioactivity in the brain tissue compartment corresponds in a constantly growing quantity to the radiometabolites. In study III, it was shown that the majority of radioactivity in the mouse brain corresponds to radiometabolites already by 20 min post injection (Figure 8).

The correlation of the parent fraction values from Studies I and II between plasma and brain is shown in Figure 10. The key indicator values for the parent fraction results and the number of subjects are presented in Table 6. The radiometabolites began to form quickly in the plasma, but it took longer for them to show up in equivalent quantities in the mouse brain than in plasma. However, the parent fraction in the brain reached even lower values than in the plasma already at 30-min time point as shown in Table 6.

Table 6. Parent fraction data from the mice that had both successfully analysed plasma and brain parent fraction data with the TLC or HPTLC method in Study I and II. The max, min, and mean values are presented in percentages.

	Plasma 10 min	Brain 10 min	Plasma 30 min	Brain 30 min	Plasma 45 min	Brain 45 min
Max	84.6	88.7	70.8	65.7	42.4	44.0
Min	46.1	38.8	21.7	12.6	23.4	6.8
Mean	68.0	73.8	44.5	41.4	32.1	28.8
SD	10.3	12.7	14.1	16.0	5.7	9.0
n	14	14	16	16	11	11

Abbreviations: Max = maximum value, Min = minimum value, SD = standard deviation, n = sample size, min = minute.

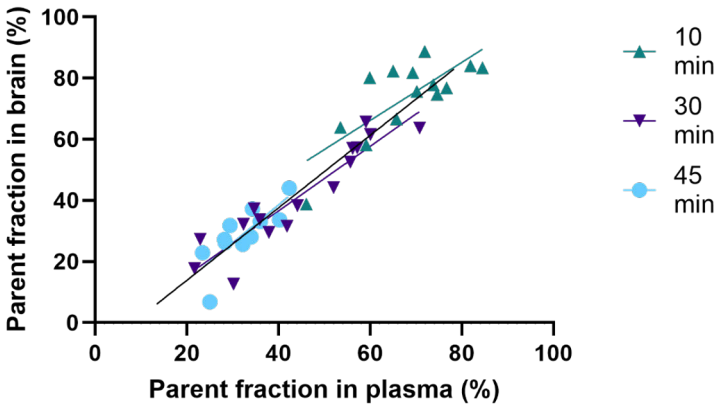

Figure 10. Correlation of the plasma and brain parent fraction analysis results from the 10, 30 and 45 min mouse samples. *Created using GraphPad Prism 9.*

In the preclinical part of Study III, the mouse plasma and brain supernatant RMA showed three major peaks of radiometabolites. To take into account all radioactivity eluted in any other part of the radiochromatogram than at the exact R_ts of the distinct peaks, the entire radiochromatogram was divided into four sections, as shown in Figure 7. The radiometabolite 1 corresponded to the 0–3 min, radiometabolite 2 to 3–7 min, radiometabolite 3 to 7–8.7 min and the [^{11}C]SMW139 to 8.7-9.4 min areas of the radiochromatogram. All the peak areas were background corrected to remove any possible errors due to wider peak areas. Any possible minor wash step peaks that were eluted after the parent compound were not taken into account, as they could just as likely be remnants of either the parent or the radiometabolites that were washed out from binding to any impurities in the column during the strong solvent wash cycle. No significant peaks of any characteristic R_t were observed in the radiochromatograms after the parent compound even during the column wash. Occasionally minor elevated intensity resembling peak forms were detected that were under the limit of detection that accounted at most for only a few percent of the total radioactivity in the sample, so such an approach did not introduce significant errors to the analysis. The brain sample radiochromatograms were analysed in the same way to integrate the possible peak of radiometabolite 2 from its characteristic R_t window, despite there being no significant peaks visually detectable there.

5.4.2 Effect of mouse age on the parent fraction of [^{11}C]SMW139

The multiple *ex vivo* time point and different age group study design enabled studying the correlation between the mouse age and the parent fraction in plasma and brain. The age did not seem to significantly affect the metabolism rate of [^{11}C]SMW139 at the 10- and 30-min time points in plasma (Figure 11 A and B).

However, the extent to how far the metabolism goes later slightly correlated with age, so that the younger mice reached more complete metabolism of [^{11}C]SMW139 through lower parent fraction values while the older mice began to plateau at higher parent fraction percentages (Figure 11 C). The corresponding results for brain samples showed less consistent correlation between parent fraction and age (Figure 11 D-F).

5.4.3 Effect of mouse sex and strain on the parent fraction of [^{11}C]SMW139

In Figure 12 the effects of mouse sex and strain on the parent fraction of [^{11}C]SMW139 in plasma and brain were visualised. The largest difference was seen

in the 30-min time points, where the TG and female groups plateaued earlier than the WT and male groups.

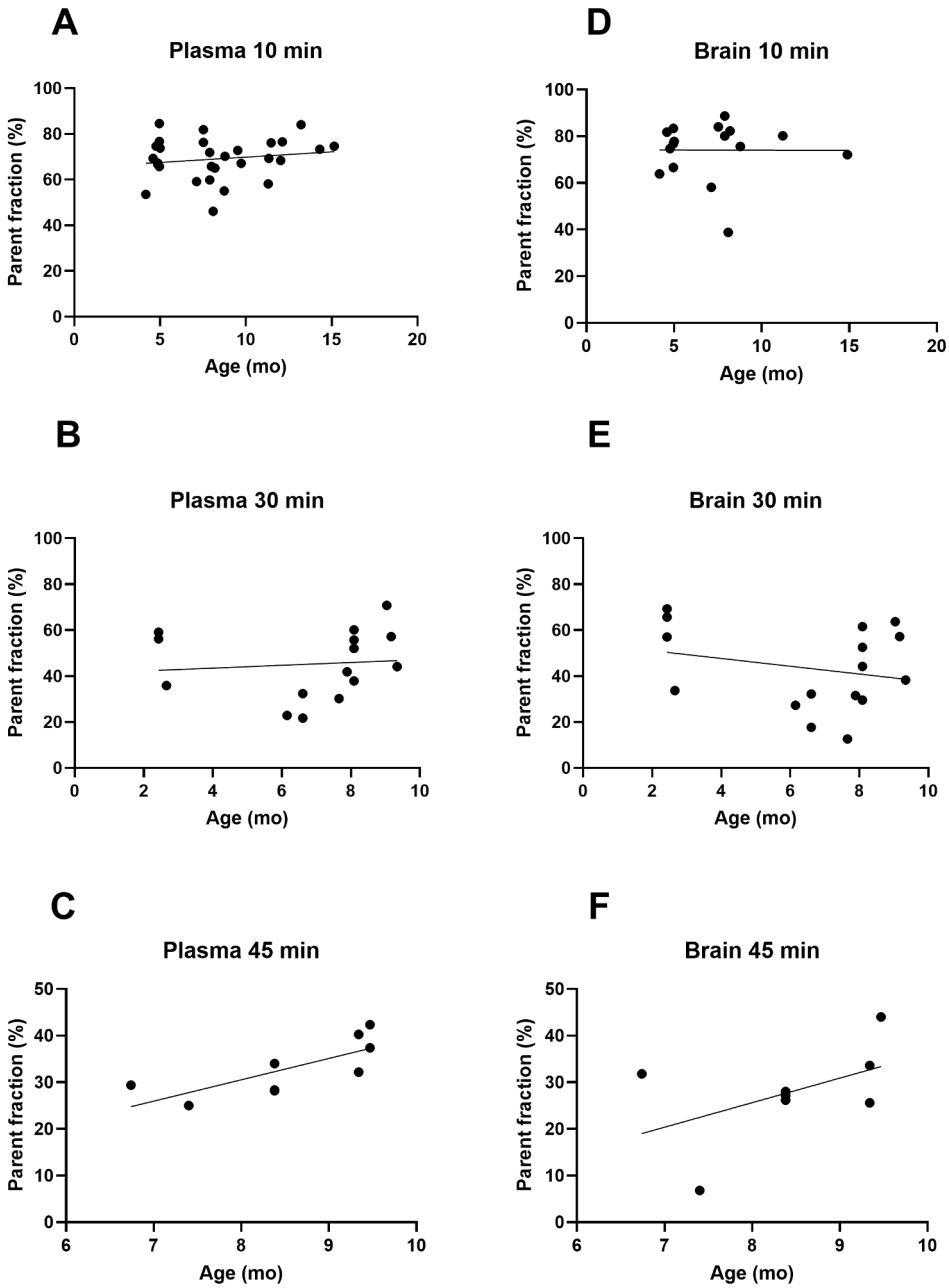

Figure 11. Correlation between parent fraction of [^{11}C]SMW139 and mouse age in months (mo) in (A–C) plasma and (D–F) brain samples analysed in Study I. *Created using GraphPad Prism 9.*

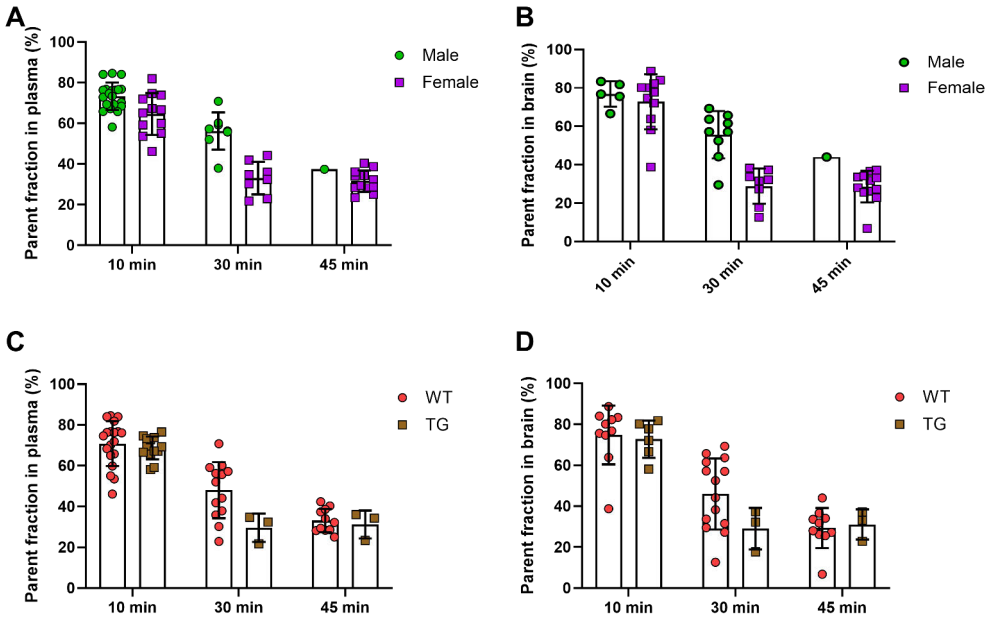

Figure 12. Percentage of parent [^{11}C]SMW139 was compared at 10, 30, and 45-min time points across different groups: (A) male vs female plasma, (B) male vs female brain, (C) wild type (WT) vs transgenic (TG) plasma, and (D) WT vs TG brain. The mean and the standard deviation is shown with the line and whiskers. *Created using GraphPad Prism 9.*

5.5 RMA in the clinical studies (Studies III and IV)

As the result of method development for the clinical studies, the RMA method was transferred to a radioHPLC based method for Studies III and IV.

In Study III, the mouse and human plasma supernatant samples were analysed using the same radioHPLC method to determine, according to the R_ts, whether the radiometabolites were the same in both. As shown in Figure 8, both subject types have the same radiometabolites in plasma according to the R_ts. However, in the HC human subjects the fractions of radiometabolites 1–3 were rather equal in quantity throughout all time points, whereas in mice, radiometabolite 1 was the most predominant one.

The plasma supernatant parent fraction curves of humans had a less steep slope than when analysed from mice (Figures 8 and 13).

As shown in the Study III preclinical findings, the radiometabolite 2 is not effectively crossing from plasma into the brain in mice. Therefore, when translating this modelling approach to humans, a two-tissue compartment model with a dual input function was used to model brain uptake with an input from the parent tracer and the BBB-crossing radiometabolites 1 and 3. Radiometabolite 2 was taken separately into account in the parent fraction and radiometabolite analyses. The

decrease of the parent fraction was almost linear up to the 90-min time point, as was for the increase of the different radiometabolites fractions (Figure 8 C).

In Study IV, the parent fractions of 10 HCs and 15 subjects with MS (six RMS and nine PMS) were successfully analysed. The parent fractions in Study IV were similar compared to the fractions in Study III, which consisted only of HCs. Between the different groups, the PMS had a faster metabolism rate of [^{11}C]SMW139 compared to other groups. However, the SDs of the curves were higher than the differences between the groups (Figure 13).

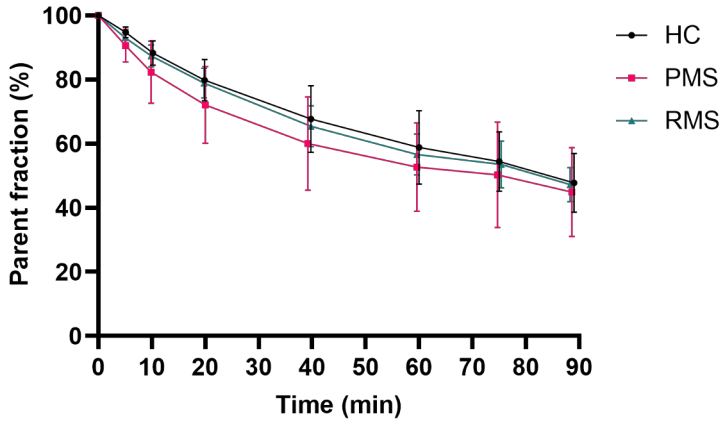

Figure 13. The mean percentages of unchanged [^{11}C]SMW139 of the total radioactivity in the plasma samples (parent fraction) of the healthy control (HC, n = 10), relapsing MS (RMS, n = 6) and progressive MS (PMS, n = 9) subject groups. Error bars denote the standard deviation. *Adapted from Study IV using GraphPad Prism 9.*

5.6 Plasma protein binding (PPB) in plasma

5.6.1 Ultrafiltration (UF) membrane correction

To obtain unbiased plasma free fraction data, membrane retention correction values for the Microcon Ultracel UF device were determined for both the parent tracer and its radiometabolites. These values enabled the calculation of their true concentrations in the plasma samples. In Study II, the membrane correction factor for the combined radiometabolites was 0.93 ± 0.04 ($n = 9$), indicating minimal reduction in concentration after filtration. In contrast, the parent tracer membrane correction was 0.63 ± 0.07 ($n = 9$), meaning that 37% of the parent tracer was retained in the membrane, and by dividing the filtered plasma with 0.63, this could be corrected for. These values showed a need for a greater correction factor for the parent tracer than for the radiometabolites. When using this correction, the parent plasma protein-free

fraction (f_P) increased by 59%. In Study IV, similar results were obtained (0.68, n = 20 for the parent tracer; 0.95, n = 7 for the radiometabolites).

5.6.2 PPB in mice

In Study II, the novel PPBA method, described in Section 4.4, was developed to separately assess the PPB of the parent and its radiometabolites. This method was then used to analyse the f_P and f_M in mice in Study II and in human subjects in Study IV.

The efflux rate of the [^{11}C]SMW139 out from plasma in addition to the rate that it is being bound to the proteins and metabolised into radiometabolites were faster than the rate that the bound [^{11}C]SMW139 was being released back into the free form in plasma as the $f_{P/A}$, fraction of free [^{11}C]SMW139 over all radioactivity, decreased over time (black line, Figure 14). Especially, this scenario is seen, as the $f_{P/P}$, fraction of free parent over all parent, showed a continuously decreasing trend in the red curve in Figure 14, revealing the overall complex equilibrium balance of the different rates.

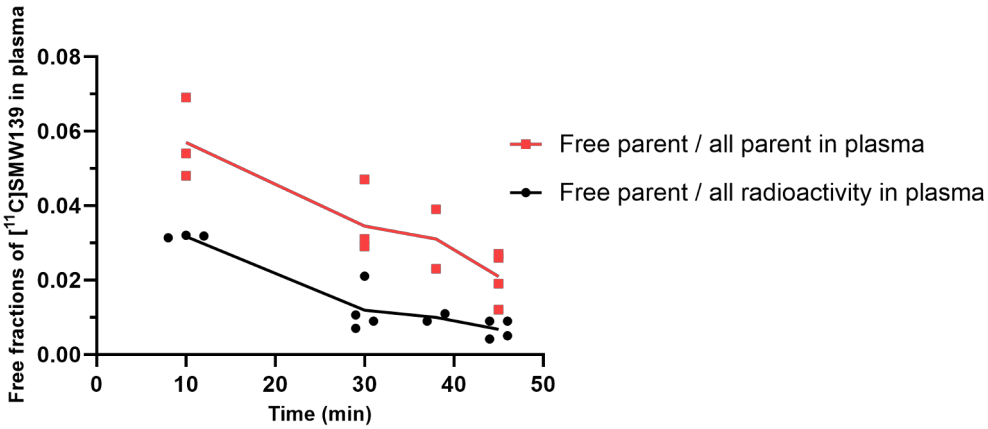

Figure 14. Fractions of plasma protein-free parent over all radioactivity (black) and over all parent radioactivity (red) in mouse plasma. Individual values are plotted and the curve shows the mean. At the 10-min, 30-min, 38-min, and 45-min time points, respectively: n = 3, 4, 2, 4. *Adapted from Study II using GraphPad Prism 9.*

The ratio between the free [^{11}C]SMW139 over all the free radioactive molecules decreased rapidly from 0.08 at 10 min to 0.02 already at 30 min as both the parent fraction and the free parent over total parent in plasma ($f_{P/P}$) decreased over time, while the fraction of radiometabolites grew and their free fraction remained high (Table 5).

The Figure 15 summarizes the plasma radioactivity concentration, parent fraction and the PPBA data as the percentage of injected radioactivity per gram of tissue (%IA/g) in plasma. The total amount of free radiometabolites remained high in plasma, while the total amount of free parent decreased rapidly.

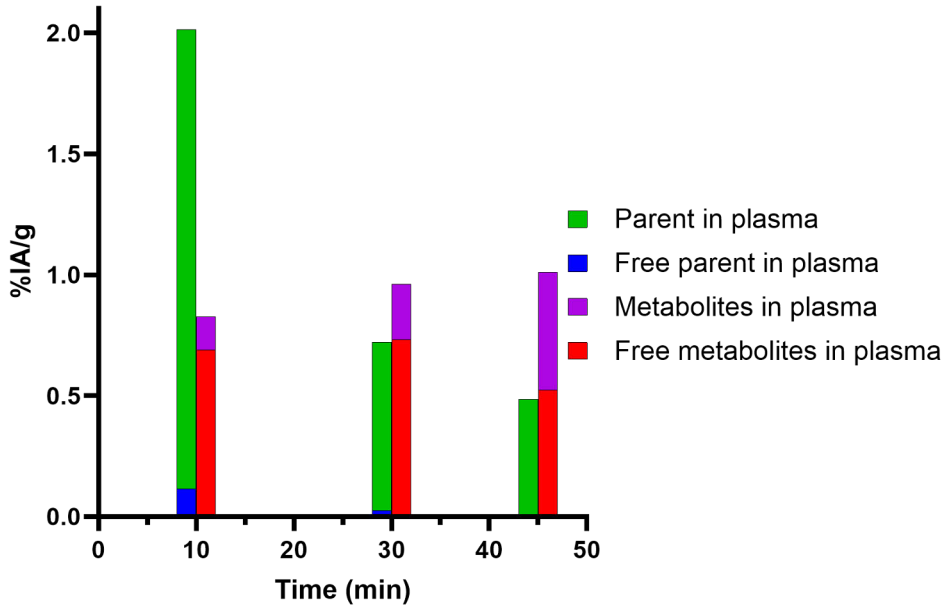

Figure 15. The percentage of injected activity per gram (%IA/g) of plasma of the total parent, free parent, total radiometabolites, and free radiometabolites in plasma as a time-activity concentration bar chart. %IA/g were analysed at the 10-min, 30-min, and 45-min time points from n = 45, 14, and 7, respectively. Free fractions were analysed at the 10-min, 30-min, and 45-min time points from n = 3, 4, and 4, respectively. *Adapted from Study II using GraphPad Prism 9.*

5.6.3 PPB in human subjects

In Study IV, the PPBA was performed from a subset of subjects. Data were successfully gathered from three HC, five PMS, and three RMS subjects. In addition, frozen plasma samples were analysed and compared with the corresponding plasma samples that were analysed directly after collection from the subject *in vitro*. The PPBA showed comparable results between frozen and fresh plasma samples. The mean(SD) $f_{P/P}$, was 0.013(0.004) for fresh and 0.013(0.002) for frozen samples (n = 11 for both, from the same subjects), and 0.010(0.004) (n = 9) for the 20-minute *in vivo* samples. At 20 min, the mean(SD) fraction of free radiometabolites over total radiometabolites ($f_{M/M}$) was 0.425(0.132), while the free radiometabolites over all free radioactivity in plasma was 0.88(0.06). The mean $f_{P/P}$ values were 0.0138 (n = 3), 0.0096 (n = 5), and 0.0093 (n = 3) for HCs, PMS, and RMS, respectively.

6 Discussion

Studying a new tracer is always challenging due to the very little initial knowledge available of its properties. When the studies using [^{11}C]SMW139 were planned in the Turku PET Centre that led up to the data enabling this thesis, there were no publications of [^{11}C]SMW139 at that time. The practical work of developing and evaluating [^{11}C]SMW139 had only recently begun, for example, at the Department of Radiology & Nuclear Medicine, Neuroscience Campus Amsterdam, VU University Medical Center (Amsterdam, Netherlands). The precursor SMW139 was developed and synthesised by researchers from the group of Professor Michael Kassiou from the University of Sydney, Australia (Wilkinson *et al.*, 2017; Janssen *et al.*, 2018; Hagens *et al.*, 2020).

These studies began in the Turku PET Centre in 2017 by setting up the [^{11}C]SMW139 tracer synthesis in the Radiopharmaceutical Chemistry Laboratory of Turku PET Centre (Turku, Finland). The reason for the use of this selected tracer in Studies I–IV was to evaluate this new and promising P2X7 receptor-binding tracer in preclinical disease models and human subjects.

6.1 [^{11}C]SMW139 synthesis key indicators

The shelf-life of [^{11}C]SMW139, like for other ^{11}C-labelled PET tracers, is typically 1 h due to the short radioactive half-life of ^{11}C. Therefore, [^{11}C]SMW139 must be synthesized and used as soon as possible after production, as the radioactivity decays quickly and limits its practical use to around 1–1.5 h post-synthesis. However, the exact usable timeframe depends on the initial radioactivity produced, the specific requirements for imaging, and the dose needed. The shelf-life of [^{11}C]SMW139 was validated up to 1 h in the Radiopharmaceutical Chemistry Laboratory of the Turku PET Centre.

When imaging receptors that are not that abundant in the body, the A_m is critical. The tracer needs to be used as fast as possible to maintain the ratio of radioactive [^{11}C]SMW139 relative to SMW139 as high as possible, ensuring that the unlabelled SMW139 does not occupy substantial proportion of the limited target sites. In addition, the stability of the tracer in the formulation solvent affects the time window during which the tracer can be used. In terms of chemical stability, the tracer may

remain stable under appropriate storage conditions. However, the rapid decay rate makes the radioactive shelf-life the limiting factor in PET studies. The P2X7 is a cell surface receptor, found for example, in the brain in astrocytes, microglia, and other glial cells, along with other locations in the body, like in the immune cells such as monocytes (Bartlett, 2014; Zhao, 2021b). The P2X7 receptor has been extensively studied. Schmidt *et al.* provides a comprehensive overview of the P2X7 receptor and the potential it has as a target for PET imaging in various pathophysiological contexts, for example, neuroinflammation and cancer (Schmidt *et al.*, 2023). The abundant P2X7 receptor quantity in the body makes the results of this tracer less susceptible for A_m fluctuations.

The study days were optimised with a strict time schedule, and careful pre-planning and prior practice were done to maximize the output of good quality data and preserve radioactivity from decaying too much for reliable measurements. To maximize the use of the [^{11}C]SMW139 tracer batches, they were shared between as many clinical and preclinical studies as possible. This caused the A_m to be lower for the mice that were injected later in the day.

The A_m expresses how much of the total SMW139 in the batch is labelled with the radioactive ^{11}C (i.e. what is the amount of radioactivity per the total amount of ^{11}C-labelled and non-labelled SMW139 substance in moles; Equation 1; van Grieken & Bruin, 2009). Usually the units of MBq/nmol or GBq/µmol are used.

$$A_m = A/n$$

Equation 1. $\boldsymbol{A}$ represents the total radioactivity at a given time, and $\boldsymbol{n}$ the amount of substance in moles.

The maximum theoretical A_m (A_m(max)) depends solely on the half-life of the radionuclide according to the following Equation 2:

$$A_m(\max) = \lambda * N_A = \frac{\ln(2) * N_A}{T½}$$

Equation 2. λ represents the decay constant, $\boldsymbol{N_A}$ the Avogadro's constant and T½ the half-life of the radionuclide in question.

By dividing the A_m of the batch by A_m(max), we can determine the true fraction of the radiolabelled SMW139 over all SMW139. The typical percentage of radiolabelled [^{11}C]SMW139 over all SMW139 was around 0.03% at the time of injection. Fortunately, even though the amount of non-radiolabelled SMW139 is vast compared to the radiolabelled version, the radioactivity is still typically measured

from thousands to millions of disintegrations per second in the region of interest during the PET scans, and the sensitivity and the temporal resolution of the radiodetectors are sufficient, then the extremely low fraction of the radiolabelled SMW139 over all SMW139 does not justify a reason to doubt the reliability of these results. A big fraction of non-radiolabelled tracer might become a problem when imaging targets, which are not abundant. In these cases, caution must be made not to over saturate the target.

For PET tracers, the minimum radiochemical purity (RCP) requirement is generally set at >90%. This threshold ensures that the majority of the administered compound is the intended radiolabelled tracer, which is crucial for obtaining accurate and specific results. In clinical settings, regulatory bodies such as the European Pharmacopoeia (Ph. Eur.) often require even higher purity levels for human administration, typically ≥95%. This high purity minimizes the presence of radiochemical impurities or by-products that could interfere with target specificity, cause adverse effects, or complicate image interpretation. For [^{11}C]SMW139 the minimum radiochemical purity requirement has been ≥95% which was exceeded well (mean(SD); 98.2(0.4)%).

Examples of other QC measures for PET radiopharmaceuticals according to the Ph. Eur. in addition to the radiochemical purity are pH, visual inspection, radionuclidic identity and purity (by isotope half-life analysis), A_m (if applicable), residual solvents, sterility, and bacterial endotoxin test (International Atomic Energy Agency, 2009; European Pharmacopoeia table 5.19.-1.). These requirements were met in all of the injected batches in these studies.

6.2 RMA of PET tracers

Generally speaking, the RMA requires multidisciplinary knowledge to enable a systematic approach to it. In the centre of RMA, there is the need for analytical chemistry for the proper applying of separation sciences, radio- and medicinal chemistry for understanding the PET tracer and its key properties to aid in developing them, and understanding the stability of the tracer in various conditions during the analysis process. Also, biologics to apply the results to the *in vivo* situation like biodistribution and the usability of the tracer into real-world research applications, and finally radiophysics in order to optimise the radiodetector capabilities as the vital backbone to the analysis methods.

RMA is essential not only for generating radiometabolite-corrected TACs, but also for evaluating the *in vivo* stability of PET tracers and guiding the design of more stable compounds. The identification of radiometabolites using analytical techniques such as LC-MS/MS and NMR often requires *in vitro* generation of radiometabolites in sufficient quantities. In this context, *in vitro* CYP enzyme panels can be

particularly useful for identifying the specific cytochrome P450 isoforms responsible for the formation of particular radiometabolites. This knowledge can support the development of strategies to inhibit undesired metabolic pathways or modify the molecular structure of the tracer to enhance metabolic stability.

Testing the metabolic stability of new PET tracers using cytochrome enzyme kits also aligns with the 3R principle, by potentially replacing some preclinical *in vivo* studies with ethically preferable *in vitro* alternatives. This approach should be considered whenever feasible to support more ethical tracer development.

Robust RMA not only enables accurate modelling of PET imaging data but also supports the assessment of tracer usability and optimisation for clinical application. Furthermore, insights gained from RMA of existing tracers can inform the design of next-generation compounds with improved pharmacokinetic profiles. For these reasons, continuous efforts should be made to validate and refine RMA methodologies, ensuring high-quality data to address critical questions regarding tracer characteristics with greater precision.

6.3 RMA method development considerations

Developing a robust method and correctly analysing the parent fraction is not always a straightforward task. With [^{11}C]SMW139, after the radioTLC method (Study I) and radioHPLC method (Study III) were developed, the methods have been robust and the results have been easy to analyse.

6.3.1 RMA sample preparation

The main objective in sample preparation is to enable sufficient separation between the different key molecules in a mixture by a chromatographic method by removing as much as possible of the interfering molecules in the mixture. They could be plasma proteins, phospholipids, salts, and other blood or tissue components. In RMA of a PET tracer, preferably all other molecules than the radioactive ones in addition to the suitable solvent for the chromatographic method should be eliminated from the mixture to as high of a degree as possible. In the case of [^{11}C]SMW139, the key molecules to isolate from the rest would be any molecule that has the original ^{11}C-radionuclide attached to it. However, isotopologues i.e. molecules that are structurally identical, except for the substitution of radionuclide with its corresponding non-radioactive isotope, cannot be separated from each other with chromatographic methods. If it were possible, it would be convenient to increase the A_m by separating the non-radiolabelled counterpart from the tracer batch.

If the blood or plasma samples would go untreated to any HPTLC, TLC or radioHPLC application, then it would be in most cases much harder or even

impossible to develop a method that would be robustly up to the separation task. The analytes of interest are in trace levels and an overwhelmingly big portion of non-radiolabelled other non-relevant molecules would be present, occupying the critical interaction sites of the stationary phase and causing unnecessary secondary interactions, thereby hindering effective separation.

One possibly surprising parameter that affects the RMA method is the mode of dissolved protein removal from the sample, which is a large part of the sample matrix load in plasma samples. The composition of the solvents in the supernatant mixture affects for example, the degree of protein precipitation (Polson *et al.*, 2003), the amount that can be injected into radioHPLC or be spotted onto the TLC or HPTLC plate's application line. For example, the sample matrix might not be suitable for applying onto a TLC plate at all, like in the case if a sulfosalicylic acid precipitated plasma sample with no organic solvent portion in it, such a sample would not be well absorbed into a reverse phase TLC plate, causing that the sample would not properly migrate and separate on the plate. The optimal precipitation solvent mixture and its ratio to plasma or tissue should be carefully optimised to gain a robust sample preparation method for a successful RMA study.

The optimal precipitation solvent usually consists of cold organic solvent, such as chilled ACN or methanol, with an acidity modifier to stabilise any ionisable groups of the analytes of interest into a single charge. If the composition contains an excessive proportion of a strong eluent for an RP-18 column, such as ACN, injecting the sample into the radio-HPLC sample loop may affect certain tracers that are sensitive to high organic solvent content. These tracers can be prematurely eluted further along the column due to the influence of the strong eluent in the supernatant. Typically, a ratio of 1.5–3 parts organic solvent to 1 part plasma is required. However, if this proportion is excessive for the radio-HPLC method, dilution or an acid-based protein precipitation method, such as one using sulfosalicylic acid, may be considered. No issues related to ACN in the supernatant were encountered with the described methods during these studies with [^{11}C]SMW139.

As it is expected to be in most cases, and found to be true in the case of [^{11}C]SMW139, the tracer and its radiometabolites bind to proteins in different fraction. Therefore, pure UF or similar methods do not yield the true parent fraction results, as a large fraction of radioactivity will remain bound to proteins in the filtration membrane. PPBA is important, as that will tell the true parent and radiometabolite fractions in plasma that are in the optimal free form – free from large biomolecules like HSA, enabling them to pass through for example, 10 kDa cut-off membranes.

Some novel blood RMA methods with other PET tracers are reported to work with minimal (Malherbe *et al.*, 2019) or even without sample preparation, like in a method that uses ultracentrifugation of plasma and the different fractions are

collected with a pipette from different layers and counted with a gamma counter (Ustsinau *et al.*, 2023). Malherbe *et al.* (2019) used direct plasma injection into a turbulent flow chromatography combined with an UHPLC to analyse the radiometabolites without further sample preparation. The automated sample matrix clean up systems might not be much faster than adding ACN, vortexing and quick centrifugation (90 s). They also include many technical aspects to them that need special expertise and resources. These would be preferred methods if they can be validated that they truly consider all aspects of the different potential sources of error and a pure separation can be made of at least the parent and the radiometabolites.

For accurate tissue RMA and biodistribution studies, transcardial perfusion should be considered to remove blood from tissues such as the brain. This is especially important if the brain is to be sectioned for autoradiography, as perfusion with saline helps to remove the radioactivity from the residual blood. However, excessive perfusion must be avoided, as it may flush out loosely bound radiometabolites, particularly those with high hydrophilicity. Hydrophilic tracers or those with low affinity to their targets may also be affected.

Therefore, standardisation of the saline volume relative to the subject's total blood volume (TBV), as well as the perfusion speed, is essential to minimise variability. These parameters should be adjusted to the specific aims of each study. For example, if the goal is to perform brain autoradiography to quantify receptor binding, removing unbound radioactivity, especially radiometabolites from the tissue is desirable, and a larger perfusion volume could be beneficial. In contrast, if the aim is to measure the parent fraction in brain tissue in a way that reflects the *in vivo* condition, minimal perfusion is preferable, as it will have less impact on the loosely bound radiotracer.

To better understand the influence of perfusion and used volume ratio on tissue fractions, comparative studies could be conducted using no perfusion, and perfusion volumes of 2, 8, and 20 times the TBV. Although subject-related biological variation may make it difficult to achieve sufficient statistical power to properly quantify the effect, such studies with even a small number of subjects could help determine, for example, whether radiometabolites are substantially flushed out at higher perfusion volumes, thereby providing insight into their affinity to the brain tissue and whether it is important to minimise the perfusion volume. Such studies might not be feasible though for ethical reasons if it requires using additional subjects unless it solves a critical aspect of the study.

If the objective is to correct for the parent fraction in the whole brain volume based on PET image data, then perfusion should generally be avoided, as the PET signal includes activity from both parent tracer and radiometabolites present in the cerebral blood volume (CBV). For short half-life tracers such as [^{11}C]SMW139, all procedures, including perfusion, must be performed rapidly. In our preclinical

studies, the transcardial saline perfusion volume was set at twice the estimated TBV of the subject, and the procedure was completed within approximately one minute using a syringe and needle.

6.3.2 Extraction efficiency considerations

Often one under reported parameter in many RMA methods is the extraction efficiency of the sample preparation step. The recovery rate reports the percentage of radioactivity that has been carried through from the original sample to the final sample that has been analysed, while the extraction efficiency is for example the fraction of radioactivity carried over during the protein precipitation step. With several steps in the sample preparation, usually a part of the analytes of interest remain unrecovered, for example, in the protein pellet, which is not commonly analysed. It is a rather simple procedure to measure this loss by measuring the total radioactivity with a gamma counter before and after any sample preparation step. However, this does not express information about the actual fractions of the parent compound and the radioactive metabolites left in the pellet. During a protein crash step, depending on what mode of precipitation is used, for instance precipitation with ice-cold ACN, the solubility of the different components can be completely different to the resulting supernatant when comparing to plasma. Therefore, the different composition of the residuals in the pellet may be one source of error when determining the true parent fraction value in plasma. Careful consideration should be made about the effects on modelling. For example, is only the free parent fraction or the total parent fraction in plasma needed when taking into account the plasma protein-bound fraction.

If the kinetic rates of the equilibrium between the bound and unbound parent or of the radiometabolites are fast, then the bound components do become eventually available to be transported through membranes into the target. Although, even in this case the rate of uptake is much slower compared to a situation where it would not have been initially highly protein-bound, and a portion of the tracer might be available too late when taking into account the PET imaging time frame. The nature of the dynamic equilibrium enables reversible components to have a steady concentration in plasma, which is usually a positive characteristic for pharmaceutical availability and biological half-life, and in some cases, for PET imaging too (Siddiqui *et al.*, 2021; Tesseromatis & Alevizou, 2008). However, these rates and fractions need to be understood to choose the right dose, imaging time frame, and modes for modelling the PET data.

The methods to analyse the extraction efficiency can vary and they are not always reported in publications comprehensively. There are many sources for errors that should be considered in order to account for them. For example, a fraction of the

supernatant remains as a residue between the precipitated proteins in the pellet when only the clear supernatant is collected from the surface with a pipette. This residue can be taken into account by several different correction methods. For example, the majority of the mass in the supernatant, other than the plasma water, comes from the dissolved proteins. By calculating the mass of the proteins that would normally be in the used volume of plasma and weighing the precipitate in the pellet and subtracting the mass of the proteins, then rest of the mass can be considered as the residual supernatant in the pellet. Another way to determine the residual supernatant in the pellet is to weigh and count the radioactivity of the fresh pellet after the supernatant has been removed, and then dry the pellet and then weigh it again. The weight loss due to evaporation can be accounted to represent the mass of the supernatant, which contains only a low mass of other solids than the proteins, and therefore we can calculate the mass of the supernatant in the pellet. After calculating the residual supernatant in the pellet with either method, the radioactivity concentration of that supernatant residue in the pellet can be calculated as the separated supernatant can be weighed and radioactivity measured and that can be then subtracted from the residue accordingly.

This residual correction is useful when the purpose of the extraction efficiency measurement is to indicate what fraction of radioactivity is truly bound to the proteins in the pellet and what fraction is rather in the dissolved form in the supernatant and in theory is therefore not bound to the pellet. Note, that this extraction efficiency result does not in my view indicate the true PPB fraction. When adding precipitation solvents to the plasma, it drastically changes the delicate equilibrium between the protein-bound and unbound fractions as the denaturation of the tertiary structure of the proteins may consequently release the weakly bound radioactive molecules. Especially, when using ACN as the precipitation agent, the attractability of a lipophilic PET tracer, such as [^{11}C]SMW139 to such a liquid phase is much higher than into purely saline-based plasma water. For example, when a radioactive component requires a sufficient ACN composition in the mobile phase until it will elute from a reverse-phase HPLC column, this simulates the effect that ACN will have in the precipitation solvent in especially releasing protein-bound lipophilic compounds from the proteins. However, the result of the extraction efficiency could indicate the plasma protein-free fraction in a way that it could still give some indicative result of the magnitude of the difference between subject groups, and therefore could be justifiably used to simply show if there are any differences between studied groups. However, when *in vivo* plasma samples that contain radiometabolites are used, the fraction in the supernatant over all radioactivity in the supernatant and the fraction that remained in the protein pellet (extraction efficiency) will likely not give the true parent free fraction result due to the radiometabolites.

As shown in Study II, it is much more rational to use the method presented there to measure the free fractions. However, the method needs to be fine-tuned for each tracer and the most suitable UF membrane material chosen to suit the tracer's properties.

The extraction efficiency is not that crucial when merely relative fractions are calculated, for example, in the parent fraction analysis. However, it will aid in understanding if we are missing a significant amount of analytes due to the sticking to the pellet, to the tube material, or to the pipette tips, in which the samples were handled in. In addition, it would be interesting to investigate if the radiometabolites and the parent are present in the pellet in similar percentages as they are in the supernatant. If a large portion of the radioactivity is remaining in the pellet, it can cause the supernatant to have inadequate radioactivity concentration that would disturb the analysis of the parent fraction due to a low signal-to-noise ratio.

For the [^{11}C]SMW139 tracer in these studies, the extraction efficiency for the plasma supernatant samples was measured in Study II to be over 99%. This meant that the protein pellet or the tube material did not bind a significant amount of radioactive components to itself and the parent fraction resembled the total situation in plasma and not the parent fraction of only the free components. This information is important when the aim is to know the true total metabolism rate of the tracer in the body. Although, just as interesting are the fractions of the free circulating radioactive molecules in plasma, as they can be very different, as shown in Study II.

The extraction efficiency is always sample preparation step dependent, tracer dependent and even affected by the parent fraction and fractions of the different radiometabolites, which may vary between different species, strains, disease state, sample drawing time point etc. The extraction efficiency has been usually reported in PET studies as the combination of all extraction efficiencies of all of the radioactive components and multiple steps combined. However, in some cases the extraction efficiency could be investigated on a molecule-specific level, to determine what components in reality are not extracted fully to the final analysing step while the other components could be fully transferred. This would show the true effect of the sample preparation steps to the results.

If the residual in the pellet or affinity to other materials in the sample preparation processing steps are significant, it would be advisable to alter the sample preparation steps towards a method with a more favourable extraction efficiency. If that is not possible, then the remnant should be further extracted and analysed for the remaining unanalysed fractions using the normal RMA method. In theory, the pellet could be washed with solvents that are known to be strong eluents to extract the residual radioactivity, to analyse it to find out whether there are any unexpected components present that are not originally extracted, and in what fractions do the different radiometabolites and the parent stick to the protein pellet. Analysing every sample

this way would be impractical. Conducting these extra analyses should be performed for a subset of samples in the early method development phases. This helps to validate the protocol and shed more light for the reporting phase of the study and strengthens the credibility of the results.

6.3.3 HPTLC to TLC method in Study I

Initially when starting the Study I, the used RMA method was based on a HPTLC method. The HPTLC method was adapted from another PET tracers RMA method with little changes (Takkinen *et al.*, 2018). The particle size of the HPTLC plate (5–7 µm) (Merck KGaA. (15.1.2025a)) being smaller should in theory enable finer separation compared to the larger particle size TLC plate (9.5–11.5 µm) (Merck KGaA. (15.1.2025b)). However, this HPTLC method was slow and could provide in most cases only moderate resolution power. Sometimes the resolution was inadequate despite the attempts to try to improve the separation power by modifying the mobile phase while still using the HPTLC plate.

During the Study I, effort was made to also explore different plates and eluent combination, along with various application volumes to find a faster, more robust method with better resolution and tolerance of larger application volumes. Method development was essential especially for the less radioactive brain samples, in order to analyse the different fractions of radiometabolites and parent fraction with confidence.

The advantages in changing the method to be based on the larger particle size, aluminium backed TLC plate (Silica gel 60 RP-18. Art. No. 1.05559.0001, Merck KGaA) were significant due to a much faster elution time from the average of 45 min down to 6 min. This alone resulted in a 280% higher intensity of the PSL signal compared to the HPTLC methods signal due to the shorter decay time. In general, the specifications of the HPTLC and TLC plates did not differ that much nor did the HPTLC in this case offer any clear advantages that would have justified using it in this specific method as the separation was better in the TLC method. In study I, it was tested that TLC had also a higher capacity to handle larger mass of sample, leading to the ability to apply more sample onto the plate without the fear of negatively affecting the resolution of the separation too much. When more mass can be concentrated with several small applications of the supernatant, then the signal can be increased and therefore the signal-to-noise ratios of the peaks on the chromatograms can be improved.

Each plate has a finite characteristic capacity to retain analytes and offer sharp separation, which depends on the interaction between the migrating analytes and the stationary phase. This capacity is limited to a certain amount of molecules due to factors, such as the specific surface area, layer thickness, particle size and porosity,

which determines the amount of free binding or interaction sites in the stationary phase. The loading mass capacity is proportional to the square root of the thin-layer plate adsorbent layer thickness. Overloading the plate's capacity significantly broadens the peaks in the radiochromatogram and often causes tailing of the peaks. Due to the much better resolution of the TLC method compared to the HPTLC method, in the cases that the TLC plate capacity would be slightly overloaded, negatively affecting the peak shape, it would still not have a significant negative impact on the ability to separate the parent from any of the radiometabolite peaks. The robustness of the new TLC method increased the confidence in the results and reduced the number of failed analyses.

The Figure 4 showed that the parent fraction curves are similar using the HPTLC or TLC methods. However, they include data from different subjects, preventing optimal comparison. As the initial comparisons show that the age, sex and strain might have an effect on the metabolism rate of [^{11}C]SMW139, this approach does not fully validate the similar results between the methods. In order to remove the normal biological variation effect from this comparison, the following comparison approach was necessary. Both methods were analysed with a subset of subjects in parallel with the same plasma and brain supernatant sample to assess if changing the method would cause differences in the parent fraction results. If more radiometabolites could be separated from the parent, then the new, different results would supersede the previous method. However, in this case changing the method to the TLC method did not markedly change any of the mean or SD of the results as shown in Table 4, indicating that the HPTLC method results were as valid even if they were harder to analyse. Some samples, especially among the brain homogenates, occasionally there were situations where there was not enough of radioactivity remaining after the elution in the samples applied to the HPTLC, so that the parent fraction was impossible to be analysed reliably. The new method in this case enabled far better signal-to-noise ratios partly due to a faster analysis time. Due to the short half-life of ^{11}C-isotope, the radioactivity decays quickly. Therefore, the protocol duration length has a crucial effect on the total radioactivity left on the plate. Faster protocols allow detecting smaller radiometabolite fractions and analysis of later time points.

In general, it is only a secondary aim in RMA to be able to separate more radiometabolites from each other, to enable deeper analysis of different radiometabolite fractions to understand the metabolism on a deeper level. However, this is important to do if the aim is to separate the radiometabolites for identification purposes. In general it might be easier to produce radiometabolites with microsomes *in vitro* for structural elucidation (Schou *et al*., 2023), still these should be confirmed to have the identical R_t or retardation factor than the *in vivo* generated radiometabolites, therefore methods are needed in these instances to separate

radiometabolites from each other with confidence. Once the structure is elucidated, it is easier to plan for more stable PET tracers. The TLC method was successfully optimised during the Study I, which enabled enhancing the method to separate more radiometabolites from each other and gain better resolution between the parent tracer and the closest radiometabolites. With the new TLC method, in plasma even up to four distinct radiometabolites were observed as shown in Figure 6. In the extreme cases where the fourth radiometabolite was visible, it was minor in quantity (retardation factor of 0.75 in panel A, C, and E in Figure 6). Up to three radiometabolites were observed in the brain. With the HPTLC method, only up to two were found in plasma and two in brain, and in the most cases a baseline separation was not achieved between them.

The use of HPTLC plates offer advantages in many other separation applications, and they have been used a lot in the Turku PET Centre (Aarnio *et al.*, 2024, Rokka *et al.*, 2017). However, for the separation of [^{11}C]SMW139 and its radiometabolites, it can be concluded that HPTLC was not the optimal choice as the stationary phase, and therefore the method was changed.

An important note should be made about the reproducibility of the chromatography separation results, especially in this instance. The manufacturing process of the HPTLC plate (silica gel 60 RP-18, Art. No. 1.05914.0001, Merck KGaA) has changed around December 2020 and our studies were performed with LOTs that were produced before that change. The same HPTLC plates with the same separation characteristics are not manufactured anymore. The article number of the product has remained the same despite the change, so the article number does not guarantee an identical product in this case. If the same studies were to be run again, it could potentially result in a very different separation and lead to other conclusions than shown in this thesis. An example of such a situation where it had a clear effect and lead to a definite need to change the method can be read in a recent publication by Aarnio *et al.* relating to [^{18}F]FTHA RMA method development (Aarnio *et al.*, 2024).

Constant effort should be made to improve RMA methods as techniques and available materials change, and they might enable to even separate new radiometabolites that were not previously separated from the parent compound as was the case in the [^{18}F]FTHA radiometabolite study (Aarnio *et al.*, 2024).

6.3.4 RadioHPLC vs radioTLC method development considerations

RadioHPLC and radioTLC methods each have distinct advantages and limitations. In clinical studies, the injected radioactivity per body mass in humans is approximately 1–10% of that in rodents, resulting in significantly lower radioactivity

concentrations in plasma. However, the sample volume obtainable from human subjects is substantially larger than that from rodents. Therefore, methods that can efficiently process larger sample volumes are advantageous when taking into account these radioactivity concentration differences. Such as using relatively large HPLC columns combined with a high-volume scintillator flow cell, like the 550 µL BGO flow cell in the flow-through radiodetector (Radiomatic 150TR, Packard, USA) used in the Studies III and IV — or methods that are capable of concentrating large volume samples, to improve the signal-to-noise ratio. However, the large volume of the flow cell necessitates more separation power from the column to achieve baseline separation of the peaks.

Considerations on the sensitivity of the radioactivity detection modes is also one of the key parts when determining what methods are viable options, along with how many samples are needed to be analysed within a given time frame. When using radioTLC, multiple samples can be applied rather rapidly onto for example, a 20 cm wide plate with ease, and eluted simultaneously. For radioHPLC, only one sample can be analysed at a time, and the gradient runtimes along with the column wash and re-equilibration time can be easily much longer than the eluting time in the most rapid TLC methods. As most PET centres do not have multiple sensitive radioHPLC systems running in parallel to enable multiple sample analysis at the same time when frequent time points need to be analysed, then in these cases radioTLC might be the best option. In addition, the use of well-optimised automated TLC sample application systems often outperform human sample pipetting in the terms of concentrating the sample on the plate in a small area. However, these automated TLC samplers are often slower than manual applying. With methods that work only with a low amount of sample volume before the chromatography starts to loose adequate performance due to the plate's stationary phase's binding site overload, then the advantage in concentration performance is lost and they do not play a significant role in such analysis. With the radioHPTLC and radioTLC [^{11}C]SMW139 RMA analysis the maximum applicable volume was only between 8-20 µL (Figure 5). The sample could be applied in a few 5-10 µL increments under a gentle room temperature hair dryer airflow to speed up the absorbing and drying process of the sample to the plate. Therefore, in these cases an automated TLC applicator would not be advantageous, as the application speed is around 1 min per 10 µL, which is much slower than manual applications. The usage of the automated TLC samplers requires careful work, with changing the syringe between applications and with manual needle washes between each sample which can take surprisingly long to do, so such methods can be sometimes much more laborious than manual applying. In some projects with other tracers, the automated TLC applicator has been tested to be useful and can enable slightly better separation between peaks (data not shown). An example for the use of an automated applicator can be found in a study comparing

radioHPLC and an automated applicator aided radioTLC methods for studying the radiometabolites of 1-^{11}C-Methyl-4-Piperidinyl n-Butyrate (^{11}C-MP4B) (Roivainen *et al.*, 2004).

A major differentiating element in radioTLC and radioHPLC is the mobile phase. Normally, radioTLC relies only on a single mobile phase throughout the whole elution process. The corresponding situation would be using only an isocratic method on the radioHPLC where the mobile phase composition would not change during the method run. However, running gradient methods requires equilibrating the column after the run, which increases the total run time. However, with a gradient method it is possible to elute the remainder parent faster out from the column once the last radiometabolites have been eluted in addition to have stronger washes from any interfering residuals from the column. Also, the ability to run gradient methods on radioHPLC, where the composition of the mobile phase can be changed continuously during the elution process, often with four distinct pure or mixture of solvents, opens up a vast possibility to enhance separation of even very similar molecules. A less used technique is 2D-TLC, where the plate is eluted twice, with two different eluents, with the plate rotated 90 degrees after the first elution. However, 2D-TLC is a lengthy process and is rarely, if ever, used with radionuclides with a short half-life. This might be one option when the separation is not possible with traditional TLC.

Both radioTLC and radioHPLC have a wide selection of stationary phases these days, but the variety of the different phases and particle sizes is much larger for radioHPLC. In addition, radioHPLC has a much larger variety of column dimensions depending on the injected sample volume and applications it is needed in, ranging from nanoLC with even less than 100 µm column diameter to preparative HPLC with a column diameter of over 21 mm. The most useful column diameter in traditional RMA applications ranges between 2.1–10 mm. RadioTLC materials continue developing in the field of TLC, such as the development of smaller particle-size stationary phase in the HPTLC plates. However, in our specific application in Study I, where we aimed to separate the radiometabolites from [^{11}C]SMW139, this method had several disadvantages. The much slower elution speed, combined with limited loading capacity, required applying a sample amount close to or even exceeding the recommended maximum. Despite this, only low levels of radioactivity was left and the resolution was poor. Using a more traditional TLC plate helped to overcome these challenges.

When running multiple samples, it is important to be able to maintain identical analysis conditions. RadioTLC has the advantage of simultaneous elution of all the samples spotted onto the same plate. However, the solvent occasionally migrates slightly faster closer to the edges. Therefore, the samples need to be close to the centre if this equal migrating distance is crucial. With radioactivity constantly

decaying, then absolute quantification is much easier when each sample is exposed to the radiodetector at the exact same time and equal length of time, which eliminates the need to decay correct each peak to the same time point as required in radioHPLC. The developed radioTLC plate is fully exposed to the autoradiography plate so all of the samples on the plate are exposed the same amount of time. In radioHPLC, with ^{11}C-tracers the peak area decay correction is significant, while for ^{18}F-tracers it is not as impactful. For example, in the radioHPLC [^{11}C]SMW139 RMA method had about 6.5 min R_t difference between the radiometabolite 1 peak and the parent peak (Figure 7), which makes the parent peak area 20% smaller compared to the radiometabolite 1, thus deflating the parent fraction results, hence requiring the correction. For a ^{18}F-tracer this 6.5 min would result in a 4% reduction. Often the R_t differences between the peaks might be a lot more in other developed RMA methods, inflating the need and impact of this correction. Decay correcting each peak is an easy task, so it should be implemented in all cases. The radioHPLC in theory can also analyse samples with identical conditions, however, the column deteriorates during each run, and when running the samples one after another, the conditions may vary slightly, although HPLC-systems and the methods are generally robust and reliable.

An additional difference should be taken into account when deciding between a radioTLC or a radioHPLC method, which relates to the analytes' affinities to the stationary phase. In some cases, the radioHPLC can retain analytes of interest so that they all do not elute out of the column as planned. To ensure that all components come out of the column and are accounted for in the analysis, a fraction collection and gamma counting should be performed for example, with a sensitive automated gamma counter. The recovery percentage can be calculated by decay-correcting all the radioactivity exiting the waste line and dividing it with the total radioactivity injected into the column to ensure that no radioactive analytes of interest remain trapped in the column, as demonstrated for example, in a study by Malherbe *et al.* (Malherbe *et al.*, 2019). This is a laborious procedure, but this should be performed for each radioHPLC method for an adequate amount of samples, just as extraction efficiency should be calculated for the sample preparation steps, to get an understanding of the analyte losses related to the method. RadioTLC does not need this recovery analysis in the same way, as the whole plate is analysed and everything that was applied onto the plate, excluding any volatilized radioactive compounds, are visible in the analysis. In many cases, with other PET tracers, a significant portion of the radioactive analytes remain immobilised on the application line even after elution. If a similar mode of separation with the same sample would be used on radioHPLC, that portion would probably be stuck in the column and could not be taken into account in the total radioactivity of the sample in the parent fraction analysis. However, with gradient method abilities, a strong solvent wash can be performed at the end of each radioHPLC run, which minimizes the chance of

radioactive components remaining in the column. This in turn lengthens the equilibrium step of the column. For methods that show strong absorption on the TLC plate, a test could be run with a strong solvent to wash such samples using a duplicate plate to analyse if those components are truly immobilized permanently to the RP-18 stationary phase or would such a washing step elute these components, as it does in radioHPLC.

Often it is speculated that the part that is stuck on the TLC plate would be precipitated protein remnants from the plasma, but that has not been an easy task to prove. Fortunately, in the case of [^{11}C]SMW139, such immobilized fraction to the TLC plates or HPLC columns has not been observed. In addition, the possible volatility of the parent or the radiometabolites should be taken into account. In such cases, where the volatility is high, cold storage of the samples before analysis is beneficial and radioHPLC should be a preferred method as radioTLC has multiple drying steps before the radioactivity of the plate is eventually exposed to the autoradiography imaging plate. When studying such properties with [^{11}C]SMW139, a comparison was made between a passively absorbed and air dried plasma supernatant sample results to a duplicate sample that was dried excessively with hot air. Since the fractions of radiometabolites and parent were the same in both cases, we can conclude that the TLC plate drying protocol does not significantly affect the radioTLC parent fraction analysis results.

From an environmental-burden and ecological perspective, the TLC methods use much less solvents during the elution than HPLC, and they do not require the same extensive stationary phase washing after use due to single use plates design. Although the radioHPLC column can be used for hundreds of sample runs, the amount of solvents used for a regular subject RMA study in Studies III and IV is around 1 litre, when the radioTLC method uses around 40 mL. The aluminium in the TLC plates is recyclable and only 0.2 g of silica gel 60 is used per 10 × 10 cm plate with the 160–200 µm silica gel coat thickness.

At the end of the day, both chromatographic modalities should be considered when RMA method development of a new PET tracer is started. Sometimes both methods can be used in the appropriate situations according to their strengths as was done in this thesis with the preclinical samples being analysed mainly with radioTLC and the clinical samples mainly with radioHPLC, or for example, as done in a [^{18}F]FDG RMA study (Rokka *et al.*, 2017).

For ^{18}F-labelled tracers, one aspect to consider is the possible detached free [^{18}F]F$^-$. It is important to quantify it for accurate pharmacokinetic modelling (Paolillo *et al.*, 2011). [^{18}F]F$^-$ exhibits vastly varying retention, depending on for example, the pH. This can be challenging on radioHPLC as part of the free fluoride can remain in the column, especially during short runs or cause broad peak areas over several minutes (Ory *et al.*, 2015). These residuals can be possibly seen in the next injections

or wide peaks can overlap with the parent compound. For this reason, radioTLC should be compared to radioHPLC and considered as the analysis method if free fluoride might be present in larger quantities (Wang *et al.*, 2020; Laferriere-Holloway et. al., 2023). Also, a successful ion-exchange cartridge with gamma counting method for quantifying [^{18}F]F$^-$ has been suggested as the preferred method (Paolillo *et al.*, 2011). However, ion-chromatography instrumentation is less common in laboratories pursuing RMA, so the implementation of this technique requires new laboratory-systems.

Other possible methods to analyse the radiometabolites are listed in Section 2.3.2. In later [^{11}C]SMW139 studies, comparisons between methodologies could be considered to enable better comparability between other [^{11}C]SMW139 studies performed with different RMA methods.

6.3.5 RMA method considerations when using TB-PET

When using TB-PET, the huge sensitivity-gain enables lower injected radioactivity doses to the study subjects. This will have a notable effect on the abilities to perform RMA through the lower radioactivity concentration in blood. In these clinical studies (Studies III and IV), SAFOV PET scanners were used (high-resolution research tomograph (HRRT), Siemens Medical Solutions, Knoxville, TN, USA). Therefore, the injected doses were around 400 MBq per human subject. This enabled sufficient radioactivity even to analyse the latest time point samples when sensitive radioHPLC radiodetectors were used. However, if the amount of radioactivity is lowered down to just a tenth part of a fraction of the original, as could easily be the case (Badawi *et al.*, 2019), then performing RMA from later time points could be impossible with the current methods and instrumentation. Efforts need to be made to concentrate the sample, gain narrower peaks, and develop more sensitive radiodetectors along other optimisations. Also, new approaches to RMA modelling should be considered, for example, using more population based corrections, and *in silico*-modelling by machine learning algorithms with artificial intelligence optimisations to model the parent fraction data from the IDIF using organ uptake information. Such methods could help to omit the invasive arterial blood sampling for good, to enable easier and more convenient PET imaging for the study subject and the researchers, and remove one more challenge (Zanotti-Fregonara *et al.*, 2011) from the use of IDIF and other image derived parameters.

6.4 RMA findings

6.4.1 RMA findings in studies I–II

In Study I, the SD for the parent fraction was large even among the age-matched groups. There were tentative evidence of differences in the plasma parent fraction seen between the genders, but as the gender balance among the number of subjects was far from optimal, there cannot be definite conclusions drawn from these results. If there were future studies including [^{11}C]SMW139, then gender and age groups should be matched precisely to enable proper comparison between age groups and the effect the gender has on [^{11}C]SMW139 metabolism rate in addition to other results. This would require a larger amount of subjects, as potential variance between for example, the age, sex and strain need to be taken into account. Ethically, the number of subjects is to be limited to as little as possible, so unless including an increased number of groups would answer an important questions with potential real-world applications, then it might not be ethical and it would be better to stick to as homogenous study material as possible and draw the needed conclusions pertaining to that study group. If the results seem promising enough, then extending the studies to the other gender, a wider age range or different strains would seem more logical and simplify the variables of the subjects used. In preclinical studies, such strict inclusion and exclusion criteria for optimally suitable subjects is much easier to apply than in human studies, where the criteria must be adapted to the realistically available potential study subject pool to maintain a practical study duration. In Study IV, we found similar tentative results of the gender effect on the results among human subjects, only that the result was reversed. The female had slightly higher parent fraction values. In the future clinical studies related to [^{11}C]SMW139, it would be best to include only one of the genders in the study.

The age of the subject did not have a large effect on the parent fraction value, as the correlation was not fully consistent, although some trends were observed in the parent fraction value in plasma. Gender and mouse strain were not considered as factors in the age correlation analyses, as the groups were otherwise too small to draw any conclusions from them (Figure 11). While the age of the mice seemed to have a small, logical effect in the parent fraction results, with the older mice showing slower metabolism of [^{11}C]SMW139 in plasma (Study I). However, variability was high. The SD and the range between the maximum to minimum values were large. The sample size was the smallest at the 45-min time point, where the age showed the strongest correlation with the plasma result. Due to these limitations, no definitive conclusions can be drawn regarding the effect of the age on the rate of metabolism of [^{11}C]SMW139.

In Study II, the RMA was required in order to gain information about the identity of the different protein-free radiolabelled components in plasma and their concentration at different time points during the study. The radioTLC method showed that the majority of the radioactive species in plasma ultrafiltrate consisted of the radiometabolites and enabled precise analysis of the free fractions. Therefore, the RMA played a key role to enable the PPBA in the Study II.

6.4.2 RMA findings in the Studies III and IV

In Study III, the mouse and human RMA had an essential role in refining the modelling approach for the clinical subjects. The comparison of the plasma radiochromatograms between the mouse and human subjects, in addition to the mouse plasma and brain radiochromatograms gave strong evidence that the radiometabolite 2, which was found in both human and mouse plasma, was not entering the mouse brain. When applying this assumption that the radiometabolite 2 would not enter the human brain either by leaving its fraction out from the dual input model, then the modelling parameters were stabilised and made much more sense. Before this finding and approach, the clinical studies encountered challenges in modelling the [^{11}C]SMW139 PET results in the brain. The abnormally high accumulation of radiometabolites in the rodents and human brain manifested as the high levels of non-specifically bound radioactivity in the brain. This is usually connected to the radiometabolites, as in theory they lack a specific binding site in the brain.

Without RMA, there would be no possibility to differentiate the identity of the radiolabelled molecule solely by using the PET scanner information.

The plasma parent fraction over time graph had a clear difference in the shape and amplitude between humans and mice. In mice, initially the parent fraction dropped steeply, whereas in humans, the decrease was much more linear even up to the last time point of 90 min post injection. This suggests hope for the use of [^{11}C]SMW139 tracer in humans, as a significantly larger fraction of the unmetabolized tracer remains intact in humans, unlike in mice.

In general, when modelling PET data and deciding on the time frames, the parent fraction curve should be taken into account, as it directly affects the available input for the target. If the parent fraction data in the specific tissue of interest would be available in humans, then this would not be as limiting. As that information is not obtainable, and relying on corrections, modelled from preclinical, human plasma or *in vitro* information is not always fully accurate, then the possible accumulating radiometabolites start to be a significant source of uncertainty in the analysis. However, the optimal period also depends on the target affinity, washout properties, and overall tracer kinetics. Therefore, if the tracer undergoes substantial metabolism

but possesses favourable properties that enable its rapid and effective target accumulation, efficient clearance from surrounding tissues, and minimal radiometabolite uptake, then fast metabolism alone does not necessarily make the tracer unsuitable for imaging.

In the clinical studies, it is clear that the quantification of the P2X7 receptor requires accurate RMA. More precisely, when performing quantification in the brain, the analysis needs to include accounting for the BBB-penetrating radiometabolites, to enhance the accuracy. In Study IV, these RMA methodologies were applied to examine P2X7 receptor binding in both new-onset and secondary progressive MS subjects. This study further supports the relevance of parent fraction correction, as only accurate quantification in clinical studies of different groups can reveal the very subtle receptor changes associated with disease pathology, which may be less evident without such accurate corrections.

6.5 *In vitro* mouse brain homogenate study findings

Both chromatographic analysis techniques of incubated brain homogenate and sham samples using the radioHPLC and TLC methods indicated that both samples contained over 99% of the parent tracer at all investigated time points. The insignificant fraction of radioactivity (<1%) outside the parent tracer retardation factor region in the radiochromatogram likely resulted from baseline irregularities, as background correction did not fully eliminate the normal background radioactivity. There were no observable peaks either at the characteristic R_ts of radiometabolites when using the radioHPLC method.

When it is purely the goal to see if even small radiometabolites would form in such conditions, the best approach was to inject into the radioHPLC an amount of radioactivity that would definitely over saturate the radiodetector at the parent peak R_ts, as this would maximize the possibility to detect even minor radiometabolites too, while losing the ability to quantify them. In this setting, as nothing was observed there, we could confidently draw the conclusions of this analysis. Also, radioTLC method was used to increase the chance to observe any radiometabolites that the radioHPLC would miss. These findings suggest that radiometabolites are not formed under *in vitro* conditions in incubated brain homogenate and are unlikely to be formed directly within brain tissue *in vivo* either; rather, they likely enter the brain by crossing the BBB from the blood.

6.6 PPBA

6.6.1 PPBA method development

When the surprisingly high accumulation of non-specifically bound radioactivity was observed in the human brain, a relevant question rose during the Study III: Do the radiometabolites cross the BBB from the blood vascular system or do they form directly inside the human or rodent brain? To answer this question during Study III, which had commenced already before Study II, an *in vitro* mouse brain homogenate study was carried out and reported within Study II as discussed in the previous section. The incubation of fresh mouse brain homogenate with [^{11}C]SMW139 clearly showed that in those conditions radiometabolites do not form. This study shows that it is not always initially clear where the radiometabolites are forming. Therefore, careful and extensive studies should be made to rule out even unlikely scenarios in tracer metabolism, in order to gain a deeper understanding of the underlying mechanisms behind the phenomena.

The unexpectedly high and continuous accumulation of radiometabolites into the brain through the BBB of the human subjects was puzzling. Similar findings had been done previously with other PET tracers (Zoghbi *et al.*, 2006). In theory, if the radiometabolites had a significantly larger free fraction, then that could at least partly explain the observations. Therefore, the idea to further develop methods to investigate the protein-free fractions of the radiometabolites and parent tracer in plasma using PPBA was initiated.

In general: small size, low molecular weight, un-ionized charge, and low hydrogen bonding potential are some of the factors that favour BBB penetration (Warren, 2018). The radiometabolites of [^{11}C]SMW139 have not been identified at the molecular structure level, so it is unclear what the parent tracer is metabolized into. It could be metabolised into smaller molecules through the metabolic Phase I pathway by hydrolysing the amide bond (Waller & Sampson, 2018), or into larger molecules, such as through the Phase II metabolic pathway of glucuronidation (Yang *et al.*, 2017).

Based on TLC retardation factor values and on the elution order in the C_{18}-reversed-phase radioHPLC, all of the radiometabolites had higher polarity, and therefore were less lipophilic, than the original parent tracer. This suggests that their ability to cross the lipophilic BBB is compromised. In other words, they should not be crossing the BBB with the same ease as the more optimally lipophilic [^{11}C]SMW139. The parent tracer's calculated logP of 2.90 and molecular weight of 386.8 g/mol are considered moderate for successful BBB penetration (Pike, 2016). However, the much higher f_M compared to f_P in plasma may explain why the

radiometabolites are still accumulating efficiently into the brain just as does the parent tracer.

In mice, where the radioactivity concentration in plasma was higher than in humans, it was possible to study the PPB even up to the 45-min time point. In humans, the last practical time point was the 20-min time point to still have adequate radioactivity concentration in the plasma for the autoradiography analysis of the TLC plates after all of the UF steps. In addition, the 20-min time point was chosen for the clinical studies as it had an optimal ratio and sufficient amount of both the radiometabolites and the parent present to analyse both simultaneously.

During the PPBA studies it became clear that the centrifugation time was an important factor to keep constant in the protocol, as the radioactivity concentration of the filtrate increased over time during the filtration process. At first, especially the parent compound, which was the component that was the most retained by the Ultracel low-binding regenerated cellulose membrane in the Microcon UF device, took time to start coming properly through the membrane. Because of this phenomenon, the parent compound had a significantly larger membrane correction factor. Increasing the centrifugation time reduced the membrane correction factor and variations as the radioactivity concentration was increased and a larger volume of the filtrate had come through, which decreased the relative error. In addition, the increased radioactivity concentration elevated the signal-to-noise ratio and made analysing the results easier. Therefore, results that are more reliable could be obtained. When the protocol is carefully standardized, then we can see lower SDs in the results, and especially in the membrane correction factor. In addition, after sufficient amount of membrane correction repetitions and seeing the low deviation in the result with a standardized protocol, the individual membrane correction studies could be omitted and an average could be applied which enormously simplifies the protocol.

The increased volume of filtrate with the longer UF times was convenient especially because the TLC plate was not as restricted concerning the volume of the ultrafiltrate that could be put onto the plate, than compared to the RMA sample volumes. When analysing radiometabolites and using ACN-precipitated plasma supernatant or brain homogenates, the TLC plate's maximum application volume due to the restricted mass loading capacity was only around 20 µL at most. The 10-kDA ultrafiltrate's matrix effect was significantly reduced by the filtration, which enabled applying all the filtrate that was accumulated. In reality, there must be an upper limit to the capacity, but with these UF times, it was possible to apply everything, even up to 54 µL onto the TLC plate without the separation being affected too much. The volume accumulated usually varied between the range of 36–45 µL.

Some UF protocols have instructed to spin the plasma to dryness, meaning that as much as possible of the plasma water is transferred through the membrane and then assuming all of the free analytes in the original state has passed through, then the proteins in the filter membrane and the filtrate are counted separately. This method does not take into account that when plasma water and the free analytes are depleting from the presence of the plasma proteins, it shifts the equilibrium of the system and can cause the f_P to change. A non-depleting way to use UF is to filter only a small fraction of the plasma water, supposing that this has no significant effect on the equilibrium as a non-depleting system, and then measuring the concentrations of the original plasma radioactivity and the radioactivity concentration of the filtrate. This non-depleting way was introduced in Study II. Also, spinning to dryness would increase the spinning time dramatically, negatively affecting the radioactivity left in the sample.

6.6.2 Discussion about the PPBA results

6.6.2.1 Ultrafiltration membrane and its correction factor

In our studies II and IV, we performed UF with the Microcon UF device, selected for its Ultracel low-binding regenerated cellulose membrane and suitability for small sample volumes (50–500 µL). The Microcon UF device is initially designed to "simply and efficiently concentrate and desalt solutions of DNA, RNA, protein or other macromolecules" (Merck KGaA. (21.1.2025)). A 10-kDa cut-off membrane was employed, in contrast to the 30-kDa cut-off commonly used in most studies (Moein & Halldin, 2020; Amini *et al.*, 2014; Zoghbi *et al.*, 2006). Some studies even have used 50-kDa cut-off (Theodoridis, 2006). Even though the most substantial protein in the human plasma is HSA (66.5 kDa), there are several other smaller proteins present. For example, the mouse plasma includes prealbumin, α1-acid glycoprotein, transferrin, lipoproteins, immunoglobulins, complement proteins, and coagulation proteins (Sigma-Aldrich. (22.1.2025)). As the specific proteins binding the parent tracer and radiometabolites remain unknown, reducing the cut-off size was a rational choice to minimize any protein flow through the membrane. As the membrane was initially designed to concentrate and collect proteins that have a larger molecular weight than the cut-off and therefore, the filtrate is not even designed to be 100% free from molecules that are above the cut-off. In a correspondence with the manufacturer, they have recommended to lower the cut-off value if the aim of the filtration is to have the filtrate as free as possible from proteins. The lower cut-off was chosen to minimize errors associated with protein leakage into the filtrate, as even a 30-kDa membrane can allow some percentage of proteins that

are above that cut-off value to pass through (Merck KGaA. (22.1.2025)). The slight increase in centrifugation time with the 10-kDa membrane was therefore justifiable.

The ultrafiltrate membrane correction factor was very similar between the clinical and preclinical studies. When the impact the UF spinning times on the membrane correction factor became clear, the times were better standardized. The PPBA method was constantly under review and such adjustments were necessary while standardizing the protocol and gathering data. The preclinical samples were analysed first, and then the method was adapted to the clinical studies. Therefore, a slight variation of the membrane correction values can be explained partly with the UF times differing more in the beginning of the preclinical samples. Also, as mentioned earlier in Section 5.5, the radiometabolite composition between radiometabolite 1–3 differed slightly between the clinical and preclinical subjects, so that the radiometabolite 1 was clearly the prevalent one in the preclinical studies, unlike in the clinical studies. The membrane correction factor was calculated for practical reasons as a combination for all radiometabolites together. In reality, the membrane correction values might slightly vary between the different radiometabolites. The radiometabolite 3 was almost as lipophilic as the parent tracer, so it is expected to have higher membrane correction value compared to radiometabolite 1. This can cause some variation between the membrane correction factor results between clinical and preclinical subjects.

The almost no need for membrane correction for the radiometabolites is rational, as they are in average much more hydrophilic according to the higher retardation factor in RP-18 radioTLC and the earlier R_ts in the RP-18 radioHPLC. As the more hydrophilic molecules have higher solubility to the plasma water phase, and therefore pulled through the membrane due to the stronger interaction to that aqueous liquid phase, then the more lipophilic [^{11}C]SMW139 will be naturally more retained by the membrane, leading to a more substantial membrane correction factor. The radiometabolites do not benefit from the membrane correction value that much and when the slightly longer spinning times were used in the clinical studies, it was close to one. If the membrane correction factor would not be used, it would clearly underestimate the fraction of the f_P in plasma.

6.6.2.2 Considerations of the PPBA results

The f_P was found to be time-dependent in the preclinical Study II (Figure 14). One theory could be that it would have something to do with the clearance of the parent tracer from plasma and the subsequent elevated availability of the plasma proteins to bind the remaining parent more effectively. Similar observations in humans have been made for other drugs, while for some drugs, like propofol, the PPB has been inversely proportional to the concentration of the drug (Nation *et al.*, 2018).

However, the average injected amount of radiolabelled and non-radiolabelled SMW139 combined in the clinical Study IV was 2.7(1.7) µg. Thus, the number of SMW139 molecules was at an average 4.2×10^{15} while the number of HSA proteins in an average weight and haematocrit possessing healthy human subject is 2×10^{21}. In addition, one HSA might have multiple binding sites with the potential to bind several molecules at the same time. For example, for propofol, there are two binding sites per single HSA (Nation *et al.*, 2018). So in clinical studies, at the time of injection, for every SMW139 molecule, there is roughly 500 000 individual HSA proteins to be bound to. This poses a question of what kind of mechanism could be underlying the time-dependency of the protein binding. As at first, it could seem intuitive that the ratio of the SMW139 to proteins would decrease due to uptake into tissues, excretion, or metabolism and so the binding would increase, as binding sites are more readily available. This could be the case. However, the low initial SMW139 to HSA ratio is not drastically affected by the decrease of SMW139 levels in plasma. As there are plenty of HSA binding sites readily available and if only every 500 000th HSA is preoccupied by a SMW139 molecule, then the probability of decreasing the SMW139-to-HSA ratio would be causing a significant effect is small. This ratio does not take into account that other molecules might be competing with the same HSA binding sites, which might have an effect on PPB (Moein *et al.*, 2019). Similar time-dependency has been studied using *in vitro* incubated samples. The time-dependency of PPB was at least not observed for different incubation times (Sorger *et al.*, 2006).

In mice, the corresponding amount is 7×10^{17} serum albumin proteins in an average-sized mouse, which has a similar molecular weight. When dividing that with the average injection and therefore the amount of SMW139 molecules injected, there were still over 2000 times more serum albumin proteins compared to SMW139 molecules. This ratio difference between preclinical and clinical subjects could have an effect, but still it is shown here that the number of proteins is nevertheless vast compared to the number of SMW139 molecules in both cases, so this should not in theory significantly affect the balance of the protein-free fraction equilibrium when this ratio changes during the study.

Notwithstanding these calculations, the time-dependency was shown in Study II, where the parent fraction corrected f_P decreased from 0.032 to 0.007 between 10 and 45 min, whereas f_M remained higher, ranging from 0.52 to 0.35. In the clinical studies, the time dependency was not analysed as only the *in vitro* and 20-min time point *in vivo* sample data was available. This could be studied in future [^{11}C]SMW139 studies.

In Study II, the fraction of free parent relative to all free radioactivity decreased significantly, roughly to a quarter, from 0.085 to 0.019 (from 10 to 45 min), indicating that most of the protein-free fraction or radiolabelled compounds consisted of radiometabolites during these time points, as was the case with clinical

subjects also. Likewise, the PPBA revealed that [^{11}C]SMW139 has a low f_P in the clinical Study IV, with radiometabolites accounting for a significant portion (88% at 20 min) of the free radioactivity that has the potential to cross the BBB. The *in vitro* sample PPBA $f_{P/P}$ resulted in 0.013 and the 20-min sample on average 0.010, which was similar in magnitude compared to the preclinical subjects. As the values are low, estimates of V_T corrected using PPB are highly sensitive to errors in any f_P measurements. Therefore, group-level corrections with insufficient number of subjects per group would further increasing variability. Correcting V_T estimates using the group-level mean f_P revealed a potential increase in free parent V_T among MS subjects compared to HCs, though incomplete protein binding data limits definitive conclusions. As the method was still new and in validation phase during this study, not all study days were used to validate this method and collect the PPB data. Future studies with [^{11}C]SMW139 should consider these findings to explore more accurate analysis approaches. In addition, concentration dependency of the PPB should be studied, as those studies has been shown to give unexpected results in some cases as mentioned before (Nation *et al.*, 2018).

6.6.2.3 Effect of PPB

To date, the analysis of f_M has not been performed with [^{11}C]SMW139 or with any other PET tracer. Understanding the f_M properties is highly valuable for evaluating tracer pharmacokinetics, modelling, usability, and safety of any PET tracer.

Previous PPBA methods have primarily used plasma spiked with a much higher amount of radioactivity than what *in vivo* samples would normally contain. While simpler and easier to use, as less sensitive radioactivity detection is required, *in vitro* methods may not fully represent the true dynamic equilibrium present *in vivo* (Gunn *et al.*, 2012), which in reality includes free and protein-bound radiometabolites and parent tracer at only trace levels. Further studies comparing the *in vivo* sample to *in vitro* sample using PPBA methods are needed. With the published method in Study II, it is possible to perform these, and to validate the results of the easier *in vitro* studies. However, comparisons can be performed only for the parent PPBA results, and not for the radiometabolites, unless they would be formed *in vitro* or identified and synthesised separately for such *in vitro* studies.

A protein-bound fraction acts as a reservoir, stabilising and buffering the free tracer concentrations (Roberts *et al.*, 2013; Siddiqui *et al.*, 2021), in addition to partly shielding the parent tracer from being metabolised too rapidly, while circulating and awaiting to be transported or diffused to the intended target (Tesseromatis & Alevizou, 2008). Without the PPB, drug time-concentration graphs and actual availability would look different and might necessitate far more frequent drug administration, or other modes of slow delivery would need to be brought into use.

This would also affect the biological half-life of the drug in plasma. According to the nature of the dynamic equilibrium of the reversible binding to plasma proteins, part of the parent tracer is released from the proteins back to the free form when the free parent diffuses out of the plasma, enabling a steadier drug availability to the target, due to the steadier drug concentration in plasma. However, the clinical importance or the applicability of the PPB results has also been commented on critically (Vuignier *et al.*, 2010). Benet & Hoener (2002) have shown that the pharmacokinetic parameters are not always influenced by changes in the drug-PPB. In the same way, Liu *et al.* (2014) demonstrated that the fraction of unbound drug in plasma is not directly proportional to the PPB degree, but rather to the intrinsic clearance. Likewise, in the brain tissue, the unbound drug concentration mostly depends on the BBB efflux transport activity (Liu *et al.*, 2014). Therefore, drawing direct conclusions from PPB results is not always easy, and the effect should be studied thoroughly.

6.6.3 PPBA method and value reporting considerations

6.6.3.1 Differences in reporting plasma protein binding

As mentioned in the previous section, PPB studies have traditionally been conducted using *in vitro* samples (Moein & Halldin, 2020). In such cases, the definition of f_P remains consistent, whether calculated as the ratio of free parent tracer to total radioactivity or as free parent to total parent radioactivity. This is because radiometabolites are typically absent from the *in vitro* samples. However, when using *in vivo* samples containing radiometabolites, two definitions of f_P can be employed: dividing the protein-free parent radioactivity by only the total parent radioactivity, $f_{P/P}$, which requires analysing the parent fraction in plasma, or dividing the protein-free parent by the total radioactivity, $f_{P/A}$.

The first definition is particularly useful for modelling the radioactivity concentration of the free parent when a radiometabolite-corrected plasma curve is already available. The second is applicable when only the plasma TAC is available. It is now possible to analyse the free fractions in the *in vivo* samples for the radiometabolites too with the methods published in Study II, so the free fraction needs to distinguish between free parent and free radiometabolites separately. With the developed method, both definitions of free fractions in Study II were presented to highlight their differences (Table 5). Studies involving *in vivo* samples and tracers with significant metabolism must explicitly define what is being measured: does f_P include the free parent tracer alone or all free radioactivity, including free radiometabolites, and is it relative to the total sample radioactivity or to the radioactivity of the parent alone. Using *in vivo* samples and employing

chromatographic methods to analyse filtrates and applying appropriate membrane correction factors from the plasma matrix are expected to yield results closer to the true values.

6.6.3.2 PPBA method reporting considerations

When publishing PPBA results, it is essential to report the exact procedures and methods used to calculate the free fractions. Leaving the critical information out makes it impossible to repeat the study or compare the results to other similar studies. Even smallest methodological details, such as whether the membrane correction was assessed and applied in membrane-based methods, or what were the filtration or equilibration times, can significantly impact the results.

Examples of insufficient method reporting are common in the literature, but specific instances will not be cited out of professional courtesy. I acknowledge that my own publications are not perfectly comprehensive in method reporting either. However, word count limitations should not be a concern, as supplementary materials can typically be included without restrictions.

The underreporting of methods may stem from the desire to present results quickly, focusing only on the most essential methodological details. In some cases, the main manuscript authors may not have conducted the experiments themselves and, therefore, may overlook methodological factors, which are in reality crucial, affecting data collection and analysis. Additionally, modern publishing culture often seems to prioritise leaning the content, making articles shorter and easier to read. However, this leaning process may remove essential details, severely limiting the usefulness and value of the published information for other researchers.

6.7 Combining TAC, RMA and PPBA data

Combining the plasma TACs, RMA data, and PPB information can appear complex to those not directly involved in processing such data. In this thesis, Study II presents Figure 15 as a visual example that integrates these three datasets into a single bar chart, illustrating how each component contributes to the accurate quantification of PET tracer kinetics. As only three time points were available, bars were used instead of a curve to represent the y-axis values. Although a line could connect these points to suggest a curve, three data points are insufficient for a reliable interpolation.

The plasma TAC reflects the tracer's temporal concentration in circulation, serving as the input function for kinetic modelling. However, without correction for radioactive metabolites, the measured radioactivity overestimates the parent compound. Multiplying the radioactivity with the parent fraction acquired in the RMA ensures that only the unmetabolised tracer is considered. This chart type

enables dividing the radioactivity-bar (as %IA/g) into separate bars visualizing the amount corresponding to the parent and radiometabolites. Additionally, assessing the plasma parent and radiometabolite free fractions $f_{P/P}$ and $f_{M/M}$ and multiplying the parent and radiometabolite bars separately with them, further enables dividing the separated bars into two parts that separately expresses the amount corresponding to plasma protein-free and bound parent tracer and radiometabolites. The combination of the stacked bars show the total quantity of the parent and radiometabolites separately, while only the height of the lower part of the bars that indicate the protein-free part provides insight into the proportion available for crossing biological barriers and reaching to the target areas. Together, these complementary datasets enhance the interpretation of PET data by accounting for metabolic degradation and bioavailability, enabling more reliable AIF *in vivo*.

In the clinical studies, Studies III and IV, it is further clarified how this data is used. In Study III, by modelling a dual-input function accounting for both the parent tracer and brain-penetrant radiometabolites, these corrections substantially reduced the variability of V_T estimates. In the relevant brain regions for P2X7 receptor binding, the two-tissue compartment model using a single input function produced highly variable V_T estimates, ranging from 0.10 to 10.74, with a large coefficient of variation (159.9%). In contrast, the dual-input model yielded more consistent V_T values, ranging from 0.04 to 0.24, and showed much lower coefficient of variation (33.3%). Similarly, in Study IV, correcting for both radiometabolites and protein binding improved the interpretation of tracer uptake in MS subjects. Parameters such as the parent tracer distribution volume, V_{Tp}, derived from the dual input compartmental models, depend directly on these corrections. Without such data of BBB-penetrant radiometabolites, single-input models can have the wrong fraction for radiometabolite uptake, affecting V_T values and make small group differences impossible to detect. This can be especially critical in diseases like MS, where target expression differences are modest. The integration of carefully analysed radiometabolite and f_P data thus can improve model fits, reducing variability stemming from individual pharmacokinetic differences.

7 Conclusions

The Study I analysed the metabolism of [^{11}C]SMW139 in a mouse model and found rapid formation of radiometabolites. The brain-penetrating radiometabolites influenced the *in vivo* PET imaging, complicating the interpretation of the tracer's binding. The findings shows the necessity of accounting for radiometabolites in PET imaging to ensure accurate data interpretation. A rapid RMA method was developed.

The Study II introduced a novel UF method to analyse PPB of the [^{11}C]SMW139 and its radiometabolites, providing insights into their pharmacokinetics. The approach, which separately examines the f_P and f_M, is valuable for understanding brain uptake and can be applied to other PET tracers. Notably, the radiometabolites have a much higher free fraction than the parent tracer, enabling efficient BBB penetration.

The Study III utilised plasma and brain parent fraction preclinical data to improve modelling and quantification of tracer binding to P2X7 receptors in human subjects. The dual input function model provided robust distribution volume estimates, enhancing the approach to modelling [^{11}C]SMW139 PET data.

In Study IV, while the dual-input model provided expected P2X7 receptor distribution, the study did not conclusively demonstrate the tracer's applicability for detecting MS-related diffuse smouldering inflammation. The radiometabolite BBB penetration and low free fraction of the [^{11}C]SMW139 compromises the ability to detect significant differences between the HC, PMS and RMS.

These conclusions show the necessity of analysing parent fraction and PPBA in new PET tracer projects. If these aspects are not taken into account, the quantification to obtain reliable data on for example, receptor availability is compromised. Future research using PET tracers could benefit from these new methodology approaches.

As a summary, these studies illustrate the translationality from preclinical to clinical applications of [^{11}C]SMW139 PET in imaging P2X7 receptors. The correction for radiometabolites and understanding of PPB enhances the tracer's otherwise challenging diagnostic precision. Preclinical and clinical studies demonstrated the potential of [^{11}C]SMW139 as a biomarker for microglial activation in diseases like MS and Alzheimer's, showing its translational value.

Acknowledgements

There are so many people to whom I am deeply grateful for helping me reach this point in my academic journey. The completion of this thesis would not have been possible without the contributions of numerous dedicated individuals, whose expertise, support, and encouragement have been vital to the success of these projects.

I have had the privilege of working at the Turku PET Centre since June 2018 and have been a part of the Drug Research Doctoral Programme (DRDP) since January 2020. I am truly grateful for the opportunities I have been given to work in the Turku PET Centre and on projects I once thought were beyond my reach. I have been trusted with responsibility, treated as an equal member of the research community, and encouraged to grow as a scientist, an experience for which I am very thankful.

I want to express my sincere gratitude to my supervisors, Adjunct Professors Merja Haaparanta-Solin and Sarita Forsback, for believing in me and for your continuous support and mentorship throughout these years. Despite your busy schedules, you always found time to guide me, and it has been a true pleasure working with you both.

I also wish to extend special thanks to Professor Olof Solin for being a constant source of inspiration through your teaching, Villa Tammekann trips, and seminars, which, together with Merja, you have organised to strengthen our researcher community. Your guidance, wisdom, and generosity in sharing your talents have had a significant influence on me, and I am especially thankful for your availability and openness whenever I had questions, no matter the topic.

I am grateful to all my co-authors for the opportunity to collaborate on publications, especially those included in this thesis. I have learned a great deal from each publication process, starting from the challenges, revisions, and eventual successes. I thank you for sharing your expertise and time.

I would like to express particular thanks to Obada Alzghool, my fellow doctoral researcher at the beginning of the [^{11}C]SMW139 preclinical projects. Thank you for your invaluable support and teamwork. I truly enjoyed our work together, as well as our conversations over lunch and the moments of fun outside the lab.

To the many colleagues in MediCity and the various preclinical PET groups, I want to sincerely thank you all for your collaboration, support, and friendship: Merja Haaparanta-Solin, Tove Grönroos, Jatta Helin, Petra Ketonen, Petra Parviainen, Sanni Tuominen, Aake Honkaniemi, Luciana Kovacs dos Santos, Kirsi Mikkola, Max Miner, Obada Alzghool, Susanne Vainio, Francisco López-Picón, Anniina Snellman, Marko Vehmanen, Päivi Kotitalo, Mira Eisala, Heidi Liljenbäck, Jenni Virta, Xiang-Guo Li, Anne Roivainen, Anu Airaksinen, Tatsiana Auchynnikava, Olli Moisio, Mia Ståhle, Heidi Nykänen, Vilhelmiina Parikka, Francisco Acosta, Anna Jalo, Saeka Shimochi, Emma Saha, Johanna Örling, Aleksanteri Tani, Jiri Funda, Petter Lövdahl, Jonne Kunnas, Xiaoqing Zhuang, and Ángel García de Lucas. I am also thankful to many others at MediCity and the PET Centre whose names may not appear here, but whose contributions are equally appreciated.

A special thank you goes to those with whom I've shared office space over the years. To Francisco López-Picón, with whom I shared an office for over five years – thank you for your patience and for always being willing to explain even the simplest of things when I was starting as a researcher. Also, thank you Obada Alzghool, Kirsi Mikkola, and my current office mate, Max Miner. I have been fortunate to work alongside such knowledgeable colleagues who have supported me, collaborated with me, and made the work environment truly inspiring.

I would also like to thank the many individuals involved in the clinical PET site. My sincere gratitude goes to Professors Juhani Knuuti, Laura Airas, Juha Rinne, Pirjo Nuutila, Hidehiro Iida, Antti Saraste, Olof Solin, Lauri Nummenmaa, and Jukka Kemppainen. Thank you for bringing such impactful projects to the Turku PET Centre and for the valuable opportunities to learn from your work. I am also especially grateful to those who are not (yet) full professors, as well as to the management staff and IT support — your contributions are equally essential to the success of our work. I would like to acknowledge Kirsi Virtanen, Kari Kalliokoski, Riku Klen, Vesa Oikonen, Tuula Tolvanen, Virva Saunavaara, Rami Mikkola, Marko Tättäläinen, Päivi Marjamäki, and many others working in the Turku PET Centre whose daily efforts make a significant difference. In addition, I would like to thank Tuulia Malen and Markus Matilainen for sharing their expertise in statistics.

I am grateful to the Radiopharmaceutical Chemistry Laboratory and the Åbo Akademi Accelerator Laboratory teams. Thank you for your dedication in producing high quality novel radionuclides and PET tracers which are essential for our work. Special thanks to Sarita Forsback, Olof Solin, Anna Kirjavainen, Semi Helin, Noora Rajala, Thomas Keller, Simo Vauhkala, Esa Kokkomäki, Johan Rajander, Mikael Bergelin, and Melina Väkiparta for your hard work and collaboration.

I am also very thankful to all the medical laboratory technicians, radiographers and other study nurse and research staff who have supported the clinical studies. I especially wish to thank Eija Salo, Hanna Liukko-Sipi, Leena Tokoi-Eklund, Sanna

Suominen, Heidi Partanen, Emilia Puhakka, Tiina Tuominen, Kia Lehtimäki, and Johanna Kulmala, who worked with me in the Clinical Chemistry laboratory during my time as a laboratory manager. Thank you for your patience when I have been busy with other research commitments, such as writing articles and my thesis, and for your consistent dedication to data quality, troubleshooting, and maintaining the lab's daily operations. My thanks also go to Minna Aatsinki and Anne Helminen for their roles in staff management.

I would like to acknowledge the Scientific Project Group at the Turku PET Centre for allowing me to be part of this group. It is an honour to contribute to our PET Centre to enable high quality research, and I hope to continue doing so after graduation. I am also grateful to the Turku University Foundation for providing a writing residency at Villa Tammekann in Tartu, Estonia. The peaceful environment and support of fellow researchers there greatly enhanced my productivity and focus.

Thank you to Katri Kulmala (MediCity), Tarja Marttila, Minna Kangasperko, and Lenita Saloranta (Turku PET Centre) for your excellent administrative support. I also wish to thank my fellow doctoral researchers, coordinators, and supervisors in the DRDP for their friendship and support, as well as for the valuable networking and training opportunities. My sincere thanks to my follow-up committee members, Johanna Rokka and Tove Grönroos, for your guidance and encouragement throughout this project.

I am very thankful to Associate Professor Cécile Philippe and Assistant Professor Pedro Brugarolas for your detailed and constructive comments during the preliminary examination process. Your insights have been highly valuable. I would also like to express my appreciation in advance to Professor Olof Eriksson for accepting the role of the opponent in the public defence. I have heard people speak highly about you as a person and a researcher, and I look forward to meeting you and our discussion on the defence day.

Finally, I wish to thank a few more individuals who have played a key role earlier in my journey. Helmi Neuvonen, Satu Mikkola and other staff from the Department of Chemistry in the University of Turku, thank you for your encouragement during my Bachelor's and Master's studies, and for inspiring me to believe in myself that I could pursue even a career as a researcher.

To my family, friends, and others not yet mentioned—including the climbing community, my floorball team, the choir I get to sing with, and my local church, thank you for your companionship. You have all contributed in meaningful ways to my personal growth and given me the strength and motivation to complete this doctoral journey.

Turku, 28.2.2025
Richard Aarnio

References

Aarnio, R., Kirjavainen, A., Rajander, J., Forsback, S., Kalliokoski, K., Nuutila, P., Milicevic, Z., Coskun, T., Haupt, A., Laitinen, I., & Haaparanta-Solin, M. (2024). New improved radiometabolite analysis method for [^{18}F]FTHA from human plasma: a test-retest study with postprandial and fasting state. EJNMMI research, 14(1), 53. https://doi.org/10.1186/s13550-024-01114-5

Abdel-Rehim, A., & Abdel-Rehim, M. (2013). Evaluation of microextraction by packed sorbent and micro-liquid chromatography-tandem mass spectrometry as a green approach in bioanalysis. Biomedical chromatography : BMC, 27(10), 1225–1233. https://doi.org/10.1002/bmc.2839

Acuña-Castillo, C., Escobar, A., García-Gómez, M., Bachelet, V. C., Huidobro-Toro, J. P., Sauma, D., & Barrera-Avalos, C. (2024). P2X7 Receptor in Dendritic Cells and Macrophages: Implications in Antigen Presentation and T Lymphocyte Activation. International journal of molecular sciences, 25(5), 2495. https://doi.org/10.3390/ijms25052495

Akaike, H. (1974). A new look at the statistical model identification. IEEE Transactions on Automatic Control, 19(6), 716–723. https://doi.org/10.1109/TAC.1974.1100705

Alberts, I., Sari, H., Mingels, C., Afshar-Oromieh, A., Pyka, T., Shi, K., & Rominger, A. (2023). Long-axial field-of-view PET/CT: perspectives and review of a revolutionary development in nuclear medicine based on clinical experience in over 7000 patients. Cancer imaging : the official publication of the International Cancer Imaging Society, 23(1), 28. https://doi.org/10.1186/s40644-023-00540-3

Amini, N., Nakao, R., Schou, M., & Halldin, C. (2013). Identification of PET radiometabolites by cytochrome P450, UHPLC/Q-ToF-MS and fast radio-LC: applied to the PET radioligands [11C]flumazenil, [18F]FE-PE2I, and [11C]PBR28. Analytical and bioanalytical chemistry, 405(4), 1303–1310. https://doi.org/10.1007/s00216-012-6541-2

Amini, N., Nakao, R., Schou, M., & Halldin, C. (2014). Determination of plasma protein binding of positron emission tomography radioligands by high-performance frontal analysis. Journal of pharmaceutical and biomedical analysis, 98, 140–143. https://doi.org/10.1016/j.jpba.2014.05.024

Anguizola, J., Joseph, K. S., Barnaby, O. S., Matsuda, R., Alvarado, G., Clarke, W., Cerny, R. L., & Hage, D. S. (2013). Development of affinity microcolumns for drug-protein binding studies in personalized medicine: interactions of sulfonylurea drugs with *in vivo* glycated human serum albumin. Analytical chemistry, 85(9), 4453–4460. https://doi.org/10.1021/ac303734c

Atcheson, B., Taylor, P. J., Pillans, P. I., & Tett, S. E. (2003). Measurement of free drug and clinical end-point by high-performance liquid chromatography–mass spectrometry. Analytica Chimica Acta, 492(1–2), 157–169. https://doi.org/10.1016/S0003-2670(03)00359-3

Auchynnikava, T., Äärelä, A., Moisio, O., Liljenbäck, H., Andriana, P., Iqbal, I., Laine, T., Palani, S., Lehtimäki, J., Rajander, J., Salo, H., Airaksinen, A. J., Virta, P., & Roivainen, A. (2025). Biological evaluation of molecular spherical nucleic acids: Targeting tumors via a hybridization-based folate decoration. ACS Omega, 10(6), 6003-6014. https://doi.org/10.1021/acsomega.4c10047

Badawi, R. D., Shi, H., Hu, P., Chen, S., Xu, T., Price, P. M., Ding, Y., Spencer, B. A., Nardo, L., Liu, W., Bao, J., Jones, T., Li, H., & Cherry, S. R. (2019). First Human Imaging Studies with the EXPLORER Total-Body PET Scanner. Journal of nuclear medicine : official publication, Society of Nuclear Medicine, 60(3), 299–303. https://doi.org/10.2967/jnumed.119.226498

Bartlett R., Stokes L., Sluyter R. The p2x7 receptor channel: Recent developments and the use of p2x7 antagonists in models of disease. Pharmacol Rev. 2014. 66(3):638–75

Barton P., Austin R.P., Fessey R.E. (2007), Comprehensive Medicinal Chemistry II, 5.14 - *In vitro* Models for Plasma Binding and Tissue Storage , Volume 5, 2007, 321-340. https://www.sciencedirect.com/science/article/pii/B008045044X001292

Baxter, A., Bent, J., Bowers, K., Braddock, M., Brough, S., Fagura, M., Lawson, M., McInally, T., Mortimore, M., Robertson, M., Weaver, R., & Webborn, P. (2003). Hit-to-Lead studies: the discovery of potent adamantane amide P2X7 receptor antagonists. Bioorganic & medicinal chemistry letters, 13(22), 4047–4050. https://doi.org/10.1016/j.bmcl.2003.08.034

Beaino, W., Jm Kooijman, E., Werry, E. L., Vellinga, R. J., Van den Hoek, J., Sohler, G., Cumbers, G. A., Genetzakis, E., Harvey-Latham, E. D., Schuit, R. C., Kassiou, M., Windhorst, A. D., & Danon, J. J. (2025). Development and evaluation of [11C]DPA-813 and [18F]DPA-814: novel TSPO PET tracers insensitive to human single nucleotide polymorphism rs6971. European journal of nuclear medicine and molecular imaging, 10.1007/s00259-025-07109-1. Advance online publication. https://doi.org/10.1007/s00259-025-07109-1

Beaino, W., Janssen, B., Kooijman, E., Vos, R., Schuit, R. C., O'Brien-Brown, J., Kassiou, M., van Het Hof, B., Vugts, D. J., de Vries, H. E., & Windhorst, A. D. (2020). PET imaging of P2X7R in the experimental autoimmune encephalomyelitis model of multiple sclerosis using [^{11}C]SMW139. Journal of neuroinflammation, 17(1), 300. https://doi.org/10.1186/s12974-020-01962-7

Belardi, R. P., & Pawliszyn, J. B. (1989). Application of chemically modified fused silica fibers in the extraction of organics from water matrix samples and their rapid transfer to capillary columns. Water Pollution Research Journal of Canada, 24, 179–191.

Belcari, N., Bisogni, M. G., & Del Guerra, A. (2023). Positron emission tomography: Its 65 years and beyond. Rivista del Nuovo Cimento, 46, 693–785. https://doi.org/10.1007/s40766-024-00050-3

Benet, L. Z., & Hoener, B. A. (2002). Changes in plasma protein binding have little clinical relevance. Clinical pharmacology and therapeutics, 71(3), 115–121. https://doi.org/10.1067/mcp.2002.121829

Berdyyeva, T., Xia, C., Taylor, N., He, Y., Chen, G., Huang, C., Zhang, W., Kolb, H., Letavic, M., Bhattacharya, A., & Szardenings, A. K. (2019). PET Imaging of the P2X7 Ion Channel with a Novel Tracer [18F]JNJ-64413739 in a Rat Model of Neuroinflammation. Molecular imaging and biology, 21(5), 871–878. https://doi.org/10.1007/s11307-018-01313-2

Besson, F. L., Nocturne, G., Noël, N., Gheysens, O., Slart, R. H. J. A., & Glaudemans, A. W. J. M. (2024). PET/CT in Inflammatory and Auto-immune Disorders: Focus on Several Key Molecular Concepts, FDG, and Radiolabeled Probe Perspectives. Seminars in nuclear medicine, 54(3), 379–393. https://doi.org/10.1053/j.semnuclmed.2023.10.005

Bogdanovic, B., Solari, E. L., Villagran Asiares, A., McIntosh, L., van Marwick, S., Schachoff, S., & Nekolla, S. G. (2022). PET/MR Technology: Advancement and Challenges. Seminars in nuclear medicine, 52(3), 340–355. https://doi.org/10.1053/j.semnuclmed.2021.11.014

Boulant, N., Mauconduit, F., Gras, V., Amadon, A., Le Ster, C., Luong, M., Massire, A., Pallier, C., Sabatier, L., Bottlaender, M., Vignaud, A., & Le Bihan, D. (2024). *In vivo* imaging of the human brain with the Iseult 11.7-T MRI scanner. Nature methods, 21(11), 2013–2016. https://doi.org/10.1038/s41592-024-02472-7

Brugarolas, P., Wilks, M. Q., Noel, J., Kaiser, J. A., Vesper, D. R., Ramos-Torres, K. M., Guehl, N. J., Macdonald-Soccorso, M. T., Sun, Y., Rice, P. A., Yokell, D. L., Lim, R., Normandin, M. D., & El Fakhri, G. (2023). Human biodistribution and radiation dosimetry of the demyelination tracer [18F]3F4AP. European journal of nuclear medicine and molecular imaging, 50(2), 344–351. https://doi.org/10.1007/s00259-022-05980-w

Burnstock G. (1972). Purinergic nerves. Pharmacological reviews, 24(3), 509–581.

Burnstock G. (2014). Purinergic signalling: from discovery to current developments. Experimental physiology, 99(1), 16–34. https://doi.org/10.1113/expphysiol.2013.071951Cai, X., Yao, Y., Teng, F., Li, Y., Wu, L., Yan, W., & Lin, N. (2021). The role of P2X7 receptor in infection and

metabolism: Based on inflammation and immunity. International immunopharmacology, 101(Pt A), 108297. https://doi.org/10.1016/j.intimp.2021.108297

Cargnin, S., Serafini, M., & Pirali, T. (2019). A primer of deuterium in drug design. Future medicinal chemistry, 11(16), 2039–2042. https://doi.org/10.4155/fmc-2019-0183

Castiaux, A. D., Pinger, C. W., & Spence, D. M. (2018). Ultrafiltration binding analyses of glycated albumin with a 3D-printed syringe attachment. Analytical and bioanalytical chemistry, 410(29), 7565–7573. https://doi.org/10.1007/s00216-018-1373-3

Chen, R., Sun, T., Huang, G., Zhou, Y., Liu, J. (2024). Current progress and future perspectives in total-body positron emission tomography/computed tomography. Part II: clinical applications. iRADIOLOGY. 2(3): 328–38. https://doi.org/10.1002/ird3.64

Cherry, S. R., Sorenson, J. A., & Phelps, M. E. (2012). Physics in nuclear medicine (4th ed.). Elsevier

Cherry, S. R., Jones, T., Karp, J. S., Qi, J., Moses, W. W., & Badawi, R. D. (2018). Total-Body PET: Maximizing Sensitivity to Create New Opportunities for Clinical Research and Patient Care. Journal of nuclear medicine: official publication, Society of Nuclear Medicine, 59(1), 3–12. https://doi.org/10.2967/jnumed.116.184028

Chitneni, S. K., Serdons, K., Evens, N., Fonge, H., Celen, S., Deroose, C. M., Debyser, Z., Mortelmans, L., Verbruggen, A. M., & Bormans, G. M. (2008). Efficient purification and metabolite analysis of radiotracers using high-performance liquid chromatography and on-line solid-phase extraction. Journal of chromatography. A, 1189(1-2), 323–331. https://doi.org/10.1016/j.chroma.2007.10.084

Dash, A., & Chakravarty, R. (2019). Radionuclide generators: the prospect of availing PET radiotracers to meet current clinical needs and future research demands. American journal of nuclear medicine and molecular imaging, 9(1), 30–66.

Daube-Witherspoon, M. E., Pantel, A. R., Pryma, D. A., & Karp, J. S. (2022). Total-body PET: a new paradigm for molecular imaging. The British journal of radiology, 95(1140), 20220357. https://doi.org/10.1259/bjr.20220357

Declercq, L., Rombouts, F., Koole, M., Fierens, K., Mariën, J., Langlois, X., Andrés, J. I., Schmidt, M., Macdonald, G., Moechars, D., Vanduffel, W., Tousseyn, T., Vandenberghe, R., Van Laere, K., Verbruggen, A., & Bormans, G. (2017). Preclinical Evaluation of 18F-JNJ64349311, a Novel PET Tracer for Tau Imaging. Journal of nuclear medicine : official publication, Society of Nuclear Medicine, 58(6), 975–981. https://doi.org/10.2967/jnumed.116.185199

Di, L., Breen, C., Chambers, R., Eckley, S. T., Fricke, R., Ghosh, A., Harradine, P., Kalvass, J. C., Ho, S., Lee, C. A., Marathe, P., Perkins, E. J., Qian, M., Tse, S., Yan, Z., & Zamek-Gliszczynski, M. J. (2017). Industry Perspective on Contemporary Protein-Binding Methodologies: Considerations for Regulatory Drug-Drug Interaction and Related Guidelines on Highly Bound Drugs. Journal of pharmaceutical sciences, 106(12), 3442–3452. https://doi.org/10.1016/j.xphs.2017.09.005

Dimitrijevic, D., Fabian, E., Funk-Weyer, D., & Landsiedel, R. (2023). Rapid equilibrium dialysis, ultrafiltration or ultracentrifugation? Evaluation of methods to quantify the unbound fraction of substances in plasma. Biochemical and biophysical research communications, 651, 114–120. https://doi.org/10.1016/j.bbrc.2023.02.021

Dreisbach, A. W., & Lertora, J. J. (2008). The effect of chronic renal failure on drug metabolism and transport. Expert opinion on drug metabolism & toxicology, 4(8), 1065–1074. https://doi.org/10.1517/17425255.4.8.1065

Ehman, E. C., Johnson, G. B., Villanueva-Meyer, J. E., Cha, S., Leynes, A. P., Larson, P. E. Z., & Hope, T. A. (2017). PET/MRI: Where might it replace PET/CT?. Journal of magnetic resonance imaging, 46(5), 1247–1262. https://doi.org/10.1002/jmri.25711

Finnema, S. J., Nabulsi, N. B., Mercier, J., Lin, S. F., Chen, M. K., Matuskey, D., Gallezot, J. D., Henry, S., Hannestad, J., Huang, Y., & Carson, R. E. (2018). Kinetic evaluation and test-retest reproducibility of [11C]UCB-J, a novel radioligand for positron emission tomography imaging of synaptic vesicle glycoprotein 2A in humans. Journal of cerebral blood flow and metabolism : official journal of the International Society of Cerebral Blood Flow and Metabolism, 38(11), 2041–2052. https://doi.org/10.1177/0271678X17724947

Fontanals, N., Marcé, R. M., & Borrull, F. (2019). Materials for Solid-Phase Extraction of Organic Compounds. Separations, 6(4), 56. https://doi.org/10.3390/separations6040056

Fu, Z., Lin, Q., Hu, B., Zhang, Y., Chen, W., Zhu, J., Zhao, Y., Choi, H. S., Shi, H., & Cheng, D. (2019). P2X7 PET Radioligand 18F-PTTP for Differentiation of Lung Tumor from Inflammation. Journal of nuclear medicine : official publication, Society of Nuclear Medicine, 60(7), 930–936. https://doi.org/10.2967/jnumed.118.222547

Gant, T. G. (2014). Using deuterium in drug discovery: leaving the label in the drug. Journal of medicinal chemistry, 57(9), 3595–3611. https://doi.org/10.1021/jm4007998

Ghosh, K. K., Padmanabhan, P., Yang, C. T., Mishra, S., Halldin, C., & Gulyás, B. (2020). Dealing with PET radiometabolites. *EJNMMI research*, *10*(1), 109. https://doi.org/10.1186/s13550-020-00692-4

Ghuman, J., Zunszain, P. A., Petitpas, I., Bhattacharya, A. A., Otagiri, M., & Curry, S. (2005). Structural basis of the drug-binding specificity of human serum albumin. Journal of molecular biology, 353(1), 38–52. https://doi.org/10.1016/j.jmb.2005.07.075

Godinez, F., Mingels, C., Bayerlein, R., Mehadji, B., & Nardo, L. (2025). Total Body PET/CT: Future Aspects. Seminars in nuclear medicine, 55(1), 107–115. https://doi.org/10.1053/j.semnuclmed.2024.10.011

Golla, S. S., Boellaard, R., Oikonen, V., Hoffmann, A., van Berckel, B. N., Windhorst, A. D., Virta, J., Haaparanta-Solin, M., Luoto, P., Savisto, N., Solin, O., Valencia, R., Thiele, A., Eriksson, J., Schuit, R. C., Lammertsma, A. A., & Rinne, J. O. (2015). Quantification of [18F]DPA-714 binding in the human brain: initial studies in healthy controls and Alzheimer's disease patients. Journal of cerebral blood flow and metabolism : official journal of the International Society of Cerebral Blood Flow and Metabolism, 35(5), 766–772. https://doi.org/10.1038/jcbfm.2014.261

Gopaul, V. S., Vildhede, A., Andersson, T. B., Erlandsson, F., Lee, C. A., Johansson, S., & Hilgendorf, C. (2021). *In vitro* Assessment of the Drug-Drug Interaction Potential of Verinurad and Its Metabolites as Substrates and Inhibitors of Metabolizing Enzymes and Drug Transporters. The Journal of pharmacology and experimental therapeutics, 378(2), 108–123. https://doi.org/10.1124/jpet.121.000549

Gu, F., & Wu, Q. (2023). Quantitation of dynamic total-body PET imaging: recent developments and future perspectives. European journal of nuclear medicine and molecular imaging, 50(12), 3538–3557. https://doi.org/10.1007/s00259-023-06299-w

Guerra, F., Leone, M. & Robotti, N. (2012). The Discovery of Artificial Radioactivity. Physics in Perspective, 14(1), 33–58. https://doi.org/10.1007/s00016-011-0064-7

Gunn, R. N., Summerfield, S. G., Salinas, C. A., Read, K. D., Guo, Q., Searle, G. E., Parker, C. A., Jeffrey, P., & Laruelle, M. (2012). Combining PET biodistribution and equilibrium dialysis assays to assess the free brain concentration and BBB transport of CNS drugs. Journal of cerebral blood flow and metabolism : official journal of the International Society of Cerebral Blood Flow and Metabolism, 32(5), 874–883. https://doi.org/10.1038/jcbfm.2012.1

Haaparanta, M., Grönroos, T., Eskola, O., Bergman, J., & Solin, O. (2006). Planar chromatographic analysis and quantification of short-lived radioactive metabolites from microdialysis fractions. Journal of chromatography. A, 1108(1), 136–139. https://doi.org/10.1016/j.chroma.2005.12.107

Hagens, M. H. J., Golla, S. S. V., Janssen, B., Vugts, D. J., Beaino, W., Windhorst, A. D., O'Brien-Brown, J., Kassiou, M., Schuit, R. C., Schwarte, L. A., de Vries, H. E., Killestein, J., Barkhof, F., van Berckel, B. N. M., & Lammertsma, A. A. (2020). The P2X7 receptor tracer [^{11}C]SMW139 as an *in vivo* marker of neuroinflammation in multiple sclerosis: a first-in man study. European journal of nuclear medicine and molecular imaging, 47(2), 379–389. https://doi.org/10.1007/s00259-019-04550-x

Hashimoto, H., Kawamura, K., Takei, M., Igarashi, N., Fujishiro, T., Shiomi, S., Watanabe, R., Muto, M., Furutsuka, K., Ito, T., Yamasaki, T., Yui, J., Nemoto, K., Kimura, Y., Higuchi, M., & Zhang, M. R. (2015). Identification of a major radiometabolite of [11C]PBB3. Nuclear medicine and biology, 42(12), 905–910. https://doi.org/10.1016/j.nucmedbio.2015.08.006

Hibell, A. D., Kidd, E. J., Chessell, I. P., Humphrey, P. P., & Michel, A. D. (2000). Apparent species differences in the kinetic properties of P2X(7) receptors. British journal of pharmacology, 130(1), 167–173. https://doi.org/10.1038/sj.bjp.0703302

Hilton, J., Yokoi, F., Dannals, R. F., Ravert, H. T., Szabo, Z., & Wong, D. F. (2000). Column-switching HPLC for the analysis of plasma in PET imaging studies. Nuclear medicine and biology, 27(6), 627–630. https://doi.org/10.1016/s0969-8051(00)00125-6

Ingelman-Sundberg M. (2005). Genetic polymorphisms of cytochrome P450 2D6 (CYP2D6): clinical consequences, evolutionary aspects and functional diversity. The pharmacogenomics journal, 5(1), 6–13. https://doi.org/10.1038/sj.tpj.6500285

International Atomic Energy Agency. (2009). Strategies for clinical implementation and quality management of pet tracers (IAEA Publication No. 1344). Retrieved from https://www-pub.iaea.org/MTCD/Publications/PDF/Pub1344_web.pdf

Isbell, J., Yuan, D., Torrao, L., Gatlik, E., Hoffmann, L., & Wipfli, P. (2019). Plasma Protein Binding of Highly Bound Drugs Determined With Equilibrium Gel Filtration of Nonradiolabelled Compounds and LC-MS/MS Detection. Journal of pharmaceutical sciences, 108(2), 1053–1060. https://doi.org/10.1016/j.xphs.2018.10.004

Janssen, B., Vugts, D. J., Wilkinson, S. M., Ory, D., Chalon, S., Hoozemans, J. J. M., Schuit, R. C., Beaino, W., Kooijman, E. J. M., van den Hoek, J., Chishty, M., Doméné, A., Van der Perren, A., Villa, A., Maggi, A., Molenaar, G. T., Funke, U., Shevchenko, R. V., Baekelandt, V., Bormans, G., … Windhorst, A. D. (2018). Identification of the allosteric P2X7 receptor antagonist [^{11}C]SMW139 as a PET tracer of microglial activation. Scientific reports, 8(1), 6580. https://doi.org/10.1038/s41598-018-24814-0

Jiao, Q., Wang, R., Jiang, Y., & Liu, B. (2018). Study on the interaction between active components from traditional Chinese medicine and plasma proteins. Chemistry Central journal, 12(1), 48. https://doi.org/10.1186/s13065-018-0417-2

Joliot, F., & Curie, I. (1934). Artificial production of a new kind of radio-element. Nature, 133, 201–202. https://doi.org/10.1038/133201a0

Jones, T., & Townsend, D. (2017). History and future technical innovation in positron emission tomography. Journal of medical imaging (Bellingham, Wash.), 4(1), 011013. https://doi.org/10.1117/1.JMI.4.1.011013

Kalliokoski, T., Tuomela, J., Haavisto, L., Forsback, S., Snellman, A., Helin, S., Grönroos, T. J., Solin, O., & Haaparanta-Solin, M. (2014). 6-[18F]fluoro-L-DOPA uptake in the rat pancreas is dependent on the tracer metabolism. Molecular imaging and biology, 16(3), 403–411. https://doi.org/10.1007/s11307-013-0701-4

Kapoor, M., & Kasi, A. (2022). PET Scanning. In StatPearls. StatPearls Publishing. https://www.ncbi.nlm.nih.gov/books/NBK559089/

Kataoka, H., Ishizaki, A., Saito, K., & Ehara, K. (2024). Developments and Applications of Molecularly Imprinted Polymer-Based In-Tube Solid Phase Microextraction Technique for Efficient Sample Preparation. Molecules (Basel, Switzerland), 29(18), 4472. https://doi.org/10.3390/molecules29184472

Keller, T., López-Picón, F. R., Krzyczmonik, A., Forsback, S., Kirjavainen, A. K., Takkinen, J. S., Alzghool, O., Rajander, J., Teperi, S., Cacheux, F., Damont, A., Dollé, F., Rinne, J. O., Solin, O., & Haaparanta-Solin, M. (2018). [18F]F-DPA for the detection of activated microglia in a mouse model of Alzheimer's disease. Nuclear medicine and biology, 67, 1–9. https://doi.org/10.1016/j.nucmedbio.2018.09.001

Kilkenny, C., Browne, W. J., Cuthill, I. C., Emerson, M., & Altman, D. G. (2010). Improving bioscience research reporting: the ARRIVE guidelines for reporting animal research. PLoS biology, 8(6), e1000412. https://doi.org/10.1371/journal.pbio.1000412

Knuuti, J., Tuisku, J., Kärpijoki, H., Iida, H., Maaniitty, T., Latva-Rasku, A., Oikonen, V., Nesterov, S. V., Teuho, J., Jaakkola, M. K., Klén, R., Louhi, H., Saunavaara, V., Nuutila, P., Saraste, A., Rinne, J., & Nummenmaa, L. (2023). Quantitative Perfusion Imaging with Total-Body PET.

Journal of nuclear medicine : official publication, Society of Nuclear Medicine, 64(Suppl 2), 11S–19S. https://doi.org/10.2967/jnumed.122.264870

Korfmacher W. A. (2005). Principles and applications of LC-MS in new drug discovery. Drug discovery today, 10(20), 1357–1367. https://doi.org/10.1016/S1359-6446(05)03620-2

Kratzer, A., Kees, F., & Dorn, C. (2016). Unbound fraction of fluconazole and linezolid in human plasma as determined by ultrafiltration: Impact of membrane type. Journal of chromatography. B, Analytical technologies in the biomedical and life sciences, 1039, 74–78. https://doi.org/10.1016/j.jchromb.2016.10.040

Kreisl, W. C., Kim, M. J., Coughlin, J. M., Henter, I. D., Owen, D. R., & Innis, R. B. (2020). PET imaging of neuroinflammation in neurological disorders. The Lancet. Neurology, 19(11), 940–950. https://doi.org/10.1016/S1474-4422(20)30346-X

Kuchar, M., & Mamat, C. (2015). Methods to Increase the Metabolic Stability of (18)F-Radiotracers. Molecules (Basel, Switzerland), 20(9), 16186–16220. https://doi.org/10.3390/molecules200916186

Laferriere-Holloway, T. S., Rios, A., Lu, Y., Okoro, C. C., & van Dam, R. M. (2023). A rapid and systematic approach for the optimization of radio thin-layer chromatography resolution. Journal of chromatography. A, 1687, 463656. https://doi.org/10.1016/j.chroma.2022.463656

Lee, J. H., Liow, J. S., Paul, S., Morse, C. L., Haskali, M. B., Manly, L., Shcherbinin, S., Ruble, J. C., Kant, N., Collins, E. C., Nuthall, H. N., Zanotti-Fregonara, P., Zoghbi, S. S., Pike, V. W., & Innis, R. B. (2020). PET quantification of brain O-GlcNAcase with [18F]LSN3316612 in healthy human volunteers. EJNMMI research, 10(1), 20. https://doi.org/10.1186/s13550-020-0616-4

Li, F., Hicks, J. W., Yu, L., Desjardin, L., Morrison, L., Hadway, J., & Lee, T. Y. (2020). Plasma radio-metabolite analysis of PET tracers for dynamic PET imaging: TLC and autoradiography. EJNMMI research, 10(1), 141. https://doi.org/10.1186/s13550-020-00705-2

Liao, K., Chen, J. H., Ma, J., Dong, C. C., Bi, C. Y., Gao, Y. B., Jiang, Y. F., Wang, T., Wei, H. Y., Hou, L., Hu, J. Q., Wei, J. J., Zeng, C. Y., Li, Y. L., Yan, S., Xu, H., Liang, S. H., & Wang, L. (2025). Preclinical characterization of [18F]D2-LW223: an improved metabolically stable PET tracer for imaging the translocator protein 18 kDa (TSPO) in neuroinflammatory rodent models and non-human primates. Acta pharmacologica Sinica, 46(2), 393–403. https://doi.org/10.1038/s41401-024-01375-9

Lindberg, A., Chassé, M., Varlow, C., Pees, A., & Vasdev, N. (2023). Strategies for designing novel positron emission tomography (PET) radiotracers to cross the blood-brain barrier. Journal of labelled compounds & radiopharmaceuticals, 66(9), 205–221. https://doi.org/10.1002/jlcr.4019

Liu, X., Wright, M., & Hop, C. E. (2014). Rational use of plasma protein and tissue binding data in drug design. Journal of medicinal chemistry, 57(20), 8238–8248. https://doi.org/10.1021/jm5007935

Ludwig, F.-A., Fischer, S., Smits, R., Deuther-Conrad, W., Hoepping, A., Tiepolt, S., Patt, M., Sabri, O., & Brust, P. (2018). Exploring the Metabolism of (+)-[18F]Flubatine *In vitro* and *In vivo*: LC-MS/MS Aided Identification of Radiometabolites in a Clinical PET Study †. Molecules, 23(2), 464. https://doi.org/10.3390/molecules23020464

Luoto, P., Laitinen, I., Suilamo, S., Någren, K., & Roivainen, A. (2010). Human dosimetry of carbon-11 labeled N-butan-2-yl-1-(2-chlorophenyl)-N-methylisoquinoline-3-carboxamide extrapolated from whole-body distribution kinetics and radiometabolism in rats. Molecular imaging and biology, 12(4), 435–442. https://doi.org/10.1007/s11307-009-0293-1

Ma, Y., Kiesewetter, D. O., Lang, L., Gu, D., & Chen, X. (2010). Applications of LC-MS in PET radioligand development and metabolic elucidation. Current drug metabolism, 11(6), 483–493. https://doi.org/10.2174/138920010791636167

Maaniitty, T., Knuuti, J., & Saraste, A. (2020). 15O-Water PET MPI: Current Status and Future Perspectives. Seminars in nuclear medicine, 50(3), 238–247. https://doi.org/10.1053/j.semnuclmed.2020.02.011

Malherbe, C., Bidault, R., Netter, C., Guilloteau, D., Vercouillie, J. and Arlicot, N. (2019). Development of a Fast and Facile Analytical Approach to Quantify Radiometabolites in Human Plasma Samples Using Ultra High Performance Liquid Chromatography. American Journal of Analytical Chemistry, 10, 185-201. https://doi.org/10.4236/ajac.2019.105016

Mansoor, A., & Mahabadi, N. (2023). Volume of distribution. In StatPearls. StatPearls Publishing. Retrieved [19.2.2025], from https://www.ncbi.nlm.nih.gov/books/NBK545280/

Matsuda, R., Li, Z., Zheng, X., & Hage, D. S. (2015). Analysis of glipizide binding to normal and glycated human serum albumin by high-performance affinity chromatography. Analytical and bioanalytical chemistry, 407(18), 5309–5321. https://doi.org/10.1007/s00216-015-8688-0

Melega, W. P., Hoffman, J. M., Luxen, A., Nissenson, C. H., Phelps, M. E., & Barrio, J. R. (1990). The effects of carbidopa on the metabolism of 6-[18F]fluoro-L-dopa in rats, monkeys and humans. Life sciences, 47(2), 149–157. https://doi.org/10.1016/0024-3205(90)90228-j

Melega, W. P., Grafton, S. T., Huang, S. C., Satyamurthy, N., Phelps, M. E., & Barrio, J. R. (1991). L-6-[18F]fluoro-dopa metabolism in monkeys and humans: biochemical parameters for the formulation of tracer kinetic models with positron emission tomography. Journal of cerebral blood flow and metabolism : official journal of the International Society of Cerebral Blood Flow and Metabolism, 11(6), 890–897. https://doi.org/10.1038/jcbfm.1991.154

Merck KGaA. (15.1.2025a). High-performance thin-layer chromatography (HPTLC). Merck Millipore. https://www.merckmillipore.com/FI/en/analytics-sample-preparation/learning-center-thin-layer-chromatography/hptlc/NGub.qB.fCoAAAFVPmJDx07N,nav

Merck KGaA. (15.1.2025b). TLC Silica gel 60 RP-18 F254s. Merck Millipore. https://www.merckmillipore.com/FI/en/product/TLC-Silica-gel-60-RP-18-F254s,MDA_CHEM-105559

Merck KGaA. (21.1.2025). Microcon® Centrifugal Filters Applications Guidelines & Specifications. Merck. Sigma Aldrich. https://www.sigmaaldrich.com/FI/en/technical-documents/technical-article/cell-culture-and-cell-culture-analysis/mammalian-cell-culture/microcon-centrifugal-filters

Merck KGaA. (22.1.2025). Pore size or NMWL (Membrane Learning Center). Merck Millipore. https://www.merckmillipore.com/FI/en/life-science-research/chromatography-sample-preparation/membrane-learning-center/Pore-Size-or-NMWL/uyKb.qB.ejgAAAFMYT188eJu,nav

Mingels, C., Chung, K. J., Pantel, A. R., Rominger, A., Alberts, I., Spencer, B. A., Nardo, L., & Pyka, T. (2025). Total-Body PET/CT: Challenges and Opportunities. Seminars in nuclear medicine, 55(1), 21–30. https://doi.org/10.1053/j.semnuclmed.2024.08.003

Mishra, V., & Heath, R. J. (2021). Structural and Biochemical Features of Human Serum Albumin Essential for Eukaryotic Cell Culture. International journal of molecular sciences, 22(16), 8411. https://doi.org/10.3390/ijms22168411

Moehrs, S., Del Guerra, A., Herbert, D. J., & Mandelkern, M. A. (2006). A detector head design for small-animal PET with silicon photomultipliers (SiPM). Physics in medicine and biology, 51(5), 1113–1127. https://doi.org/10.1088/0031-9155/51/5/004

Moein, M. M., & Halldin, C. (2020). Sample preparation techniques for protein binding measurement in radiopharmaceutical approaches: A short review. Talanta, 219, 121220. https://doi.org/10.1016/j.talanta.2020.121220

Moein, M. M., Nakao, R., Amini, N., Abdel-Rehim, M., Schou, M., & Halldin, C. (2019). Sample preparation techniques for radiometabolite analysis of positron emission tomography radioligands; trends, progress, limitations and future prospects. TrAC Trends in Analytical Chemistry, 110, 1–7. https://doi.org/10.1016/j.trac.2018.10.019

Moein, M. M., Tóth, M., Tari, L., Varrone, A., Abdel-Rehim, M., & Halldin, C. (2020). New approach in radiometabolite analysis of positron emission tomography (PET) radioligands; lead-shielded microextraction by packed sorbent as a tool for *in vivo* radiometabolite analysis of [11C]SMW139 in rat plasma. Talanta, 208, 120449. https://doi.org/10.1016/j.talanta.2019.120449

Muranova, A., & Shanina, E. (2023). Levodopa/Carbidopa/Entacapone Combination Therapy. In StatPearls. StatPearls Publishing. Retrieved from https://www.ncbi.nlm.nih.gov/books/NBK599508/

Nakamoto, Y., Inui, Y., Hotta, M., Wakabayashi, H., & Hanaoka, H. (2024). Recent advancements in new tracers from first-in-human studies. Annals of nuclear medicine, 38(11), 877–883. https://doi.org/10.1007/s12149-024-01979-5

Nakao, R., & Halldin, C. (2013). A simplified radiometabolite analysis procedure for PET radioligands using a solid phase extraction with micellar medium. Nuclear medicine and biology, 40(5), 658–663. https://doi.org/10.1016/j.nucmedbio.2013.02.007

Nakao, R., Amini, N., & Halldin, C. (2013). Simultaneous determination of protein-free and total positron emission tomography radioligand concentrations in plasma using high-performance frontal analysis followed by mixed micellar liquid chromatography: application to [^{11}C]PBR28 in human plasma. Analytical chemistry, 85(18), 8728–8734. https://doi.org/10.1021/ac401742v

Nation, R. L., Theuretzbacher, U., Tsuji, B. T., & International Society of Anti-Infective Pharmacology (ISAP) (2018). Concentration-dependent plasma protein binding: Expect the unexpected. European journal of pharmaceutical sciences : official journal of the European Federation for Pharmaceutical Sciences, 122, 341–346. https://doi.org/10.1016/j.ejps.2018.07.004

Nesterov, S. V., Han, C., Mäki, M., Kajander, S., Naum, A. G., Helenius, H., Lisinen, I., Ukkonen, H., Pietilä, M., Joutsiniemi, E., & Knuuti, J. (2009). Myocardial perfusion quantitation with ^{15}O-labelled water PET: high reproducibility of the new cardiac analysis software (Carimas). European journal of nuclear medicine and molecular imaging, 36(10), 1594–1602. https://doi.org/10.1007/s00259-009-1143-8

Nilsson L. B. (2013). The bioanalytical challenge of determining unbound concentration and protein binding for drugs. Bioanalysis, 5(24), 3033–3050. https://doi.org/10.4155/bio.13.274

Nutma, E., Fancy, N., Weinert, M., Tsartsalis, S., Marzin, M. C., Muirhead, R. C. J., Falk, I., Breur, M., de Bruin, J., Hollaus, D., Pieterman, R., Anink, J., Story, D., Chandran, S., Tang, J., Trolese, M. C., Saito, T., Saido, T. C., Wiltshire, K. H., Beltran-Lobo, P., … Owen, D. R. (2023). Translocator protein is a marker of activated microglia in rodent models but not human neurodegenerative diseases. Nature communications, 14(1), 5247. https://doi.org/10.1038/s41467-023-40937-z

Ory, D., Van den Brande, J., de Groot, T., Serdons, K., Bex, M., Declercq, L., Cleeren, F., Ooms, M., Van Laere, K., Verbruggen, A., & Bormans, G. (2015). Retention of [^{18}F]fluoride on reversed phase HPLC columns. Journal of pharmaceutical and biomedical analysis, 111, 209–214. https://doi.org/10.1016/j.jpba.2015.04.009

Otagiri M. (2005). A molecular functional study on the interactions of drugs with plasma proteins. Drug metabolism and pharmacokinetics, 20(5), 309–323. https://doi.org/10.2133/dmpk.20.309

Otagiri M. (2009). Yakugaku zasshi : Journal of the Pharmaceutical Society of Japan, 129(4), 413–425. https://doi.org/10.1248/yakushi.129.413

Paolillo, V., Yeh, H. H., Mukhopadhyay, U., Gelovani, J. G., & Alauddin, M. M. (2011). Improved detection and measurement of low levels of [^{18}F]fluoride metabolized from [18F]-labeled pyrimidine nucleoside analogues in biological samples. Nuclear medicine and biology, 38(8), 1129–1134. https://doi.org/10.1016/j.nucmedbio.2011.05.008

Patt, M., Becker, G. A., Grossmann, U., Habermann, B., Schildan, A., Wilke, S., Deuther-Conrad, W., Graef, S., Fischer, S., Smits, R., Hoepping, A., Wagenknecht, G., Steinbach, J., Gertz, H. J., Hesse, S., Schönknecht, P., Brust, P., & Sabri, O. (2014). Evaluation of metabolism, plasma protein binding and other biological parameters after administration of (-)-[(18)F]Flubatine in humans. Nuclear medicine and biology, 41(6), 489–494. https://doi.org/10.1016/j.nucmedbio.2014.03.018

Pauwels, E. K., Ribeiro, M. J., Stoot, J. H., McCready, V. R., Bourguignon, M., & Mazière, B. (1998). FDG accumulation and tumor biology. Nuclear medicine and biology, 25(4), 317–322. https://doi.org/10.1016/s0969-8051(97)00226-6

Pawelke B. (2005). Metabolite analysis in positron emission tomography studies: examples from food sciences. Amino acids, 29(4), 377–388. https://doi.org/10.1007/s00726-005-0202-0

Percie du Sert, N., Hurst, V., Ahluwalia, A., Alam, S., Avey, M. T., Baker, M., Browne, W. J., Clark, A., Cuthill, I. C., Dirnagl, U., Emerson, M., Garner, P., Holgate, S. T., Howells, D. W., Karp, N. A., Lazic, S. E., Lidster, K., MacCallum, C. J., Macleod, M., Pearl, E. J., … Würbel, H. (2020). The ARRIVE guidelines 2.0: Updated guidelines for reporting animal research. PLoS biology, 18(7), e3000410. https://doi.org/10.1371/journal.pbio.3000410

Pereira de Sousa, I., & Bernkop-Schnürch, A. (2014). Pre-systemic metabolism of orally administered drugs and strategies to overcome it. Journal of controlled release : official journal of the Controlled Release Society, 192, 301–309. https://doi.org/10.1016/j.jconrel.2014.08.004

Perera Molligoda Arachchige, A. S. (2023). Neuroimaging with PET/MR: Moving beyond 3 T in preclinical systems, when for clinical practice? Clinical and Translational Imaging, 11(2), 315–319. https://doi.org/10.1007/s40336-023-00572-6

Pike V. W. (1995). Radioligands for PET studies of central 5-HT receptors and re-uptake sites--current status. Nuclear medicine and biology, 22(8), 1011–1018. https://doi.org/10.1016/0969-8051(95)02024-1

Pike V. W. (2009). PET radiotracers: crossing the blood-brain barrier and surviving metabolism. Trends in pharmacological sciences, 30(8), 431–440. https://doi.org/10.1016/j.tips.2009.05.005

Pike V. W. (2016). Considerations in the Development of Reversibly Binding PET Radioligands for Brain Imaging. Current medicinal chemistry, 23(18), 1818–1869. https://doi.org/10.2174/0929867323666160418114826

Polson, C., Sarkar, P., Incledon, B., Raguvaran, V., & Grant, R. (2003). Optimization of protein precipitation based upon effectiveness of protein removal and ionization effect in liquid chromatography-tandem mass spectrometry. Journal of chromatography. B, Analytical technologies in the biomedical and life sciences, 785(2), 263–275. https://doi.org/10.1016/s1570-0232(02)00914-5

Pretze, M., Wängler, C., & Wängler, B. (2014). 6-[18F]fluoro-L-DOPA: a well-established neurotracer with expanding application spectrum and strongly improved radiosyntheses. BioMed research international, 2014, 674063. https://doi.org/10.1155/2014/674063

Price, J. C., Lopresti, B. J., Meltzer, C. C., Smith, G. S., Mason, N. S., Huang, Y., Holt, D. P., Gunn, R. N., & Mathis, C. A. (2001). Analyses of [(18)F]altanserin bolus injection PET data. II: consideration of radiolabeled metabolites in humans. Synapse (New York, N.Y.), 41(1), 11–21. https://doi.org/10.1002/syn.1055

Qiu, L., Jiang, H., Cho, K., Yu, Y., Jones, L. A., Huang, T., Perlmutter, J. S., Gropler, R. J., Brier, M. R., Patti, G. J., Benzinger, T. L. S., & Tu, Z. (2024). Metabolite Study and Structural Authentication for the First-in-Human Use Sphingosine-1-phosphate Receptor 1 Radiotracer. ACS chemical neuroscience, 15(9), 1882–1892. https://doi.org/10.1021/acschemneuro.4c00077

Ramos-Torres, K., Sun, Y., Takahashi, K., Zhou, Y.-P., & Brugarolas, P. (2024). Common anesthetic used in preclinical PET imaging inhibits metabolism of the PET tracer [^{18}F]3F4AP. Journal of Neurochemistry, 168, 2577–2586. https://doi.org/10.1111/jnc.16118

Raval, K., & Patel, H. (2020). Review on common observed HPLC troubleshooting problems. International Journal of Pharma Research and Health Sciences, 8(4), 3195–3202. https://doi.org/10.21276/ijprhs.2020.04.02

Ren, W., Rubini, P., Tang, Y., Engel, T., & Illes, P. (2021). Inherent P2X7 Receptors Regulate Macrophage Functions during Inflammatory Diseases. International journal of molecular sciences, 23(1), 232. https://doi.org/10.3390/ijms23010232

Reyes-Garcés, N., Gionfriddo, E., Gómez-Ríos, G. A., Alam, M. N., Boyacı, E., Bojko, B., Singh, V., Grandy, J., & Pawliszyn, J. (2018). Advances in Solid Phase Microextraction and Perspective on Future Directions. Analytical chemistry, 90(1), 302–360. https://doi.org/10.1021/acs.analchem.7b04502

Riccardi, K., Cawley, S., Yates, P. D., Chang, C., Funk, C., Niosi, M., Lin, J., & Di, L. (2015). Plasma Protein Binding of Challenging Compounds. Journal of pharmaceutical sciences, 104(8), 2627–2636. https://doi.org/10.1002/jps.24506

Roberts, J. A., Pea, F., & Lipman, J. (2013). The clinical relevance of plasma protein binding changes. Clinical pharmacokinetics, 52(1), 1–8. https://doi.org/10.1007/s40262-012-0018-5

Roivainen, A., Rinne, J., Virta, J., Järvenpää, T., Salomäki, S., Yu, M., & Någren, K. (2004). Biodistribution and blood metabolism of 1-11C-methyl-4-piperidinyl n-butyrate in humans: an

imaging agent for *in vivo* assessment of butyrylcholinesterase activity with PET. Journal of nuclear medicine : official publication, Society of Nuclear Medicine, 45(12), 2032–2039.

Sabri, O., Becker, G. A., Meyer, P. M., Hesse, S., Wilke, S., Graef, S., Patt, M., Luthardt, J., Wagenknecht, G., Hoepping, A., Smits, R., Franke, A., Sattler, B., Habermann, B., Neuhaus, P., Fischer, S., Tiepolt, S., Deuther-Conrad, W., Barthel, H., Schönknecht, P., … Brust, P. (2015). First-in-human PET quantification study of cerebral α4β2* nicotinic acetylcholine receptors using the novel specific radioligand (-)-[(18)F]Flubatine. NeuroImage, 118, 199–208. https://doi.org/10.1016/j.neuroimage.2015.05.065

Saha, E., Shimochi, S., Keller, T., Eskola, O., López-Picón, F., Rajander, J., Löyttyniemi, E., Forsback, S., Solin, O., Grönroos, T. J., & Parikka, V. (2024). Evaluation of PET imaging as a tool for detecting neonatal hypoxic-ischemic encephalopathy in a preclinical animal model. Experimental neurology, 373, 114673. https://doi.org/10.1016/j.expneurol.2023.114673

Salerno, S., Viviano, M., Baglini, E., Poggetti, V., Giorgini, D., Castagnoli, J., Barresi, E., Castellano, S., Da Settimo, F., & Taliani, S. (2024). TSPO Radioligands for Neuroinflammation: An Overview. Molecules, 29(17), 4212. https://doi.org/10.3390/molecules29174212

Salinas, C. A., Searle, G. E., & Gunn, R. N. (2015). The simplified reference tissue model: model assumption violations and their impact on binding potential. Journal of cerebral blood flow and metabolism : official journal of the International Society of Cerebral Blood Flow and Metabolism, 35(2), 304–311. https://doi.org/10.1038/jcbfm.2014.202

Schou, M., Amini, N., Takano, A., Arakawa, R., Dahl, K., Toth, M., Svedberg, M., Varrone, A., & Halldin, C. (2023). Microsome Mediated in Vitro Metabolism: A Convenient Method for the Preparation of the PET Radioligand Metabolite [18F]FE-PE2I-OH for Translational Dopamine Transporter Imaging. ACS chemical neuroscience, 14(20), 3732–3736. https://doi.org/10.1021/acschemneuro.3c00458

Schmidt, S., Isaak, A., & Junker, A. (2023). Spotlight on P2X7 Receptor PET Imaging: A Bright Target or a Failing Star?. International journal of molecular sciences, 24(2), 1374. https://doi.org/10.3390/ijms24021374

Schröder, S., Wenzel, B., Deuther-Conrad, W., Teodoro, R., Egerland, U., Kranz, M., Scheunemann, M., Höfgen, N., Steinbach, J., & Brust, P. (2015). Synthesis, 18F-Radiolabelling and Biological Characterization of Novel Fluoroalkylated Triazine Derivatives for *in vivo* Imaging of Phosphodiesterase 2A in Brain via Positron Emission Tomography. Molecules (Basel, Switzerland), 20(6), 9591–9615. https://doi.org/10.3390/molecules20069591

Shave, S., Pham, N. T., Śmieja, C. B., & Auer, M. (2020). Quantitative Microdialysis: Experimental Protocol and Software for Small Molecule Protein Affinity Determination and for Exclusion of Compounds with Poor Physicochemical Properties. Methods and protocols, 3(3), 55. https://doi.org/10.3390/mps3030055

Shetty, H. U., Morse, C. L., Zhang, Y., & Pike, V. W. (2013). Characterization of fast-decaying PET radiotracers solely through LC-MS/MS of constituent radioactive and carrier isotopologues. EJNMMI research, 3(1), 3. https://doi.org/10.1186/2191-219X-3-3

Shields, A. F., Graham, M. M., Kozawa, S. M., Kozell, L. B., Link, J. M., Swenson, E. R., Spence, A. M., Bassingthwaighte, J. B., & Krohn, K. A. (1992). Contribution of labeled carbon dioxide to PET imaging of carbon-11-labeled compounds. Journal of nuclear medicine : official publication, Society of Nuclear Medicine, 33(4), 581–584.

Shields, A. F., Briston, D. A., Chandupatla, S., Douglas, K. A., Lawhorn-Crews, J., Collins, J. M., Mangner, T. J., Heilbrun, L. K., & Muzik, O. (2005). A simplified analysis of [18F]3'-deoxy-3'-fluorothymidine metabolism and retention. European journal of nuclear medicine and molecular imaging, 32(11), 1269–1275. https://doi.org/10.1007/s00259-005-1813-0

Shimochi, S., Ihalainen, J., Parikka, V., Kudomi, N., Tolvanen, T., Hietanen, A., Kokkomäki, E., Johansson, S., Tsuji, M., Kanaya, S., Yatkin, E., Grönroos, T. J., & Iida, H. (2024). Small animal PET with spontaneous inhalation of 15O-labelled oxygen gases: Longitudinal assessment of cerebral oxygen metabolism in a rat model of neonatal hypoxic-ischaemic encephalopathy. Journal

of cerebral blood flow and metabolism : official journal of the International Society of Cerebral Blood Flow and Metabolism, 44(6), 1024–1038. https://doi.org/10.1177/0271678X231220691

Siddiqui, S., Ameen, F., Rehman, S. U., Sarwar, T., & Tabish, M. (2021). Studying the interaction of drug/ligand with serum albumin. Journal of Molecular Liquids, 336, 116200. https://doi.org/10.1016/j.molliq.2021.116200

Sigma-Aldrich. (22.1.2025). P9275: Mouse plasma, citrated, pooled (Product page). Merck KGaA. https://www.sigmaaldrich.com/FI/en/product/sigma/p9275?context=product

Silva, C., Cavaco, C., Perestrelo, R., Pereira, J., & Câmara, J. S. (2014). Microextraction by Packed Sorbent (MEPS) and Solid-Phase Microextraction (SPME) as Sample Preparation Procedures for the Metabolomic Profiling of Urine. Metabolites, 4(1), 71–97. https://doi.org/10.3390/metabo4010071

Singnurkar, A., Poon, R., & Metser, U. (2024). Head-to-Head Comparison of the Diagnostic Performance of FDG PET/CT and FDG PET/MRI in Patients With Cancer: A Systematic Review and Meta-Analysis. AJR. American journal of roentgenology, 223(3), e2431519. https://doi.org/10.2214/AJR.24.31519

Sluyter R. (2017). The P2X7 Receptor. Advances in experimental medicine and biology, 1051, 17–53. https://doi.org/10.1007/5584_2017_59

Sokias, R., Zhao, A., Werry, E., Montgomery, A., Hibbs, D., Sullivan, M., McKenzie, A. D. J., Cumbers, G. A., Allen, B. M., Danon, J. J., & Kassiou, M. (2025). PK 11195 derivatives: Exploring the influence of amide and heterocyclic substitution on A147T TSPO discrimination. RSC Medicinal Chemistry. https://doi.org/10.1039/D4MD00798K

Sorger, D., Becker, G. A., Hauber, K., Schildan, A., Patt, M., Birkenmeier, G., Otto, A., Meyer, P., Kluge, M., Schliebs, R., & Sabri, O. (2006). Binding properties of the cerebral alpha4beta2 nicotinic acetylcholine receptor ligand 2-[18F]fluoro-A-85380 to plasma proteins. Nuclear medicine and biology, 33(7), 899–906. https://doi.org/10.1016/j.nucmedbio.2006.07.012

Šrámková, I. H., Horstkotte, B., Carbonell-Rozas, L., Erben, J., Chvojka, J., Lara, F. J., García-Campaña, A. M., & Šatínský, D. (2022). Nanofibrous Online Solid-Phase Extraction Coupled with Liquid Chromatography for the Determination of Neonicotinoid Pesticides in River Waters. Membranes, 12(7), 648. https://doi.org/10.3390/membranes12070648

Srivastava, A., Pike, A., Williamson, B., & Fenner, K. (2021). A Novel Method for Preventing Non-specific Binding in Equilibrium Dialysis Assays Using Solutol® as an Additive. Journal of pharmaceutical sciences, 110(3), 1412–1417. https://doi.org/10.1016/j.xphs.2020.11.018

Steiner, D., Krska, R., Malachová, A., Taschl, I., & Sulyok, M. (2020). Evaluation of Matrix Effects and Extraction Efficiencies of LC-MS/MS Methods as the Essential Part for Proper Validation of Multiclass Contaminants in Complex Feed. Journal of agricultural and food chemistry, 68(12), 3868–3880. https://doi.org/10.1021/acs.jafc.9b07706

Sun, S., Long, C., Tao, C., Meng, S., & Deng, B. (2014). Ultrasonic microdialysis coupled with capillary electrophoresis electrochemiluminescence study the interaction between trimetazidine dihydrochloride and human serum albumin. Analytica chimica acta, 851, 37–42. https://doi.org/10.1016/j.aca.2014.08.012

Sun, Y., Ramos-Torres, K. M., & Brugarolas, P. (2023). Metabolic Stability of the Demyelination Positron Emission Tomography Tracer [18F]3-Fluoro-4-Aminopyridine and Identification of Its Metabolites. The Journal of pharmacology and experimental therapeutics, 386(1), 93–101. https://doi.org/10.1124/jpet.122.001462

Surti S. (2015). Update on time-of-flight PET imaging. Journal of nuclear medicine : official publication, Society of Nuclear Medicine, 56(1), 98–105. https://doi.org/10.2967/jnumed.114.145029

Takkinen, J. S., López-Picón, F. R., Kirjavainen, A. K., Pihlaja, R., Snellman, A., Ishizu, T., Löyttyniemi, E., Solin, O., Rinne, J. O., & Haaparanta-Solin, M. (2018). [^{18}F]FMPEP-d2 PET imaging shows age- and genotype-dependent impairments in the availability of cannabinoid receptor 1 in a mouse model of Alzheimer's disease. Neurobiology of aging, 69, 199–208. https://doi.org/10.1016/j.neurobiolaging.2018.05.013

Territo, P. R., Meyer, J. A., Peters, J. S., Riley, A. A., McCarthy, B. P., Gao, M., Wang, M., Green, M. A., Zheng, Q. H., & Hutchins, G. D. (2017). Characterization of 11C-GSK1482160 for Targeting the P2X7 Receptor as a Biomarker for Neuroinflammation. Journal of nuclear medicine : official publication, Society of Nuclear Medicine, 58(3), 458–465. https://doi.org/10.2967/jnumed.116.181354

Tesseromatis, C., & Alevizou, A. (2008). The role of the protein-binding on the mode of drug action as well the interactions with other drugs. European journal of drug metabolism and pharmacokinetics, 33(4), 225–230. https://doi.org/10.1007/BF03190876

Theodoridis G. (2006). Application of solid-phase microextraction in the investigation of protein binding of pharmaceuticals. Journal of chromatography. B, Analytical technologies in the biomedical and life sciences, 830(2), 238–244. https://doi.org/10.1016/j.jchromb.2005.10.050

Thermo Fisher Scientific. (21.1.2025). Plasma protein binding equilibrium dialysis. Retrieved January 13, 2025, from https://www.thermofisher.com/fi/en/home/life-science/protein-biology/protein-purification-isolation/protein-dialysis-desalting-concentration/dialysis-products/plasma-protein-binding-equilibrium-dialysis.html

Tonietto, M., Rizzo, G., Veronese, M., Fujita, M., Zoghbi, S. S., Zanotti-Fregonara, P., & Bertoldo, A. (2016). Plasma radiometabolite correction in dynamic PET studies: Insights on the available modeling approaches. Journal of cerebral blood flow and metabolism : official journal of the International Society of Cerebral Blood Flow and Metabolism, 36(2), 326–339. https://doi.org/10.1177/0271678X15610585

Trotter, J., Pantel, A. R., Teo, B. K., Escorcia, F. E., Li, T., Pryma, D. A., & Taunk, N. K. (2023). Positron Emission Tomography (PET)/Computed Tomography (CT) Imaging in Radiation Therapy Treatment Planning: A Review of PET Imaging Tracers and Methods to Incorporate PET/CT. Advances in radiation oncology, 8(5), 101212. https://doi.org/10.1016/j.adro.2023.101212

Tuomela, J., Forsback, S., Haavisto, L., Vahlberg, T., Grönroos, T. J., Solin, O., & Haaparanta-Solin, M. (2013). Enzyme inhibition of dopamine metabolism alters 6-[18F]FDOPA uptake in orthotopic pancreatic adenocarcinoma. EJNMMI research, 3(1), 18. https://doi.org/10.1186/2191-219X-3-18

Ustsinau, U., Ehret, V., Fürnsinn, C., Scherer, T., Helbich, T. H., Hacker, M., Krššák, M., & Philippe, C. (2023). Novel approach using [^{18}F]FTHA-PET and de novo synthesized VLDL for assessment of FFA metabolism in a rat model of diet induced NAFLD. Clinical nutrition (Edinburgh, Scotland), 42(10), 1839–1848. https://doi.org/10.1016/j.clnu.2023.08.001

van der Weijden, C. W. J., Mossel, P., Bartels, A. L., Dierckx, R. A. J. O., Luurtsema, G., Lammertsma, A. A., Willemsen, A. T. M., & de Vries, E. F. J. (2023). Non-invasive kinetic modelling approaches for quantitative analysis of brain PET studies. European journal of nuclear medicine and molecular imaging, 50(6), 1636–1650. https://doi.org/10.1007/s00259-022-06057-4

van Grieken, R. & de Bruin, M. (1994). Nomenclature for radioanalytical chemistry (IUPAC Recommendations 1994). Pure and Applied Chemistry, 66(12), 2513-2526. https://doi.org/10.1351/pac199466122513

Varrone, A., Bundgaard, C., & Bang-Andersen, B. (2022). PET as a Translational Tool in Drug Development for Neuroscience Compounds. Clinical pharmacology and therapeutics, 111(4), 774–785. https://doi.org/10.1002/cpt.2548

Vasdev, N., & Collier, T. L. (2016). Design and Prototype of an Automated Column-Switching HPLC System for Radiometabolite Analysis. Pharmaceuticals (Basel, Switzerland), 9(3), 51. https://doi.org/10.3390/ph9030051

Velikyan I. (2015). 68Ga-Based radiopharmaceuticals: production and application relationship. Molecules (Basel, Switzerland), 20(7), 12913–12943. https://doi.org/10.3390/molecules200712913

Vuignier, K., Schappler, J., Veuthey, J. L., Carrupt, P. A., & Martel, S. (2010). Drug-protein binding: a critical review of analytical tools. Analytical and bioanalytical chemistry, 398(1), 53–66. https://doi.org/10.1007/s00216-010-3737-1

Wagner H. N., Jr (1998). A brief history of positron emission tomography (PET). Seminars in nuclear medicine, 28(3), 213–220. https://doi.org/10.1016/s0001-2998(98)80027-5

Walker, M. D., Dinelle, K., Kornelsen, R., McCormick, S., Mah, C., Holden, J. E., Farrer, M. J., Stoessl, A. J., & Sossi, V. (2013). In-vivo measurement of LDOPA uptake, dopamine reserve and turnover in the rat brain using [^{18}F]FDOPA PET. Journal of cerebral blood flow and metabolism : official journal of the International Society of Cerebral Blood Flow and Metabolism, 33(1), 59–66. https://doi.org/10.1038/jcbfm.2012.120

Waller, D. G., & Sampson, A. P. (2018). Pharmacokinetics. In D. G. Waller & A. P. Sampson (Eds.), Medical pharmacology and therapeutics (5th ed., pp. 33–62). Elsevier. https://doi.org/10.1016/B978-0-7020-7167-6.00002-6

Wang, R. F., Loc'h, C., & Mazière, B. (1997). Determination of unchanged [^{18}F]dopamine in human and non-human primate plasma during positron emission tomography studies: a new solid-phase extraction method comparable to radio-thin-layer chromatography analysis. Journal of chromatography. B, Biomedical sciences and applications, 693(2), 265–270. https://doi.org/10.1016/s0378-4347(97)00086-8

Wang, H., Seidel, J., Bartos, C., Byrum, R., Sayre, P. J., Cooper, K., Cong, Y., Kim, D.-Y., Calcagno, C., Kuhn, J. H., Crane, A., Wada, J., Johnson, R. F., Hammoud, D. A., & Lee, J. H. (2022). Intramuscular [^{18}F]F-FDG Administration for Successful PET Imaging of Golden Hamsters in a Maximum Containment Laboratory Setting. Viruses, 14(11), 2492. https://doi.org/10.3390/v14112492

Wang, J., Rios, A., Lisova, K., Slavik, R., Chatziioannou, A. F., & van Dam, R. M. (2020). High-throughput radio-TLC analysis. Nuclear medicine and biology, 82-83, 41–48. https://doi.org/10.1016/j.nucmedbio.2019.12.003

Warren K. E. (2018). Beyond the Blood:Brain Barrier: The Importance of Central Nervous System (CNS) Pharmacokinetics for the Treatment of CNS Tumors, Including Diffuse Intrinsic Pontine Glioma. Frontiers in oncology, 8, 239. https://doi.org/10.3389/fonc.2018.00239

Waterhouse R. N. (2003). Determination of lipophilicity and its use as a predictor of blood-brain barrier penetration of molecular imaging agents. Molecular imaging and biology, 5(6), 376–389. https://doi.org/10.1016/j.mibio.2003.09.014

Waters, N. J., Jones, R., Williams, G., & Sohal, B. (2008). Validation of a rapid equilibrium dialysis approach for the measurement of plasma protein binding. Journal of pharmaceutical sciences, 97(10), 4586–4595. https://doi.org/10.1002/jps.21317

Werkhoven-Goewie, C. E., de Ruiter, C., Brinkman, U. A., Frei, R. W., de Jong, G. J., Little, C. J., & Stahel, O. (1983). Automated determination of drugs in blood samples after enzymatic hydrolysis using precolumn switching and post-column reaction detection. Journal of chromatography, 255, 79–90. https://doi.org/10.1016/s0021-9673(01)88275-3

Wilkinson, S. M., Barron, M. L., O'Brien-Brown, J., Janssen, B., Stokes, L., Werry, E. L., Chishty, M., Skarratt, K. K., Ong, J. A., Hibbs, D. E., Vugts, D. J., Fuller, S., Windhorst, A. D., & Kassiou, M. (2017). Pharmacological Evaluation of Novel Bioisosteres of an Adamantanyl Benzamide P2X7 Receptor Antagonist. ACS chemical neuroscience, 8(11), 2374–2380. https://doi.org/10.1021/acschemneuro.7b00272

Wiltschko, L., Roblegg, E., Raml, R., & Birngruber, T. (2023). Small volume rapid equilibrium dialysis (RED) measures effects of interstitial parameters on the protein-bound fraction of topical drugs. Journal of pharmaceutical and biomedical analysis, 234, 115571. https://doi.org/10.1016/j.jpba.2023.115571

Yang, G., Ge, S., Singh, R., Basu, S., Shatzer, K., Zen, M., Liu, J., Tu, Y., Zhang, C., Wei, J., Shi, J., Zhu, L., Liu, Z., Wang, Y., Gao, S., & Hu, M. (2017). Glucuronidation: driving factors and their impact on glucuronide disposition. Drug metabolism reviews, 49(2), 105–138. https://doi.org/10.1080/03602532.2017.1293682

Yang, L., Said, R., & Abdel-Rehim, M. (2017). Sorbent, device, matrix and application in microextraction by packed sorbent (MEPS): A review. Journal of chromatography. B, Analytical technologies in the biomedical and life sciences, 1043, 33–43. https://doi.org/10.1016/j.jchromb.2016.10.044

Yang, N. J., & Hinner, M. J. (2015). Getting across the cell membrane: an overview for small molecules, peptides, and proteins. Methods in molecular biology (Clifton, N.J.), 1266, 29–53. https://doi.org/10.1007/978-1-4939-2272-7_3

Yang, N., Poh, A. W. J., Giltrap, A. M., Isenegger, P. G., Sap, J. B. I., Ford, J., Auchynnikava, T., Tan, K. V., Able, S., Levin, N., Davy, M., Josephson, B., Yu, Y., Miner, M. W. G., Helin, J. S., Kovacs, L., Aarnio, R., Rajala, N. A., Tredwell, M., ... Davis, B. G. (2025). Isostere ^{18}F-protein post-translational editing enables dynamic tracking of neurodegeneration biomarkers. bioRxiv. https://doi.org/10.1101/2025.01.26.634877

Ye, Z., Zetterberg, C., & Gao, H. (2017). Automation of plasma protein binding assay using rapid equilibrium dialysis device and Tecan workstation. Journal of pharmaceutical and biomedical analysis, 140, 210–214. https://doi.org/10.1016/j.jpba.2017.03.019

Yu, Z., Westerlund, D., & Boos, K. S. (1997). Evaluation of liquid chromatographic behavior of restricted-access media precolumns in the course of direct injection of large volumes of plasma samples in column-switching systems. Journal of chromatography. B, Biomedical sciences and applications, 704(1-2), 53–62. https://doi.org/10.1016/s0378-4347(97)00471-4

Zanger, U. M., & Schwab, M. (2013). Cytochrome P450 enzymes in drug metabolism: regulation of gene expression, enzyme activities, and impact of genetic variation. Pharmacology & therapeutics, 138(1), 103–141. https://doi.org/10.1016/j.pharmthera.2012.12.007

Zanotti-Fregonara, P., Chen, K., Liow, J. S., Fujita, M., & Innis, R. B. (2011). Image-derived input function for brain PET studies: many challenges and few opportunities. Journal of cerebral blood flow and metabolism : official journal of the International Society of Cerebral Blood Flow and Metabolism, 31(10), 1986–1998. https://doi.org/10.1038/jcbfm.2011.107

Zatcepin, A., & Ziegler, S. I. (2023). Detectors in positron emission tomography. Zeitschrift fur medizinische Physik, 33(1), 4–12. https://doi.org/10.1016/j.zemedi.2022.08.004

Zhang, C., Liang, Z., Liu, W., Zeng, X., & Mo, Y. (2023). Comparison of whole-body ^{18}F-FDG PET/CT and PET/MRI for distant metastases in patients with malignant tumors: a meta-analysis. BMC cancer, 23(1), 37. https://doi.org/10.1186/s12885-022-10493-8

Zhao, M., Ma, J., Li, M., Zhang, Y., Jiang, B., Zhao, X., Huai, C., Shen, L., Zhang, N., He, L., & Qin, S. (2021a). Cytochrome P450 Enzymes and Drug Metabolism in Humans. International journal of molecular sciences, 22(23), 12808. https://doi.org/10.3390/ijms222312808

Zhao, Y. F., Tang, Y., & Illes, P. (2021b). Astrocytic and Oligodendrocytic P2X7 Receptors Determine Neuronal Functions in the CNS. Frontiers in molecular neuroscience, 14, 641570. https://doi.org/10.3389/fnmol.2021.641570

Zhou, S. N., Oakes, K. D., Servos, M. R., & Pawliszyn, J. (2008). Application of solid-phase microextraction for *in vivo* laboratory and field sampling of pharmaceuticals in fish. Environmental science & technology, 42(16), 6073–6079. https://doi.org/10.1021/es8001162

Zhou, Y., Ye, W., Brasić, J. R., & Wong, D. F. (2010). Multi-graphical analysis of dynamic PET. NeuroImage, 49(4), 2947–2957. https://doi.org/10.1016/j.neuroimage.2009.11.028

Zoghbi, S. S., Shetty, H. U., Ichise, M., Fujita, M., Imaizumi, M., Liow, J. S., Shah, J., Musachio, J. L., Pike, V. W., & Innis, R. B. (2006). PET imaging of the dopamine transporter with 18F-FECNT: a polar radiometabolite confounds brain radioligand measurements. Journal of nuclear medicine: official publication, Society of Nuclear Medicine, 47(3), 520–527

Original Publications

Alzghool, OM., Aarnio, R., Helin, JS., Wahlroos, S., Keller, T., Matilainen, M., Solis, J., Danon, JJ., Kassiou, M., Snellman, A., Solin, O., Rinne, JO. & Haaparanta-Solin, M. (2024)
Glial reactivity in a mouse model of beta-amyloid deposition assessed by PET imaging of P2X7 receptor and TSPO using [^{11}C]SMW139 and [^{18}F]F-DPA.
European Journal of Nuclear Medicine and Molecular Imaging – Research

I

Alzghool *et al. EJNMMI Research (2024) 14:25*
https://doi.org/10.1186/s13550-024-01085-7

EJNMMI RESEARCH

ORIGINAL RESEARCH

Open Access

Glial reactivity in a mouse model of beta-amyloid deposition assessed by PET imaging of P2X7 receptor and TSPO using [^{11}C]SMW139 and [^{18}F]F-DPA

Obada M. Alzghool[1,2,3,4*], Richard Aarnio[1,2,3], Jatta S. Helin[1,2], Saara Wahlroos[5], Thomas Keller[5], Markus Matilainen[4], Junel Solis[6], Jonathan J. Danon[7], Michael Kassiou[7], Anniina Snellman[1], Olof Solin[5,8,9], Juha O. Rinne[4,10] and Merja Haaparanta-Solin[1,2]

Abstract

Background P2X7 receptor has emerged as a potentially superior PET imaging marker to TSPO, the gold standard for imaging glial reactivity. [^{11}C]SMW139 is the most recently developed radiotracer to image P2X7 receptor. The aim of this study was to image reactive glia in the APP/PS1-21 transgenic (TG) mouse model of Aβ deposition longitudinally using [^{11}C]SMW139 targeting P2X7 receptor and to compare tracer uptake to that of [^{18}F]F-DPA targeting TSPO at the final imaging time point. TG and wild type (WT) mice underwent longitudinal in vivo PET imaging using [^{11}C]SMW139 at 5, 8, 11, and 14 months, followed by [^{18}F]F-DPA PET scan only at 14 months. In vivo imaging results were verified by ex vivo brain autoradiography, immunohistochemical staining, and analysis of [^{11}C]SMW139 unmetabolized fraction in TG and WT mice.

Results Longitudinal change in [^{11}C]SMW139 standardized uptake values (SUVs) showed no statistically significant increase in the neocortex and hippocampus of TG or WT mice, which was consistent with findings from ex vivo brain autoradiography. Significantly higher [^{18}F]F-DPA SUVs were observed in brain regions of TG compared to WT mice. Quantified P2X7-positive staining in the cortex and thalamus of TG mice showed a minor increase in receptor expression with ageing, while TSPO-positive staining in the same regions showed a more robust increase in expression in TG mice as they aged. [^{11}C]SMW139 was rapidly metabolized in mice, with 33% of unmetabolized fraction in plasma and 29% in brain homogenates 30 min after injection.

Conclusions [^{11}C]SMW139, which has a lower affinity for the rodent P2X7 receptor than the human version of the receptor, was unable to image the low expression of P2X7 receptor in the APP/PS1-21 mouse model. Additionally, the rapid metabolism of [^{11}C]SMW139 in mice and the presence of several brain-penetrating radiometabolites significantly impacted the analysis of in vivo PET signal of the tracer. Finally, [^{18}F]F-DPA targeting TSPO was more suitable for imaging reactive glia and neuroinflammatory processes in the APP/PS1-21 mouse model, based on the findings presented in this study and previous studies with this mouse model.

Keywords Positron emission tomography, [^{11}C]SMW139, [^{18}F]F-DPA, Alzheimer's disease, APP/PS1-21, Microglia, P2X7, TSPO, P2Y12

*Correspondence:
Obada M. Alzghool
obalzg@utu.fi
Full list of author information is available at the end of the article

Background

Sustained glial reactivity to pathological changes underlies neuroinflammation in Alzheimer's disease (AD) [1] and other neurodegenerative disorders [2]. Glial reactivity in the brain could be beneficial by degrading beta-amyloid (Aβ) plaques, or detrimental by secreting cytokines and other promoters of neuroinflammation [3]. In response to disease, microglia undergo distinct changes in shape, count, function, and upregulation of surface bioactive molecules expression [1]. Purinergic 2 type X receptor subtype 7 (P2X7) is a key surface receptor in microglia, the expression of which is upregulated when the cells are in a reactive state [4]. P2X7 receptor is an ATP-gated ion channel that is widely distributed in the brain and expressed abundantly in microglia, but also in neurons and other glial cells, such as astrocytes and oligodendrocytes [5]. Among the physiological roles of P2X7 receptor is regulating neurotransmitters release [6]. P2X7 receptor also has several immune response functions in reactive microglia; it is implicated in the release of pro-inflammatory cytokines, production of reactive oxygen and nitrogen species, caspase activation, and the induction of apoptosis, collectively fueling neuroinflammation [4].

In the context of AD, P2X7 receptor expression has been observed to co-localize with microglia surrounding Aβ plaques in the brains of AD patients and rodent models of AD [7–9]. It is a well-established fact that Aβ causes microglial reactivity in AD [10–12]. Microglia react to Aβ plaques by releasing various pro-inflammatory cytokines, and upregulating P2X7 receptor expression, a response that potentially contributes to the inflammatory environment around Aβ plaques [13, 14]. Interestingly, P2X7 receptor seems to play a fundamental role in microglial response to Aβ plaques, as P2X7-deficient microglia were not reactive to Aβ plaques in mice [14]. The upregulated expression of P2X7 receptor in AD has also been associated with reactive microglia inflammatory reaction to neurodegeneration and tissue damage [13, 15]. The purinergic 2 type Y receptor subtype 12 (P2Y12) is another key receptor in microglia, the expression of which is downregulated in the brain of patients with AD and tauopathies and mouse models of tau pathology [16]. Accordingly, P2X7 and P2Y12 receptors have attracted a lot of interest as positron emission tomography (PET) imaging markers of reactive microglia and neuroinflammation.

P2X7 receptor emerged as a potentially superior imaging marker to translocator protein-18 kDa (TSPO), which remains the gold standard for imaging glial reactivity despite its drawbacks, including the low brain uptake and high non-specific binding of TSPO-targeting radiotracers, and TSPO polymorphism effect on the binding affinity between subjects [17, 18]. A number of potent and selective P2X7 receptor antagonist ligands have already been developed as PET radiotracers [19]. However, only [^{11}C]JNJ-54173717 [20], [^{18}F]JNJ-64413739 [21] and the most recently developed radiotracer targeting P2X7 receptor, [^{11}C]SMW139 [22], advanced from in vitro and preclinical development to clinical evaluation. [^{11}C]SMW139 preliminary assessment in a small cohort of MS patients demonstrated slightly higher brain uptake compared to healthy controls [23]. Preclinical studies showed that [^{11}C]SMW139 could detect increased expression of human and endogenous rat P2X7 receptor in rats [22, 24], despite the lower binding affinity of [^{11}C]SMW139 to rodent than human P2X7 receptor [24, 25]. However, [^{11}C]SMW139 binding on post-mortem brain sections did not differentiate AD patients from healthy subjects [22], which raised concerns on [^{11}C]SMW139 applicability to image P2X7 receptor in AD.

In our study, we used the APP/PS1-21 transgenic (TG) mouse model of Aβ deposition, a reliable model to validate radiotracers in preclinical settings, which has been used in the development of novel PET radiotracers targeting reactive glia [26, 27] and misfolded proteins, such as tau [28]. In this model, early onset Aβ plaques are associated with simultaneous and robust neuroinflammation, represented by the presence of increased reactive microglia around the Aβ plaques [29]. The aim of the present study was to image reactive glia in the APP/PS1-21 TG mouse model of Aβ deposition longitudinally with [^{11}C]SMW139 targeting P2X7 receptor and compare tracer uptake in the same mice to that of [^{18}F]F-DPA targeting TSPO at the final imaging time point. In previous studies, [^{18}F]F-DPA targeting TSPO in the APP/PS1-21 mouse model has shown the ability to image reactive glia, differentiate transgenic from age-matched wild type mice, and superior brain uptake to the TSPO PET tracers [^{18}F]DPA-714 and [^{11}C] PBR28 [30, 31]. This study contributes to the development of [^{11}C]SMW139 and [^{18}F]F-DPA for imaging reactive glia in the APP/PS1-21 mouse model.

Methods

Radiotracers

The radiotracers [^{11}C]SMW139 (2-chloro-5-[^{11}C]methoxy-*N*-((3,5,7-trifluoroadamantan-1-yl)methyl)benzamide) and [^{18}F]F-DPA (*N*,*N*-diethyl-2-(2-(4-([^{18}F]fluoro)phenyl)-5,7-dimethylpyrazolo[1,5-a] pyrimidin-3-yl) acetamide) were produced in the radiopharmaceutical laboratory at Turku PET Centre as described previously [32, 33]. For the 32 batches of [^{11}C]SMW139, the molar activity was 33.0 (21.0) GBq/μmol at the time of injection, radiochemical purity 98.3% (0.5%), and radiotracer shelf-life 1 h. For the three batches of [^{18}F]F-DPA, the molar

activity was 3.2 (0.6) GBq/μmol at the time of injection, radiochemical purity > 99%, and radiotracer shelf-life at least 4 h.

Animals

The APP/PS1-21 TG mice and their wild type (WT) littermates were used in the longitudinal in vivo PET imaging. In the ex vivo studies, additional C57BL/6 J WT mice were used with the PET-imaged mice (after imaging was completed). One to four mice were housed in individually ventilated cages with ad libitum access to soy-free chow (RM3 (E) Soya Free, Special Diets Service, Essex, UK) and tap water under the following housing conditions: temperature 21 °C (3 °C), humidity 55% (15%), light cycle 12 h (7:00 to 19:00 light), and aspen wood bedding.

The APP/PS1-21 mice were originally provided by KÖESLER (Rottenburg, Germany). The colony was bred and maintained with C57BL/6Cn mice according to the guidelines of the International Council of Laboratory Animal Science (ICLAS) in the Central Animal Laboratory of the University of Turku. Animal studies were performed in accordance with the European Ethics Committee (decree 86/609/CEE), and adhered to the ARRIVE guidelines, except randomization or blinding [34]. In addition, animal studies adhered to the 3Rs principle (Replacement, Reduction, and Refinement) by employing a longitudinal in vivo PET imaging design, and utilizing tissue samples from the same mouse efficiently for all ex vivo studies. The Animal Experiment Board of the Province of Southern Finland (ESAVI/4660/04.10.07/2016) granted ethical approval of this study.

In vivo PET imaging

The longitudinal in vivo PET imaging using [^{11}C]SMW139 with a 13-mouse cohort (TG $n=6$, including 4 females; WT $n=7$, including 6 females) consisted of a baseline scan at the age of 5 months and three follow-up scans at 8, 11, and 14 months. In addition, mice were imaged with [^{18}F]F-DPA after the final [^{11}C]SMW139 scan at 14 months, and both tracers brain uptake was compared only at this time point. At 5 months, PET scans were not obtained from 1 TG and 2 WT mice due to unsuccessful radiotracer injections. At 8 months, PET scans were successfully obtained from all TG and WT mice. At 11 months, 2 TG and 2 WT mice had to be sacrificed due to poor health conditions, and they were not scanned. Similarly, at 14 months, 1 TG and 1 WT mice needed to be sacrificed and were not scanned. The study design and final mice count at each time point are presented in Fig. 1. The mice were sacrificed after the final PET scan by cardiac puncture under deep isoflurane anesthesia and received cardiac perfusion with saline, then used in ex vivo brain autoradiography, immunohistochemical staining and radiometabolite analysis.

The same PET imaging protocol was used with [^{11}C]SMW139 and [^{18}F]F-DPA; the mice were imaged in pairs using the Inveon Multimodality PET/CT scanner (12.7 cm axial and 10 cm transaxial field of view, PET camera spatial resolution 1.4 mm, energy window 350–650 keV; Siemens Medical Solutions, Knoxville, TN). Mice were anesthetized with inhaled isoflurane (300 mL/min 3.5% isoflurane/O_2 for induction and 2% for maintenance), cannulated in the lateral tail vein and moved to the scanner, where a CT scan was first performed for attenuation correction and anatomical reference. The mice received an intravenous bolus injection of the radiotracer ([^{11}C]SMW139: injected activity 9.5 (0.5) MBq, injected mass 6.06 (5.61) μg/kg; [^{18}F]F-DPA: injected activity 6.7 (0.5) MBq, injected mass 22.5 (4.32) μg/kg; injected volume ≤ 200 μL) and underwent a dynamic 60 min (min) PET scan. During the scans, the mice laid prone on a heating pad and their eyes were protected from dryness with an ophthalmic gel (Oftagel, Santen Oy, Tampere, Finland).

PET data was converted from 3D list mode to 2D sinograms by a Fourier rebinning algorithm, then reconstructed with a 2D-filtered back-projection algorithm

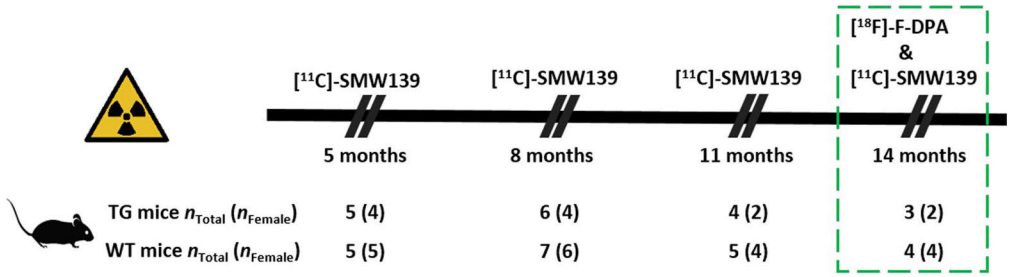

Fig. 1 In vivo PET imaging study design and mice counts at each imaging time point. The green box illustrates that at 14 months, mice were imaged with both radiotracers [^{11}C]SMW139 and [^{18}F]F-DPA. *TG* transgenic, *WT* wild type

into an image with a voxel size of 0.78×0.78×0.80 mm, or approximately 0.5 mm^3. Image data were divided into 49-time frames (30×10 s, 15×60 s, 4×300 s) and decay-corrected to the injection time. PET images were analyzed using Inveon Research Workplace analysis software v. 4.2 (Siemens Medical Solutions). Rigid co-registration to a 3D magnetic resonance imaging (MRI) mouse brain template (MRM NAt Mouse Brain Database, McKnight Brain Institute) was used as an anatomical reference for the CT and corresponding dynamic PET images of each mouse. The PET image and MRI template were positioned by translation (moving on X, Y, Z-axes)/angle rotation within the CT image. Brain uptake of the radiotracers was quantified in the hippocampus as a representative non-cortical region, and neocortex on the co-registered CT image and MRI template in the absence of the PET image (i.e., not guided by observed radioactivity in the brain to avoid potential bias). The size of each volume of interest (VOI) template was adjusted according to the size of the brain, so that almost identical volumes were analyzed. The averaged standardized uptake values (SUVs) for [^{11}C]SMW139 were calculated in the 3–15 min time frame as already 30 min after the radiotracer injection, at least 46% of brain radioactivity originated from the radiometabolites (more details in the discussion). Averaged SUVs for [^{18}F]F-DPA were calculated in the 25–50 min time frame. Regional time-activity curves were plotted for the completely dynamic scans.

Ex vivo brain autoradiography

30 mice (TG $n=13$, including 6 female; WT $n=17$, including 8 female) at 5, 8–10, 12 and 14 months (including the longitudinally imaged mice) (Table 1) were used to investigate [^{11}C]SMW139 binding on mouse brain cryosections using ex vivo autoradiography. Mice were sacrificed 10 min after [^{11}C]SMW139 injection (injected dose 10.0 (0.7) MBq), with cardiac puncture under deep isoflurane anesthesia and received cardiac perfusion with saline. Mice brains were then dissected, frozen and sliced as described previously [26]. From each mouse, cryosections were sliced at the level of cortex and thalamus as a representative non-cortical region. For both brain regions, ^{11}C-radioactivity intensity expressed as background-erased photo-stimulated luminescence per pixel (PSL/pixel—Bkg) was obtained by manually drawing a region of interest on the cortex and thalamus from the mouse sections. Regional uptake of [^{11}C]SMW139 was then calculated as SUV using the PSL/pixel-Bkg of cortex and thalamus and the pre-measured cortical percentage injected activity per gram value. Autoradiography images were analyzed using Aida Image Analyzer v. 4.5 (Raytest Isotopenmessgeräte GmbH, Straubenhardt, Germany).

Immunohistochemical staining

The expression of P2X7 receptor, TSPO and purinergic 2 type Y receptor subtype 12 (P2Y12) receptor was investigated in TG and WT mice at 5, 8–10, 12, 14, and 15 months (Table 1) utilizing cryosections used in ex vivo brain autoradiography. Immunohistochemical staining was performed using the semi-automated Labvision autostainer (ThermoFisher Scientific). The staining protocols are described in Additional file 1: Table S1. P2X7 receptor staining ($n=13$, including 7 TG), TSPO and P2Y12 receptor staining ($n=27$, including 15 TG) were performed in the same TG and WT mice only at 5 and 12 months. Staining were performed in all animals using non-consecutive slides.

The stained brain sections were digitized using Panoramic 250 Flash slide scanners (3DHistech, Budapest, Hungary). Images were examined using Case Viewer v. 2.1 (3DHistech). P2X7 receptor, TSPO and P2Y12 receptor staining were quantified from the digitized brain section images as positive object counts/mm^2 from two sections/mouse. The size of the quantification region of interest matched that of thalamus (both hemispheres) and cortex (one hemisphere). TSPO and P2Y12 receptor quantification was achieved in QuPath software using the positive cell detection function [35]. P2X7 receptor quantification was achieved using the artificial intelligence object detection algorithm You Only Learn One Representation (YOLOR) [36]. A description of the analytical workflow and image processing source code for the quantification of P2X7 receptor staining are available in Additional file 1. Negative staining was performed to verify the specificity of the P2X7 receptor and TSPO antibodies (Additional file 1: Fig. S1).

Radiometabolite analysis

To understand the in vivo metabolic profile of [^{11}C]SMW139 in mice, and to assist in the imaging data quantification, plasma and brain homogenate samples from TG and WT mice, including the ex vivo brain autoradiography mice cohort (Table 1) were analyzed by thin-layer chromatography or high-performance thin-layer chromatography (Protocols described in Additional file 1) for the fraction of unmetabolized [^{11}C]SMW139 (i.e., parent fraction). Cardiac blood (~500 µL) and brain tissue samples were collected after 10, 30, or 45 min of [^{11}C]SMW139 injection. Mice sacrificed at 10 min were divided into 5, 8–10, and 12–15 months, at 30 min into 3 and 7–10 months, and at 45 min as 7–10 months. Aida Image Analyzer v. 4.5 was used to calculate the percentage of unmetabolized [^{11}C]SMW139 from the total ^{11}C-radioactivity in the samples.

Table 1 Mice used in ex vivo studies

	Age (mo)	Genotype	N_{GENDER}		N_{TOTAL}
			F	M	
Ex vivo brain autoradiography	5	TG	3	1	4
		WT	2	2	4
	8–10	TG	3	2	5
		WT	2	5	7
	12	TG	–	2	2
		WT	–	1	1
	14	TG	1	1	2
		WT	3	2	5
P2X7 immunohistochemical staining	5	TG	1	–	1
		WT	–	1	1
	8–10	TG	1	1	2
		WT	–	2	2
	12	TG	–	2	2
		WT	–	2	2
	14	TG	1	–	1
		WT	1	–	1
	15	TG	1	–	1
		WT	–	–	–
TSPO & P2Y12 immunohistochemical staining	5	TG	2	1	3
		WT	1	2	3
	8–10	TG	2	1	3
		WT	1	2	3
	12	TG	–	3	3
		WT	–	2	2
	14	TG	2	1	3
		WT	4	–	4
	15	TG	1	2	3
		WT	–	–	–
	Δt (min)	**Genotype**	N_{GENDER}		N_{TOTAL}
			F	M	
Plasma radiometabolites analysis	10	TG	4	9	13
		WT	8	8	16
	30	TG	3	–	3
		WT	5	8	13
	45	TG	3	–	3
		WT	9	2	11
Brain radiometabolites analysis	10	TG	4	2	6
		WT	7	3	10
	30	TG	3	–	3
		WT	5	9	14
	45	TG	3	–	3
		WT	9	1	10

mo month, *min* minutes, *F* female, *M* male, *TG* transgenic, *WT* wild type

Statistical analysis

In all studies, results are reported as mean and standard deviation in parentheses when $n \geq 3$, or only the mean or individual values when $n < 3$. In the longitudinal in vivo PET imaging study, linear mixed model with compound symmetry covariance structure were used to assess the relationship between [^{11}C]SMW139 SUVs in the investigated VOIs at all time points with one within-subject factor (time) and one between-subjects factor (TG and WT group), as well as their interaction term. The interaction term examined whether the groups had different trends of change over time. If the interaction term was deemed not significant, it was dropped from the model. As a post-hoc analysis, differences in least squares means were assessed for all significant factors in order to find the individual differences between groups and time points. The difference in [^{11}C]SMW139 and [^{18}F]F-DPA SUVs between TG and WT mice in the investigated VOIs at 14 months was evaluated using t-test with Welch's correction (unpaired, parametric), after datasets were tested for normalization using Shapiro–Wilk's test. All statistical tests were performed as two-sided with the threshold for statistical significance set at 0.05. All analyses were performed using SAS software (version 9.4 for Windows; SAS Institute Inc., Cary, NC, USA).

Results

Longitudinal in vivo PET imaging with [^{11}C]SMW139 and comparison to [^{18}F]F-DPA

Longitudinal analysis of [^{11}C]SMW139 SUV change in the neocortex and hippocampus revealed no significant difference with ageing from baseline at 5 months to the three follow-up scans at 8, 11, and 14 months (neocortex $p = 0.53$, hippocampus $p = 0.54$) in TG ($n = 6$, including 4 females) or WT ($n = 7$, including 6 females) mice. In addition, we found no significant difference in [^{11}C]SMW139 SUVs between TG and age-matched WT mice at any time point ($p > 0.53$ for all time points) in the neocortex or hippocampus (Fig. 2a, b). Representative PET images of longitudinal [^{11}C]SMW139 SUVs in the brain of TG and WT mice are shown in Fig. 2c.

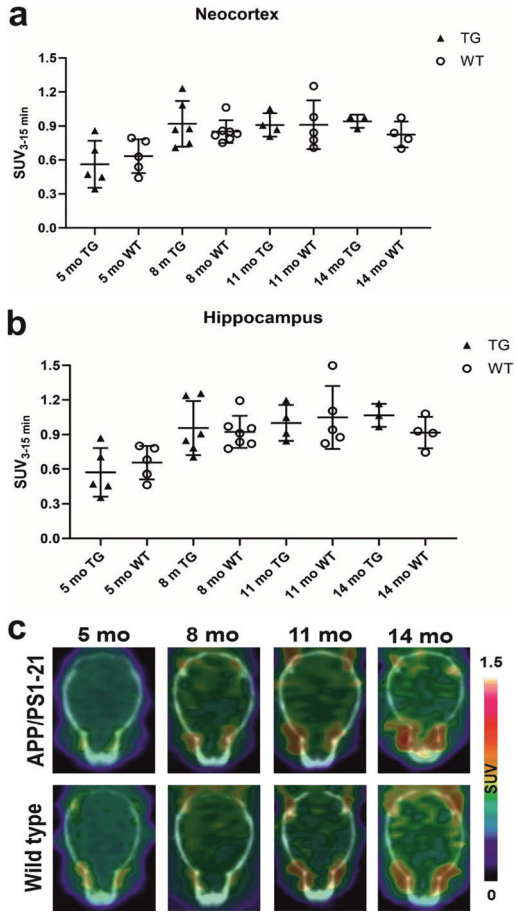

Fig. 2 [^{11}C]SMW139 longitudinal brain uptake in APP/PS1-21 transgenic (TG) and wild type (WT) mice. **a** and **b** Longitudinal [^{11}C]SMW139 standardized uptake values (SUVs) in the neocortex and hippocampus of TG and WT mice at 5, 8, 11 and 14 months of age. Statistical analysis: linear mixed model with compound symmetry covariance structure. **c** Representative axial brain PET/CT images of [^{11}C]SMW139 longitudinal SUVs in the same TG and WT mice at 5, 8, 11 and 14 months of age

At 14 months, mice were imaged with both [^{11}C]SMW139 and [^{18}F]F-DPA to compare the brain uptake of both radiotracers in the same mice, when neuroinflammation is known to be present in the APPPS1-21 mouse model [29]. [^{11}C]SMW139 PET images and averaged time-activity curves in the neocortex showed no difference in radioactivity signal between TG ($n = 3$) and WT ($n = 4$) mice (Fig. 3a, b). On the contrary, higher [^{18}F]F-DPA uptake was detected in the PET images and averaged time-activity curves of TG compared to WT mice in the neocortex (Fig. 3c, d). Moreover, [^{11}C]SMW139 binding SUVs of TG and WT mice were similar in the neocortex (average SUV 0.94 (0.06) for TGs and 0.82 (0.11) for WTs, $p = 0.14$) and hippocampus (average SUV 1.07 (0.1) for TGs and 0.91 (0.17) for WTs, $p = 0.15$) (Fig. 4a, c). In contrast, in the same animals, significantly higher [^{18}F]F-DPA binding SUVs were present in TG compared to WT mice in the neocortex (average SUV 0.7 (0.06) for TGs and 0.44 (0.4) for WTs, $p = 0.03$) and hippocampus (average SUV 0.68 (0.06) for TGs and 0.45 (0.06) for WTs, $p = 0.01$) (Fig. 4b, d).

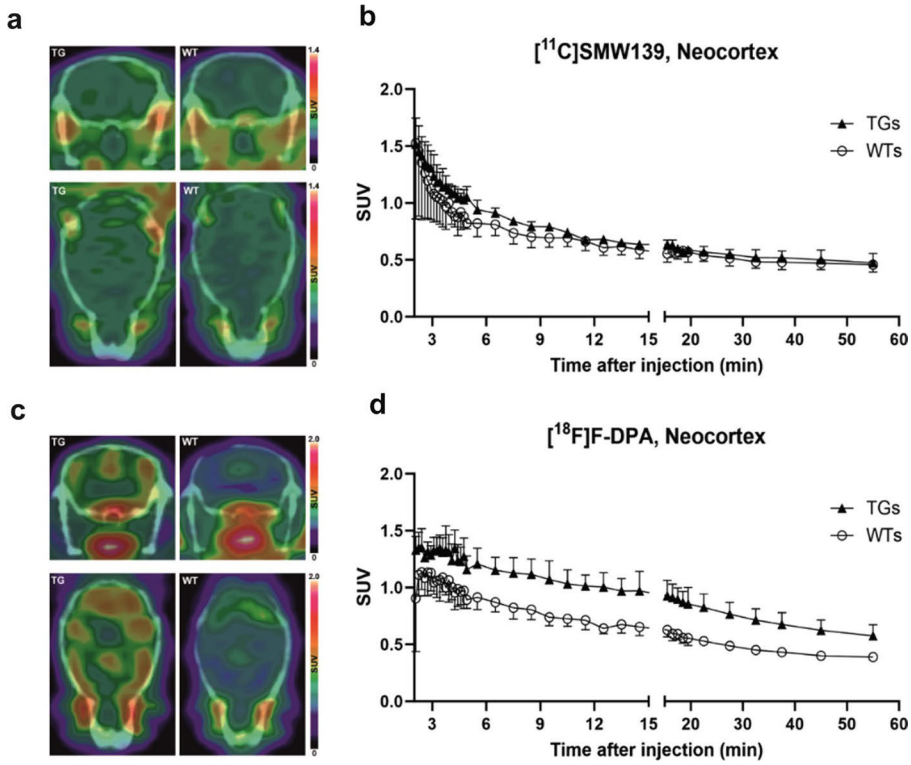

Fig. 3 In vivo PET imaging using [^{11}C]SMW139 and [^{18}F]F-DPA in the same APP/PS1-21 transgenic (TG) and age-matched wild type (WT) mice at 14 months. **a** and **c** Representative coronal and axial brain PET/CT images of TG ($n=1$) and WT ($n=1$) mice at 14 months imaged with [^{11}C]SMW139 (**a**) and [^{18}F]F-DPA (**c**). [^{11}C]SMW139 images were summed over 3–15 min and adjusted to the same color scale. [^{18}F]F-DPA were summed over 25–50 min and scaled to the same color scale. **b** and **d** Averaged [^{11}C]SMW139 (**b**) and [^{18}F]F-DPA (**d**) time-activity curves in the neocortex of the same TG ($n=3$) and WT ($n=4$) mice at 14 months. Error bars indicate standard deviation

Ex vivo brain autoradiography

Qualitative and quantitative assessment of brain autoradiography images from 30 mice ($n=13$ TG, $n=17$ WT) sacrificed 10 min after [^{11}C]SMW139 injection showed that the radiotracer has similar uptake in the cortex and thalamus of TG and WT mice with a consistent trend at 5, 8–10, 12 and 14 months (Fig. 5).

Immunohistochemical staining

Qualitative assessment of P2X7 receptor immunohistochemical staining in mouse brain sections showed a subtle increase in receptor expression in TG mice aged between 5 and 10 months. Expression became slightly more prominent between 10 and 15 months, mainly in the cortex and thalamus. In WT mice, receptor expression remained consistent with ageing. Inline with these observations, quantification of P2X7-positive staining in cortex and thalamus of TG, but not WT, mice demonstrated a subtle increase in receptor expression with ageing (Fig. 6). P2X7-positive staining was also detectable in the white matter corpus callosum of TG, but not WT, mice starting from 8 months (Additional file 1: Fig. S2).

TSPO-positive staining in brain sections of TG mice was detectable already at 5 months. At 8 months, TSPO-positive staining covered the entire brain and further increased in quantity and intensity with ageing. A similar expression pattern was absent in age-matched WT mice. Quantification of TSPO-positive staining in the cortex and thalamus showed that TSPO expression is higher in TG mice and generally increases with ageing, but reaching a plateau at 10 months (Fig. 7). Similar to TSPO, P2Y12-positive staining was detectable in most brain regions of TG, but not WT, mice at 5 months and increased with ageing in all brain regions. Quantification of P2Y12-positive staining in the cortex and thalamus showed a similar increasing trend as TSPO (Additional file 1: Fig. S3).

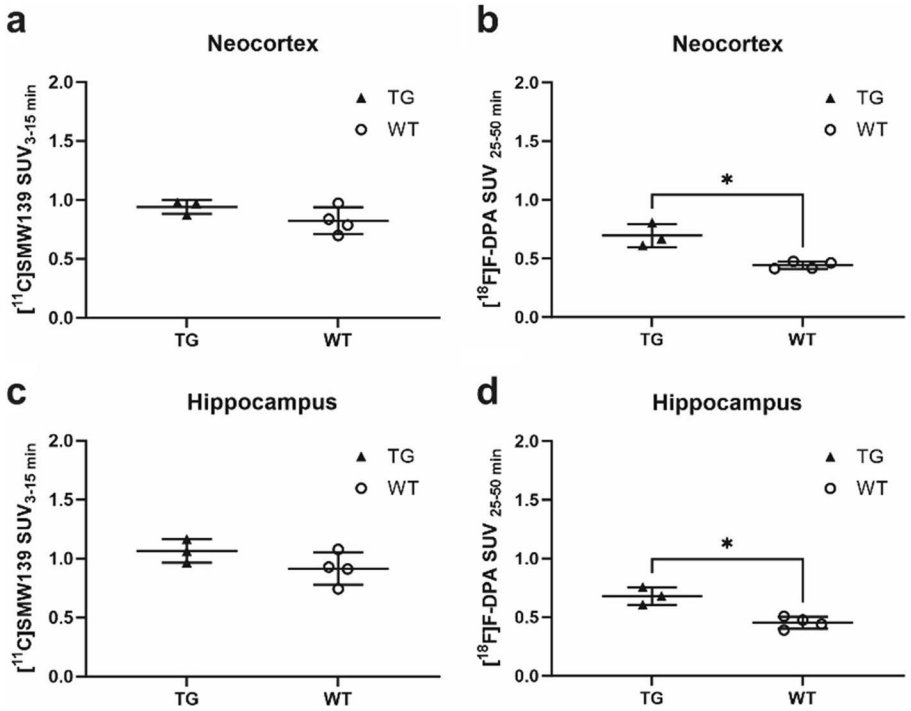

Fig. 4 [^{11}C]SMW139 and [^{18}F]F-DPA standardized uptake value (SUV) in the same APP/PS1-21 transgenic (TG) and wild type (WT) mice at 14 months. **a** and **c** [^{11}C]SMW139 averaged SUV in the neocortex (**a**) and hippocampus (**c**) of TG ($n=3$) and WT ($n=4$) mice. **b** and **d** [^{18}F]F-DPA averaged SUV in the neocortex (**b**) and hippocampus (**d**) of the same TG and WT mice. Statistical test: t-test with Welch's correction. SUV values are presented with mean and standard deviation. *$p<0.05$

Radiometabolite analysis

The percentage of unmetabolized [^{11}C]SMW139 from the total ^{11}C-radioactivity in plasma and brain homogenates at 10, 30, and 45 min showed that [^{11}C]SMW139 is metabolized quickly. Thirty minutes after radiotracer injection, the mean percentage of [^{11}C]SMW139 parent fraction was 33% in plasma and 29% in brain homogenates from female mice, whereas in male mice the percentage was 56% in both plasma and brain homogenates (Fig. 8). The fast metabolism of [^{11}C]SMW139 is also accompanied by a gender difference, as the radiotracer is metabolized faster and to a greater extent in female than male WT mice, as seen at 30 and 45 min in plasma and brain homogenates. In the same sex, the radiometabolites of [^{11}C]SMW139 accumulate in plasma and brain homogenates in similar fractions and to a similar extent (Fig. 8). At 10, 30, and 45 min, we found no difference between TG and WT mice or mice from different age groups in the percentage of unmetabolized [^{11}C]SMW139 in plasma or brain homogenate (t-test with Welch's correction, $p>0.25$ for all).

Discussion

Glial reactivity increases with ageing in the APP/PS1-21 mouse model [29], and previous PET studies have demonstrated this phenomenon using different radiotracers [26, 30]. Here, we investigated the P2X7 receptor targeting PET radiotracer, [^{11}C]SMW139, for detecting increased glial activity in this mouse model in vivo. In our study, both longitudinal in vivo PET and ex vivo autoradiography imaging of APP/PS1-21 TG and WT mice using [^{11}C]SMW139 showed that (1) there were no significant differences in [^{11}C]SMW139 uptake between the genotypes in any of the evaluated time points, and (2) brain [^{11}C]SMW139 uptake in both TG and WT mice remained around the same level until 14 months. One explanation for these findings is the inadequate expression of P2X7 receptor in the APP/PS1-21 mouse model as presented in this study (discussed further below). Another explanation is the difference between the rodent and human P2X7 receptors, which results in a lower affinity of [^{11}C]SMW139 for the rodent compared to the human version of the receptor, complicating the

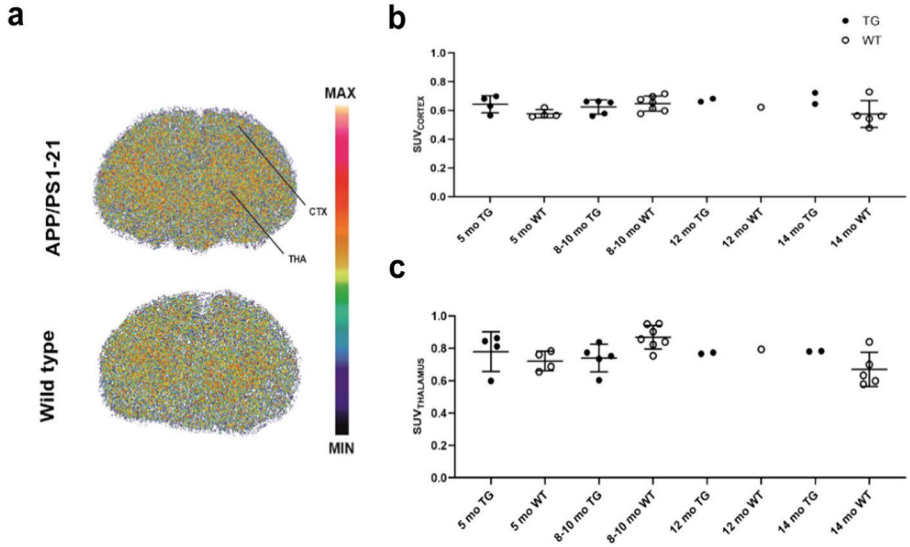

Fig. 5 Ex vivo brain autoradiography imaging using [^{11}C]SMW139 in APP/PS1-21 transgenic (TG) and wild type (WT) mice. **a** Representative autoradiography images of TG ($n = 1$) and WT ($n = 1$) mice at 8–10 months. Images are adjusted to the same color bar. **b** and **c** [^{11}C]SMW139 standardized uptake value (SUV) in cortex (**b**) and thalamus (**c**) of TG ($n = 4, 5, 2, 2$) and WT ($n = 4, 7, 1, 5$) mice at 5, 8–10, 12 and 14 months

preclinical use of [^{11}C]SMW139 [24, 25]. Our findings raise concerns about the ability of other PET radiotracer to quantify P2X7 receptor expression in the APP/PS1-21 mouse model, due to the inadequate expression of the receptor. Moreover, our findings suggest that the APP/PS1-21 mouse model might not be suitable for P2X7 receptor imaging using PET. Janssen et al. reported a ten-fold higher binding of [^{11}C]SMW139 in rat striatum overexpressing the human P2X7 receptor compared to the control striatum at one time point [23]. This finding, when compared with our longitudinal imaging results in mice, indicates different binding of [^{11}C]SMW139 to the human and mouse P2X7 receptor, and possibly different tracer binding in mice and rats. Additional preclinical imaging studies in rodents would be needed to assess [^{11}C]SMW139 binding to both human and rodent P2X7 receptors. Janssen et al. also demonstrated that [^{11}C]SMW139 binding did not differ significantly between AD patients and age-matched healthy subjects on post-mortem brain sections, despite a significant increase in P2X7 receptor expression in AD patients [23]. To establish the utility of [^{11}C]SMW139 in AD, future studies focusing on evaluating its in vivo binding to the P2X7 receptor in AD patients are needed.

Our immunohistochemical staining findings revealed only a subtle increase in P2X7 receptor expression in the cortex and thalamus of TG mice. In the case of TSPO and P2Y12 receptor, expression in TG mice increased prominently with ageing and compared to age-matched WT mice. At the age of 10 months, expression of all three neuroinflammatory markers in the APP/PS1-21 mouse brain seemed to reach a plateau. This phenomenon aligns with previous findings in this mouse model, as previous reports referred to plateau and variability in detecting microglial activation [37] and AD pathology [28]. A study using brain tissue from both rats and MS patients has indicated a predominant upregulation of P2X7 receptor expression in pro-inflammatory reactive microglia, while P2Y12 receptor expression is mainly upregulated in anti-inflammatory reactive microglia [38]. This same study demonstrated that enhanced expression of microglial P2X7 receptor is accompanied by decreased expression of P2Y12 receptor on the same cells [38]. While further studies in AD are essential to validate these findings, it is conceivable that in our study, the weaker upregulated expression of P2X7 receptor compared to P2Y12 receptor in the APP/PS1-21 mouse model may be attributed to the predominantly anti-inflammatory microglial activation status. This association could be linked to the increased expression of P2Y12 receptor. Nevertheless, additional studies are warranted to characterize the microglial activation status, validate the presence of anti-inflammatory markers in the APP/PS1-21 mouse model, and provide further support for this hypothesis. It is noteworthy that the expression of P2Y12 receptor in AD rodent models is inconsistent. While tau pathology mouse models show reduced expression of P2Y12 receptor, amyloid pathology mouse models show either an increased or an unchanged

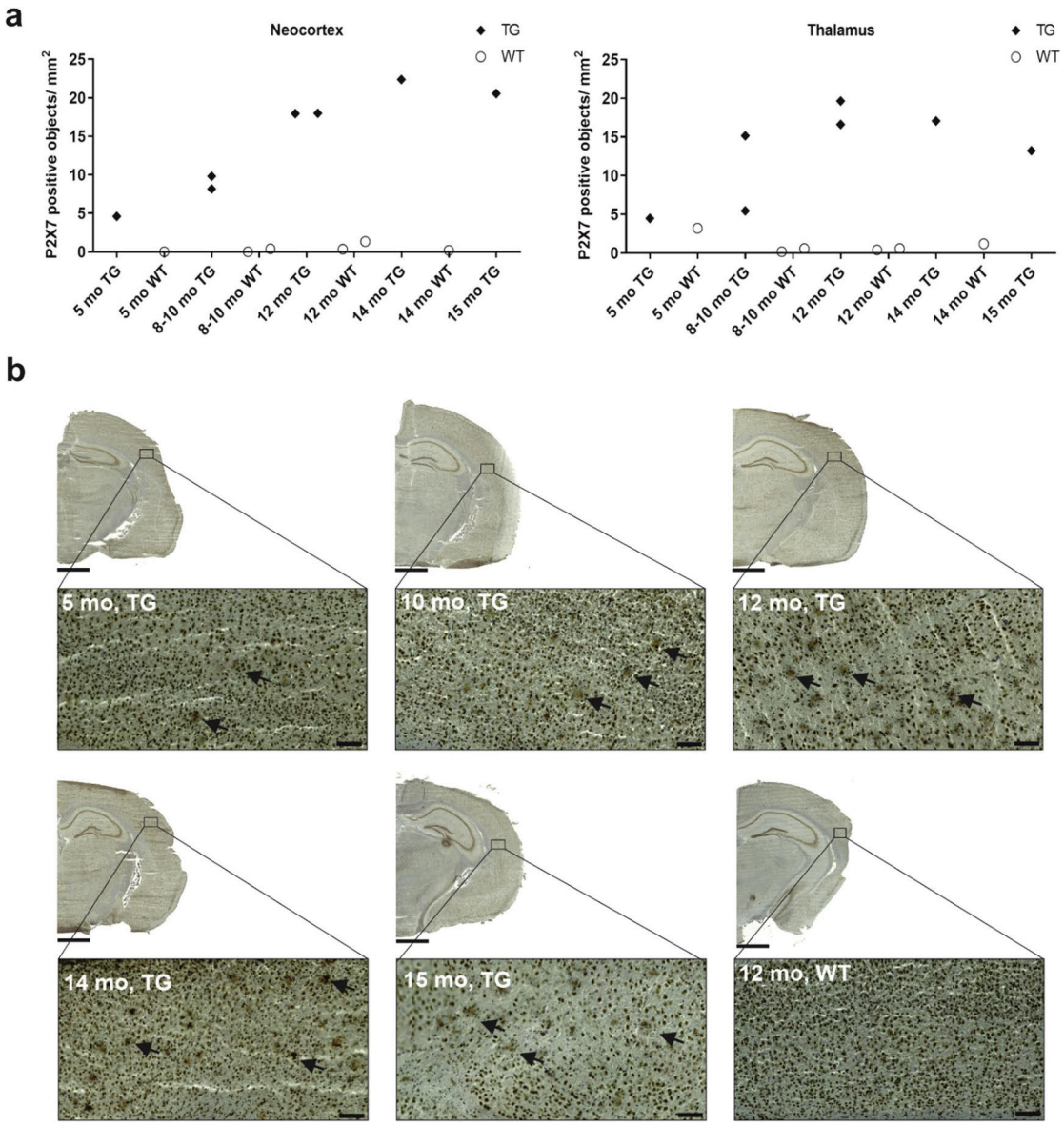

Fig. 6 Immunohistochemical staining of P2X7 receptor in brain cryosections of APP/PS1-21 transgenic (TG) and wild type (WT) mice. **a** Quantification of P2X7-positive staining as object counts/mm^2. Staining was evaluated in the cortex and thalamus of TG and WT mice at 5, 8–10, 12, 14, and 15 months. **b** Representative images of P2X7-positive staining in TG and WT mice at the investigated time points. Arrows point at the P2X7-positive staining detected by the artificial intelligence object detection algorithm. Scale bar = 1000 µm for the half-hemisphere brain section image, 100 µm for the cortex view image. Magnification = 1.5× for the half-hemisphere brain section image, 15.0× for the cortex view image

expression of P2Y12 compared to wild type mice [16]. In our study, we observed a significant upregulation of P2Y12 receptor expression in the APP/PS1-21 mouse model compared to wild-type mice, which is similar to the findings reported in the APP23 mouse model of Aβ deposition [16]. The biological relevance of the inconsistent P2Y12 receptor expression in mouse models is debatable, considering the discrepancy with the downregulated receptor expression in human AD and tauopathies [16]. Nonetheless, the upregulated P2Y12 receptor expression

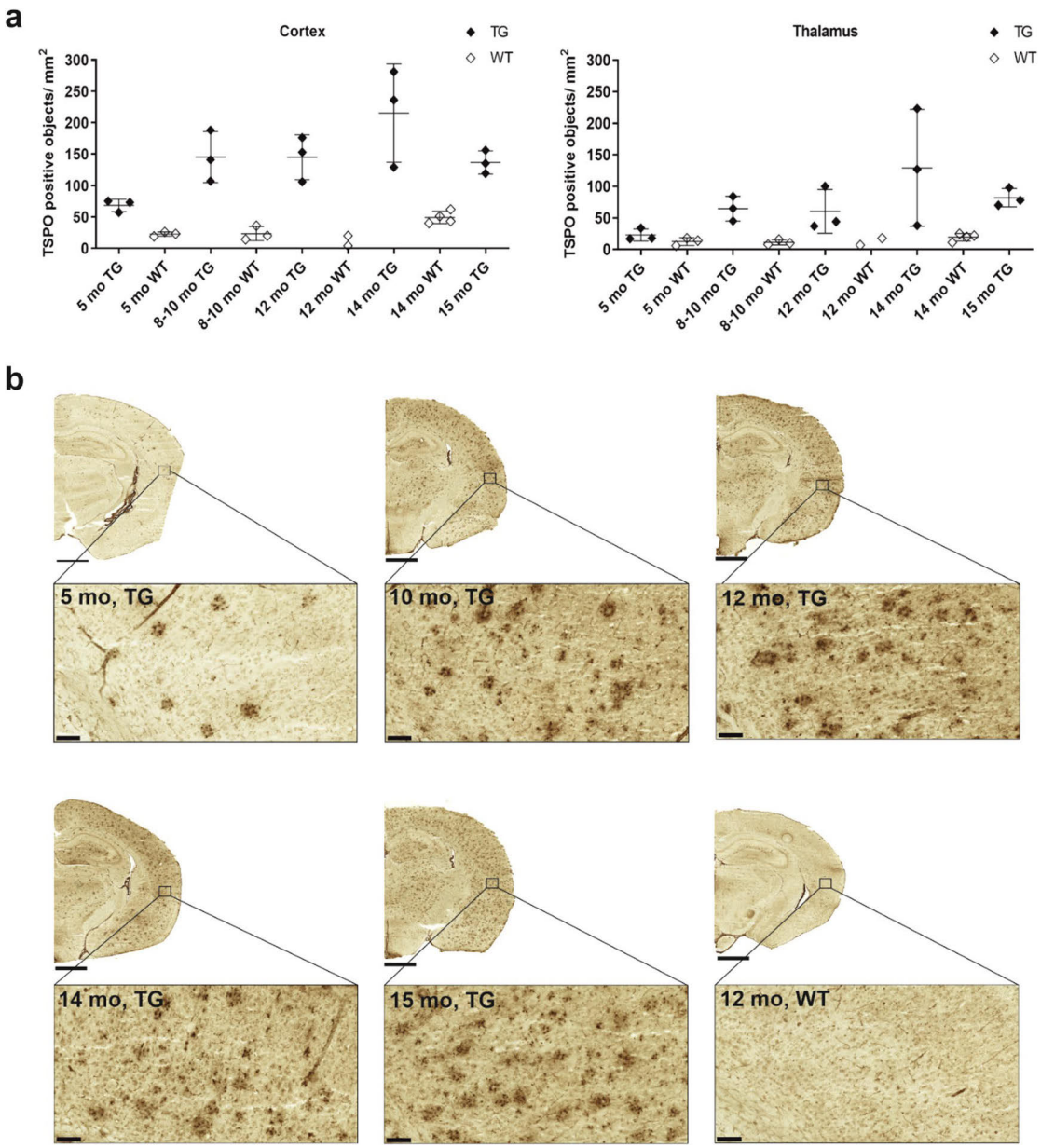

Fig. 7 Immunohistochemical staining of TSPO in brain cryosections of APP/PS1-21 transgenic (TG) and wild type (WT) mice. **a** Quantification of TSPO-positive staining as object counts/mm^2. Staining was evaluated in the cortex and thalamus of TG and WT mice at 5, 8–10, 12, 14, and 15 months. Error bars indicate standard deviation. **b** Representative images of TSPO-positive staining in TG and WT mice at the investigated time points. Scale bar = 1000 µm for the half-hemisphere brain section image, 100 µm for the cortex view image. Magnification = 1.5× for the half-hemisphere brain section image, 15.0 × for the cortex view image

in the APP/PS1-21 mouse model could still be beneficial for imaging purposes, especially in the development of PET tracers for imaging P2Y12 receptor.

In a previous study, we showed that [^{18}F]F-DPA targeting TSPO is capable of revealing neuroinflammation trend and its peak at 12–15 months in the APP/PS1-21

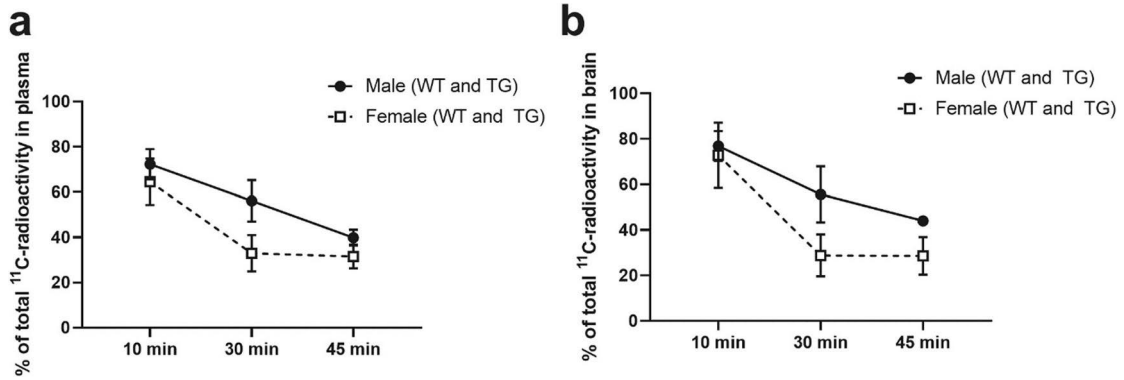

Fig. 8 Fractions of unmetabolised [^{11}C]SMW139 in APP/PS1-21 transgenic (TG) and wild type (WT) mice plasma and brain homogenates at 10, 30, and 45 min. **a** and **b** Percentage of unmetabolised [^{11}C]SMW139 over all radioactivity in male and female mice in plasma (**a**) and brain homogenates (**b**). Error bars indicate standard deviation

mouse model with in vivo PET and ex vivo autoradiography [30]. In the present study, [^{18}F]F-DPA showed superiority over [^{11}C]SMW139 to detect reactive glia in the APP/PS1-21 mouse model at 14 months. For years, targeting TSPO has been the gold standard for imaging glial activity and neuroinflammation, despite its limitations [17, 18]. Besides, more recent studies highlighted that TSPO expression in humans is related to different phenomena than in mice, and that TSPO-PET signals in humans reflect the density of inflammatory cells (microglia and macrophages) rather than the activation status in mice, raising concerns about the translatability of TSPO-PET from rodents to humans [39–41]. Finding a superior imaging marker to TSPO remains a hurdle, although several PET ligands targeting other imaging markers of neuroinflammation are being explored [17]. One challenge is the lack of glia selectivity; like TSPO, the majority of the potential imaging markers are expressed in different glial cell types, which react heterogeneously during different phases of neuroinflammation, resulting in unpredictability of the imaging markers expression profiles, thus complicating the in vivo PET imaging quantification. An imaging marker superior to TSPO needs to be specific for a certain glial cell type, and have different expression patterns in physiological and neuroinflammatory conditions.

Defining the time frame for quantifying [^{11}C]SMW139 in vivo uptake was complicated by the fast metabolic profile in mice, and the presence of radioactive metabolites in the brain tissue. In a previous study with [^{11}C]SMW139, we detected up to three brain penetrant radiometabolites of [^{11}C]SMW139 in mouse brain homogenates and one radiometabolite more in plasma already at 10 min after tracer injection [32]; similar findings were also reported by Brumberg and colleagues [42]. Accordingly, an appropriate time frame needs to be selected in which there is still a reasonable percentage of the parent fraction and as little interference as possible from the radiometabolite fraction. Considering that [^{11}C]SMW139 started to washout around 90 s after injection in mice, 3–15 min was selected to calculate the averaged SUVs for group comparisons. Although it is not known if these three radiometabolites of [^{11}C]SMW139 bind to P2X7 receptor or another target, their presence in the brain disturbs the PET data quantification and hamper the utilization of [^{11}C]SMW139 in any in vivo PET application. Defining the time frame for quantifying [^{18}F]F-DPA in vivo uptake in the same mice was more straightforward. The time frame 25–50 min was used to calculate the averaged SUVs, considering that [^{18}F]F-DPA has no brain penetrating radiometabolites in mice [30]. SUVs were used to analyze both tracers brain uptake, as a reference region for binding ratio calculations was not found. In plasma samples and brain homogenates, [^{11}C]SMW139 parent fraction was similar in mice at all ages, indicating that [^{11}C]SMW139 metabolism is independent of aging. However, our results show that the [^{11}C]SMW139 parent fraction decreased faster in plasma and brain homogenates from female compared to male mice, indicating a gender difference in [^{11}C]SMW139 metabolism in mice. In contrast, no difference has been reported in [^{11}C]SMW139 plasma metabolism between male and female rats [22]. Moreover, our results showed that the [^{11}C]SMW139 parent fraction at 45 min was similar in plasma and brain homogenate (40% and 44%, respectively), whereas the [^{11}C]SMW139 parent fraction at 45 min in male rats was different in plasma (42%) and brain homogenates (66%) [22], and fractions within the same range were reported in female rats at the same

time points [24]. Taken together, these findings show that [^{11}C]SMW139 is metabolized to a greater extent in mouse brain (44%) than rat brain (66%).

There were strengths in this study. First, using a longitudinal imaging design with [^{11}C]SMW139 allowed the assessment of reactive microglia in the same animals with ageing. The investigated groups, comprising 6 TG and 7 WT mice, were small because of the longitudinal nature of the study. This design involved repeated imaging of the same animals, which enables making within-subject comparisons of imaging findings, controlling for between-subject variability. This is an excellent advantage of in vivo PET imaging, particularly when assessing age-related pathophysiological changes. Therefore, despite the smaller number of mice, the results remain reliable because each mouse served as its own control. Second, performing the radiotracers comparison in the same animals excludes potential variability due to using different animals. Third, the availability of immunohistochemical staining of both radiotracers imaging targets assessed in explaining the in vivo imaging findings. On the other hand, our study had limitations. Firstly, it was not possible to scan each mouse of the starting cohort at all four follow-up time points because some mice needed to be sacrificed during the study. Secondly, both male and female mice were included in this imaging study. Ideally, including only one gender would help mitigate potential variability arising from gender differences. Thirdly, fewer animals per age group were used in the immunohistochemical staining of P2X7 receptor in comparison to TSPO and P2Y12 receptor. Additionally, immunohistochemical staining of P2X7 receptor and TSPO were performed in the same animals only at two of the four investigated time points, which did not allow for a thorough comparison of the imaging markers solely based on the immunohistochemical staining findings. Moreover, due to the inferior quality and different features of P2X7 receptor staining compared to that of TSPO and P2Y12 receptor, we were forced to use a different analysis method to quantify P2X7 receptor staining, which could be seen as a limitation to the direct comparison of imaging markers. Lastly, neither P2X7 receptor nor TSPO are expressed exclusively in microglia, rather generally in glia and the potentially infiltrating macrophages to the central nervous system from the periphery, thus [^{11}C]SMW139 and [^{18}F]F-DPA in vivo brain uptake represent binding to glia collectively, not solely microglia.

Conclusions

This study aimed to use the P2X7 receptor as an imaging marker for reactive glia in an Alzheimer's disease mouse model. However, [^{11}C]SMW139, which has lower affinity for the rodent P2X7 receptor compared to the human version of the receptor, was unable to measure the low expression of P2X7 receptor in the APP/PS1-21 mouse model. Additionally, the fast metabolism of [^{11}C]SMW139 in mice and the presence of several brain-penetrating radiometabolites significantly impacted the analysis of in vivo PET signal of the tracer. Finally, [^{18}F]F-DPA targeting TSPO was more suitable for imaging reactive glia and neuroinflammatory processes in the APP/PS1-21 mouse model, based on the findings presented in this study and previous studies with this mouse model.

Abbreviations

AD	Alzheimer's disease
Aβ	Beta-amyloid
P2X7	Purinergic 2 type X receptor subtype 7
TSPO	Translocator protein-18 kDa
P2Y12	Purinergic 2 type Y receptor subtype 12
PET	Positron emission tomography
MS	Multiple sclerosis
TG	Transgenic
WT	Wild type
MRI	Magnetic resonance imaging
VOI	Volume of interest
SUV	Standardized uptake value

Supplementary Information

The online version contains supplementary material available at https://doi.org/10.1186/s13550-024-01085-7.

Additional file 1. Supplementary methods.

Acknowledgements

We acknowledge the personnel of the Preclinical Imaging Laboratory of Turku PET Centre for assisting with the studies, and the personnel of the Accelerator Laboratory for radionuclide production. We thank the staff of the Central Animal Laboratory of the University of Turku for assistance with the animal studies. We acknowledge that the histological methods were performed by the Histology core facility of the Institute of Biomedicine, University of Turku, Finland. We acknowledge the Turku BioImaging Image Data Team jointly operated by the Åbo Akademi University and the University of Turku for their support in image data management and analysis.

Author contributions

Study was planned by OA, RA, AS, OS, JOR, and MHS. OA drafted the manuscript, and RA, AES and MHS participated in the subsequent drafts. JJD and MK prepared the [^{11}C]SMW139 precursor and standards. SW performed the [^{11}C]SMW139 synthesis. TK performed the [^{18}F]F-DPA synthesis. OA, JSH, AES, and MHS performed the animal studies. RA performed the radiochromatography and analyzed the radiometabolites. MM performed the statistical analyses of the in vivo PET imaging study. JS performed the P2X7 immunohistochemical staining quantification. All authors read and approved the final manuscript.

Funding

This work was funded by the Drug Research Doctoral Program at the University of Turku, the Swedish Cultural Foundation in Finland (OS and MHS), Finnish governmental research funding (Nos. 13250 (MHS) and 11133 (OS)), and the Academy of Finland (nos. 310962 (JOR) and 334310 (OS)).

Availability of data and materials

The datasets used and/or analyzed during the current study are available from the corresponding author on reasonable request.

Declarations

Ethics approval and consent to participate
The Animal Experiment Board of the Province of Southern Finland (ESAVI/4660/04.10.07/2016) granted ethical approval of this study. Animal studies were performed in accordance with the European Ethics Committee (decree 86/609/CEE), and adhered to the ARRIVE guidelines, except randomization or blinding.

Consent for publication
Not applicable.

Competing interests
The authors declare that they have no competing interests.

Author details
[1]PET Preclinical Imaging Laboratory, Turku PET Centre, University of Turku, Tykistökatu 6 A, 20520 Turku, Finland. [2]Medicity Research Laboratory, University of Turku, Tykistökatu 6 A, 20520 Turku, Finland. [3]Drug Research Doctoral Programme, University of Turku, Turku, Finland. [4]Turku University Hospital, Turku PET Centre, Kiinamyllynkatu 4-8, 20520 Turku, Finland. [5]Radiopharmaceutical Chemistry Laboratory, Turku PET Centre, University of Turku, Kiinamyllynkatu 4-8, 20520 Turku, Finland. [6]Turku BioImaging, Åbo Akademi University and University of Turku, Turku, Finland. [7]School of Chemistry, The University of Sydney, Sydney, NSW 2006, Australia. [8]Department of Chemistry, University of Turku, Henrikinkatu 2, 20500 Turku, Finland. [9]Accelerator Laboratory, Turku PET Centre, Åbo Akademi University, Kiinamyllynkatu 4-8, 20520 Turku, Finland. [10]Department of Neurology, Turku University Hospital, Kiinamyllynkatu 4-8, 20520 Turku, Finland.

Received: 28 September 2023 Accepted: 22 February 2024
Published: 6 March 2024

References

1. Gao HM, Hong JS. Why neurodegenerative diseases are progressive: uncontrolled inflammation drives disease progression. Trends Immunol. 2008;29(8):357–65.
2. Block ML, Zecca L, Hong JS. Microglia-mediated neurotoxicity: uncovering the molecular mechanisms. Nat Rev Neurosci. 2007;8:57–69.
3. Wyss-Coray T, Mucke L. Inflammation in neurodegenerative disease—a double-edged sword. Neuron. 2002;35:419–32.
4. Savio LEB, Mello PA, da Silva CG, Coutinho-Silva R. The P2X7 receptor in inflammatory diseases: Angel or demon? Front Pharmacol. 2018;9:52.
5. Yu Y, Ugawa S, Ueda T, Ishida Y, Inoue K, Kyaw Nyunt A, et al. Cellular localization of P2X7 receptor mRNA in the rat brain. Brain Res. 2008;15(1194):45–55.
6. Sperlágh B, Köfalvi A, Deuchars J, Atkinson L, Milligan CJ, Buckley NJ, et al. Involvement of P2X7 receptors in the regulation of neurotransmitter release in the rat hippocampus. J Neurochem. 2002;81(6):1196–211.
7. McLarnon JG, Ryu JK, Walker DG, Choi HB. Upregulated expression of purinergic P2X7 receptor in Alzheimer disease and amyloid-β peptide-treated microglia and in peptide-injected rat hippocampus. J Neuropathol Exp Neurol. 2006;65(11):1090–7.
8. Parvathenani LK, Tertyshnikova S, Greco CR, Roberts SB, Robertson B, Posmantur R. P2X7 mediates superoxide production in primary microglia and is up-regulated in a transgenic mouse model of Alzheimer's disease. J Biol Chem. 2003;278(15):13309–17.
9. Lee HG, Won SM, Gwag BJ, Lee YB. Microglial P2X7 receptor expression is accompanied by neuronal damage in the cerebral cortex of the APPswe/PS1dE9 mouse model of alzheimer's disease. Exp Mol Med. 2011;43(1):7–14.
10. Halliday G, Robinson SR, Shepherd C, Kril J. Alzheimer's disease and inflammation: a review of cellular and therapeutic mechanisms. Clin Exp Pharmacol Physiol. 2000;27:1–8.
11. Combs CK, Johnson DE, Karlo JC, Cannady SB, Landreth GE. Inflammatory mechanisms in Alzheimer's disease: inhibition of β-amyloid-stimulated proinflammatory responses and neurotoxicity by PPARγ agonists. J Neurosci. 2000;20(2):558–67.
12. Sasaki A, Yamaguchi H, Ogawa A, Sugihara S, Nakazato Y. Microglial activation in early stages of amyloid β protein deposition. Acta Neuropathol. 1997;94(4):316–22.
13. Bhattacharya A, Biber K. The microglial ATP-gated ion channel P2X7 as a CNS drug target. Glia. 2016;64:1772–87.
14. Sanz JM, Chiozzi P, Ferrari D, Colaianna M, Idzko M, Falzoni S, et al. Activation of microglia by amyloid β requires P2X 7 receptor expression. J Immunol. 2009;182(7):4378–85.
15. Helmut K, Hanisch UK, Noda M, Verkhratsky A. Physiology of microglia. Physiol Rev. 2011;91(2):461–553.
16. Maeda J, Minamihisamatsu T, Shimojo M, Zhou X, Ono M, Matsuba Y, et al. Distinct microglial response against Alzheimer's amyloid and tau pathologies characterized by P2Y12 receptor. Brain Commun. 2021;3(1):fcab011.
17. Narayanaswami V, Dahl K, Bernard-Gauthier V, Josephson L, Cumming P, Vasdev N. Emerging PET radiotracers and targets for imaging of neuroinflammation in neurodegenerative diseases: outlook beyond TSPO. Mol Imaging. 2018;17:1–25.
18. Janssen B, Vugts DJ, Windhorst AD, Mach RH. PET imaging of microglial activation—beyond targeting TSPO. Molecules. 2018;23:607.
19. Zarrinmayeh H, Territo PR. Purinergic receptors of the central nervous system: biology, PET ligands, and their applications. Mol Imaging. 2020. https://doi.org/10.1177/1536012120927609.
20. Van Weehaeghe D, Koole M, Schmidt ME, Deman S, Jacobs AH, Souche E, et al. [^{11}C]JNJ54173717, a novel P2X7 receptor radioligand as marker for neuroinflammation: human biodistribution, dosimetry, brain kinetic modelling and quantification of brain P2X7 receptors in patients with Parkinson's disease and healthy volunteers. Eur J Nucl Med Mol Imaging. 2019;46(10):2051–64.
21. Koole M, Schmidt ME, Hijzen A, Ravenstijn P, Vandermeulen C, Van Weehaeghe D, et al. ^{18}F-JNJ-64413739, a novel PET ligand for the P2X7 ion channel: radiation dosimetry, kinetic modeling, test-retest variability, and occupancy of the P2X7 antagonist JNJ-54175446. J Nucl Med. 2019;60(5):683–90.
22. Janssen B, Vugts DJ, Wilkinson SM, Ory D, Chalon S, Hoozemans JJM, et al. Identification of the allosteric P2X7 receptor antagonist [^{11}C]SMW139 as a PET tracer of microglial activation. Sci Rep. 2018;8(1):6580.
23. Hagens MHJ, Golla SSV, Janssen B, Vugts DJ, Beaino W, Windhorst AD, et al. The P2X7 receptor tracer [^{11}C]SMW139 as an in vivo marker of neuroinflammation in multiple sclerosis: a first-in man study. Eur J Nucl Med Mol Imaging. 2020;47(2):379–89.
24. Beaino W, Janssen B, Kooijman E, Vos R, Schuit RC, O'Brien-Brown J, et al. PET imaging of P2X7R in the experimental autoimmune encephalomyelitis model of multiple sclerosis using [^{11}C]SMW139. J Neuroinflamm. 2020;17(1):300.
25. Wilkinson SM, Barron ML, O'Brien-Brown J, Janssen B, Stokes L, Werry EL, et al. Pharmacological evaluation of novel bioisosteres of an adamantanyl benzamide P2X7 receptor antagonist. ACS Chem Neurosci. 2017;8(11):2374–80.
26. Takkinen JS, López-Picón FR, Al Majidi R, Eskola O, Krzyczmonik A, Keller T, et al. Brain energy metabolism and neuroinflammation in ageing APP/PS1-21 mice using longitudinal ^{18}F-FDG and ^{18}F-DPA-714 PET imaging. J Cereb Blood Flow Metab. 2017;37(8):2870–82.
27. López-Picón FR, Keller T, Bocancea D, Helin JS, Krzyczmonik A, Helin S, et al. Direct Comparison of [^{18}F]F-DPA with [^{18}F]DPA-714 and [^{11}C]PBR28 for neuroinflammation imaging in the same Alzheimer's disease model mice and healthy controls. Mol Imaging Biol. 2021;24:1–10.
28. Alzghool OM, Rokka J, López-Picón FR, Snellman A, Helin JS, Okamura N, et al. (*S*)-[^{18}F]THK5117 brain uptake is associated with Aβ plaques and MAO-B enzyme in a mouse model of Alzheimer's disease. Neuropharmacology. 2021;196: 108676.
29. Radde R, Bolmont T, Kaeser SA, Coomaraswamy J, Lindau D, Stoltze L, et al. Aβ42-driven cerebral amyloidosis in transgenic mice reveals early and robust pathology. EMBO Rep. 2006;7(9):940–6.
30. Keller T, López-Picón FR, Krzyczmonik A, Forsback S, Kirjavainen AK, Takkinen JS, et al. [^{18}F]F-DPA for the detection of activated microglia in a mouse model of Alzheimer's disease. Nucl Med Biol. 2018;67:1–9.
31. López-Picón FR, Keller T, Bocancea D, Helin JS, Krzyczmonik A, Helin S, et al. Direct comparison of [^{18}F]F-DPA with [^{18}F]DPA-714 and [^{11}C]PBR28 for neuroinflammation imaging in the same Alzheimer's disease model mice and healthy controls. Mol Imaging Biol. 2022;24(1):157–66.

32. Aarnio R, Alzghool OM, Wahlroos S, O'Brien-Brown J, Kassiou M, Solin O, et al. Novel plasma protein binding analysis method for a PET tracer and its radiometabolites: a case study with [^{11}C]SMW139 to explain the high uptake of radiometabolites in mouse brain. J Pharm Biomed Anal. 2022;219: 114860.
33. Keller T, Krzyczmonik A, Forsback S, Picón FRL, Kirjavainen AK, Takkinen J, et al. Radiosynthesis and preclinical evaluation of [^{18}F]F-DPA, a novel pyrazolo[1,5a]pyrimidine acetamide TSPO radioligand, in healthy sprague dawley rats. Mol Imaging Biol. 2017;19(5):736–45.
34. Percie du Sert N, Hurst V, Ahluwalia A, Alam S, Avey MT, Baker M, et al. The ARRIVE guidelines 2.0: updated guidelines for reporting animal research. Br J Pharmacol. 2020;177(16):3617–24.
35. Bankhead P, Loughrey MB, Fernández JA, Dombrowski Y, McArt DG, Dunne PD, et al. QuPath: open source software for digital pathology image analysis. Sci Rep. 2017;7(1):1–7.
36. Wang CY, Yeh IH, Liao HYM. You only learn one representation: unified network for multiple tasks. 2021. Available from: https://arxiv.org/abs/2105.04206v1.
37. López-Picón FR, Snellman A, Eskola O, Helin S, Solin O, Haaparanta-Solin M, et al. Neuroinflammation appears early on PET imaging and then plateaus in a mouse model of Alzheimer disease. J Nucl Med. 2018;59(3):509–15.
38. Beaino W, Janssen B, Kooij G, van der Pol SMA, van Het Hof B, van Horssen J, et al. Purinergic receptors P2Y12R and P2X7R: potential targets for PET imaging of microglia phenotypes in multiple sclerosis. J Neuroinflamm. 2017;14(1):259.
39. Nutma E, Fancy N, Weinert M, Tsartsalis S, Marzin MC, Muirhead RCJ, et al. Translocator protein is a marker of activated microglia in rodent models but not human neurodegenerative diseases. Nat Commun. 2023;14(1):1–25.
40. Nutma E, Gebro E, Marzin MC, van der Valk P, Matthews PM, Owen DR, et al. Activated microglia do not increase 18 kDa translocator protein (TSPO) expression in the multiple sclerosis brain. Glia. 2021;69(10):2447–58.
41. Nutma E, Stephenson JA, Gorter RP, De Bruin J, Boucherie DM, Donat CK, et al. A quantitative neuropathological assessment of translocator protein expression in multiple sclerosis. Brain. 2019;142(11):3440–55.
42. Brumberg J, Aarnio R, Forsberg A, Marjamäki P, Kerstens V, Moein MM, et al. Quantification of the purinergic P2X 7 receptor with [^{11}C]SMW139 improves through correction for brain-penetrating radiometabolites. J Cereb Blood Flow Metab. 2022;43:258–68.

Publisher's Note

Glial reactivity in a mouse model of beta-amyloid deposition assessed by PET imaging of P2X7 receptor and TSPO using [^{11}C]SMW139 and [^{18}F]F-DPA

Obada M. Alzghool[1,2,3*], Richard Aarnio[1,2,3], Jatta S. Helin[1,2], Saara Wahlroos[1], Thomas Keller[1], Markus Matilainen[1], Junel Solis[4], Jonathan J. Danon[5], Michael Kassiou[5], Anniina Snellman[1], Olof Solin[1,6,7], Juha O. Rinne[1] and Merja Haaparanta-Solin[1,2]

[1]Turku PET Centre, University of Turku, Kiinamyllynkatu 4-8, FI-20520 Turku, Finland

[2]Medicity Research Laboratory, University of Turku, Tykistökatu 6 A, FI-20520 Turku, Finland

[3]Drug Research Doctoral Programme, University of Turku, Turku, Finland

[4]Turku BioImaging, Åbo Akademi University and University of Turku, Turku, Finland

[5]School of Chemistry, The University of Sydney, Sydney, NSW 2006, Australia

[6]Department of Chemistry, University of Turku, Henrikinkatu 2, FI-20500 Turku, Finland

[7]Accelerator Laboratory, Turku PET Centre, Åbo Akademi University, Kiinamyllynkatu 4-8, FI-20520 Turku, Finland

Corresponding author: Obada M. Alzghool, Turku PET Centre, University of Turku, Tykistökatu 6 A, 4th floor, FI-20520, Turku, Finland, obalzg@utu.fi

Supplementary methods

Immunohistochemical staining

Table S1. Immunohistochemical staining protocol for P2X7, TSPO and P2Y12 receptors using 20-µm fresh-frozen non-fixed mouse brain sections. The washing buffer was Tris-HCl 0.05 M, pH 7.6 (Reagena 112270) with 0.05% Tween 20 detergent. All incubations were done at room temperature (RT).

Step	Details		
1. Preparation	Let sections dry, 30 min, RT		
2. Fixation	Formalin incubation, 10 min, RT		
3. Washing	Washing buffer, 2x3 min		
4. Antigen retrieval	Citrate buffer (pH 6) incubation, pre-heated to boil, 20 min, RT		
5. Washing	Washing buffer, 2x3 min		
6. Endogenous hydrogen peroxidase enzyme blocking	0.3% H_2O_2 in buffer, 10 min, RT		
7. Rinsing	Rinse slides in dH_2O		
8. Pre-protein blocking	Normal antibody diluent (WellMed BD09-125) incubation, 10 min, RT		
9. Primary antibody incubation in buffer	Anti-P2X7 (APR-008) 1:1000 60 min	Anti-P2Y12 (AS-55043A) 1:1000 60 min	Anti-PBR (EPR5384) 1:3000 60 min
10. Rinsing	Rinse slides in dH_2O		
11. Secondary antibody incubation	Goat anti-rabbit IgG HRP (WellMed DPVR110HRP), 30 min, RT		
12. Rinsing	Rinse slides in dH_2O		
13. Substrate	Substrate DAB (WellMed BS04-110) incubation, 10 min, RT		
14. Rinsing	Rinse slides in dH_2O		
15. Counter stain (if needed)	Mayers hematoxylin (histolab 01820), 1 min		
16. Rinsing	Rinse slides in dH_2O		
17. Dehydration and mounting	Alcohol series and mounting medium		

Quantification of P2X7 receptor staining using the artificial intelligence object detection algorithm You Only Learn One Representation (YOLOR) (1)

A dataset with a total of 1,765 images (each 800 x 800 pixels) was annotated for quantification, with a random split of 60%-20%-20%. This dataset was used to train a YOLOR model to detect P2X7-positive staining. Training was done using the PyTorch framework with an NVIDIA GeForce RTX 3070 graphics processing unit, batch size 20, input image sizes of 448 x 448 pixels, for 200 epochs. The trained model was used to identify spots of PX27-positive staining in the NC and THA images from both WT and TG animals. Python scripting was used to measure the ratio of P2X7-positive objects count to NC or THA area.

Source code for quantification of P2X7-positive staining: The image processing source code for the quantification of P2X7-positive staining is available via the following link: https://github.com/Turku-BioImaging/idt-p2x7-object-detection

Radiometabolite analysis

The radiometabolite analysis was initially performed using high-performance thin-layer chromatography (HPTLC), but the method was further improved during the study and later analysis performed using thin-layer chromatography (TLC). During the transition stage of the method change, the samples were run using both methods to validate that the parent fraction results were the same.

High-performance thin-layer chromatography (HPTLC): The obtained plasma was mixed with acetonitrile (plasma:acetonitrile 1:1.4 *v/v*) in an Eppendorf tube to precipitate the plasma proteins. The mixture was vortexed and centrifuged (12100 ×g, 90 s) to separate the protein-free supernatant, and 5-12 µL aliquots of the supernatant were placed on the HPTLC plate (HPTLC, silica gel 60 RP-18, art no. 1.05914.0001, Merck KGaA, Darmstadt, Germany).

A piece of mouse brain was cut and placed into a glass homogenizer and homogenized into the mobile phase. The volume of mobile phase used as solvent was kept as small as possible. The homogenate was centrifuged and aliquots of 8-20 µL were applied onto the same HPTLC plate as the standard and plasma. The application line was 1.5 cm from the bottom of the plate, and the migration distance was 4 cm. The plate was dried carefully on low heat and placed in an elution chamber (10 × 10 cm Twin Trough Chamber, Camag, Muttenz, Switzerland; 75:25:0.1 acetonitrile:water:trifluoroacetic acid (*v/v/v*) as the mobile phase; volume of mobile phase: 5 mL in each compartment). The migration time was 35-50 min.

Thin-layer chromatography (TLC): The TLC method was published previously (2). The main differences from the HPTLC method were that TLC (Silica gel 60 RP-18. art no. 1.05559.0001, Merck KGaA, Darmstadt, Germany) plates were used, the mobile phase was 65:35:0.1 acetonitrile:water:trifluoroacetic acid (*v/v/v*), and the plasma:acetonitrile ratio was 1:2 when precipitating the plasma proteins. The amount of plasma and brain samples applied was up to 16 µL. The migration time for 4 cm of travel was 6 min.

Common for both methods:

A radioactive standard of [^{11}C]SMW139 was prepared in the mobile phase. The radioactivity concentration was chosen so that it corresponded roughly to the radioactivity concentration of the plasma sample. The standard was placed on each plate on which samples were analyzed.

After the elution, the plates were dried carefully using the medium-heat setting and fixed in an autoradiography developing cassette and exposed to an erased autoradiography imaging plate (BAS-TR2025, Fuji Photo Film Co., Ltd., Tokyo, Japan) for approximately 1 hour. The autoradiography plate was digitalized using a phosphorimager (BAS-5000, Fuji Photo Film Co., Ltd., Tokyo, Japan) and analyzed using Aida Image Analyzer (v.4.22, Elysia-Raytest GmbH, Straubenhardt, Germany).

The parent fraction was analyzed as the photostimulated luminescence corresponding to the unchanged [^{11}C]SMW139 (identified by the radioactive standard) divided by the total photostimulated luminescence of the whole sample. Correction for background radioactivity was performed.

References

1. Wang C-Y, Yeh I-H, Liao H-YM. You Only Learn One Representation: Unified Network for Multiple Tasks. 2021 May 10 [cited 2022 Jun 28]; Available from: https://arxiv.org/abs/2105.04206v1

2. Aarnio R, Alzghool OM, Wahlroos S, O'Brien-Brown J, Kassiou M, Solin O, et al. Novel plasma protein binding analysis method for a PET tracer and its radiometabolites: A case study with [11C]SMW139 to explain the high uptake of radiometabolites in mouse brain. J Pharm Biomed Anal. 2022 Sep 20;219:114860.

Supplementary figures

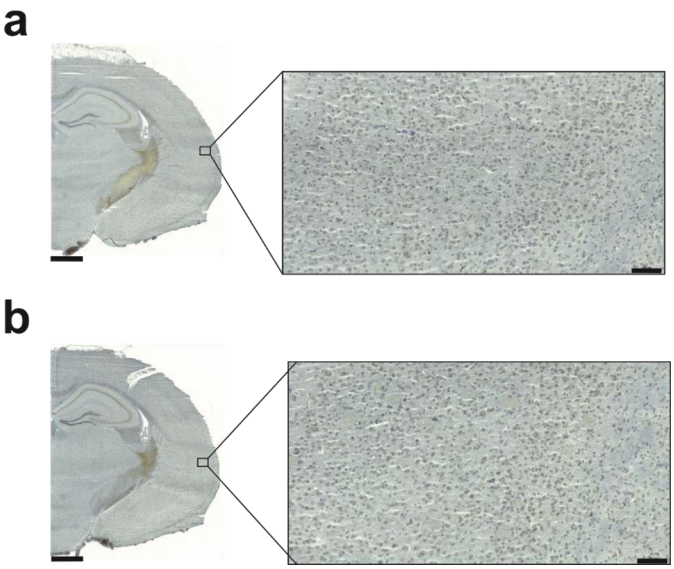

Fig S1. Negative staining of P2X7 (A) and TSPO (B) receptors in TG mouse 10 months old by omitting the primary antibody confirms antibody specificity. Scale bar = 1000 µm for the half hemisphere brain section image, 100 µm for the cortex view image. Magnification = 1.5x for the half hemisphere brain section image, 15.0x for the cortex view image.

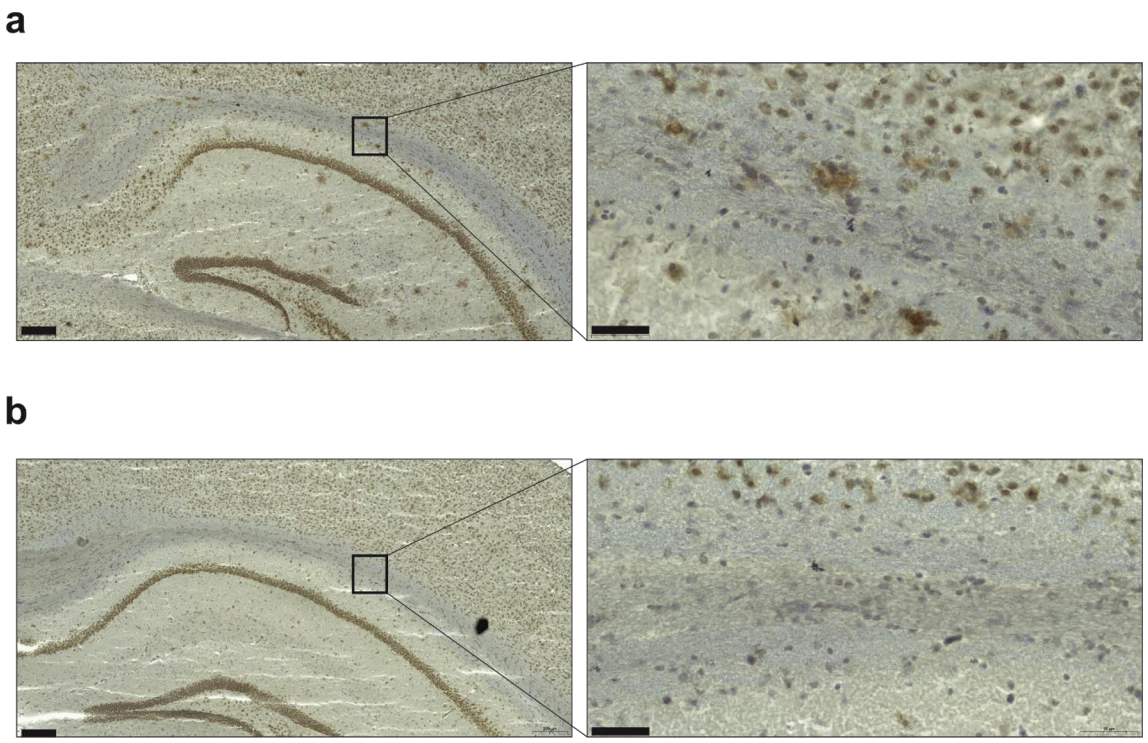

Fig S2. Representative images of P2X7 receptor positive staining detectable in the white matter corpus callosum of TG (A) but not WT (B) mouse at 14 mo. Scale bar = 200 µm for the half hemisphere brain section image, 50 µm for the corpus callosum view image.

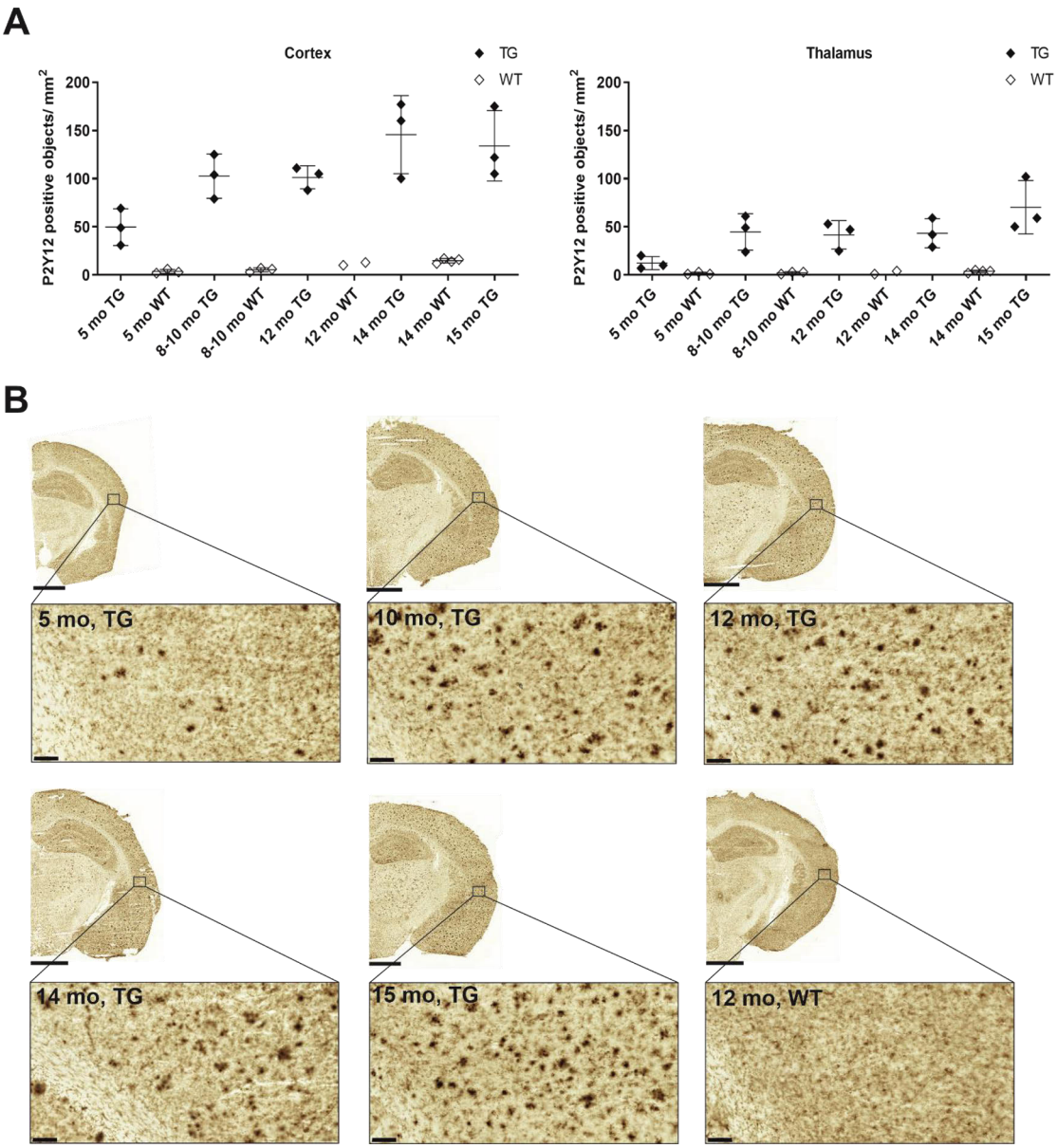

Fig S3. Immunohistochemical staining of P2Y12 receptor in brain cryosections of APPPS1-21 transgenic (TG) and wild-type (WT) mice. (A) Quantification of P2Y12-positive staining as object counts/mm^2. Staining was evaluated in the cortex and thalamus of TG and WT mice at 5, 8-10, 12, 14, and 15 months. Error bars indicate standard deviation. (B) Representative images of P2Y12-positive staining in TG mice at 5, 10, 12, 14 and 15 mo, and WT mice at 12 mo. Scale bar = 1000 µm for the half hemisphere brain section image, 100 µm for the cortex view image. Magnification = 1.5x for the half hemisphere brain section image, 15.0x for the cortex view image.

Aarnio, R., Alzghool, OM., Wahlroos, S., O'Brien-Brown, J., Kassiou, M., Solin, O., Rinne, JO., Forsback, S., & Haaparanta-Solin, M. (2022) Novel plasma protein binding analysis method for a PET tracer and its radiometabolites: A case study with [^{11}C]SMW139 to explain the high uptake of radiometabolites in mouse brain.
Journal of Pharmaceutical and Biomedical Analysis

II

Journal of Pharmaceutical and Biomedical Analysis 219 (2022) 114860

Contents lists available at ScienceDirect

Journal of Pharmaceutical and Biomedical Analysis

journal homepage: www.journals.elsevier.com/journal-of-pharmaceutical-and-biomedical-analysis

Novel plasma protein binding analysis method for a PET tracer and its radiometabolites: A case study with [^{11}C]SMW139 to explain the high uptake of radiometabolites in mouse brain

Richard Aarnio [a,b,c], Obada M. Alzghool [a,b], Saara Wahlroos [c], James O'Brien-Brown [d], Michael Kassiou [d], Olof Solin [c,e,f], Juha O. Rinne [c,g], Sarita Forsback [c], Merja Haaparanta-Solin [a,*]

[a] MediCity Research Laboratory, University of Turku, Tykistökatu 6A, FI-20520 Turku, Finland
[b] Drug Research Doctoral Programme, University of Turku, Turku, Finland
[c] Turku PET Centre, University of Turku, Kiinamyllynkatu 4-8, FI-20520 Turku, Finland
[d] School of Chemistry, The University of Sydney, Sydney, NSW 2006, Australia
[e] Department of Chemistry, University of Turku, Henrikinkatu 2, FI-20500 Turku, Finland
[f] Accelerator Laboratory, Turku PET Centre, Åbo Akademi University, Kiinamyllynkatu 4-8, FI-20520 Turku, Finland
[g] Division of Clinical Neurosciences, Turku University Hospital, Turku, Finland

ARTICLE INFO

Keywords:
Plasma protein binding
Ultrafiltration
RadioTLC
[^{11}C]SMW139
Radiometabolite analysis
Parent fraction
Positron emission tomography

ABSTRACT

Radiometabolites of PET tracers interfere with imaging and need to be taken into account when modeling PET data. Various tracer and radiometabolite characteristics affect the uptake rate into tissue. In this study, we investigated two such factors, lipophilicity and protein-free fraction. A novel rapid method was developed using thin-layer chromatography with digital autoradiography (radioTLC) and ultrafiltration for analyzing the protein-free fractions of an exemplar PET tracer, [^{11}C]SMW139 (f_P, free parent tracer over all radioactivity), and its radiometabolites (f_M, free radiometabolites over all radioactivity). Detailed understanding of the uptake of radiometabolites into extravascular cells requires analyzing f_M, which has not previously been performed for PET tracers. Mice were injected with [^{11}C]SMW139, and time-activity curves from plasma and brain coupled with the parent fraction and free fraction data were analyzed to demonstrate the true levels of protein-free and protein-bound [^{11}C]SMW139 and its radiometabolites in plasma. The ultrafiltration method included separate membrane correction factors for the parent tracer and its radiometabolites for analysis of unbiased f_P and f_M. Metabolism of [^{11}C]SMW139 was rapid, and after 45 min, the parent fraction was 0.33 in plasma and 0.28 in brain. Ultrafiltration membrane correction had a significant effect on the f_P but not the f_M. From 10–45 min, the f_P decreased from 0.032 to 0.007, while f_M remained between 0.52 and 0.35. The much higher f_M in plasma could explain why the less lipophilic radiometabolites enter the brain efficiently. This detailed understanding of f_P and f_M from rodents can be used in translational studies to explain the behavior of the tracer in humans. Similar parent fraction and plasma protein binding methods can be used for human *in vivo* analysis.

1. Introduction

Positron emission tomography (PET) is a medical imaging technique for the quantitative measurement of metabolic processes *in vivo* by means of a PET tracer. Neuroimaging is one field where the non-invasiveness of PET is valuable. For intravenous use in neuroimaging, the PET tracer needs to have specific characteristics, including the ability to cross the blood–brain barrier (BBB) and bind with high specificity to the desired target in the brain [1]. The pharmacokinetics of the tracer must be well understood for PET data to be interpreted correctly. Therefore, in this study, we aimed to develop methods to study some of the key properties of tracers and to explain what underlies their distribution, metabolism, and excretion characteristics.

An analyte's lipophilicity, for example, is an important determinant of its ability to cross the BBB. The increased lipophilicity affects the crossing of the BBB by two mechanisms: aiding it by improving the solubility into the lipid bilayer of the endothelial cell membrane [2] and by hampering it by increasing the protein-bound fraction. A previous

* Correspondence to: Turku PET Centre, University of Turku, Tykistökatu 6A, 4th floor, FI-20520 Turku, Finland.
E-mail address: mehaaso@utu.fi (M. Haaparanta-Solin).

https://doi.org/10.1016/j.jpba.2022.114860
Received 9 December 2021; Received in revised form 20 May 2022; Accepted 25 May 2022
Available online 28 May 2022

study by Zoghbi et al. has shown the correlation between the lipophilicity of tracers and the parent free fraction (*i.e.*, free parent tracer over all radioactivity in plasma, f_P), indicating that the high lipophilicity correlates with low f_P [3]. However, how the body metabolizes the parent tracer generally reduces its lipophilicity, as in glucuronidation, which aids renal excretion but yields metabolites with increased hydrophilicity and lower BBB-penetrating abilities. Also, to effectively cross the BBB, the analyte must be free, *i.e.*, not bound to proteins in the vascular system [1,4,5], making studies of the free fraction crucial for determining the true input of the parent tracer and its radiometabolites. Other tracer characteristics also affect BBB penetration, but here we focused on the protein-free fraction and lipophilicity characteristics.

The uptake of radiometabolites in the target organ often disturbs the analysis of the uptake and specific binding of the original PET tracer, hampering analysis of the PET data. PET detects the signal originating from the annihilation of any positron, so it cannot distinguish whether the signal originates from the parent tracer or its radiometabolites. For this reason, investigating the radiometabolism of tracers reveals the true parent concentration in the target organ. Combining this information with knowledge of the tracer protein binding and its radiometabolites can yield the correct input to extravascular tissue during a PET study.

To our knowledge, the plasma protein binding of radiometabolites has not been previously analyzed separately from the parent tracer. Robust and rapid methods to separate the protein-free and protein-bound parent tracer and radiometabolites from each other need to be developed to quantify the f_P and separately the free fraction of radiometabolites in plasma (free radiometabolites over all radioactivity in plasma, f_M). The novel method introduced here combines a new rapid and robust radiometabolite analysis method using thin-layer chromatography combined with digital autoradiography (radioTLC) for parent fraction analysis and an ultrafiltration (UF) method to analyze the f_P and f_M. In addition, filter membrane correction factors are determined separately for parent tracer and its radiometabolites that take into account the various sources of error, such as nonspecific binding to the UF device and different mobilities through the semipermeable membrane of plasma water and analytes from the same plasma matrix. These factors are commonly acknowledged sources of error in a UF method and various ways to overcome these effects have been introduced [6,7]. However, the applied correction methods (*i.e.*, pretreatment) to minimize nonspecific binding often may introduce other error sources. Many other methods to analyze the f_P have been developed [8]. Further development and comparison of these methods is important for standardization and to make best practices widely available.

The $P2X_7$ receptor antagonist 2-chloro-5-[^{11}C]methoxy-N-((3,5,7-trifluoroadamantan-1-yl)methyl)benzamide ([^{11}C]SMW139) (Fig. 1) is a novel tracer for imaging the $P2X_7$ receptor [9,10]. In the brain, $P2X_7$ receptor is predominantly expressed in microglia and is involved in mediating neuroinflammation [11,12]. Hence, [^{11}C]SMW139 holds broad potential for use in detecting and quantitating neuroinflammation in several neurodegenerative conditions, including Alzheimer's disease, Parkinson's disease, and multiple sclerosis [13,14]. The first radiometabolite study of [^{11}C]SMW139 used a high-performance liquid chromatography system combined with a radiodetector (radioHPLC) method to analyze the parent fraction in rat plasma and brain tissue [9]. Janssen et al. have shown that radiometabolites of [^{11}C]SMW139 are found in large concentrations in rat brain tissue even though less lipophilic radiometabolites in general have worse BBB-penetrating abilities compared to the more lipophilic parent tracer, raising the question of why they enter the brain so effectively. Answering this question requires studying the free fractions in more detail.

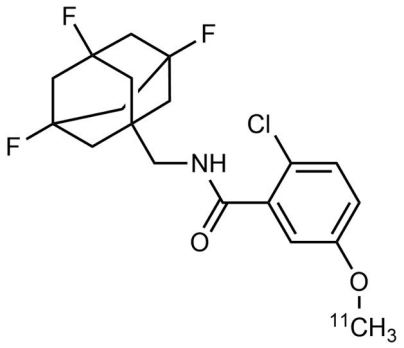

Fig. 1. Chemical structure of [^{11}C]SMW139.

In this study, *in vitro* mouse brain homogenate studies were performed to address whether the radiometabolites actually penetrate the BBB or are formed in the brain after penetration of the parent tracer. In addition, time-activity curves (TACs) of plasma and brain were analyzed from a large number of mice injected with [^{11}C]SMW139 to demonstrate the difference in the free fraction–corrected concentrations of the parent tracer and its radiometabolites.

Here, we introduce a novel method to determine the f_P of the parent tracer [^{11}C]SMW139 and f_M in mouse plasma. This work adds a more detailed understanding of the pharmacokinetic properties and aids in modeling the uptake of [^{11}C]SMW139 into organs. By studying the f_M and comparing it with the f_P, we can also partly explain why a less lipophilic tracer enters the brain so efficiently.

2. Material and methods

2.1. Radiochemistry

[^{11}C]SMW139 was synthesized at the Radiopharmaceutical Chemistry Laboratory of Turku PET Centre (for the synthesis procedure, see supplementary materials). A total of 27 syntheses were used for the animals in this study. At the end of synthesis, the radiochemical purity was 98.3 ± 0.5 %, and the molar activity was 110 ± 49 GBq/μmol. All work with radioactivity was performed following the regulations from the Finnish Radiation and Nuclear Safety Authority.

2.2. Experimental animals and chemicals

This study was performed in accordance with the EU Directive 2010/63/EU on the protection of animals used for scientific purposes, and in keeping with the ARRIVE guidelines. All animal procedures were approved by the Regional State Administrative Agency for Southern Finland (license number ESAVI/16273/2019).

Three to four mice were group-housed in individually ventilated cages with the following standard conditions: temperature 21 ± 1.2 °C, humidity 55 % ± 5 %, and a 12-h light/dark cycle. Soy-free chow (RM3 (E) Soya Free, 801710, Special Diets Service, Essex, UK) and tap water were provided *ad libitum*.

For this study, 73 C57BL/6 J (43 females and 30 males; 31.7 ± 5.5 g) mice were bred and maintained according to the guidelines of the International Council of Laboratory Animal Science (ICLAS) in the Central Animal Laboratory of University of Turku. Animal studies were performed in accordance with the European Ethics Committee (decree 86/609/CEE). The mice were injected with [^{11}C]SMW139 (14.5 ± 5.8 MBq; molar activity at the time of injection, 37 ± 27 GBq/μmol; injected mass per body weight, 8.3 ± 6.9 μg/kg). All of the chemicals for the preclinical experiments were HPLC-grade and obtained from Sigma-Aldrich.

2.3. Collection of mouse plasma and brain samples and radioactivity measurements

Blood samples (200–500 μL) were collected under deep isoflurane anesthesia by cardiac puncture into heparinized gel tubes (Microtainer,

Becton, Dickinson and Company, Franklin Lakes, NJ). Transcardial perfusion with saline was conducted to eliminate the blood from the brain. The blood was centrifuged (12,100 ×*g*, 90 s) to separate the plasma so that the TAC of plasma could be determined as percentage of injected radioactivity per gram of tissue (%IA/g) at 10-min (n = 45), 30-min (n = 14), and 45-min (n = 7) time points post radiotracer injection (p.i.). This step was accomplished by using a cross-calibrated automated gamma counter (Wizard^2 2480 3", PerkinElmer, Turku, Finland) to measure the decay-corrected radioactivity of the plasma and brain.

2.4. Parent fraction analysis of plasma and brain samples

For chromatographic analyses, the plasma was pipetted into an Eppendorf tube and mixed with acetonitrile (plasma:acetonitrile 1:2 *v/v*) to precipitate the plasma proteins. The mixture was vortexed for approximately 10 s and centrifuged (12,100 × *g*, 90 s), and the supernatant was collected for radioTLC analysis.

The brain tissue was cut into pieces, and approximately one third of the brain was homogenized into the TLC mobile phase. The homogenate was centrifuged (12,100 × *g*, 90 s), and the clear supernatant was used for TLC analysis.

Various radioTLC methods were tested to find a fast and robust separation of the parent tracer and its radiometabolites and the following method parameter goals were used to guide the method selection process: a retardation factor (R_f) of 0.3–0.5 for the parent tracer with more polar radiometabolites eluting with R_f 0.6–0.9 was deemed optimal. A baseline separation with resolution above 1.5 was required between the parent tracer and its radiometabolites. In addition, efforts were made to optimize the separation of different radiometabolites, but separation of the parent tracer from all of the other radioactive components in the sample was prioritized. The following TLC-plate and TLC mobile phase combinations were tested: high-performance TLC (HPTLC, silica gel 60 RP-18, art no. 1.05914.0001, Merck KGaA, Darmstadt, Germany), TLC (Silica gel 60 RP-18. art no. 1.05559.0001, Merck KGaA), and HPTLC W (W = wettable, silica gel 60 RP-18 W, art no. 1.14296.0001, Merck KGaA) plates were examined with various acetonitrile, water, and trifluoroacetic acid compositions ranging from 60 % to 75 % organic and 0.1–0.4 % acid modifier compositions. The gas phase was allowed to saturate (>45 min) before the elution chamber was used (10 × 10 cm Twin Trough Chamber, Camag, Muttenz, Switzerland; volume of mobile phase: 15 mL).

The best method for a fast and robust separation of the parent tracer from its radiometabolites was selected and is described below. A [^{11}C]SMW139 standard (30 Bq/μL) was prepared in the TLC mobile phase. Standard (5 μL), plasma (10 μL), and brain (10 μL) supernatants (Fig. 2) were applied with a pipette onto the TLC plate (Silica gel 60 RP-18, art no. 1.05559.0001, Merck KGaA) and acetonitrile:water:trifluoroacetic acid (65:35:0:1 *v/v/v*) was used as the TLC mobile phase. The TLC plate was developed until the migration distance was 4 cm. Additional samples were applied to this same plate, as described in Section 2.6. The developed and dried plate was exposed to an erased autoradiography imaging plate (BAS-TR2025, Fuji Photo Film Co., Ltd., Tokyo, Japan) for approximately one hour to record the distribution of the separated radioactive compounds. The imaging plate then was scanned with a laser using a BAS-5000 phosphorimager (Fuji Photo Film Co., Ltd., Tokyo, Japan) and analyzed using an Aida Image Analyzer (v.4.22, Elysia-Raytest, GmbH, Straubenhardt, Germany). From the obtained chromatogram, the parent fraction was analyzed as the photostimulated luminescence (PSL) corresponding to the unchanged [^{11}C]SMW139 divided by the total PSL corresponding to the whole sample. Background radioactivity correction was performed on all autoradiography analyses.

The parent fraction was successfully analyzed with the selected method from the following numbers of mice: plasma, 10 min, n = 19; 30 min, n = 14; 45 min, n = 13; and brain: 10 min, n = 9; 30 min, n = 14; 45 min, n = 11.

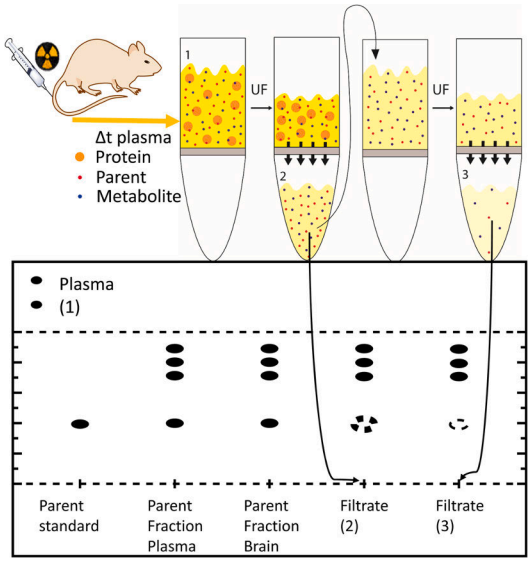

Fig. 2. Depicted design of plasma filtration procedures and [^{11}C]SMW139 standard, plasma, brain, and filtrate (1-3) sample application to TLC plate application line and simulation of the separation of the components in the sample in an autoradiograph of the developed TLC. Application line (lower) and solvent front line (upper) marked with dashed lines. Results are used to calculate the parent fraction in plasma and brain, and to calculate separately the parent and radiometabolite free fraction (f_P and f_M) and filter membrane correction factors.

2.5. Metabolite correlation in plasma and brain

To investigate the correlation between percentage of radiometabolites in plasma and brain, we plotted the percentages of radiometabolites over all radioactivity in plasma and brain from mice with successful parent fraction data for both (n = 47, including data from other tested radioTLC methods (*i.e.*, HPTLC-plate, not only the selected radioTLC method)). The slope, Pearson's correlation (r), and coefficient of determination (R^2) were calculated.

2.6. f_P and f_M in plasma and UF membrane correction

To determine the f_P and f_M, the radioactivity concentration of the *in vivo* plasma sample (c_{plasma}) was measured by applying a known volume of plasma(1) (3 μL) in duplicate on the top part of a TLC plate (Silica gel 60 RP-18, art no. 1.05559.0001, Merck KGaA) above the mobile phase front line (Fig. 2). Autoradiography was used to calculate the PSL/volume concentration. The plasma parent fraction analysis result was used to determine the concentrations of parent tracer (Eq. 1) and its radiometabolites (Eq. 2) in the plasma sample as follows:

$$c_{\text{plasma,parent}} = \text{parent } \textit{fraction} * c_{plasma} \quad (1)$$

$$c_{\text{plasma,metabolites}} = (1 - \text{parent fraction}) * c_{plasma} \quad (2)$$

To separate the protein-free [^{11}C]SMW139 and its protein-free radiometabolites from the protein-bound ones, we used a 10-kDa UF semipermeable membrane (Microcon-10 kDa Centrifugal Filter Unit with Ultracel-10 membrane, Merck KGaA). Roughly, a minimum of 80 μL of plasma was needed to carry out this analysis, including the membrane correction analysis. The plasma(1) was centrifuged (14,100 ×*g*, 7 min) to gain at least 40 μL of filtrate(2). The filtrate(2) was transferred into another identical UF device and centrifuged for

4 min to gain at least 15 μL of filtrate(3), while the original plasma(1) was simultaneously centrifuged further to collect more of the filtrate(2). A radioactive standard of the parent tracer, a plasma and a brain supernatant sample (as described in Section 2.4), filtrate(2) (10 μL), and filtrate(3) (10 μL) were applied onto the application line of the same TLC plate (Fig. 2). The dried plate was developed, digitized, and analyzed as described in Section 2.4.

To calculate the membrane correction factor for the parent tracer, the concentration (PSL/applied volume of sample) ratio of the parent tracer in filtrate(3) and filtrate(2) was calculated as follows:

$$Membrane \quad correction_{\text{parent}} = \frac{c_{parent \quad in \quad filtrate(3)}}{c_{parent \quad in \quad filtrate(2)}} \tag{7}$$

The parent concentration in filtrate(2) was divided by the membrane

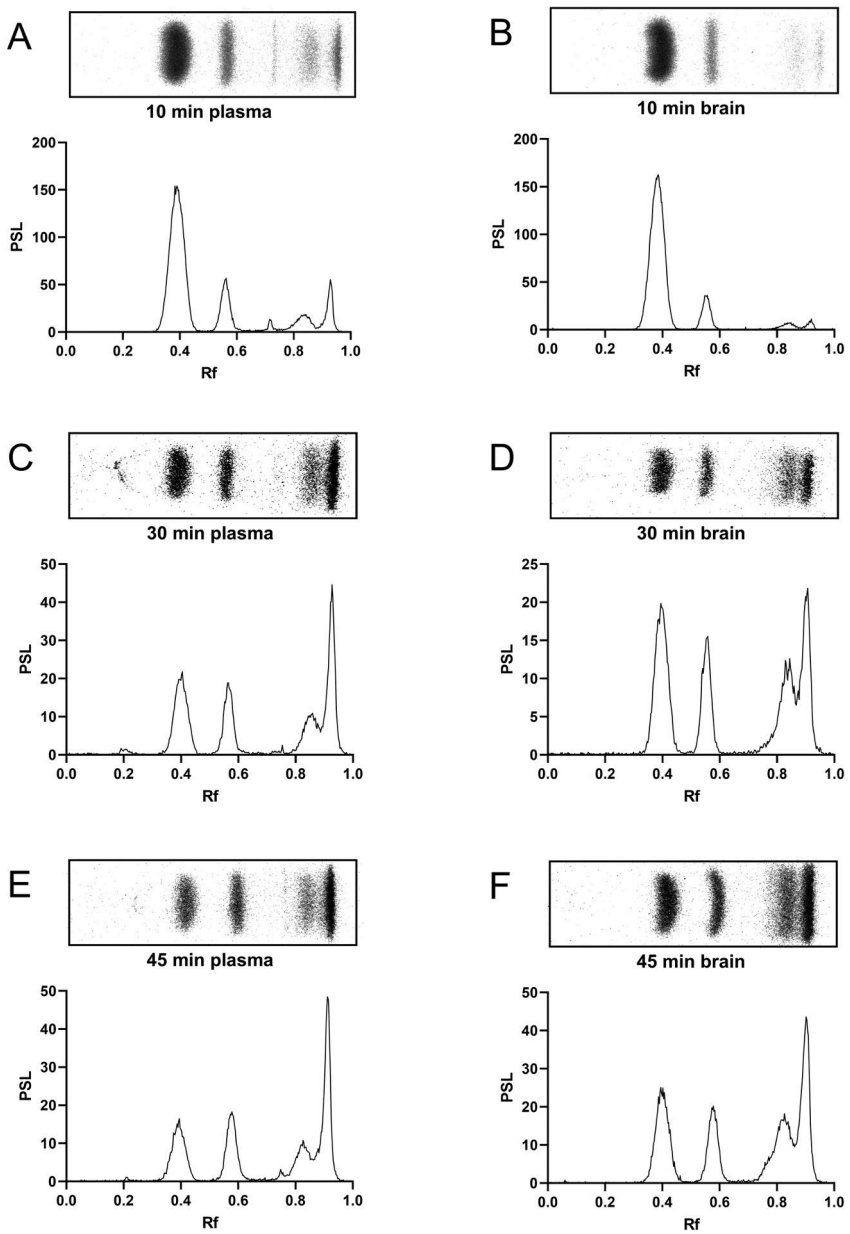

Fig. 3. Representative digital autoradiograph images and corresponding chromatograms of parent tracer and its radiometabolites for different time points. (A) 10 min plasma, (B) 10 min brain, (C) 30 min plasma, (D) 30 min brain, (E) 45 min plasma, and (F) 45 min brain. Standard sample confirmed that the R_f for the parent tracer is 0.4.

correction factor to calculate the true amount of the free parent in the filtrate(2) (as if the membrane would not have limited the amount of free parent passing through the membrane). The corrected free parent concentration in filtrate(2) was divided by the concentration of total radioactivity in plasma(1) to gain f_P. For the radiometabolites, the membrane correction factor and concentration in filtrate(2) was calculated likewise using the values for radiometabolites. The corrected, true concentration of radiometabolites in filtrate(2) was divided by the concentration of all radioactivity in plasma(1) to yield f_M.

2.7. In vitro mouse brain homogenate study

To determine whether radiometabolites can form directly in mouse brain *in vitro*, one mouse was euthanized under deep isoflurane anesthesia by cardiac puncture immediately followed by transcardial perfusion with saline. The freshly dissected mouse brain was homogenized (Ultra-Turrax T8, IKA, Staufen, Germany) in PBS solution (36 °C, 4 mL). A high radioactivity concentration was achieved by adding 1 MBq of [^{11}C]SMW139 to the mixture, followed by vortexing for 1 min at medium speed and then incubation (36 °C, 45 min). The mixture was shaken gently every 5 min. A sample of the incubated brain homogenate was taken at 10, 30, and 45 min. The samples were prepared and analyzed with radioTLC as described in Section 2.4. A sham sample without the brain homogenate was prepared and analyzed exactly as the brain sample with [^{11}C]SMW139. If radiometabolites were found to form in brain tissue *in vitro*, they were analyzed as a fraction of the total radioactivity of the sample.

2.8. Statistics

All results are reported as mean ± standard deviation (SD) where standard deviation could be calculated. The correlation (Section 3.4) was fitted with a simple linear regression, and the slope, r, and R^2 values were analyzed (GraphPad Prism 9, GraphPad Software, San Diego, CA).

3. Results and discussion

3.1. Method selection for analysis of [^{11}C]SMW139 and its radiometabolites

The selected radioTLC method fulfilled all of the requirements for a method with a short run time and high separation power. The mobile phase migration of 4 cm took only 6 min. The method exceeded the required resolution. In addition to separating the parent tracer from all of its radiometabolites, in most cases, the method managed to separate between two to four radiometabolites from each other with almost baseline separation (Fig. 3). Separating the radiometabolites from each other enables more comprehensive modeling if multiple radiometabolite compartments are needed.

Using radioTLC allows for simultaneous analysis of multiple samples with the benefit that samples analyzed on the same autoradiography imaging plate do not need to be decay corrected if only ratios are calculated. This approach is unlike radioHPLC, which involves relatively long run times and the need to run each sample separately, hindering sample throughput and effective use of expensive tracer batches when tracers are labeled with a short-lived radionuclide, such as carbon-11 ($T_{½}$ = 20.4 min). In addition, radioHPLC requires expensive equipment, more solvents, and individual decay correction of all peaks. On the other hand, radioHPLC has some advantages, including more versatile separation options because of, for example, gradient methods. A low radioactivity concentration and low volume samples necessitate extremely sensitive and linear-ranged radioactivity-detecting capabilities. These issues are not associated with the radioTLC method because quantitation of the radioactivity using digital autoradiography for the low radioactivity concentration samples is linear with a wide range of radioactivity [15].

For plasma sample preparation using protein precipitation, we chose the 1:2 ratio of plasma to acetonitrile to effectively precipitate as much as possible of plasma proteins without diluting the sample excessively so that the radioactivity concentration stayed as high as possible for optimal parent fraction quantification. Polson et al. demonstrated that this ratio of plasma and acetonitrile precipitates 96.4 % of the dissolved proteins [16]. Precipitation is intended to enable optimal chromatographic separation by reducing the matrix to prevent TLC plate overload. This effect facilitates absorption of the sample into the TLC plate before elution, as generally C-18–modified TLC plates do not absorb aqueous samples well. In addition, changing the conformation of the proteins with an organic solvent releases the binding between the analytes and proteins [16]. The addition of acetonitrile also increases the solubility of lipophilic analytes into the supernatant instead of their binding to the protein pellet. These effects maximize the radioactivity concentration in the supernatant by increasing the extraction efficiency, which aids parent fraction analysis by enhancing the signal-to-noise ratio and by including all components present in plasma to the analysis. This disruption is especially important as not only the f_P and f_M represent the true parent fraction value in plasma because the compounds also are largely bound to plasma proteins in different ratios and also that part needs to be included in the analysis. The extraction efficiency, *i.e.*, the percentage of radioactivity transferred to the supernatant from the plasma sample for the selected precipitation method was over 99 % for mouse plasma (n = 3). The residual radioactivity of the supernatant was taken into account and deducted from the protein pellet radioactivity.

3.2. TAC and parent fraction in plasma and brain

In this study, the radiometabolite analysis and total and metabolite-corrected TACs of plasma and brain showed that [^{11}C]SMW139 and its radiometabolites cross the BBB and enter the brain (Fig. 4), as previously reported [9]. From 10–45 min p.i., the volume of distribution of the brain (metabolite-corrected radioactivity of brain over metabolite-corrected radioactivity of plasma) decreased slightly from 0.79 to 0.58. The equilibrium value of the volume of distribution was set by 30 min. The metabolite-corrected TACs (Fig. 4) showed a rather steady washout in plasma and brain. A rapid uptake into the target tissue and a steady washout are generally good receptor- or transporter-binding radiotracer characteristics.

The average radiochemical purity of [^{11}C]SMW139 was used as the maximum parent fraction value (0.98). The parent fraction decreased from 0.71 to 0.33 in plasma and from 0.79 to 0.28 in the brain at 10 and 45 min p.i., respectively (Fig. 4). This decrease was more rapid than that seen in humans (data not shown), but the results are similar to those using other separation methods in rats [9].

3.3. Parent and metabolite free fraction in plasma (f_P and f_M)

3.3.1. Membrane correction

To gain unbiased free fraction data, we determined membrane correction values for the Microcon Ultracel UF device individually for the parent tracer and its radiometabolites to calculate the concentration of free parent tracer and radiometabolites in the plasma sample. The membrane correction value for the radiometabolites was 0.93 ± 0.04 (n = 9), indicating that the free radiometabolites passed through the filter membrane with almost no reduction in concentration. However, the concentration of the free parent tracer after filtration was reduced to 0.63 ± 0.07 (n = 9) compared to the concentration prior to filtration. Thus, the correction of this phenomenon was much more significant for the parent tracer than for the radiometabolites. As the f_P was corrected, the value increased by 59 %.

Because of the low f_P of [^{11}C]SMW139, the radioactivity concentration of the parent tracer in the filtrates was also low, which occasionally led to unanalyzable membrane correction values because of

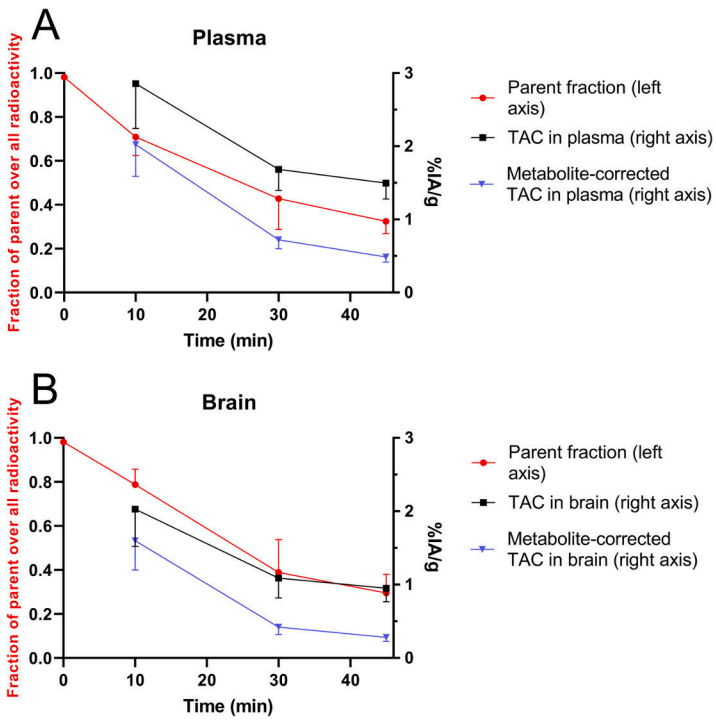

Fig. 4. Parent fraction (red, left y-axis) in plasma (A) and brain (B) as mean and standard deviation of mean. Time-activity curves (TACs, right y-axis) expressing uptake in plasma (A) and brain (B). At the 10-min, 30-min, and 45-min time points, respectively: parent fraction, plasma: n = 19, 14, 13; brain: n = 9, 14, 11; TAC, plasma and brain: n = 45, 14, 7.

insufficient signal-to-noise ratio of the peak corresponding to the parent tracer. In these few cases, we used the mean from the successfully analyzed membrane correction values, which caused only slight inaccuracies because the SD of the membrane filter correction value was minor (Table 1).

3.3.2. f_P and f_M

The f_P was clearly time-dependent (Fig. 5, Table 1). This dependence might have been the result of parent clearance from plasma and freeing of more proteins to bind the remaining analytes at the later time points as the parent-to-protein ratio decreased. Similar explanations have been presented previously [17].

The parent fraction in plasma is presented along with the results for f_P and f_M (Table 1). In addition, the free parent divided by all free radioactivity was calculated to yield the true ratio of parent tracer and radiometabolite concentrations which are free to cross the BBB. The amount of free parent decreased rapidly throughout the studied time points, while the amount of free metabolites remained rather constant (Fig. 6). From 10–45 min, the fraction of free parent relative to all free radioactivity decreased rapidly from 0.085 to 0.019, indicating that most of the protein-free fraction consisted of radiometabolites during these time points. The f_P was low, decreasing from 0.032 to 0.007 from 10 min to 45 min, while f_M remained at much higher levels, between 0.52 and 0.35, during the same time points. A protein-bound fraction acts as a reservoir, stabilizing the concentrations of free analytes [18]. For example, to maintain dynamic equilibrium, part of the parent tracer will be released from the plasma proteins when part of the free parent is diffused out from plasma.

Small size, low molecular weight, un-ionized charge, and low hydrogen bonding potential are other characteristics of a molecule that further favors BBB penetration [19] and should be taken into account, if possible. The radiometabolites of [^{11}C]SMW139 have not been

Table 1
Mean (*M*) and standard deviation of the mean (*SD*) for plasma parent fraction and parent and radiometabolite (metab) free fractions (f_P and f_M). Measured from the same mice. At the 10-min, 30-min, 38-min, and 45-min time points, respectively: n = 3, 4, 2, 4.

	Time point (min)	Plasma parent fraction	f_P, free parent/ all radio- activity	Free parent/ all parent	f_M, free metab/ all radio- activity	Free metab/ all metab	Free parent/ all free radio- activity	Free radio-activity/ all radio- activity
M	10	0.567	0.032	0.057	0.368	0.835	0.085	0.399
SD		0.098	0.000	0.009	0.113	0.119	0.019	0.113
M	30	0.347	0.012	0.034	0.508	0.760	0.023	0.520
SD		0.077	0.005	0.007	0.083	0.092	0.011	0.081
M	38	0.336	0.010	0.031	0.520	0.778	0.019	0.530
SD		0.050	0.001	0.008	0.076	0.056	0.000	0.077
M	45	0.323	0.007	0.021	0.350	0.518	0.019	0.356
SD		0.043	0.002	0.006	0.017	0.035	0.006	0.019

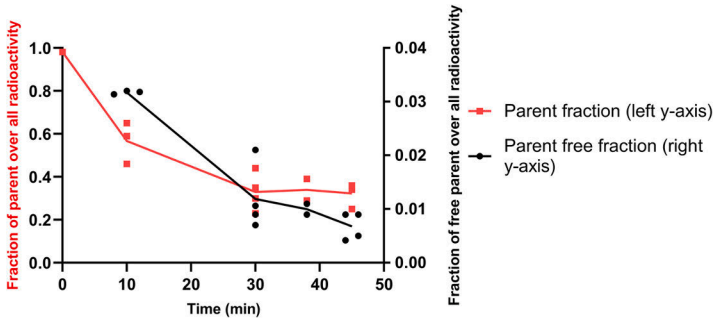

Fig. 5. Parent fraction in plasma (protein-bound + free parent tracer over all ^{11}C-radioactivity in sample, left axis) and free parent fraction, (f_P, free parent over all ^{11}C-radioactivity in sample, right axis) as analyzed from the same mice. Individual values are plotted to show the low variation and correlation of curves. At the 10-min, 30-min, 38-min, and 45-min time points, respectively: n = 3, 4, 2, 4.

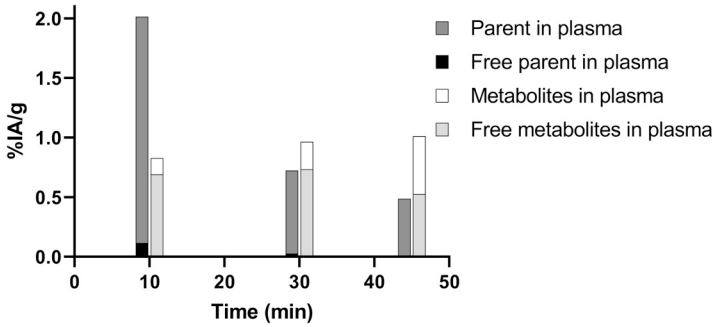

Fig. 6. Total percentage of injected activity/g of plasma (%IA/g) of parent, free parent, total metabolites, and free metabolites in plasma as a time-activity bar chart. %IA/g were analyzed at the 10-min, 30-min, and 45-min time points from n = 45, 14, and 7, respectively. Free fractions were analyzed at the 10-min, 30-min, and 45-min time points from n = 3, 4, and 4, respectively.

identified at the molecular structure level, so we cannot say if the parent tracer is catabolized into smaller molecules or has a larger molecule size and hydrophilicity, for example, because of glucuronidation. In this study, we can only evaluate the lipophilicity (based on the TLC R_f) and free fractions to understand BBB penetration abilities. As the R_f was higher in reversed-phase separation, the radiometabolites were more polar and therefore less lipophilic, so their ability to cross the lipophilic BBB would have been compromised compared to the parent tracer. However, the lipophilicities of the radiometabolites are nevertheless sufficient enough to enable the BBB penetration. The CLogP = 2.90 (Chemdraw Professional 19, PerkinElmer Informatics, Inc.) of [^{11}C]SMW139 is considered to be moderate for crossing the BBB, and the molecular weight of 386.8 g/mol is also acceptable for crossing the BBB [1]. The much higher f_M compared to f_P in plasma at least partly explains why the less lipophilic radiometabolites of [^{11}C]SMW139 accumulate efficiently in the brain.

3.3.3. UF

The Microcon UF device was selected because of the Ultracel low-binding regenerated cellulose membrane and suitability for low-volume samples. A cutoff value of 10 kDa was used, contrary to the 30-kDa cutoff value commonly used in previously published UF methods in protein binding studies [8,20]. The 30-kDa cutoff does not guarantee 100 % protein-free filtrates, as stated in the manufacturer's Membrane Learning Centre, "For example, an UF membrane rated at 30 kDa will exclude a test protein with a molecular weight of 30 kDa. Ninety percent of that test protein will be retained on the upstream side and 10 % will pass through into the filtrate, resulting in concentration of the protein" [21]. Because we are interested in the protein-free filtrate and not the concentrated protein mass in the filter, we reduced the cutoff value to the smallest size generally available to limit possible error sources that could not be properly quantified. The increase in the spinning times was minor with the 10-kDa membrane. One of the main proteins that lipophilic drugs bind to in plasma is albumin (66.5 kDa). Other common proteins in mouse plasma are prealbumin, α1-acid glycoprotein, transferrin, lipoproteins, immunoglobulins, complement proteins, and coagulation proteins [22]. Because we do not know which proteins bind the parent tracer and its radiometabolites, it is rational to keep the cutoff as small as possible.

During UF, the temperature of the sample may slightly affect the equilibrium of the protein binding. The starting temperature here was room temperature, but it generally increases during UF. The optimal situation could be maintaining centrifugation temperature at 36 °C. Also, plasma pH was not adjusted during the study. However, adjustment would have affected the concentrations of the solutions, in turn influencing the delicate equilibrium between the protein-bound and unbound analytes. Our assumption was that introducing such sample preparation steps into the protocol would probably have entailed more harms than improvements to the accuracy of the data. Also, the repeatability could be hampered because it is often difficult to measure and adjust the pH of plasma samples < 100 μL. Toma et al. [23] addressed the effects of such factors recently.

3.3.4. Analyzing free fraction data

To our knowledge, previous studies with [^{11}C]SMW139 or with any other tracer have not analyzed or adequately addressed the importance of the f_M and their part in radioactivity uptake into tissues. Being able to analyze the f_M will increase understanding of the pharmacokinetics of the tracer, which is important when assessing the modeling, usability, and safety of a tracer for new applications. Previous plasma free fraction methods have mostly used plasma samples spiked with high levels of the parent tracer. Such methods are less complex and can use larger radioactivity concentrations. However, *in vitro* methods might not fully represent the delicate dynamic equilibrium present *in vivo*, which also includes free and protein-bound radiometabolites and the parent tracer in low trace-level concentrations. More studies to compare these methods should be performed.

There are several methods to analyze the f_P in drug research. One of the most prevalent has been equilibrium dialysis (ED). ED also has been used for protein binding studies involving PET tracers, but only with *in vitro* samples. The slowness of ED limits its wider use for short-lived PET tracers. Also, ED is not suitable for traditional *in vivo* sample PET studies where the administered tracer amount and especially the amount of radiolabeled free parent tracer and radiometabolites are really low (in the magnitude of pmol/mL in plasma) and the half-life of the radionuclide is short, as with carbon-11 tracers [8,24].

3.3.5. RadioTLC for rapid and simultaneous data collection of many samples at the same time

The time from plasma separation to placing the developed TLC plate with the standard, plasma, brain supernatant, and filtrates into the exposure cassette can be as low as 12 min. Several samples from multiple subjects can be applied to this same plate and analyzed simultaneously, which is a tremendous advantage. Multiple plates also can be developed at the same time. This is a method of choice particularly when short-lived radionuclides are used. The technique developed in this study is rapid and comparable in throughput speed to other fast protein binding analysis techniques, such as high-performance frontal analysis (<12 min per sample) [20].

3.4. Radiometabolite correlation between plasma and brain

The correlation between the percentages of radiometabolites over all radioactivity in plasma and brain correlated significantly (Pearson's, $r = 0.94$), with $R^2 = 0.89$ ($p < 0.001$) and slope = 1.2 (Fig. 7). The percentages of radiometabolites were initially lower in the brain compared to plasma. The percentages of radiometabolites must first rise in the plasma before they can start to accumulate in the brain. The ratio of the radiometabolite fractions rapidly became even between plasma and brain, but with the average slope of 1.2, the fraction of radiometabolites increased faster in the brain than in the plasma. Soon after, the percentages of radiometabolites in the brain exceeded the percentages found in plasma, indicating that the accumulation of radiometabolites through the BBB into the brain was efficient compared to accumulation of the parent tracer in all observed mice and time points. Generally, the metabolites, being less lipophilic, have a poorer ability to cross the BBB. The reason behind the observed correlation can be at least partly explained by the much higher f_M compared to f_P as only the free fraction can diffuse out of the blood vessels into the brain tissue [6].

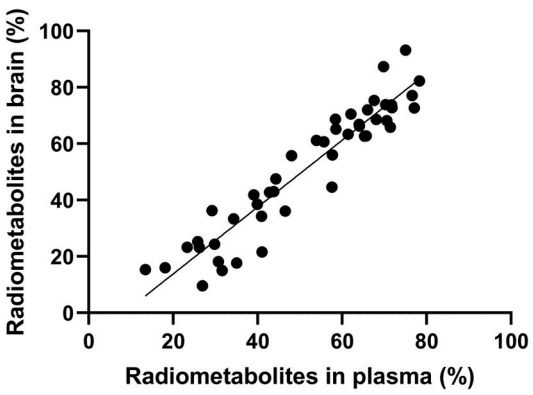

Fig. 7. Correlation plot of percentage of radiometabolites in plasma and brain from mice in which the parent fraction analysis was successfully performed from both plasma and brain (n = 47, including all data from different radioTLC methods (*i.e.*, HPTLC-plate) and all time point mice).

3.5. Radiometabolites crossing the BBB – in vitro mouse brain homogenate study

The chromatographic analyses of the incubated brain homogenate and sham samples showed that they both consisted of > 99 % of parent tracer at all investigated time points. In the chromatogram, the < 1 % of radioactivity that corresponded to R_f regions outside the parent tracer R_f was probably the result of unevenness of the baseline, as the background correction did not remove 100 % of the PSL originating from background radioactivity. Thus, we conclude that radiometabolites are not formed under *in vitro* conditions in brain homogenate, and it is unlikely that they are formed directly in the brain tissue *in vivo*, but rather enter the brain by penetrating the BBB.

3.6. Rationale for the f_P calculating method

As plasma protein binding studies commonly are done with *in vitro* samples [8], the definition for the f_P is the same whether calculating for f_P as free parent over all radioactivity or free parent over all parent radioactivity, because radiometabolites are not considered to be present in *in vitro* samples. When using *in vivo* samples that contain radiometabolites, there are two ways to define f_P. The first is to divide the free parent by all parent (requires analyzing the parent fraction in plasma), and the second is dividing free parent by all radioactivity. The first option can be used for modeling the radioactivity concentration of the free parent when a metabolite-corrected plasma curve is available, and the second can be used if we have just the plasma TAC. It should be noted that the *in vivo* sample containing the free fractions should be analyzed for free parent and free radiometabolite ratio. Hence, with the developed method, we have generated results using both ways to calculate the free fractions to demonstrate their difference (Table 1). The studies that use *in vivo* samples and tracers with significant radiometabolism must define carefully what is being calculated. Is it what is being measured only the free parent, or is it all free radioactivity combined, including the free radiometabolites, divided by the total radioactivity of the sample to yield only the radioactivity-free fraction? Thus, analyzing filtrates by chromatographic methods and the appropriate membrane correction factors from the plasma matrix probably yields results that are more in line with the true values in the plasma.

4. Conclusions

In this study, we introduced a novel method to analyze and calculate the plasma protein binding of a PET tracer, [^{11}C]SMW139, and its radiometabolites to add tools for a more accurate understanding of the pharmacokinetics. The method developed and principles explained here, relying on separate analysis of the f_P and f_M that contribute to the true influx of radioactivity through the BBB into the brain, can be applied for other PET tracers. The approach is especially useful when modeling the behavior of the PET tracers and their radiometabolites in entering the brain. We found that the radiometabolites of [^{11}C]SMW139 have a much larger free fraction than the parent tracer. These

radiometabolites can cross the BBB and are not formed directly in the brain. In addition, a more detailed understanding of f_P and f_M from rodents can be used in translational studies to explain the behavior of the tracer in humans. Similar parent tracer and radiometabolite plasma protein binding methods can be developed for human *in vivo* blood sample analysis.

CRediT authorship contribution statement

Richard Aarnio: Conceptualization, Project administration, Methodology, Validation, Investigation, Writing – original draft, Visualization. **Obada M. Alzghool:** Methodology, Project administration, Investigation, Writing – review & editing. **Saara Wahlroos:** Resources, Formal analysis, Writing – original draft. **James O'Brien-Brown:** Writing – review & editing, Resources. **Michael Kassiou:** Writing – review & editing, Resources. **Olof Solin:** Writing – review & editing, Resources, Funding acquisition. **Juha O. Rinne:** Writing – review & editing, Funding acquisition. **Sarita Forsback:** Supervision, Writing – review & editing. **Merja Haaparanta-Solin:** Supervision, Conceptualization, Investigation, Writing – review & editing, Funding acquisition.

Declaration of Competing Interest

The authors declare that they have no known competing financial interests or personal relationships that could have appeared to influence the work reported in this paper.

Acknowledgements

This study was supported by a grant from state funding for University-level Health Research (project 13250 (MHS), 11133 (OS)), the Swedish Cultural Foundation in Finland (project 178133), and the Academy of Finland (projects 310962 (JOR) and 334310 (OS)).

We thank Marko Vehmanen, Päivi Kotitalo, Aake Honkaniemi, Mira Eisala, and other staff for laboratory technical support in the PET Preclinical Imaging Laboratory, the Central Animal Laboratory of the University of Turku for laboratory animal maintenance, and the staff of the Accelerator Laboratory for radionuclide production. Also, we thank Vesa Oikonen and Francisco López-Picón for valuable comments on the manuscript and Katri Kulmala for image visualization aids.

Appendix A. Supporting information

Supplementary data associated with this article can be found in the online version at doi:10.1016/j.jpba.2022.114860.

References

[1] V.W. Pike, Considerations in the development of reversibly binding PET radioligands for brain imaging, Curr. Med. Chem. 23 (2016) 1818–1869, https://doi.org/10.2174/0929867323666160418114826.
[2] B.K. Lawther, S. Kumar, H. Krovvidi, Blood–brain barrier, Continuing Educat. Anaesth. Crit. Care Pain 11 (2011) 128–132, https://doi.org/10.1093/bjaceaccp/mkr018.
[3] S.S. Zoghbi, K.B. Anderson, K.J. Jenko, D.A. Luckenbaugh, R.B. Innis, V.W. Pike, On quantitative relationships between drug-like compound lipophilicity and plasma free fraction in monkey and human, J. Pharm. Sci. 101 (2012) 1028–1039, https://doi.org/10.1002/jps.22822.
[4] K. Vuignier, J. Schappler, J.-L. Veuthey, P.-A. Carrupt, S. Martel, Drug-protein binding: a critical review of analytical tools, Anal. Bioanal. Chem. 398 (2010) 53–66.
[5] K.K. Ghosh, P. Padmanabhan, C.-T. Yang, S. Mishra, C. Halldin, B. Gulyás, Dealing with PET radiometabolites, EJNMMI Res. 10 (2020) 109.
[6] P.K. Deb, Protein and Tissue Binding: Implication on Pharmacokinetic Parameters, Advances in Pharmaceutical Product Development and Research, Elsevier Inc, 2018, pp. 371–399, https://doi.org/10.1016/B978-0-12-814423-7.00011-3.
[7] C. Wang, N.S. Williams, A mass balance approach for calculation of recovery and binding enables the use of ultrafiltration as a rapid method for measurement of plasma protein binding for even highly lipophilic compounds, J. Pharm. Biomed. Anal. 75 (2013) 112–117.
[8] M.M. Moein, C. Halldin, Sample preparation techniques for protein binding measurement in radiopharmaceutical approaches: a short review, Talanta 219 (2020), https://doi.org/10.1016/j.talanta.2020.121220.
[9] B. Janssen, D.J. Vugts, S.M. Wilkinson, D. Ory, S. Chalon, J.J.M. Hoozemans, R. C. Schuit, W. Beaino, E.J.M. Kooijman, J. van den Hoek, M. Chishty, A. Doméné, A. Van der Perren, A. Villa, A. Maggi, G.T. Molenaar, U. Funke, R.V. Shevchenko, V. Baekelandt, G. Bormans, A.A. Lammertsma, M. Kassiou, A.D. Windhorst, Identification of the allosteric $P2X_7$ receptor antagonist [^{11}C]SMW139 as a PET tracer of microglial activation, Sci. Rep. 8 (2018) 6580, https://doi.org/10.1038/s41598-018-24814-0.
[10] M.H.J. Hagens, S.S.V. Golla, B. Janssen, D.J. Vugts, W. Beaino, A.D. Windhorst, J. O'Brien-Brown, M. Kassiou, R.C. Schuit, L.A. Schwarte, H.E. de Vries, J. Killestein, F. Barkhof, B.N.M. van Berckel, A.A. Lammertsma, The $P2X_7$ receptor tracer [^{11}C]SMW139 as an *in vivo* marker of neuroinflammation in multiple sclerosis: a first-in man study, Eur. J. Nucl. Med. Mol. Imaging 47 (2020) 379–389, https://doi.org/10.1007/s00259-019-04550-x.
[11] M.F. Lister, J. Sharkey, D.A. Sawatzky, J.P. Hodgkiss, D.J. Davidson, A.G. Rossi, K. Finlayson, The role of the purinergic $P2X_7$ receptor in inflammation, J. Inflamm. 4 (2007), https://doi.org/10.1186/1476-9255-4-5.
[12] Q.-H. Zheng, Radioligands targeting purinergic P2X7 receptor, Bioorg. Med. Chem. Lett. 30 (2020), 127169, https://doi.org/10.1016/j.bmcl.2020.127169.
[13] E. Beamer, F. Gölöncsér, G. Horváth, K. Bekő, L. Otrokocsi, B. Koványi, B. Sperlágh, Purinergic mechanisms in neuroinflammation: an update from molecules to behavior, Neuropharmacology 104 (2016) 94–104, https://doi.org/10.1016/j.neuropharm.2015.09.019.
[14] M. Pissarek, Positron emission tomography in the inflamed cerebellum: addressing novel targets among G protein-coupled receptors and immune receptors, Pharmaceutics 12 (2020) 925, https://doi.org/10.3390/pharmaceutics12100925.
[15] M. Haaparanta, T. Grönroos, O. Eskola, J. Bergman, O. Solin, Planar chromatographic analysis and quantification of short-lived radioactive metabolites from microdialysis fractions, J. Chromatogr. A 1108 (2006) 136–139, https://doi.org/10.1016/j.chroma.2005.12.107.
[16] C. Polson, P. Sarkar, B. Incledon, V. Raguvaran, R. Grant, Optimization of protein precipitation based upon effectiveness of protein removal and ionization effect in liquid chromatography–tandem mass spectrometry, J. Chromatogr. B 785 (2003) 263–275, https://doi.org/10.1016/S1570-0232(02)00914-5.
[17] R.L. Nation, U. Theuretzbacher, B.T. Tsuji, Concentration-dependent plasma protein binding: expect the unexpected, Eur. J. Pharm. Sci. 122 (2018) 341–346, https://doi.org/10.1016/j.ejps.2018.07.004.
[18] J.A. Roberts, F. Pea, J. Lipman, The clinical relevance of plasma protein binding changes, Clin. Pharmacokinet. 52 (2013) 1–8, https://doi.org/10.1007/s40262-012-0018-5.
[19] K.E. Warren, Beyond the blood:brain barrier: the importance of central nervous system (CNS) pharmacokinetics for the treatment of CNS tumors, including diffuse intrinsic pontine glioma, Front. Oncol. 8 (2018) 239, https://doi.org/10.3389/fonc.2018.00239.
[20] N. Amini, R. Nakao, M. Shcou, C. Halldin, Determination of plasma protein binding of positron emission tomography radioligands by high-performance frontal analysis, J. Pharm. Biomed. Anal. 98 (2014) 140–143, https://doi.org/10.1016/j.jpba.2014.05.024.
[21] Merck KGaA, Darmstadt, Germany, Membrane Learning Centre, 2021. ⟨https://www.merckmillipore.com/FI/en/life-science-research/chromatography-sample-preparation/membrane-learning-center/Pore-Size-or-NMWL/uyKb.qB.ejgAAAFMYT188eJu,nav⟩. (Accessed 16 November 2021).
[22] Merck KGaA, Darmstadt, Germany, Description of Plasma from Mouse, 2021. ⟨https://www.sigmaaldrich.com/FI/en/product/sigma/p9275?context=product⟩. (Accessed 16 November 2021).
[23] C.-M. Toma, S. Imre, C.-E. Vari, D.-L. Muntean, A. Tero-Vescan, Ultrafiltration method for plasma protein binding studies and its limitations, Processes 9 (2021) 382, https://doi.org/10.3390/pr9020382.
[24] R.N. Gunn, S.G. Summerfield, C.A. Salinas, K.D. Read, Q. Guo, G.E. Searle, C. A. Parker, P. Jeffrey, M. Laruelle, Combining PET biodistribution and equilibrium dialysis assays to assess the free brain concentration and BBB transport of CNS drugs, J. Cereb. Blood Flow Metab. 32 (2012) 874–883, https://doi.org/10.1038/jcbfm.2012.1.

SUPPLEMENTARY DATA

Novel plasma protein binding analysis method for a PET tracer and its radiometabolites: A case study with [^{11}C]SMW139 to explain the high uptake of radiometabolites in mouse brain

Richard Aarnio[a, b, c], Obada M. Alzghool[a, b], Saara Wahlroos[c], James O'Brien-Brown[d], Michael Kassiou[d], Olof Solin[c, e, f], Juha O. Rinne[c, g], Sarita Forsback[c], Merja Haaparanta-Solin[a]

[a] MediCity Research Laboratory, University of Turku, Tykistökatu 6 A, FI-20520 Turku, Finland

[b] Drug Research Doctoral Programme, University of Turku, Turku, Finland

[c] Turku PET Centre, University of Turku, Kiinamyllynkatu 4-8, FI-20520 Turku, Finland

[d] School of Chemistry, The University of Sydney, Sydney NSW 2006, Australia

[e] Department of Chemistry, University of Turku, Henrikinkatu 2, FI-20500 Turku, Finland

[f] Accelerator Laboratory, Turku PET Centre, Åbo Akademi University, Kiinamyllynkatu 4-8, FI-20520 Turku, Finland

[g] Division of Clinical Neurosciences, Turku University Hospital, Turku, Finland

Radiochemistry

[^{11}C]Carbon dioxide ([^{11}C]CO_2) was produced in-target via the $^{14}N(p,\alpha)^{11}C$ reaction on nitrogen mixed with up to 0.2% of oxygen, with 17.5 MeV protons using a ACSI TR19 cyclotron (Advanced Cyclotron Systems, Inc., Richmond, BC, Canada). Typically, the target gas was irradiated for 15 min with a beam current of 40 μA. The whole synthesis was done in GE TRACERlab $FX_{C\text{-}Pro}$ synthesizer (GE, Uppsala, Sweden). [^{11}C]CO_2 was released from the target, reduced by H_2/Ni at 370 °C into [^{11}C]CH_4, and collected in Carbosphere (60–80 mesh) trap cooled with liquid nitrogen. After collection, the [^{11}C]CH_4 was released from the trap by heating and subsequently [^{11}C]CH_4 was mixed with iodine crystal vapor at 100 °C followed by a radical reaction at 720 °C. The formed [^{11}C]CH_3I was collected in a Porapak Q trap at room temperature and the unreacted [^{11}C]CH_4 was recirculated for 3 min. [^{11}C]CH_3I was released from the Porapak Q trap by heating at 190 °C. Carbon-11 labelled SMW139 was obtained by trapping [^{11}C]CH_3I at room temperature into the reaction vessel containing the precursor desmethyl-SMW139 (2-chloro-5-hydroxy-N-(((3s,5s,7s)-3,5,7-trifluoroadamantan-1-

yl)methyl) benzamide) (School of Chemistry, The University of Sydney, Sydney NSW 2006, Australia), (0.5 mg, 1.34 µmol) and NaOH (2 M, 3 µL) in DMSO (200 µL). The reaction mixture was diluted with HPLC mobile phase (500 µL) before injecting to the HPLC system (Sykam S 1122 pump; GE, Uppsala, Sweden) with a Phenomenex Luna column (C18, 10 × 250 mm, 10 µm particle size) and a Knauer UV detector 2.1S (Knauer GmbH, Berlin, Germany). Acetonitrile / 0.1% Trifluoroacetic acid (TFA), 50:50 (v/v) was used as HPLC mobile phase with a flow rate of 5 mL/min. The radioactive fraction corresponding to pure [^{11}C]SMW139 was collected to sterile water (30 mL), pushed through SPE cartridge (SepPak C18 light, Waters, Milford, MA, USA)and washed with water (15 mL). The product was removed from the cartridge with ethanol (1 mL) and diluted with phosphate buffer (0.1 M, 8.5 mL) to a vial containing propylene glycol (1.5 mL). The product was then sterile filtered through a Millipore Millex® GV filter unit (0.22 µm) for further use.

Quality control and molar activity determination

The radiochemical purity, identity, stability and the molar activity of [^{11}C]SMW139 was determined by analytical HPLC system which included a SymmetryShield RP18 column (5 µm, 150 x 3.0 mm), Agilent 1260 infinity quaternary pump, Agilent 1260 infinity VWD, Agilent 1260 standard autosampler and a 2x2” NaI-detector with suitable electronics for radioactivity determination. The mobile phase $CH_3CN/NH_4H_2PO_4$ (0.01 M aq. solution, pH = 2.5) with an isocratic HPLC method (43:57) and flow rate of 1 mL/min was used to elute the product. The effluent was monitored with an UV absorbance detector (ƛ = 230 nm) and the radioactivity detector. The retention time (R_t) of [^{11}C]SMW139 was 7.34 min. The identity of [^{11}C]SMW139 was confirmed by using HPLC with the co-injection of the authentic non-radioactive SMW139 (2-chloro-5-methoxy-N-(((3s,5s,7s)-3,5,7-trifluoroadamantan-1-yl)methyl)benzamide) reference. The MA was calibrated for UV absorbance (ƛ = 230 nm) response per mass of ligand and calculated as the radioactivity of the radioligand (GBq) divided by the amount of the associated carrier substance (µmol).

References

1. Andersson J, Truong P, Halldin C. In-target produced [11C]methane: Increased specific radioactivity. *Appl Radiat Isot.* 2009;67:106-110.

Brumberg, J., Aarnio, R., Forsberg, A., Marjamäki, P., Kerstens, V., Moein, MM., Nag, S., Wahlroos, S., Kassiou, M., Windhorst, AD., Halldin, C., Haaparanta-Solin, M., Fazio, P., Oikonen, V., Rinne, JO., & Varrone, A. (2023)

Quantification of the purinergic P2X7 receptor with [^{11}C]SMW139 improves through correction for brain-penetrating radiometabolites.

Journal of Cerebral Blood Flow & Metabolism

III

Original Article

JCBFM

Journal of Cerebral Blood Flow & Metabolism
2023, Vol. 43(2) 258–268

DOI: 10.1177/0271678X221126830
journals.sagepub.com/home/jcbfm

Quantification of the purinergic $P2X_7$ receptor with [^{11}C]SMW139 improves through correction for brain-penetrating radiometabolites

Joachim Brumberg[1,2], Richard Aarnio[3], Anton Forsberg[1], Päivi Marjamäki[3], Vera Kerstens[1], Mohammad M Moein[1], Sangram Nag[1], Saara Wahlroos[3], Michael Kassiou[4], Albert D Windhorst[5,6], Christer Halldin[1], Merja Haaparanta-Solin[3], Patrik Fazio[1,7], Vesa Oikonen[3], Juha O Rinne[3] and Andrea Varrone[1]

Abstract

The membrane-based purinergic 7 receptor ($P2X_7R$) is expressed on activated microglia and the target of the radioligand [^{11}C]SMW139 for *in vivo* assessment of neuroinflammation. This study investigated the contribution of radiolabelled metabolites which potentially affect its quantification. *Ex vivo* high-performance liquid chromatography with a radio detector (radioHPLC) was used to evaluate the parent and radiometabolite fractions of [^{11}C]SMW139 in the brain and plasma of eleven mice. Twelve healthy humans underwent 90-min [^{11}C]SMW139 brain PET with arterial blood sampling and radiometabolite analysis. The volume of distribution was estimated by using one- and two- tissue compartment (TCM) modeling with single (V_T) and dual (V_{Tp}) input functions. RadioHPLC showed three major groups of radiometabolite peaks with increasing concentrations in the plasma of all mice and humans. Two radiometabolite peaks were also visible in mice brain homogenates and therefore considered for dual input modeling in humans. 2TCM with single input function provided V_T estimates with a wide range (0.10–10.74) and high coefficient of variation (COV: 159.9%), whereas dual input function model showed a narrow range of V_{Tp} estimates (0.04–0.24; COV: 33.3%). In conclusion, compartment modeling with correction for brain-penetrant radiometabolites improves the *in vivo* quantification of [^{11}C]SMW139 binding to $P2X_7R$ in the human brain.

Keywords

[^{11}C]SMW139 PET, dual input modeling, neuroinflammation, purinergic receptor, radiometabolite

Received 3 April 2022; Revised 12 July 2022; Accepted 31 July 2022

Introduction

Inflammatory response to cerebral accumulation of misfolded proteins contributes to disease development of neurodegenerative diseases.[1,2] Microglia are the main immune cells of the central nervous system and detect changes in their cellular environment, provide physiological function, and promote tissue repair mechanisms.[3] Whereas initial microglial activation is assumed to have a beneficial effect, chronic and excessive stimuli may result in neuronal damage and thus, trigger the progression of neurodegeneration.[4,5]

[1]Centre for Psychiatry Research, Department of Clinical Neuroscience, Karolinska Institutet & Stockholm Health Care Services, Stockholm, Sweden
[2]Department of Nuclear Medicine, Medical Center – University of Freiburg, Freiburg, Germany
[3]Turku PET Centre, University of Turku and Turku University Hospital, Turku, Finland
[4]School of Chemistry, The University of Sydney, Sydney, Australia
[5]Department of Radiology and Nuclear Medicine, Amsterdam UMC location Vrije Universiteit Amsterdam, Amsterdam, The Netherlands
[6]Amsterdam Neuroscience, Brain Imaging, Amsterdam, The Netherlands
[7]Department of Neurology, Karolinska University Hospital, Stockholm, Sweden

Corresponding author:
Joachim Brumberg, Karolinska Hospital, R5:02 SE-17176 Stockholm, Sweden.
Email: joachim.brumberg@ki.se

The membrane-based purinergic, ligand-gated ion channel 7 receptor ($P2X_7R$) is an adenosine triphosphate (ATP)-gated, non-selective cation channel and is upregulated in activated microglia.[6–8] Whereas it physiologically has trophic actions on neurons, microglia, and astrocytes, it is activated by high ATP-levels after tissue injury, leading to the release of pro-inflammatory substances.[9] This triggers further microglial activation, promotes neuronal damage, and subsequent apoptosis, that induces a continued ATP-release and thus, sustains a vicious circle of neuronal inflammation and cell loss.[6] Due to its involvement in this cycle, the $P2X_7R$ is a promising molecular target to reveal the pathophysiologic mechanisms of neuroinflammation and for new therapeutic approaches.

Four radiolabeled adamantanyl benzamide analogues with high affinity to the human $P2X_7R$ have been evaluated in rodent animal models, of which [^{11}C]SMW139 showed highest binding to the receptor.[10] The radioligand is not a substrate of the P-glycoprotein at the blood-brain-barrier (BBB) and uptake can be blocked with $P2X_7R$ antagonists.[11] [^{11}C]SMW139 was evaluated in humans including the characterization of [^{11}C]SMW139 pharmacokinetics.[12] However, the suggested kinetic model did not account for the possible presence of brain-penetrating radiometabolites of [^{11}C]SMW139 as indicated by preclinical evidence.[10] Therefore, this study aims to extend previous findings on brain-penetrating radiometabolites by evaluating [^{11}C]SMW139 metabolism preclinically and to assess whether kinetic modeling with dual (i.e. parent and radiometabolite) input functions improves the *in vivo* quantification of $P2X_7R$ expression in humans.

Materials and methods

Small animal study

Eleven C57BL/6J mice were examined with [^{11}C]SMW139 (all female; weight: 34 ± 4 g; age: 8.7 ± 1.9 months; injected activity: 17.9 ± 6.2 MBq; molar activity: 42.2 ± 24.1 MBq/nmol; injected mass: 0.21 ± 0.12 µg; for radiochemistry see Supplemental methods [13,14]). *Ex vivo* sampling for parent fraction analysis was performed at 10 min ($n = 4$), 30 min ($n = 3$) and 45 min ($n = 4$) post radioligand injection (p.i.) by cardiac puncture and by collecting perfused brain samples. Sample size of $n \geq 3$ per group was considered sufficient for exploratory radiometabolite analysis. All experimental animal procedures were done in accordance with the EU Directive 2010/63/EU on the protection of animals used for scientific purposes, and with the ARRIVE guidelines at Turku PET Centre, University of Turku, Finland [TU] and approved by the Regional State Administrative Agency for Southern Finland (ESAVI/16273/2019).

Blood and brain radiometabolite analysis. Blood samples were collected into heparinized tubes (Microtainer, BD, Franklin Lakes, NJ, USA) and centrifuged (12100 g, 90 s). The plasma pipetted into an Eppendorf tube and mixed with 1:2 (v/v) plasma:acetonitrile to precipitate the proteins. The mixture was vortexed for 10 s, centrifuged, and the supernatant (200–700 µL) was collected for subsequent radio detector high-performance liquid chromatography (radioHPLC) analysis. Obtained brains were homogenized in a glass homogenizer with a 9:1 (v/v) acetonitrile:water solution. The homogenized solution was centrifuged (12100 g, 90 s) and the supernatant (200–700 µL volume) was analysed with radioHPLC (see Supplemental methods).

Human study

Human participants were prospectively enrolled and examined at two study sites (TU and Centre for Psychiatry Research, Karolinska Institutet, Stockholm, Sweden, [KI]). The study was approved by the Ethics Committee of the South Western Finland Hospital District, the Finnish Medicinal Agency, the Ethics Committee of the Stockholm Region, and the Radiation Safety Committee of the Karolinska University Hospital. The study was registered as Clinical Trial in the EudraCT database (2017-001585-19). All human participants provided written, informed consent before participating in the study, which was conducted in accordance with the Declaration of Helsinki and its later amendments. Twelve healthy subjects (TU: seven, KI: five) were recruited through public advertisement. Inclusion criteria were: age between 45 and 80 years, good health according to medical and psychiatric history, physical examination, cognitive assessment (Mini-Mental State Examination ≥ 28), laboratory tests, electrocardiogram, and unremarkable magnetic resonance (MR) imaging of the brain.

Imaging procedures. All subjects underwent brain MR scans, including T1-weighted three-dimensional sequences on a 3 Tesla system prior to PET examination as part of the initial evaluation and to delineate anatomic brain volumes of interests (VOI). Six min transmission scans with a ^{137}Cs source and the dynamic PET measurements were performed on a High-Resolution Research Tomograph system (Siemens Medical Solutions) at both study sites. [^{11}C]SMW139 (424.0 ± 54.8 MBq; 152.0 ± 131.5 MBq/nmol; 1.91 ± 1.31 µg) was injected as bolus into the cubital vein and the catheter was flushed with 10 mL 0.9% NaCl

solution. Following injection, emission data were collected in list mode for 90 min. PET data were reconstructed in 21 frames of increasing duration (3×5 s, 3×10 s, 4×60 s, 2×150 s, 2×300 s, 7×600 s) using 3D ordinary Poisson ordered subset expectation maximization (8 iterations, 16 subsets, voxel size of $1.22 \times 1.22 \times 1.22$ mm). Frame-to-frame co-registration of reconstructed images was applied as previously published.[15]

Image analysis. All data were processed at KI using an in-house pipeline written in MATLAB (MATLAB r2014b, The MathWorks, Inc.). Individual T1-weighted sequences were segmented with FreeSurfer (FreeSurfer v6.0.0, http://surfer.nmr.mgh.harvard.edu/).[16] The generated segmentation masks were used to define bilateral VOIs of the frontal cortex, parietal cortex, temporal cortex, caudate nucleus, putamen, thalamus, brainstem, cerebellar cortex, and the whole-brain grey matter. Thereafter, MR and dynamic PET data were co-registered and time-activity curves (TAC) of VOIs were obtained.

Arterial blood sampling, radiometabolite analysis, and data processing. A catheter was placed into the radial artery of each participant and arterial blood was collected continuously during the first 5-10 min using an automated blood sampling system (ABSS, Allogg AB). A series of arterial blood samples were drawn manually at ~2, 5, 10, 20, 40, 60, 75, and 90 min p.i. (Supplemental Table 1). The radioactivity in blood and plasma samples (0.7–1.7 mL) were measured in a well counter cross-calibrated with the PET system. The fraction of unchanged [^{11}C]SMW139 (i.e. parent fraction) in arterial blood was measured using radioHPLC analysis. At TU, the same chromatographic method as described for the small animal studies was used. At KI, the plasma was precipitated after centrifugation utilizing a simple protein precipitation method [17] and the supernatant was analysed by a reversed-phase radioHPLC as previously described.[18] The radio-chromatograms for radioactive compounds were integrated and their areas were calculated as a percentage of the total of the decay corrected areas of all detected radioactive fractions. Blood data were processed as previously described with slight modifications to generate plasma TACs,[19] parent input of [^{11}C]SMW139, and one input curve representing the activity of presumably brain-penetrant [^{11}C]SMW139 radiometabolites in the plasma (see Supplemental methods).

Kinetic modeling. Three kinetic models were assessed to characterize [^{11}C]SMW139 kinetics using PMOD (version 3.7, PMOD Technologies LLC). All models were applied by fitting the blood volume (V_B) as an additional parameter.[12] First, standard two-tissue compartment model with a single (i.e. parent) input curve was assessed with a dual run procedure (2TSI[k_4]), for which the efflux rate from the specific to the non-specific compartment, k_4, was first estimated in the whole-brain grey matter VOI and then used to fix k_4 for subsequent volume of distribution (V_T) estimation in (sub-)cortical grey matter VOIs.[12] This resulted in four parameters estimated in the second run (V_B, K_1, k_2, k_3). Second, one- and two-tissue compartment models with dual (i.e. parent and radiometabolite) input curves were evaluated (1TDI and 2TDI).[20] This led to five parameters for 1TDI (V_B, K_{1p}, k_{2p}, K_{1m}, k_{2m}) and seven parameters to fit for 2TDI (V_B, K_{1p}, k_{2p}, k_3, k_4, K_{1m}, k_{2m}). In analogy to 2TSI[k_4], the dual input two-tissue compartment model was also assessed with a two-step procedure (2TDI[k_4]; six parameters: V_B, K_{1p}, k_{2p}, k_3, K_{1m}, k_{2m}). According to the models, the total distribution volumes [21] can be achieved by solving equation (1) for 2TSI, equation (2) for 1TDI, and equation (3) for 2TDI where V_{Tp} is the distribution volume of the unchanged radioligand. The models assumed that the brain-penetrant radiometabolites did not specifically bind to the $P2X_7R$, so that the rate constants k_3 and k_4 represent solely the association and dissociation of the parent radioligand to the receptor. For model overview see Table 1.

$$V_T = \frac{K_1}{k_2} \times \left(1 + \frac{k_3}{k_4}\right) \quad (1)$$

$$V_{Tp} = \frac{K_{1p}}{k_{2p}} \quad (2)$$

$$V_{Tp} = \frac{K_{1p}}{k_{2p}} \times \left(1 + \frac{k_3}{k_4}\right) \quad (3)$$

Table 1. Model overview.

Model	Abbreviation	Fitted parameters
Two tissue compartment model with single input function and fixed k_4	2TSI[k_4]	V_B, K_1, k_2, k_3
One tissue compartment model with dual input function	1TDI	V_B, K_{1p}, k_{2p}, K_{1m}, k_{2m}
Two tissue compartment model with dual input function	2TDI	V_B, K_{1p}, k_{2p}, k_3, k_4, K_{1m}, k_{2m}
Two tissue compartment model with dual input function and fixed k_4	2TDI[k_4]	V_B, K_{1p}, k_{2p}, k_3, K_{1m}, k_{2m}

Statistical analysis. The coefficient of variation (COV) was calculated to assess the variability of distribution volumes and obtained by dividing the standard deviation by the mean, of all regions and subjects. The goodness of fit was assessed with the Akaike information criterion (AIC) [22] and the reliability of V_T and V_{Tp} by using the percentage standard error (%SE) of the estimates. The fits of dual input models were compared by using *F*-test statistics. The correlations of V_{Tp} estimates were assessed by using linear regression analysis and Spearman's correlation coefficient r_s. A *p*-value below 0.05 was considered significant. Data are presented as mean and standard deviation or median and range, as appropriate.

Results

Ex vivo *radiometabolite analysis*

There was no exclusion within the small animal study. RadioHPLC showed three major groups of

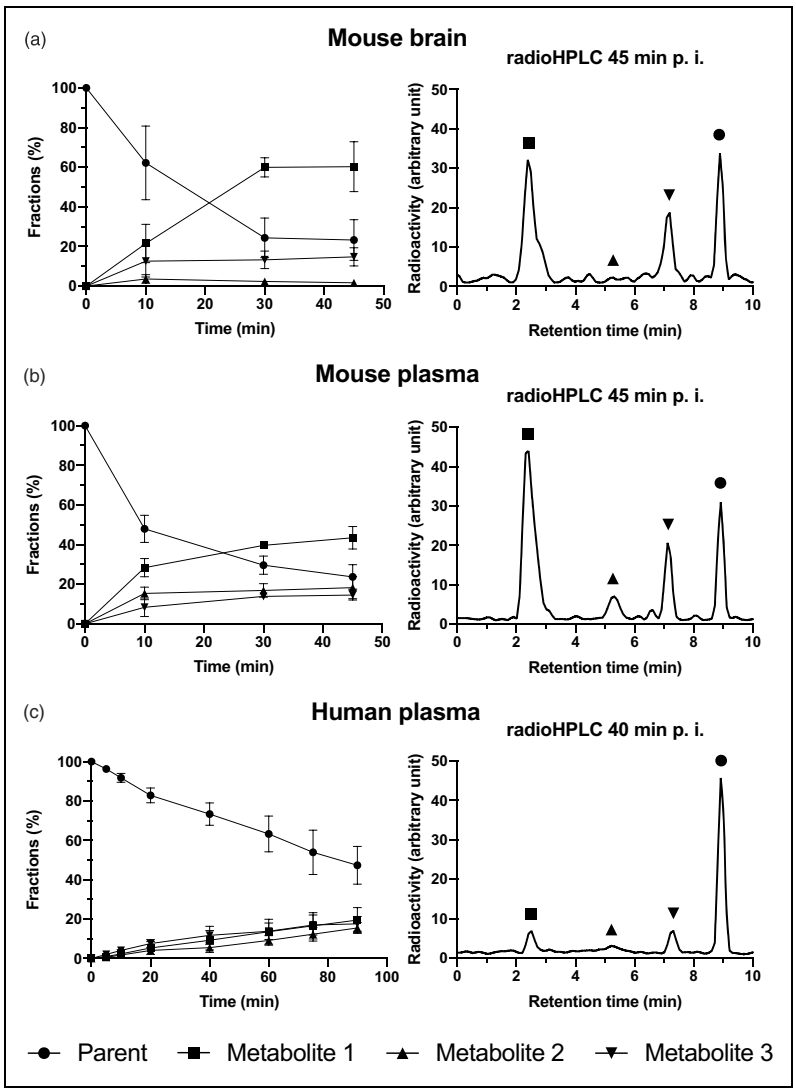

Figure 1. [^{11}C]SMW139 radiometabolite analysis. Left panels show mean and standard deviation of parent radioligand and radiometabolite fractions of the whole radioactivity in the sample in mouse brain (a) and mouse plasma (b) (n = 4, 3, and 4, at 10, 30, and 45 min, respectively), and human plasma (c; n = 10). Right panels show exemplary radioHPLC chromatograms from mouse (a, b) and human plasma (c).

radiometabolite peaks (numbered radiometabolite 1–3 according to the appearance order in radioHPLC chromatogram) with increasing concentrations over time in the plasma of all mice (Figure 1(b)). Only two peaks, the most polar radiometabolite 1 (retention time [Rt] 1.5–3.5 min) and the least polar radiometabolite 3 (Rt 7–8 min), were also clearly present in the mice's brain homogenates, whereas radiometabolite 2 (Rt 3.5–7 min) was only present in barely quantifiable levels (Figure 1(a)). The mean fraction of unchanged [^{11}C]SMW139 at 45 min after injection was similar in plasma and brain: around $23.7 \pm 6.2\%$ and $23.3 \pm 10.3\%$, respectively. A high fraction of radioligand metabolites after 10 min (plasma: $52.1 \pm 6.8\%$; brain: $37.8 \pm 18.6\%$) and an apparent transformation into a plateau phase in plasma and brain starting around 30 min p.i. indicates a much faster metabolism of [^{11}C]SMW139 in mice compared to humans (Figure 1).

Human plasma radiometabolites and brain uptake

Two subjects were excluded due to incomplete blood and plasma data. Plasma radioHPLC measurements showed three groups of radiometabolites peaking with an identical Rt when compared to mice plasma (Figure 1(c)). Human metabolism, however, was slower than that of mice yielding $47.3 \pm 9.6\%$ unchanged [^{11}C]SMW139 and continuing slightly increasing curves of all three radiometabolites fractions at 90 min p.i. (Figure 1(c)). Visual evaluations of TACs from the whole-brain grey matter showed that five subjects (50%; TU: two subjects, KI: three subjects), after the initial peak during the perfusion and uptake phase, had a clear washout of the tracer until the end of the scan. In contrast, the TACs of the remaining showed a washout up to 20–40 min, followed by a slight and steady increase until the last frame (Figure 2).

Kinetic modeling

Tissue distribution volumes of single and dual input models. Estimated distribution volumes and %SEs for each evaluated model is presented region-wise in Table 2. 2TDI yielded unstable fits with unreliably high V_{Tp} estimates and $\%SE > 50\%$ in nine (11.3%) out of 80 evaluated regions (eight regions per patient). The observed fitting failures were equally distributed across regions and subjects without a particular VOI that performed poorly. Therefore, these regions were excluded from subsequent comparisons. 2TSI[k_4], 2TDI[k_4], and 1TDI yielded robust fits for all regions with predominantly low $\%SE < 20\%$ except few outliers (Table 2). None of the regions were excluded. 2TSI [k_4] single input model showed a high COV of V_T (159.9%), whereas dual input models had a consistently narrow V_{Tp} range between 0.04 and 0.24 (COV: 2TDI, 33.3%; 2TDI[k_4], 36.3%; 1TDI, 35.0%; see also Figure 3). V_B estimates were in close agreement for all evaluated models (V_B [median, range]: 2TSI [k_4], 0.07, 0.02–0.13; 2TDI, 0.07, 0.02–0.13; 2TDI[k_4], 0.07, 0.01–0.13; 1TDI, 0.07, 0.02–0.13) with a consistently low %SE (median <3.5 for all models).

Model comparison. Two tissue compartment models showed overall comparable ranges of AIC's with slight differences between regions. AIC was predominantly smallest for 2TDI[k_4]. Median AIC of 1TDI was tendentially higher than two tissue compartment models (Table 3). Median F-value of the comparison between 2TDI and 2TDI[k_4] was below the tabulated value at a p-level of 0.05 (F critical value: 4.60) for all

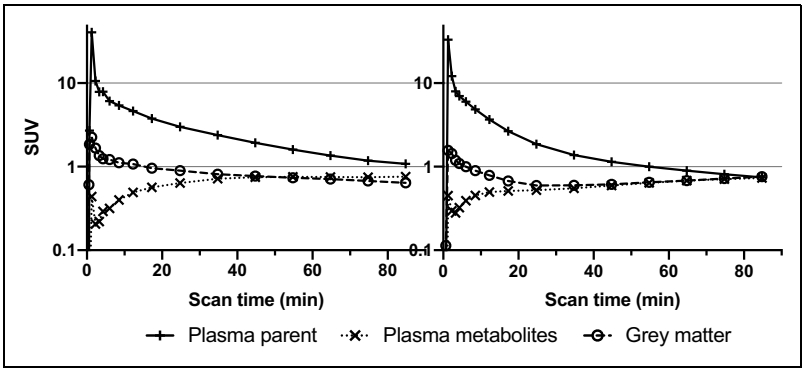

Figure 2. Human time-activity curves. Left panel shows an exemplary finding in one subject with initial peaking followed by washout from the whole-brain grey matter time-activity curves. Right panel shows an exemplary whole-brain grey matter time-activity curve with a slight and steady increase after 20–40 min. Both are depicted with corresponding plasma parent and plasma radiometabolite standardized uptake value (SUV) curves.

Table 2. Estimated tissue distribution volumes and percentage standard error.

	Two tissue compartment model, single input, k_4 fixed		Two tissue compartment model, dual input[a]		Two tissue compartment model, dual input, k_4 fixed		One tissue compartment model, dual input	
Volume of interest	V_T	%SE V_T	V_{Tp}	%SE V_{Tp}	V_{Tp}	%SE V_{Tp}	V_{Tp}	%SE V_{Tp}
Frontal cortex	0.58 (0.17–10.06)	4.4 (2.8–9.5)	0.14 (0.07–0.21)	8.3 (3.8–13.1)	0.13 (0.07–0.17)	4.9 (2.4–24.0)	0.09 (0.06–0.12)	5.8 (3.3–11.4)
Parietal cortex	0.71 (0.21–10.74)	3.9 (2.2–12.1)	0.15 (0.09–0.20)	13.4 (4.2–32.8)	0.14 (0.07–0.16)	5.5 (2.6–37.7)	0.09 (0.06–0.16)	6.5 (3.7–10.7)
Temporal cortex	0.53 (0.16–8.97)	3.8 (1.7–13.2)	0.13 (0.070.16)	5.9 (2.6–36.3)	0.14 (0.06–0.18)	5.4 (2.3–11.9)	0.10 (0.06–0.16)	4.4 (3.8–12.2)
Caudate	0.43 (0.10–7.24)	5.2 (4.0–7.9)	0.10 (0.04–0.14)	23.0 (6.9–40.4)	0.08 (0.04–0.16)	10.6 (3.5–17.1)	0.07 (0.04–0.12)	7.1 (3.2–20.4)
Putamen	0.61 (0.15–9.20)	6.2 (3.0–15.2)	0.14 (0.07–0.24)	13.6 (4.6–20.1)	0.15 (0.07–0.20)	9.2 (4.4–38.8)	0.10 (0.06–0.14)	6.1 (4.7–13.5)
Thalamus	0.53 (0.13–7.76)	5.5 (3.5–17.4)	0.16 (0.06–0.20)	6.3 (4.7–24.5)	0.14 (0.07–0.24)	6.0 (2.8–21.2)	0.11 (0.07–0.17)	5.4 (2.9–17.6)
Brainstem	0.41 (0.11–6.33)	4.7 (2.8–10.3)	0.14 (0.04–0.20)	9.7 (2.7–32.4)	0.14 (0.05–0.20)	8.3 (3.9–12.6)	0.11 (0.05–0.17)	5.9 (1.9–8.9)
Cerebellar cortex	0.51 (0.15–9.04)	5.0 (2.2–17.4)	0.13 (0.07–0.18)	13.3 (4.2–34.1)	0.11 (0.06–0.18)	5.5 (1.9–23.9)	0.09 (0.05–0.15)	5.0 (3.0–15.5)

Data of healthy volunteers (n = 10) are presented as median and range.
V_T: volume of distribution; V_{Tp}: distribution volume of unchanged radioligand; %SE: percentage standard error.
[a]Estimates of nine brain regions excluded.

eight brain regions, suggesting that the simplification of the 2TDI (i.e. using a dual run procedure to fix k_4) can be considered equivalent in terms of the model fit. However, when further simplifying the model to the 1TDI, median F-values are predominantly above the critical value (3.74), suggesting that the fit is significantly worsened and thus, this model does not completely describe the pharmacokinetics of [^{11}C]SMW139.

Correlation analysis

Linear regression showed that V_{Tp} estimates of all brain regions derived from 2TDI and 2TDI[k_4] ($r^2 = 0.74$, $p < 0.001$) as well as 2TDI[k_4] and 1TDI ($r^2 = 0.78$, $p < 0.001$) strongly correlated with each other, whereas the correlation between 2TDI and 1TDI ($r^2 = 0.64$, $p < 0.001$) was less pronounced (Figure 4). The same applied to each region separately which had high to excellent correlations (2TDI vs. 2TDI[k_4]: $r_s = 0.80$–1.00, all $p < 0.01$; 2TDI vs. 1TDI: $r_s = 0.70$–0.88, all $p < 0.05$; 2TDI[k_4] vs. 1TDI: $r_s = 0.81$–0.94, all $p < 0.01$; Supplemental Table 2).

Discussion

This study investigating [^{11}C]SMW139 metabolism in mice and pharmacokinetics in healthy human participants showed evidence that two [^{11}C]SMW139 radiometabolites are present in the brain and must be considered for accurate *in vivo* quantification of [^{11}C]SMW139 binding to the human P2X$_7$R. Kinetic modeling with plasma parent and radiometabolite input functions allows robust estimation of [^{11}C]SMW139 distribution volumes with low variability.

The P2X$_7$R is thought to have low expression levels in normal physiology and is upregulated in case of neuronal damage like in neurodegenerative disorders.[6,9] Since neurodegeneration is a chronic process, neuroinflammatory effects and regulatory mechanisms such as P2X$_7$R expression are expected to be subtle.[4,23] In this context, the correction for possibly confounding, brain-penetrant radiometabolites is of particular importance when evaluating tracers with low V_T values as it is the case for [^{11}C]SMW139.[12,20]

In our cohort of ten healthy volunteers, who were enrolled and examined at two different study sites, kinetic modeling with single input function yielded highly variable V_T estimates. Furthermore, V_T estimates in some cases were unexpectedly high and exceeded values that were previously reported with [^{11}C]SMW139.[12] Although the single input model showed robust fitting parameters, the fitted line undershot the late part of the TACs (Figure 3;[12]) suggesting that the assumption of [^{11}C]SMW139 radiometabolites

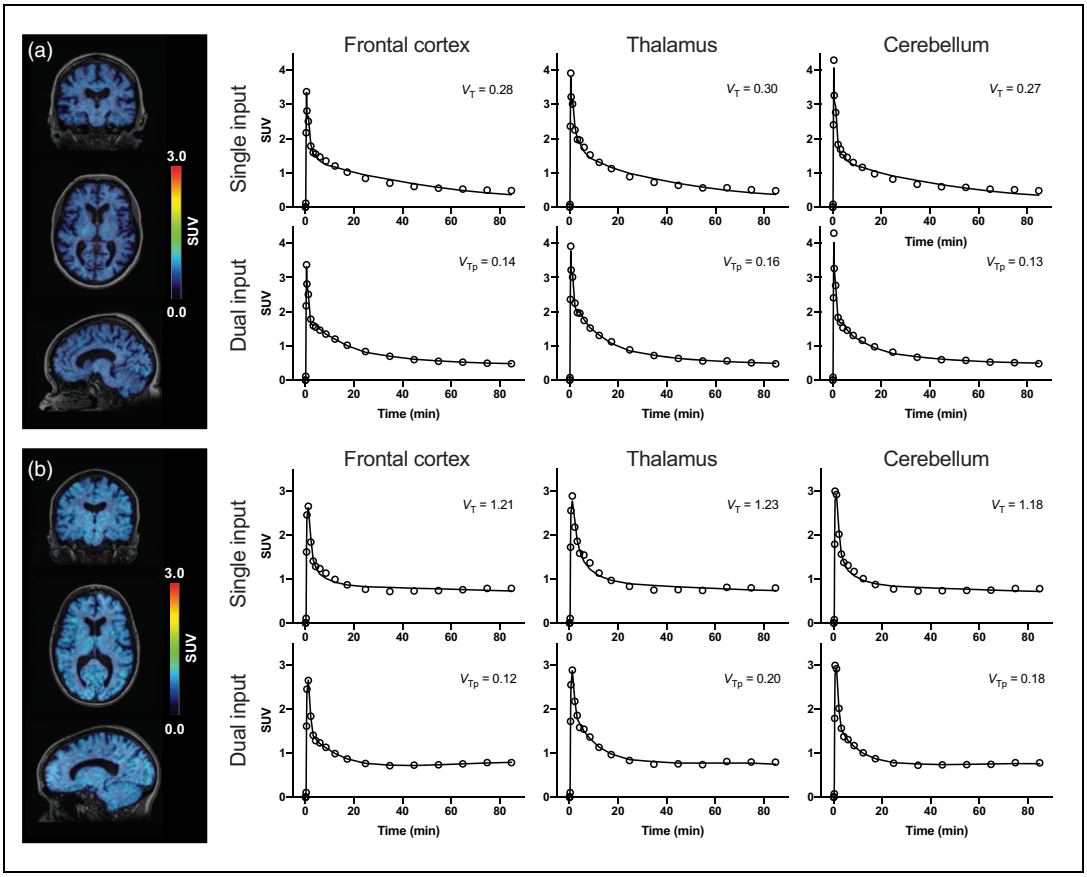

Figure 3. Two tissue compartment model fits with single and dual input function. Summarized standardized uptake value (SUV) images between 40 and 90 min after [^{11}C]SMW139 injection and exemplary model fits of two patients with low (a) and high (b) contribution of radiometabolites to brain radioactivity. Abbreviations: V_T, volume of distribution; V_{Tp}, distribution volume of the parent fraction.

not penetrating BBB in humans does not reflect the tracer's kinetics.

In the presence of three major groups of radiometabolites in the human plasma, however, it is unclear which radiometabolites may enter the brain and hamper the quantification of specific binding of [^{11}C]SMW139 to the P2X$_7$R. We, therefore, evaluated the [^{11}C]SMW139 metabolism in eleven C57BL/6J mice, in order to establish an analogy between humans and mice: considering a faster metabolism in mice as compared to humans,[24,25] the metabolization of [^{11}C]SMW139 is congruent by showing the three [^{11}C]SMW139 radiometabolites peaking with the same Rt (Figure 1). The most polar radiometabolite 1 and the least polar radiometabolite 3, were proven to be present in the brain of the mice, whereas radiometabolite 2 was detected only in low amounts in the examined perfused brain homogenates and showed in average around 15% of the fraction levels found in plasma. Notwithstanding the state-of-the-art technique used in perfusion by pumping saline through blood vessels via the mouse's cardiac chambers after cardiac puncture, the brain may include small residuals of blood and thus, minor fractions of radiometabolite components in the plasma may affect the analysis of brain homogenates. This allows to disregard radiometabolite 2 for kinetic modeling assuming a similarly low ability to penetrate the human BBB.

Consecutively, we adjusted our assumptions for kinetic modeling by accounting for the presence of radiometabolite 1 and 3 within the human brain without specific binding to the P2X$_7$R. The variability of V_{Tp} estimates was reduced and the 2TDI fits were closer in agreement with the TACs (Figure 3). By reducing the number of fit parameters from seven to six, the precision of V_{Tp} values was improved without

Table 3. Model fit and model comparison.

	Akaike information criterion				*F*-value		% of regions with better fits than 2TDI[‡]	
Volume of interest	2TSI[k_4]	2TDI	2TDI[k_4]	1TDI	2TDI vs. 2TDI[k_4][*]	2TDI vs. 1TDI[†]	2TDI[k_4]	1TDI
Frontal cortex	19.7 (8.5–45.1)	5.0 (−23.1–21.5)	6.0 (−23.7–38.7)	21.4 (−3.9–50.7)	3.0 (−3.1–13.8)	15.3 (−0.4–78.7)	70.0	20.0
Parietal cortex	18.7 (−3.8–58.8)	−0.1 (−33.5–66.9)	14.5 (−9.4–53.4)	27.7 (3.9–63.3)	0.23 (−4.8–138.4)	14.4 (1.9–94.4)	70.0	10.0
Temporal cortex	15.1 (−22.7–53.3)	2.1 (1.8–72.7)	7.9 (−15.7–55.4)	18.1 (−8.2–57.2)	1.3 (−4.6–17.2)	10.8 (−0.8–41.9)	60.0	30.0
Caudate	30.0 (21.4–38.9)	32.9 (13.3–46.7)	32.5 (12.5–59.2)	31.3 (16.5–50.2)	0.12 (−5.0–2.8)	2.8 (−2.2–43.4)	90.0	60.0
Putamen	33.0 (18.9–62.3)	31.0 (0.9–68.6)	32.5 (2.7–51.8)	38.6 (26.4–60.7)	0.0 (−6.2–5.0)	4.6 (0.24–32.7)	90.0	50.0
Thalamus	28.5 (13.5–64.1)	28.0 (1.8–72.7)	18.4 (−1.1–70.5)	32.2 (8.5–67.6)	1.7 (−8.4–6.4)	2.1 (−2.6–46.5)	90.0	60.0
Brainstem	16.0 (−1.2–30.2)	13.4 (−18.0–48.6)	12.8 (−16.8–29.1)	18.4 (−2.5–38.5)	0.11 (−9.5–7.5)	5.6 (−4.5–69.3)	80.0	50.0
Cerebellar cortex	20.7 (−13.1–68.9)	31.9 (−12.1–74.2)	17.8 (−14.9–75.1)	23.2 (−10.2–72.2)	0.31 (−2.4–5.5)	6.5 (1.4–17.4)	90.0	50.0

Data of healthy volunteers ($n = 10$) are presented as median and range. The tabulated value for *F* statistics at a *p*-level of 0.05 is [*]4.60 and [†]3.74, respectively. [‡]refers to the *F*-test.
2TSI[k_4]: two tissue compartment model with single input function and fixed k_4; 2TDI: two tissue compartment model with dual input function; 2TDI[k_4]: two tissue compartment model with dual input function and fixed k_4; 1TDI: one tissue compartment model with dual input function.

significantly increasing the residual variation of the fit and by yielding highly correlated V_{Tp} estimates. Although a further reduction of the parameters by using the one tissue compartment model resulted in slightly more stable outcome measures, the model fit deteriorated (as indicated by AIC and *F*-test). Furthermore, 1TDI underestimates the radioligand's V_{Tp}. The overall small V_{Tp} of dual input models seems to be related to a high plasma protein binding of [^{11}C]SMW139 ($97.2 \pm 1.1\%$), since a low K_{1p}/k_{2p} ratio (Supplemental Table 3) is usually caused by high affinity to plasma proteins. It is also noteworthy that the combination of two metabolites into one input and one tissue metabolite compartment violates the concept of compartment and might impair the model fit to a certain degree. However, modeling with three input functions (by separating K_{1m} and k_{2m} for both radiometabolites) would – although theoretically more precise – require two additional fitting parameters and therefore be less feasible.

Taken together, the 2TDI[k_4] can be recommended as the preferred model for P2X$_7$R quantification with [^{11}C]SMW139, though the benefit of adding stability due to fixing k_4 must be confirmed in the respective patient population. The estimation of k_4 is weighted on late time points of the scan and therefore particularly hampered by the observed tracer kinetics with increasing TACs due to brain-penetrant radiometabolites. We initially expected that the consideration of radiometabolites would improve the stability of k_4 such that the added benefit of fixing k_4 is negligible. The combination of low non-displaceable distribution volume and low levels of target expression, however, might not only lead to small V_{Tp}, but also hamper the stable estimation of "true" k_4. Therefore, adding stability due to reducing the parameters to fit might outweigh variability of k_4 in healthy subjects and patients with subtle neuroinflammatory abnormalities,[4,23] but a strong inflammatory response accompanied by local heterogeneity of the brain tissue [26] due to microglia activation may result in a more pronounced variability of k_4.

Some limitations of this study need to be mentioned. Due to their earlier Rt than the parent tracer in radioHPLC (i.e. greater hydrophilicity), the metabolites are more polar than the parent tracer, and thus, they have a less pronounced ability to cross the BBB. The study does not reveal if radiometabolite 1 crosses the BBB or is metabolized within the brain. To our knowledge, the structure of these radiometabolites is unknown and separate studies are needed to identify the radiometabolites and evaluate the route of metabolism of [^{11}C]SMW139.[27] The radioHPLC analysis of the plasma samples indicates that the metabolism of [^{11}C]SMW139 in mice was faster than the metabolism in human subjects. Therefore, it is reasonable to

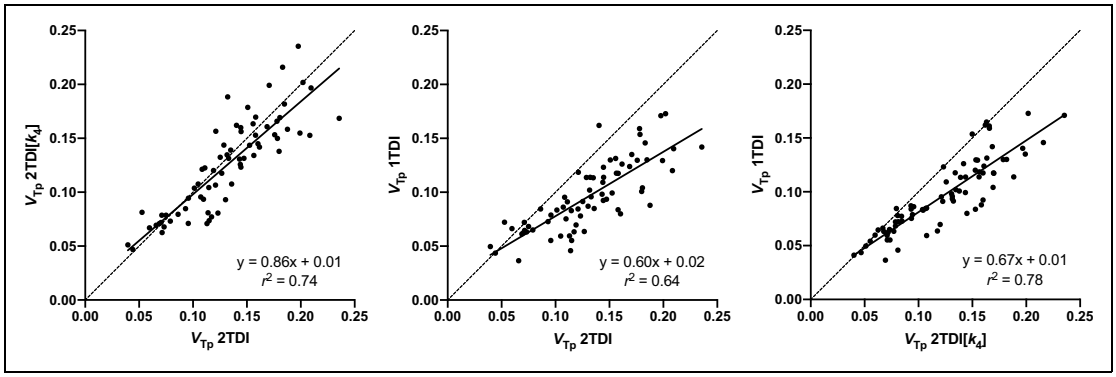

Figure 4. Scatter plots and linear regression analysis. Distribution volume estimates of unchanged [^{11}C]SMW139 (V_{Tp}) within all evaluated brain regions obtained with three models using dual input function: two tissue compartment model (2TDI), two tissue compartment model with a dual run procedure and fixed k_4 (2TDI[k_4]), and one tissue compartment model (1TDI).

assume that the accumulation rates of radiometabolites 1 and 3 in the human brain are low and might not represent major confounders in this study. The determination of the exact radiometabolite fractions in human subjects was also affected by the low radioactivity concentrations of the samples collected at later time points causing a low signal-to-noise ratio in the radioHPLC analysis. The uncertainty in the estimation of the radiometabolite fractions might have contributed to some variability. However, the kinetic analysis performed using all the plasma radiometabolite fractions (including radiometabolite 2) provided similar results (data not shown), suggesting that the exact determination of the individual fractions did not affect the results to a large extent.

The homogeneous cohort of participants and the combination of data from two study sites with minor methodological differences (see also Supplemental Table 1 and Supplemental Figure 1), make the results fairly generalizable. However, further validation work is required for [^{11}C]SMW139 PET. In particular, the model comparison should be validated in patient populations or with an inflammation model in healthy humans or nonhuman primates.[28,29] In presence of a strong neuroinflammatory response, a simplified pseudo-reference approach for [^{11}C]SMW139 is imaginable, assuming no specific binding of the radiometabolites to the $P2X_7R$ and thus, a similar amount of metabolites in the target and pseudo-reference region. Recent studies with the $P2X_7R$ radioligand [^{11}C] JNJ54173717 did not report an increase of $P2X_7R$ in patients with Parkinson's disease or amyotrophic lateral sclerosis.[30,31] Additional work is ongoing to measure $P2X_7R$ availability in neurodegenerative disorders using [^{11}C]SMW139.

In conclusion, the quantification of the binding of [^{11}C]SMW139 to human $P2X_7R$ is greatly enhanced by using a dual input function model, with the assumption of a similar path of metabolism and BBB penetration ability of radiometabolites in mice and humans. In this cohort of ten healthy volunteers, kinetic modeling with plasma parent and radiometabolite input function allowed robust estimation of [^{11}C]SMW139 distribution volumes with low variability.

Funding

The author(s) disclosed receipt of the following financial support for the research, authorship, and/or publication of this article: The study was supported by funds from the Michael J Fox Foundation to AV, ADW, CH, and JR (grant: 12062). JB received a scholarship from the Deutsche Forschungsgemeinschaft, (grant: BR6121/1-1).

Acknowledgements

The authors thank the staff of the Karolinska Institutet and Turku PET Centres for supporting the PET studies.

Declaration of conflicting interests

The author(s) declared the following potential conflicts of interest with respect to the research, authorship, and/or publication of this article: All authors report no conflict of interest.

Authors' contributions

JB: study design, data analysis, data interpretation, writing; RA: study design, data acquisition, data analysis, data interpretation, writing; AF: data analysis, data interpretation, revising the manuscript; PM: data acquisition, data analysis, revising the manuscript; VK, SW: data acquisition, revising the manuscript; MMM: data acquisition, data analysis, writing; SN: data acquisition, writing; MK, ADW, CH, MHS, PF: study design, data interpretation, revising the manuscript; VO: data analysis, data interpretation, revising the manuscript; JOR: study design, data acquisition, data interpretation, revising the manuscript; AV: study design, data

acquisition, data interpretation, writing. All authors read and approved the final manuscript.

ORCID iDs

Joachim Brumberg https://orcid.org/0000-0003-0959-4776
Richard Aarnio https://orcid.org/0000-0002-6420-514X

Supplemental material

Supplemental material for this article is available online.

References

1. Laurent C, Buee L and Blum D. Tau and neuroinflammation: what impact for Alzheimer's disease and tauopathies? *Biomed J* 2018; 41: 21–33.
2. Refolo V and Stefanova N. Neuroinflammation and glial phenotypic changes in alpha-synucleinopathies. *Front Cell Neurosci* 2019; 13: 263.
3. Hickman S, Izzy S, Sen P, et al. Microglia in neurodegeneration. *Nat Neurosci* 2018; 21: 1359–1369.
4. Jacobs AH and Tavitian B. Noninvasive molecular imaging of neuroinflammation. *J Cereb Blood Flow Metab* 2012; 32: 1393–1415.
5. Perry VH, Nicoll JA and Holmes C. Microglia in neurodegenerative disease. *Nat Rev Neurol* 2010; 6: 193–201.
6. Monif M, Burnstock G and Williams DA. Microglia: proliferation and activation driven by the P2X7 receptor. *Int J Biochem Cell Biol* 2010; 42: 1753–1756.
7. Inoue K and Tsuda M. Purinergic systems, neuropathic pain and the role of microglia. *Exp Neurol* 2012; 234: 293–301.
8. Jiang LH, Baldwin JM, Roger S, et al. Insights into the molecular mechanisms underlying mammalian P2X7 receptor functions and contributions in diseases, revealed by structural modeling and single nucleotide polymorphisms. *Front Pharmacol* 2013; 4: 55.
9. Mesuret G, Engel T, Hessel EV, et al. P2X7 receptor inhibition interrupts the progression of seizures in immature rats and reduces hippocampal damage. *CNS Neurosci Ther* 2014; 20: 556–564.
10. Janssen B, Vugts DJ, Wilkinson SM, et al. Identification of the allosteric P2X7 receptor antagonist [(11)C]SMW139 as a PET tracer of microglial activation. *Sci Rep* 2018; 8: 6580.
11. Beaino W, Janssen B, Kooijman E, et al. PET imaging of P2X7R in the experimental autoimmune encephalomyelitis model of multiple sclerosis using [(11)C]SMW139. *J Neuroinflammation* 2020; 17: 300.
12. Hagens MHJ, Golla SSV, Janssen B, et al. The P2X7 receptor tracer [(11)C]SMW139 as an in vivo marker of neuroinflammation in multiple sclerosis: a first-in man study. *Eur J Nucl Med Mol Imaging* 2020; 47: 379–389.
13. Andersson J, Truong P and Halldin C. In-target produced [11C]methane: Increased specific radioactivity. *Appl Radiat Isot* 2009; 67: 106–110.
14. Aarnio R, Alzghool OM, Wahlroos S, et al. Novel plasma protein binding analysis method for a PET tracer and its radiometabolites: a case study with [(11)C]SMW139 to explain the high uptake of radiometabolites in mouse brain. *J Pharm Biomed Anal* 2022; 219: 114860.
15. Schain M, Toth M, Cselenyi Z, et al. Improved mapping and quantification of serotonin transporter availability in the human brainstem with the HRRT. *Eur J Nucl Med Mol Imaging* 2013; 40: 228–237.
16. Fischl B, Salat DH, Busa E, et al. Whole brain segmentation: automated labeling of neuroanatomical structures in the human brain. *Neuron* 2002; 33: 341–355.
17. Moein MM, Nakao R, Amini N, et al. Sample preparation techniques for radiometabolite analysis of positron emission tomography radioligands; trends, progress, limitations and future prospects. *Trac Trend Anal Chem* 2019; 110: 1–7.
18. Moein MM, Toth M, Tari L, et al. New approach in radiometabolite analysis of positron emission tomography (PET) radioligands; lead-shielded microextraction by packed sorbent as a tool for in vivo radiometabolite analysis of [(11)C]SMW139 in rat plasma. *Talanta* 2020; 208: 120449.
19. Jucaite A, Svenningsson P, Rinne JO, et al. Effect of the myeloperoxidase inhibitor AZD3241 on microglia: a PET study in Parkinson's disease. *Brain* 2015; 138: 2687–2700.
20. Fujita M, Seibyl JP, Verhoeff NP, et al. Kinetic and equilibrium analyses of [(123)I]epidepride binding to striatal and extrastriatal dopamine D(2) receptors. *Synapse* 1999; 34: 290–304.
21. Innis RB, Cunningham VJ, Delforge J, et al. Consensus nomenclature for in vivo imaging of reversibly binding radioligands. *J Cereb Blood Flow Metab* 2007; 27: 1533–1539.
22. Akaike H. New look at statistical-model identification. *Ieee Trans Automat Contr* 1974; 19: 716–723. Ac19:
23. Berdyyeva T, Xia C, Taylor N, et al. PET imaging of the P2X7 ion channel with a novel tracer [(18)F]JNJ-64413739 in a rat model of neuroinflammation. *Mol Imaging Biol* 2019; 21: 871–878.
24. Hashimoto H, Kawamura K, Igarashi N, et al. Radiosynthesis, photoisomerization, biodistribution, and metabolite analysis of 11C-PBB3 as a clinically useful PET probe for imaging of tau pathology. *J Nucl Med* 2014; 55: 1532–1538.
25. Maruyama M, Shimada H, Suhara T, et al. Imaging of tau pathology in a tauopathy mouse model and in alzheimer patients compared to normal controls. *Neuron* 2013; 79: 1094–1108.
26. Delforge J, Syrota A and Bendriem B. Concept of reaction volume in the in vivo ligand-receptor model. *J Nucl Med* 1996; 37: 118–125.
27. Osman S, Lundkvist C, Pike VW, et al. Characterisation of the appearance of radioactive metabolites in monkey and human plasma from the 5-HT1A receptor radioligand, [carbonyl-11C]WAY-100635 – explanation of high signal contrast in PET and an aid to biomathematical modelling. *Nucl Med Biol* 1998; 25: 215–223.
28. Hannestad J, Gallezot JD, Schafbauer T, et al. Endotoxin-induced systemic inflammation activates microglia: [(1)(1)C]PBR28 positron emission tomography in nonhuman primates. *Neuroimage* 2012; 63: 232–239.

29. Sandiego CM, Gallezot JD, Pittman B, et al. Imaging robust microglial activation after lipopolysaccharide administration in humans with PET. *Proc Natl Acad Sci U S A* 2015; 112: 12468–12473.
30. Van Weehaeghe D, Koole M, Schmidt ME, et al. [^{11}C] JNJ54173717, a novel P2X7 receptor radioligand as marker for neuroinflammation: human biodistribution, dosimetry, brain kinetic modelling and quantification of brain P2X7 receptors in patients with Parkinson's disease and healthy volunteers. *Eur J Nucl Med Mol Imaging* 2019; 46: 2051–2064.
31. Van Weehaeghe D, Van Schoor E, De Vocht J, et al. TSPO versus P2X7 as a target for neuroinflammation: an *in vitro* and *in vivo* study. *J Nucl Med* 2020; 61: 604–607.

SUPPLEMENTAL MATERIAL

Radiochemistry

Karolinska Institutet. [^{11}C]Methane ([^{11}C]CH_4) was produced in-target via the $^{14}N(p,\alpha)^{11}C$ reaction on nitrogen mixed with 10% of hydrogen, with 16.4 MeV protons using a GEMS PET trace cyclotron (GE, Uppsala, Sweden). Typically, the target gas was irradiated for 15–20 min with a beam current of 35 μA. ^{11}C-Labeled methyl iodide, [^{11}C]CH_3I, was produced following the previously published method [1]. In short, the produced [^{11}C]CH_4 was released from the target and collected in a Porapak Q trap cooled in liquid nitrogen. After collection, the [^{11}C]CH_4 was released from the trap by heating with pressurized air and subsequently [^{11}C]CH_4 was mixed with iodine crystal vapor at 60 °C followed by a radical reaction at 720 °C. The formed [^{11}C]CH_3I was collected in a Porapak Q trap at room temperature and the unreacted [^{11}C]CH_4 was recirculated for 3 min. [^{11}C]CH_3I was released from the Porapak Q trap by heating the trap using a custom-made oven at 180 °C. [^{11}C]CH_3OTff was produced by online transfer of [^{11}C]CH_3I through a glass column packed with silver triflate at 165 °C. Carbon-11 labelled [^{11}C]SMW139 was obtained by trapping [^{11}C]CH_3OTff at room temperature in a reaction vessel containing the desmethyl precursor SMW167 (2-chloro-5-hydroxy-N-(((3s,5s,7s)-3,5,7-trifluoroadamantan-1-yl)methyl) benzamide), (0.5 – 1 mg, 1.3 μmol-2.6 μmol) and NaOH (0.5M, 3 μL) in acetone (400 μL). The reaction mixture was diluted with sterile water (500 μL) before injecting to the built-in high-performance liquid chromatography (HPLC) system for the purification of the desired radiolabelled product. The HPLC system consisted of a semi-preparative reverse phase XBridge column (C18, 10 × 250 mm, 5 μm particle size) and a Merck Hitachi UV detector (λ = 254 nm) (VWR, International, Stockholm, Sweden) in series with a GM-tube (Carroll-Ramsey, Berkley, CA, USA) used for radioactivity detection. Acetonitrile / 0.1% Trifluoroacetic acid (TFA), 50:50 (v/v) was used as HPLC mobile phase with a flow rate of 6 mL/min. The radioactive fraction corresponding to pure [^{11}C]SMW139 was collected from HPLC and evaporated to dryness. The final purified [^{11}C]SMW139 was formulated in 6–mL phosphate buffered saline (pH7.4) and the formulated product was then sterile filtered through a Millipore Millex® GV filter unit (0.22 μm) for further use in vivo.

Turku PET Centre. Radiochemistry was performed as previously described [2].

Quality control and molar activity (MA) determination.

Karolinska Institutet. The radiochemical purity, identity, and stability of [^{11}C]SMW139 was determined by an analytical HPLC system which included an XBridge RP column (C18, 4.6µm × 150 mm,), Merck Hitachi L-7100 Pump, L-7400 UV detector and GM-tube for radioactivity detection (VWR International). The mobile phase CH_3CN/H_3PO_4 (0.01M aq. solution) with an isocratic HPLC method (43:57) and flow rate of 2 mL/min was used to elute the product. The effluent was monitored with a UV absorbance detector (ƛ = 230 nm) coupled to a radioactive detector (b-flow, Beckman, Fullerton, CA). The retention time (Rt) of [^{11}C]SMW139 was 4–5 min. The identity of [^{11}C]SMW139 was confirmed by using HPLC with the co-injection of the authentic non-radioactive SMW139 (2-chloro-5-methoxy-N-(((3s,5s,7s)-3,5,7-trifluoroadamantan-1-yl)methyl) benzamide) standard. The MA of the final product was measured by analytical HPLC which included XBridge RP column (C18, 4.6µm × 150 mm,), Merck-Hitachi L-7100 Pump, L-7400 UV detector. The mobile phase CH_3CN/H_3PO_4 (0.01M aq. solution) with an isocratic HPLC method (46:54) and flow rate of 2 mL/min. MA was calibrated for UV absorbance (ƛ = 230 nm) response per mass of ligand and calculated as the radioactivity of the radioligand (GBq) divided by the amount of the associated carrier substance (µmol). Each sample was analysed three times and compared to a reference standard also analysed three times.

Turku PET Centre. The radiochemical purity, identity, stability and the MA of [^{11}C]SMW139 was determined as previously described[2].

Small animal study

Radio detector high-performance liquid chromatography analysis. The supernatant was injected into the radioHPLC (Merck Hitachi L-7100 gradient pump system coupled with a Radiomatic 150 TR, Packard, USA) using a 1 mL loop which was filled with distilled water to minimize the acetonitrile composition prior to the injection. The loop and Hamilton injection syringe were rinsed three times with 1.0 mL 1:1 (v/v) acetonitrile:water solution between each injection to remove any residuals from previous samples. All samples were analysed using a

5.0 mL/min eluent flow, Phenomenex Luna 5µm C18(2) 100 Å 250x10 mm column and with the following method: a gradient of acetonitrile (A), 0.1 % Trifluoroacetic acid in water (B) was used: 0–8.0 min (A/B) 30:70 → 90:10, 8.0–9.0 min (A/B) 90:10, 9.0–10.0 min (A/B) 90:10 → 30:70, 10.0–12.0 min (A/B) 30:70. A radioactive standard was prepared by spiking 65:35 (v/v) acetonitrile:water with [^{11}C]SMW139 (~3 kBq/mL) and injected into the same system to confirm the Rt of the unmetabolized [^{11}C]SMW139. RadioHPLC data were analysed using Merck Hitachi D-7000 HSM software (Merck, Darmstadt, Germany). Radio-chromatograms were integrated, decay corrected with the Rt of the peak, and the amount of parent compound and radioactive metabolites were calculated as a percentage of the total of the areas of all detected radioactive fractions.

Human study

Arterial plasma input for [^{11}C]SMW139 and radioactive [^{11}C]SMW139 metabolites. At Karolinska Institutet, the individual blood curve over the first 5 min from the ABSS was merged with the curve from manual blood samples. Radioactivity concentrations in plasma and blood were divided yielding a plasma/blood ratio curve. Using linear interpolation, the plasma/blood ratio curve was extrapolated from 0 s to the end of sampled ABSS data. Plasma time-activity curves covering the whole scan were generated by multiplying the extrapolated plasma/blood ratio curve with the ABSS blood curve and by fusing the result with the plasma curve from manual samples. At Turku PET Centre, input processing assumed that parent radioligand concentration in blood cells is zero during the time of ABSS data collection. Plasma time-activity curves covering the whole scan were generated by dividing the ABSS blood curve by (1 - hematocrit) and by merging the result with the plasma curve from manual samples. Subsequent processing was performed concordantly for both study sites with PMOD (version 3.7, PMOD Technologies LLC). Data for parent fraction of [^{11}C]SMW139 were fitted using a mono-exponential fit and were multiplied with the uncorrected plasma time-activity-curve to obtain the parent input curve (i.e. the plasma radioactivity of unchanged [^{11}C]SMW139). Furthermore, we estimated an input curve representing the activity of presumably brain-penetrant [^{11}C]SMW139 radiometabolites in the plasma. Therefore, the parent fraction and the

fraction of the radiometabolite, which was assumed not to be present within the brain, were combined, fitted with a mono-exponential function and multiplied with the plasma time-activity-curve. The obtained curve was subsequently subtracted from the plasma input curve, which resulted in the radiometabolite input curve. Finally, blood and plasma input curves were delay corrected.

References

1. Andersson J, Truong P, Halldin C. In-target produced [11C]methane: Increased specific radioactivity. *Appl Radiat Isot.* 2009;67:106-110.

2. Aarnio R, Alzghool OM, Wahlroos S, et al. Novel plasma protein binding analysis method for a PET tracer and its radiometabolites: A case study with [(11)C]SMW139 to explain the high uptake of radiometabolites in mouse brain. *J Pharm Biomed Anal* 2022; 219: 114860.

SUPPLEMENTAL TABLE 1. Differences of data acquisition and processing methods

Imaging procedures		
	Karolinska Institutet	Turku PET Centre
MR system	GE Healthcare Discovery MR750	Philips Ingenuity TF PET/MR
PET reconstruction, matrix size	256 x 256 x 207	200 x 200 x 150
Arterial blood sampling and input processing		
	Karolinska Institutet	Turku PET Centre
ABSS duration	10 min	5 min
Manual blood samples	2 mL at ~ 2, 5, 10, 20 min, and 4 mL at ~ 40, 60, 75, and 90 min p.i.	2 mL at ~ 5, 10, 20, 40, 60, 75, and 90 min p.i.

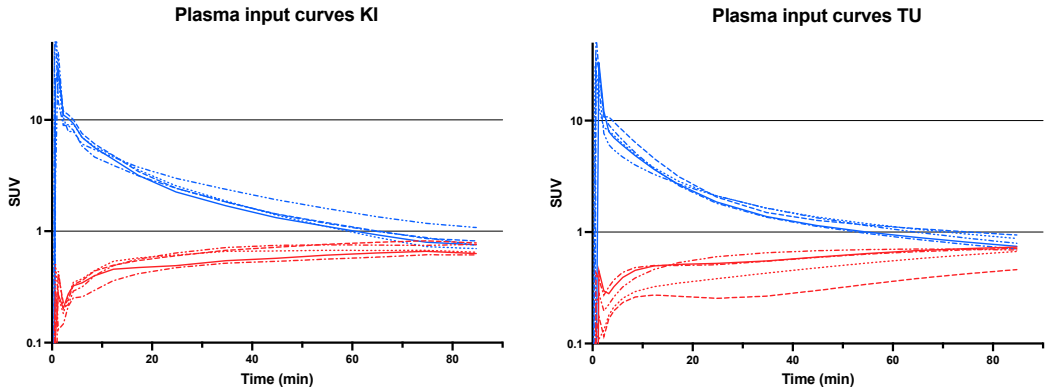

SUPPLEMENTAL FIGURE 1 Plasma parent and metabolites input curves. Plasma parent (blue) and metabolites (red) input curves of each participant enrolled at the Karolinska Institutet (KI; left panel) and at Turku PET Centre (TU; right panel). Line patterns indicate the corresponding plasma and metabolites input curves for each participant.

SUPPLEMENTAL TABLE 2. Correlation analysis

Volume of interest	2TDI vs. 2TDI[k_4]		2TDI vs. 1TDI		2TDI[k_4] vs. 1TDI	
	r_s	*p*-value	r_s	*p*-value	r_s	*p*-value
Frontal cortex	0.95	<0.001	0.70	0.036	0.81	0.005
Parietal cortex	0.82	0.007	0.88	0.002	0.89	<0.001
Temporal cortex	0.92	<0.001	0.82	0.007	0.92	<0.001
Caudate	0.98	<0.001	0.71	0.047	0.87	0.001
Putamen	0.90	<0.001	0.78	0.013	0.82	0.004
Thalamus	1.00	<0.001	0.87	0.003	0.89	<0.001
Brainstem	0.80	0.010	0.85	0.004	0.94	<0.001
Cerebellar cortex	0.85	0.004	0.83	0.005	0.84	0.002

n = 10 healthy volunteers. Abbreviations: 2TDI, two tissue compartment model with dual input function; 2TDI[k_4], two tissue compartment model with dual input function and fixed k_4; 1TDI, one tissue compartment model with dual input function.

SUPPLEMENTAL TABLE 3. Estimates of blood volume and *k*-ratios for two tissue compartment model, dual input, k_4 fixed

Volume of interest	V_B	%SE V_B	K_{1p}/k_{2p}	%SE K_{1p}/k_{2p}	k_3/k_4	%SE k_3/k_4	K_{1m}/k_{2m}	%SE K_{1m}/k_{2m}
Frontal cortex	0.06 (0.03-0.11)	2.0 (1.0-16.2)	0.06 (0.04-0.10)	6.5 (2.8 -11.4)	0.70 (0.28-2.65)	13.9 (4.2-45.6)	0.92 (0.57-1.35)	5.7 (2.0-23.4)
Parietal cortex	0.07 (0.03-0.13)	2.5 (1.3-8.5)	0.06 (0.02-0.12)	6.6 (3.7-18.6)	1.17 (0.01-3.43)	15.8 (10.1-295.3)	1.04 (0.68-1.55)	5.8 (3.4-14.6)
Temporal cortex	0.06 (0.04-0.12)	1.9 (0.8-11.3)	0.06 (0.03-0.14)	8.8 (2.9-25.2)	0.97 (0.19-1.70)	17.8 (8.2-104.4)	0.84 (0.60-1.33)	6.0 (4.1-20.8)
Caudate	0.05 (0.04-0.08)	3.8 (2.0-14.3)	0.05 (0.01-0.11)	10.3 (5.8-100.4)	0.45 (0.10-3.37)	47.6 (22.7-110.7)	0.79 (0.38-1.20)	8.9 (4.8-25.4)
Putamen	0.07 (0.01-0.11)	3.7 (1.7-94.8)	0.07 (0.06-0.11)	8.2 (4.2-13.5)	0.82 (0.23-1.80)	20.8 (13.2-88.1)	0.92 (0.52-1.67)	13.5 (5.4-44.9)
Thalamus	0.07 (0.01-0.13)	3.4 (1.3-50.9)	0.07 (0.05-0.13)	8.6 (4.0-19.3)	0.43 (0.18-1.53)	25.8 (7.5-221.2)	0.78 (0.52-1.45)	12.2 (4.0-25.8)
Brainstem	0.06 (0.03-0.11)	1.9 (1.2-8.6)	0.07 (0.03-0.16)	11.9 (5.7-28.4)	0.99 (0.01-3.32)	34.9 (5.8-195.8)	0.74 (0.32-0.96)	8.4 (2.8-22.4)
Cerebellar cortex	0.08 (0.04-0.13)	2.8 (1.0-6.3)	0.06 (0.04-0.10)	9.5 (3.9-36.2)	0.63 (0.12-2.85)	35.2 (4.9-163.4)	0.96 (0.55-1.33)	8.5 (3.0-30.8)

Data of healthy volunteers (n = 10) are presented as median and range. Abbreviations: %SE, percentage standard error.

Lehto, J., Aarnio, R., Tuisku, J., Sucksdorff, M., Koivumäki, EM., Nylund, M., Helin, S., Rajander, J., Danon, JJ., Gilchrist, J., Kassiou, M., Oikonen, V., & Airas, L. (2024)
P2X7-receptor binding in new-onset and secondary progressive MS – a [^{11}C]SMW139 PET study.
European Journal of Nuclear Medicine and Molecular Imaging – Research

IV

EJNMMI Research

ORIGINAL RESEARCH

Open Access

P2X$_7$-receptor binding in new-onset and secondary progressive MS – a [^{11}C]SMW139 PET study

Jussi Lehto[1,2,3*], Richard Aarnio[1], Jouni Tuisku[1], Marcus Sucksdorff[1,2,4], Esa Mikko Koivumäki[1], Marjo Nylund[1,2,3,4], Semi Helin[1], Johan Rajander[1,5], Jonathan Danon[6], Jayson Gilchrist[6], Michael Kassiou[6], Vesa Oikonen[1] and Laura Airas[1,2,3,4]

Abstract

Background PET imaging of activated microglia has improved our understanding of the pathology behind disability progression in MS, and pro-inflammatory microglia at 'smoldering' lesion rims have been implicated as drivers of disability progression. The P2X$_7$R is upregulated in the cellular membranes of activated microglia. A single-tissue dual-input model was applied to quantify P2X$_7$R binding in the normal appearing white matter, perilesional areas and thalamus among progressive MS patients, healthy controls and newly diagnosed relapsing MS patients.

Results Overall, tracer uptake in the MS brain was not significantly higher compared to HCs. In the 3 mm perilesional rim of all T1 lesions, tracer binding was higher among relapsing patients compared to progressive patients. Tracer binding was higher in males compared to females. Disease duration correlated with tracer binding in the normal appearing white matter. Age correlated negatively with tracer binding in the perilesional rims.

Conclusions Even as binding estimates obtained with the dual-input model were consistent with the expected distribution of P2X$_7$Rs in the MS brain, the small free fraction of the parent tracer may limit its accuracy and applicability, and binding estimates between subjects were highly variable. Conclusive evidence for the applicability of [^{11}C]SMW139 to detect MS-related diffuse smoldering inflammation was not obtained.

Keywords Multiple sclerosis, Microglia, PET, Kinetic modelling

*Correspondence:
Jussi Lehto
juleht@utu.fi
[1]Turku PET Centre, Turku, Finland
[2]Neurocenter, Turku University Hospital, Turku, Finland
[3]InFLAMES Research Flagship, University of Turku, Turku, Finland
[4]Clinical Neurosciences, University of Turku, Turku, Finland
[5]Åbo Akademi University, Turku, Finland
[6]School of Chemistry, The University of Sydney, Sydney, Australia

Background

During the last two decades, extensive use of 18-kDa translocator protein positron emission tomography (TSPO-PET) [1] in in vivo imaging of activated microglia [2] has improved our understanding of the pathology behind disability progression [3–5] and treatment outcomes [6–9] in multiple sclerosis (MS). The translational applicability of this method is somewhat limited by its inability to distinctly differentiate between pro-inflammatory and anti-inflammatory phenotypes of activated microglia [10]. Activation of pro-inflammatory microglia at 'smoldering' lesion rims has been implicated as a driver of disability progression in MS [11, 12].

The adenosine triphosphate -gated cation channel receptor ($P2X_7R$) is upregulated in the cellular membranes of activated microglia [13] and has been identified as a potential therapeutic [14] and imaging target [10] in neurodegenerative disease, which offers improved specificity towards microglia that are in the pro-inflammatory end of the phenotype spectrum. The $P2X_7R$ activates the inflammasome, and results in pro-inflammatory interleukin release and proliferation of activated microglia [13, 15]. Compared to non-stimulated and homeostatic microglia in vitro, microglia polarized into an inflammatory phenotype over-express the $P2X_7R$ 5-folds, whereas a mere 1.5-fold difference is seen in TSPO expression [10]. In rodents, bacterial lipopolysaccharide –induced neuroinflammation leads to significant brain uptake of $P2X_7R$-specific radiotracers [16, 17], and uptake is also high at the peak of the MS disease model experimental autoimmune encephalitis (EAE) [18]. While also found on neurons and other glial cells, $P2X\times_7R$ signaling is primarily associated with activated inflammatory microglia [14, 19].

SMW139 is a potent antagonist (Ki 32 nM) of the $P2X_7R$ [20]. A mouse biodistribution study with radiolabeled [^{11}C]SMW139 demonstrated rapid brain uptake and clearance via liver metabolism: brain standardized uptake values decreased approximately 80–90% fom 5 min to 45 min post injection (p.i.) [21]. According to Akaike information criterion (AIC) [22], a reversible 90-minute two-tissue compartment model (2TCM) with a blood volume parameter provided the best fit for [^{11}C]SMW139 kinetics in a first in man study. Increased volumes of distribution (V_T) were observed among MS patients compared to healthy controls throughout the cerebral white matter, cortical grey matter (cGM) and deep gray matter (dGM) including the thalamus [23].

However, the specific tissue compartment of [^{11}C]SMW139 is small [23], and rapid metabolism results in a significant fraction of activity from brain-penetrant radiometabolites [21, 24, 25]. It is debatable whether a single-input 2TCM improves the fit by correcting for unspecific radiometabolite activity, rather than providing an accurate estimate of specific parent tracer binding. To address this, Aarnio et al. [24] utilized a rapid analysis method, which combines thin-layer chromatography with digital autoradiography for the parent fraction analysis. It was concluded that a dual-input (DI) function improves the quantification of specific [^{11}C]SMW139 binding [25].

In the current study we applied a single tissue compartment dual-input (1TDI) model to obtain estimates for the ratios of parent tracer rate constants between the blood compartment and the tissue compartment (k1p/k2p; V_{TDI} i.e. V_{T_parent}). We also aimed to further validate [^{11}C]SMW139 for MS studies by imaging progressive MS (PMS) patients with longer disease duration and no recent disease activity, and compared tracer binding in the normal appearing white matter (NAWM), perilesional areas and the thalamus to healthy controls, and to newly diagnosed relapsing MS (RMS). We also tested whether tracer uptake is increased around MS lesions by comparing perilesional V_T to lesional and NAWM V_T.

Methods

Subjects and procedures

The study was performed at the Turku PET Centre. Recruitment took place at the Turku University Hospital Neurocenter between Feb 2019 and Jun 2022. Inclusion criteria for all MS patients included a confirmed diagnosis according to the 2017 McDonald criteria and a written informed consent. Additional requirements were at least one Gd+lesion of at least 0.5 cm in diameter, and a clinical diagnosis of secondary progression for the RMS and PMS cohorts, respectively. Key exclusion criteria included pregnancy, claustrophobia, and other significant central nervous system pathology besides MS. All MS patients underwent baseline neurological assessments, magnetic resonance imaging (MRI) and [^{11}C]SMW139 PET. Age matched healthy control subjects (HCs) were imaged for comparison. The study protocol was approved by the Ethics Committee of the Hospital District of Southwest Finland. The study was conducted according to the principles of the Declaration of Helsinki.

[^{11}C]SMW139 production and PET

Irradiations were performed with a TR-19 (ACSI, Richmond, Canada) cyclotron to produce the carbon-11 radioisotope according to previously described procedures [8]. The complete synthesis procedure of [^{11}C]SMW139 at the Radiopharmaceutical Chemistry Laboratory of Turku PET Centre is described in the supplementary material of Aarnio et al. 2022 [24].

A ninety-minute dynamic PET scan was acquired for each subject with a high-resolution research tomograph (HRRT; Siemens Medical Solutions, Knoxville, TN, USA). The mean (SD) injected specific activity and mass

of [^{11}C]SMW139 were 95 (88) MBq/nmol and 2.7 (1.7) μg, respectively. The mean (SD) injected dose of radioactivity was 402 (12.2) MBq, 404 (13.5) MBq and 404 (10.7) MBq in the RMS, PMS and HC groups, respectively. List mode data was histogrammed into 21 timeframes (3×5s, 3×10s, 4×60s, 2×150s, 2×300s, 7×600s) and reconstructed using an OP-OSEM3D algorithm with 16 subsets and 10 iterations and with point spread function modelling [26] to reduce the partial volume effect. Reconstructed images were post-processed with a 2.5 mm FWHM (full width at half maximum) Gaussian filter.

Arterial blood sampling and PET modelling

A hematocrit sample was drawn within 1 h before PET imaging. An automated blood pump (ABSS, Allogg AB, Mariefred, Sweden) running at 60 rpm (6 mL/min) was used to obtain a continuous arterial blood time activity curve (TAC) from 0 to 5 min p.i., and manual arterial blood sampling ensued at 5, 10, 20, 40, 60, 75 and 90 min p.i. Arterial plasma activity were then converted to whole blood with individual plasma-to-blood ratio curves. Next, input curves for PET modelling were estimated by fitting the parent fraction with a monoexponential function $f(x) = (A\text{-}B)e^{-Cx} + B$, where A=1, B>=0, C>0, and multiplied with the arterial plasma data to obtain metabolite corrected arterial input TACs. The resulting curves were subtracted from the uncorrected plasma input curves to obtain the TACs corresponding to the radioactive metabolites in plasma. The differences in appearance times of radioactivity between PET and plasma, whole blood and metabolite TACs were corrected by first estimating the delay of the arterial plasma input TAC, which produced the best fit of two-tissue compartment model to whole brain TAC, and then shifting all other input TACs accordingly. Cerebral blood volume was fixed to 5% in all tested models.

The 1TDI model was fitted with five parameters (V_B, K_{1P}, K_{2P}, K_{1M}, K_{2M}; P=parent, M=metabolite). The distribution volume of [^{11}C]SMW139 was estimated with the ratio of rate constants of the intact parent tracer between the plasma compartment and the combined tissue compartment; K_{1P}/K_{2P} (V_{TDI}). Additionally, tracer binding was quantified with the total volume of distribution V_{T2T} of a reversible 2TCM, where the model was fitted with five parameters (V_B, K_1, K_2, K_3, K_4) and where $V_{T2T} = K_1/K_2(1+K_3/K_4)$. The modelling was carried out with in house software (fitk2di and fitk4; http://www.turkupetcentre.net/programs/doc/).

Parent fraction and plasma protein binding of the parent tracer and its radiometabolites

Arterial blood samples were drawn at 0, 5, 10, 20, 40, 60 and 90 min p.i. and the plasma was separated by centrifugation (4 °C, 2118 g, 5 min). The plasma proteins were precipitated by adding 700 μL of acetonitrile to 500 μL of plasma, vortexing and centrifuging (3370 g, 3 min). The protein free supernatant was analyzed with high-performance liquid chromatography (HPLC) using a method described in the supplementary material of Brumberg et al. [25] to obtain fractions of intact [^{11}C]SMW139 and its radioactive metabolites for correcting the plasma TAC. A radioactive standard was prepared by spiking the time point 0 plasma supernatant with [^{11}C]SMW139 in order to analyze the correct peak of the chromatograms to correspond to the parent.

Parent and radiometabolite binding to plasma proteins was analyzed for a subset of subjects from blood samples drawn prior to [^{11}C]SMW139 injection and from 20 min p.i. From the time point 0 plasma drawn for in vitro protein binding analysis, 1 mL was frozen for later duplicate analysis. The in vitro plasma and in vivo 20 min parent fraction analysis plasma samples were used to analyze parent and radiometabolite plasma protein binding with separate ultrafiltration membrane corrections.

MRI and PET image processing and analysis

A 3T MRI (Philips Ingenia/Philips Ingenuity, Best, The Netherlands) was acquired for all study participants with T1, T2, FLAIR, 3DT1, and gadolinium-enhanced T1. The dynamic PET images were smoothed, realigned, and co-registered using statistical parametric mapping (SPM12; Wellcome Trust Center for Neuroimaging, London, UK) according to a previously described procedure [6]. The images were resliced to match the 1-mm^3 voxel size of the MRI images.

The Lesion Segmentation Toolbox (LST) [27] was used in SPM to create FLAIR masks, which were manually edited to correspond to chronic T1 lesions to create T1 masks following a previously described procedure [8]. Perilesional masks were created by dilating the lesion mask by 3 mm, and then subtracting the core image from the dilated image. Separate masks were created for the Gd+lesions. NAWM masks were created for each subject by subtracting edited FLAIR lesion masks from segmented white matter. Finally, T1 images were filled with the T1 masks by employing the lesion filling tool of LST in SPM. The filled T1 image was used to segment whole-brain volume (BV) and volumes of different brain areas with FreeSurfer (https://surfer.nmr.mgh.harvard.edu/) for PET assessments.

Statistical analysis

The statistical analysis was performed with SPSS 28.0 (IBM Corp., Armonk, NY, USA). Figures were created with Prism 10.1.2 (GraphPad software Inc. La Jolla, CA, USA). Group level means of V_T estimates across different brain areas were compared between MS patients and

HCs, and between PMS and RMS with Student's t-test. Among MS patients, Group level means of V_T estimates were compared between the T1 lesion masks, the 3 mm perilesional rim masks, and the NAWM masks with paired t-tests. Normality of the data was confirmed with the Shapiro-Wilk test. Linear correlations between V_T estimates, lesion volume, BV, thalamus volume, and demographic variables were measured with the Pearson correlation coefficient. The effects of disease duration and BV on V_{TDI} were estimated with multiple linear regression. All tests were two-tailed, and the alpha was set to 0.05 for all analyses with no correction for multiple comparisons.

Results

Study subject demographics and other baseline characteristics

26 subjects underwent the study procedures and the final analyzed cohorts consisted of 15 MS patients ($n=6$ for RMS, $n=9$ for PMS) and 9 HCs. 2 subjects (1 PMS and 1 HC) were excluded from the analysis due to technical issues during the PET visits. All RMS patients were enrolled < 0.5 years (mean 0.12 years, SD 0.06) from diagnosis and PET imaged with [^{11}C]SMW139 approximately 4 months thereafter. PMS patients were imaged > 10 years (mean 16.9 years, SD 4.3) from diagnosis immediately after inclusion. Compared to patients with MS, the HCs were of comparable age [mean (SD) 47,5 (10.1) vs. 49.6 (14.5) years, $p=0.479$, respectively]. Compared to the RMS patients, the PMS cohort had a significantly higher EDSS (median 2.0 vs. 6.0, mean 2.5 vs. 5.1, $p=0.005$, respectively), and the two patient cohorts were of comparable age [mean (SD) 45.0 (11.7) vs. 49.2 (9.3) years, $p=0.712$, respectively]. The male to female (M/F) ratio was unequal between all cohorts but comparable between all MS and HCs: 6/3 (33% F), 9/6 (40% F), 4/5 (56% F) and 5/1 (17% F) for HCs, MS, PMS and RMS, respectively. At the time of PET imaging, two patients in the RMS cohort had started treatment with i.v. natalizumab, 1 patient had received a single dose of i.v ocrelizumab, and 3 patients had received a single i.v. dose of rituximab. Three PMS patients were treated with rituximab, one with natalizumab, and one with fingolimod. MS lesion loads and other imaging characteristics are displayed in Table 1.

Parent fraction and protein binding of [^{11}C]SMW139

The plasma parent fraction decreased steadily down to approximately 45% over the course of the 90 min sampling time. The mean parent fraction in the PMS group was indicative of slightly faster metabolism, while metabolism of [^{11}C]SMW139 was non-significantly slower among the RMS and HC groups (Fig. 1).

The plasma protein binding analysis of frozen and fresh plasma samples yielded similar results. The mean (SD) parent free fraction (free parent over all parent in plasma, $f_{P/P}$) of [^{11}C]SMW139 was 0.013 (0.004) and 0.013 (0.002) ($n=11$ for both) for fresh and frozen samples, respectively, and 0.010 (0.004) ($n=9$) for the in vivo 20 min sample. The mean (SD) fraction of free radiometabolites over all radiometabolites was 0.425 (0.132) and the fraction of free radiometabolites over all free radioactivity in plasma was 0.88 (0.06) at 20 min. The mean $f_{P/P}$ was

Table 1 MRI variables and [^{11}C]SMW139 V_{TDI} (0–60 min)

	n	Min.	Max.	Mean	SD	*p*
Brain Volume (cm^3) HC	9	939.20	1267.21	1148.24	109.16	0.665*
Brain Volume (cm^3) RMS	6	1069.40	1231.09	1172.81	61.34	0.276**
Brain Volume (cm^3) PMS	9	814.63	1347.18	1055.53	173.10	
T1 lesion volume (cm^3) RMS	6	2.12	48.17	17.21	18.45	0.940**
T1 lesion volume (cm^3) PMS	9	2.62	44.14	16.60	12.57	
Number of Gd + lesions RMS	6	1	20	8.33	7.97	NA
SMW V_{TDI} T1 lesions RMS	6	0.09	0.14	0.11	0.02	0.194**
SMW V_{TDI} T1 lesions PMS	9	0.02	0.12	0.09	0.03	
SMW V_{TDI} 3 mm rim RMS	6	0.11	0.15	0.12	0.02	0.113**
SMW V_{TDI} 3 mm rim PMS	9	0.03	0.14	0.10	0.03	
SMW V_{TDI} Thalamus HC	9	0.03	0.32	0.13	0.09	0.723*
SMW V_{TDI} Thalamus RMS	6	0.10	0.19	0.14	0.03	0.071**
SMW V_{TDI} Thalamus PMS	9	0.04	0.16	0.11	0.04	
SMW V_{TDI} NAWM HC	9	0.04	0.16	0.11	0.04	0.962*
SMW V_{TDI} NAWM RMS	6	0.09	0.14	0.12	0.02	0.121**
SMW V_{TDI} NAWM PMS	9	0.04	0.14	0.10	0.03	

*For the comparison all MS vs. HC

**For the comparison RMS vs. PMS

V_{TDI} = dual-input distribution volume of parent tracer (K_{1P}/K_{2P}). 3 mm rim = T1 perilesional 3 mm rim. NAWM = Normal appearing white matter. HC = Healthy control. RMS = Relapsing MS. PMS = Progressive MS

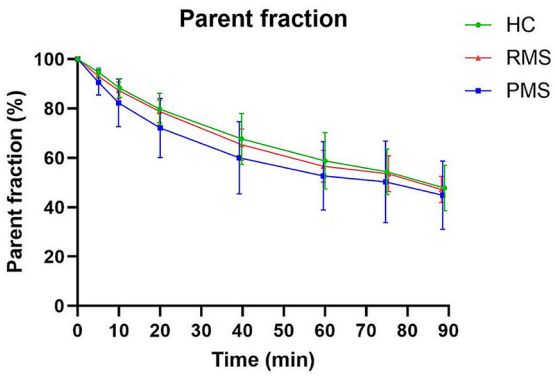

Fig. 1 The mean percentages of unchanged [^{11}C] SMW139 of the total radioactivity in the plasma samples (parent fraction) of the healthy controls (HC), relapsing MS (RMS) and progressive MS (PMS)

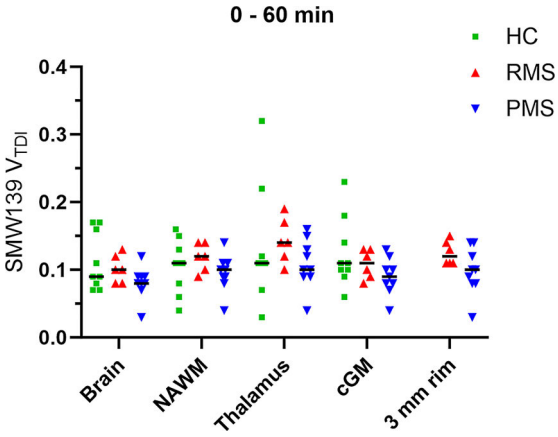

Fig. 2 [11 C]SWM139 V_{TDI} (0–60 min) in the normal appearing white matter (NAWM), thalamus, cortical gray matter (cGM) and T1 perilesional 3 mm rim (3 mm rim) among healthy controls (HC), relapsing MS (RMS) and progressive MS (PMS)

0.0138 (n=3), 0.0096 (n=5) and 0.0093 (n=3) for HCs, PMS and RMS, respectively.

PET modelling

According to visual inspection (Supplement 1), AIC and logarithm of mean residual sum of squares (log (1/n) (model – data)^2, where n=no. data points) (Supplement 2), both tested models fitted the data well. Coefficients of variation (CoV) of V_T estimates were substantially higher with the 2TCM (Supplement 2). Compared to HCs, the overall performance of 1TDI was better among MS patients, and 0–40 min and 0–60 min performed similarly according to AIC (Supplement 3). Finally, 0–60 min data was chosen for the primary analyses based on marginally lower CoV compared to 0–40 min and 0–90 min (Supplement 2–3). Additional exploratory analyses were performed with 0–40 min and 0–90 min data for

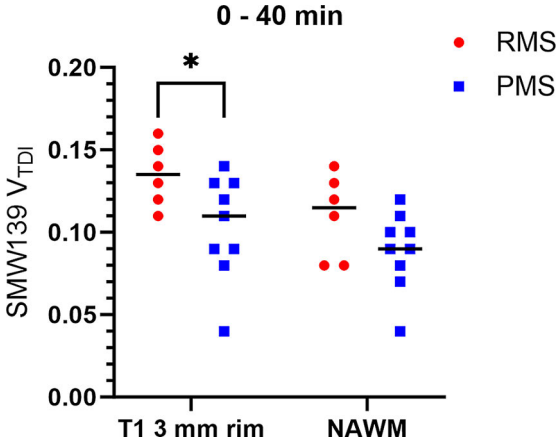

Fig. 3 T1 perilesional 3 mm rim and normal appearing white matter (NAWM) among relapsing MS (RMS) and progressive MS (PMS). *p=0.049

the 1TDI and 2TCM models, respectively. V_T estimates from thalamus (R=0.800, p<0.001) and cGM (R=0.630, p<0.001) correlated significantly between the models (0–60 min 1TDI and 0–90 min 2TCM), while estimates from NAWM (R=0.158, p=0.461) and lesional or perilesional (R=-0.04, p=0.888) white matter did not.

[^{11}C]SMW139 binding in RMS and PMS patients compared to healthy control subjects

Compared to healthy controls, whole-brain, NAWM, thalamic and cGM uptake of [^{11}C]SMW139 was similar in MS patients (n=15) at group level. After explorative correction for group level mean $f_{P/P}$ (V_{TDI} / $f_{P/P}$), mean (SD) NAWM V_{TDI} was significantly higher among all MS compared to HCs [11.15 (3.09) vs. 7.69 (2.80), p=0.012, respectively].

V_{TDI} estimates were somewhat higher in the RMS cohort compared to PMS and HCs, but the differences were not statistically significant (Table 1; Fig. 2). In the 3 mm perilesional rim of all T1 lesions, the mean (SD) V_{TDI} was 0.123 (0.02) vs. 0.097 (0.03) (p=0.113) in the RMS and PMS cohorts, respectively. Exploratory analysis with 0–40 min data revealed a significant difference between the two groups [Fig. 3.133 (0.02) vs. 0.101 (0.03), p=0.049, respectively]. The 2TCM yielded no significant differences between the groups, when all MS was compared to HCs (Supplement 4), or when RMS was compared to PMS (Supplement 5).

Exploratory analysis of [^{11}C]SMW139 binding in MS lesions compared with NAWM and the perilesional areas

Compared to MS lesion core areas, V_{TDI} estimates were significantly higher in the NAWM and perilesional 3 mm rims among all MS patients (Table 2; Fig. 4). Analyzed separately, perilesional tracer uptake was significantly

Table 2 Lesional, perilesional and NAWM [^{11}C]SMW139 V_{TDI}

Comparison	Mean	SD	*p*
3 mm rim - T1 lesions MS	0.0123	0.0140	**0.004**
3 mm rim - NAWM MS	0.0017	0.0124	0.611
NAWM MS - T1 lesions MS	0.0106	0.0176	**0.034**
3 mm rim - T1 lesions PMS	0.0097	0.0144	0.078
3 mm rim - NAWM PMS	0.0007	0.0136	0.879
NAWM PMS - T1 lesions PMS	0.0090	0.0178	0.170
3 mm rim - T1 lesions RMS	0.0162	0.0138	**0.034**
3 mm rim - NAWM RMS	0.0031	0.0114	0.536
NAWM RMS - T1 lesions RMS	0.0131	0.0185	0.143
Gd + T1 lesions - T1 lesions RMS	0.0067	0.0138	0.403
Gd + 3 mm rim – 3 mm rim RMS	0.0164	0.0510	0.623

3 mm rim = T1 perilesional 3 mm rim, NAWM = Normal appearing white matter RMS = Relapsing MS. PMS = Progressive MS

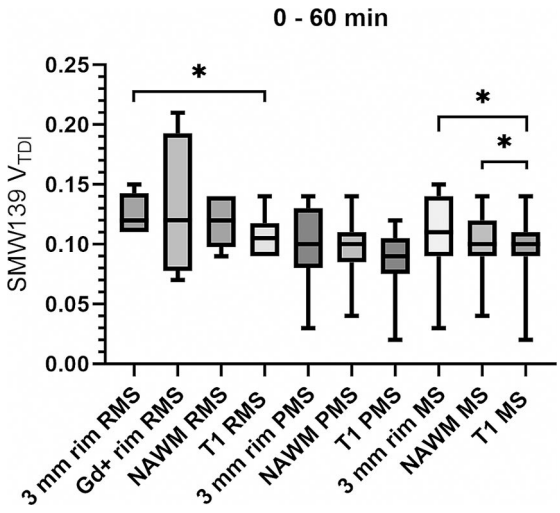

Fig. 4 [11 C]SWM139 V_{TDI} in the 3 mm perilesional rims, normal appearing white matter (NAWM) and T1 lesions among relapsing MS (RMS), progressive MS (PMS) and all MS. ***p < 0.05** (Table 2 for pairwise comparisons)

higher compared to lesions among RMS patients, but not among PMS patients. V_{TDI} estimates within the Gd + lesions and in the 3 mm rim around Gd + lesions were not significantly higher compared to all RMS T1 lesions and the perilesional 3 mm area in general, respectively (Table 2). Lesional V_{T2T} estimates were significantly higher compared to the NAWM and the perilesional area among all MS patients. (Supplement 6).

Exploratory analysis of [^{11}C]SMW139 binding in relation to demographic characteristics and MRI variables

Age correlated negatively with V_{TDI} in the 3 mm perilesional area among all MS patients (R= -0.558, p=0.031; Fig. 5B), and non-significantly with NAWM V_{TDI} (R= -0.465, p=0.081), but no correlation with NAWM V_{TDI} was seen among all subjects (n=24, R=0.024, p=0.91). Among all MS patients or among RMS or PMS, V_{TDI} estimates did not correlate with EDSS (results not shown). Among PMS patients, time from diagnosis correlated with NAWM V_{TDI} (Fig. 5). Of note, BV or age did not correlate with disease duration among PMS patients (R= -0.259, p=0.501 and R= -0.350, p=0.365, respectively). Among all subjects, V_{TDI} estimates in the NAWM correlated with BV, and the same was true for the 3 mm perilesional rim among all MS (Fig. 5).

Among PMS with NAWM V_{TDI} as the dependent variable, both disease duration (β=0.561, t=2.603, p=0.041) and BV (β=0.547, t=2.536, p=0.044) added significantly to the prediction (R^2=0.855, F(2,6)=8.166, p=0.019). V_{TDI} in the perilesional area or NAWM did not correlate with overall T1 lesion volume (results not shown). No significant correlations with V_{T2T} estimates and demographic variables or brain or lesion volume were found with the 2TCM model. V_{TDI} estimates and BV were significantly higher among male subjects compared to females across all examined brain areas. The two groups were of similar age and EDSS, and lesion volumes were comparable, but the time from diagnosis among female subjects was somewhat longer (p>0.05, Supplement 7). The correlation of NAWM V_{TDI} with BV was abolished (R=0.076, p=0.791), when all male subjects (n=15) were analyzed separately.

Discussion

Even though uptake in the 3 mm perilesional rims of T1 lesions suggested in vivo sensitivity towards activated microglia in MS, tracer uptake in this cohort of MS patients was not significantly higher compared to HCs. Exploratory analyses indicated increased tracer binding in the NAWM among subjects with longer disease duration, which is consistent with previous MS imaging studies indicating diffuse activation of microglia in the NAWM as MS progresses [4, 12], but this finding is to be interpreted with caution. Despite high affinity of [^{11}C] SMW139 for inflammatory microglia [10], the wide range of $P2X_7$R-expression across different neural and cellular targets [28] may have influenced the highly variable binding estimates, and reduced accuracy with regards to inflammatory microglia.

Hagens and colleagues reported somewhat improved single-input 2TCM fits with longer p.i. time and, due to unreliable estimation of the disassociation rate (k4) in smaller regions of interest (ROIs), by binding k4 to the whole-brain value [23]. Even as all kinetic parameters were fitted with the 2TCM in the present study, higher V_{T2T} inside MS lesions compared to the surrounding white matter (Supplement 6) was consistent with previously published findings [23], where a discrepancy with lesional binding potential estimates was also observed. In the present study, thalamic and cGM V_T estimates correlated moderately and strongly between 1TDI and 2TCM,

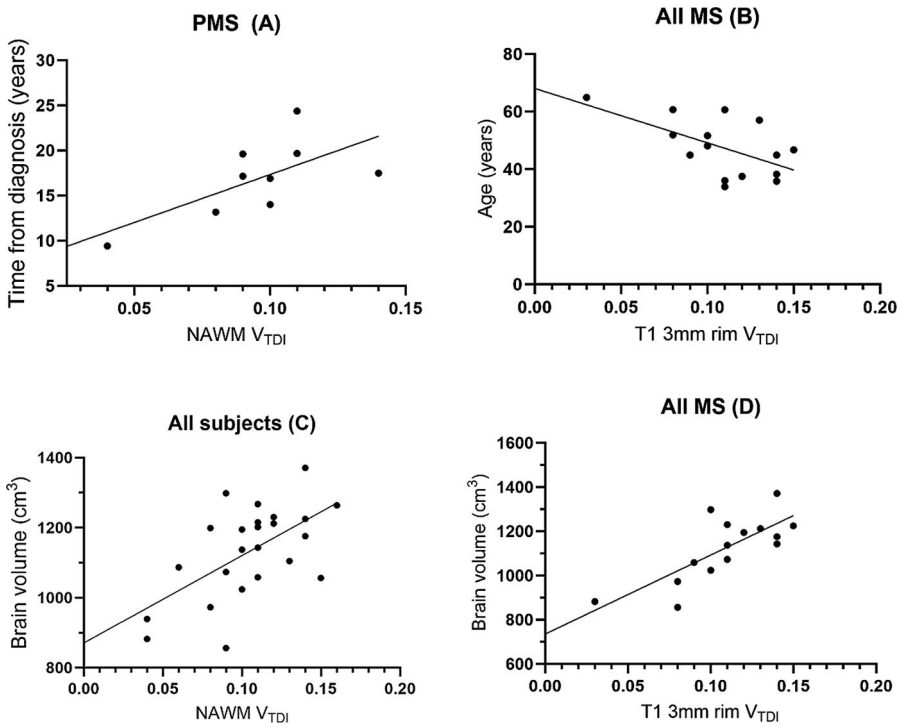

Fig. 5 V_{TDI} in the normal appearing white matter (NAWM) among progressive MS (PMS) correlated with disease duration (A; $R = 0.666$, $p = 0.05$). V_{TDI} in the T1 perilesional 3 mm rim among all MS correlated with age (B; $R = -0.558$, $p = 0.031$). V_{TDI} in the NAWM among all subjects correlated with brain volume (C; $R = 0.577$, $p = 0.003$). V_{TDI} in the T1 perilesional 3 mm rim among all MS correlated with brain volume (D; $R = 0.734$, $p = 0.002$)

respectively, while WM estimates did not. Considering the above, it is deemed likely that two-compartment models improve AIC with [^{11}C]SMW139 by fitting radiometabolite build-up between the tissue compartments, and this effect is accentuated with longer fits. A strong correlation between the 1TDI and 2TCM was seen in the cGM, an area with a relatively scarce distribution of activated microglia in MS [29].

In addition, Brumberg and colleagues reported markedly superior 2TDI AIC only in the cGM, whereas the 1TDI was associated with robust fits across all examined regions, and with somewhat lower %SE [25]. A 2TDI model does not reliably fit in all cases and smaller regions of interest with [^{11}C]SMW139, while the 1TDI could be more sensitive to inaccuracies in plasma input data. The locus of interest [7, 30–32] in MS brain imaging is primarily in the NAWM, where the 1TDI performed significantly better in the present study compared to previous GM fits [25] according to AIC, and in small perilesional WM regions, where estimates may also be affected by the partial volume effect. Based on the above, 1TDI was chosen for the primary analysis. In addition to CoV and AIC, the 0–60 min fit was preferred based on the theoretically reduced effect of radioactive metabolites, while it was also assumed that fits significantly below 60 min would describe the data inadequately. Together with rapid tracer metabolism, the 20-min half-life of carbon-11 reduces the reliability estimates beyond 60 min p.i. even further.

Beyond pharmacokinetic considerations, a viable PET model is expected to produce estimates of target engagement that are in line with the known distribution of the tracer's cognate receptors. In MS, microglia-associated TSPO expression is concentrated to active lesions and chronic lesion rims, and to a lesser extent chronic lesion centers and the NAWM, while inactive lesions and grey matter lesions are relatively devoid of microglia. HLADR+inflammatory microglia are most abundant at chronic lesion rims [29]. Similarly, $P2X_7R$-expression is more prominent in acute active lesions and chronic active lesion rims [10]. Compared to chronic and chronic active lesions, acute active MS lesions represent a small fraction of overall lesion count [33, 34]. The fraction of early active lesions declines rapidly, and has been estimated to represent < 5% of all lesios at 5–10 years after disease onset [33].

Thus it was postulated that at group level, most specific binding of [^{11}C]SMW139 in the WM of MS patients would take place in the immediate area around T1

lesions, and that lesional binding would decline after the initial phase of the disease. In the current study, perilesional binding was significantly higher than lesional binding, but not significantly higher than NAWM binding. In the newly diagnosed cohort of RMS, perilesional tracer binding was increased compared to PMS patients, although it is acknowledged that the groups were not sex-matched. Lesions that Gd-enhanced approximately 4 months prior to PET imaging did not exhibit significantly higher tracer uptake, which indicates that disruption of the blood brain barrier did not significantly affect perilesional binding estimates among RMS.

The free fraction of [^{11}C]SMW139 was low, while radiometabolites contributed significantly to overall radioactivity passing through the blood brain barrier. 88% of the free radioactivity was due to circulating radiometabolites at 20 min. Estimates obtained by using protein binding to correct V_{TP} are susceptible to minor errors in $f_{p/P}$ analysis, and thus correcting for the group level mean of the free parent was explored. This resulted in a significantly higher mean free parent V_T among MS patients compared to HCs, but incomplete protein binding data precludes conclusions on group level differences based on this sub-analysis. This approach should be considered in subsequent studies with [^{11}C]SMW139.

[^{11}C]SMW139 uptake was significantly increased in male subjects compared to females, and the strong correlation with BV was completely abolished when male subjects were analyzed separately. A similar sex disparity in tracer uptake has been observed with the microglial TSPO tracer [^{11}C]PK11195 [35]. While it is acknowledged that genetic polymorphism of the P2X$_7$R is considerable both between and within species [36], these findings are in agreement with sex-dependent purinergic receptor expression [37], and an inflammatory microglial transcriptome in male mice [38].

Interestingly, MS disease duration correlated with tracer uptake, and this correlation was not explained by age or sex, as disease duration was somewhat longer among females. Significant correlations with MS-related disability and NAWM uptake of [^{11}C]PK11195 have been reported previously [3, 4]. Also considering the higher uptake in RMS, lower tracer uptake in the perilesional rims among older subjects suggests that P2X$_7$R-signaling may be significant at the early stages of chronic active lesion formation. [^{11}C]SMW139 uptake peaks at the early stage of EAE [18].

Conclusions

No conclusive evidence for the applicability of [^{11}C]SMW139 to detect MS-related smoldering inflammation was obtained. Even though disease duration correlated with tracer binding in the NAWM, overall tracer uptake in the MS brain was not significantly higher compared to HCs. Age and sex are to be matched with a careful emphasis when studies with this tracer are conducted. Further information on the applicability of [^{11}C]SMW139 PET in MS could be obtained by correlating the current results with longitudinal clinical outcomes and progression-related biomarkers.

Abbreviations

TSPO	18-kDa translocator protein
P2X$_7$R	Adenosine triphosphate -gated cation channel receptor
AIC	Akaike information criterion
CoV	Coefficient of variation
cGM	Cortical grey matter
dGM	Deep gray matter
k4	Disassociation rate from the specific tissue compartment
V_{TDI}	Distribution volume of parent [11 C]SMW139
DI	Dual-input
EAE	Experimental autoimmune encephalitis
FWHM	Full width at half maximum
HC	Healthy control subject
HPLC	High-performance liquid chromatography
HRRT	High-resolution research tomograph
LST	Lesion segmentation toolbox
MRI	Magnetic resonance imaging
MS	Multiple sclerosis
NAWM	Normal appearing white matter
PET	Positron emission tomography
p.i.	Post injection
PMS	Progressive MS
ROI	Region of interest
RMS	Relapsing MS
1TDI	Single tissue compartment dual-input model
SD	Standard deviation
SPM	Statistical parametric mapping
TAC	Time activity curve
2TCM	Two-tissue compartment model
VT	Volume of distribution
BV	Whole-brain volume

Supplementary Information

The online version contains supplementary material available at https://doi.org/10.1186/s13550-024-01186-3.

Supplementary Material 1

Acknowledgements

Not applicable.

Author contributions

JL: Writing – original draft (lead), Writing - review and editing (lead), Visualization (lead), Investigation (equal), Formal analysis (equal). RA: Writing – original draft (supporting), Investigation (supporting), Writing - review and editing (supporting); Visualization (supporting). JT: Formal analysis (equal), Writing - review and editing (supporting). MS: Investigation (equal); Conceptualization (supporting). EMK: Investigation (equal). MN: Project management (lead); Funding acquisition (supporting), Investigation (supporting). SH: Resources (equal). JR: Resources (equal). JD: Investigation (supporting), Resources (supporting). JG: Investigation (supporting), Resources (supporting). MK: Supervision (supporting), Resources (supporting). VO: Formal analysis (supporting), Conceptualization (supporting). LA: Supervision (lead); Conceptualization (lead); Funding acquisition (lead); Writing – review and editing (supporting).

Funding

This work was supported by a grant from the National Multiple Sclerosis Society, The Jane and Aatos Erkko Foundation, The Research Council of Finland (decision number: 330902), the Sigrid Juselius Foundation, State research funding of the Turku University Hospital expert responsibility area,

Finnish Governmental Research Funding (VTR) for Turku University Hospital, and the InFLAMES Flagship Programme of The Research Council of Finland (decision number 337530).

Data availability
Any anonymized data used in the preparation of this article will be made available by the request of a qualified investigator.

Declarations

Ethics approval and consent to participate
The study was conducted according to the principles of the Declaration of Helsinki. All subjects were adults (> 18 years old), and provided written informed consent. The study was approved by the Ethics Committee of the Hospital District of Southwest Finland.

Consent for publication
Not applicable.

Conflict of interest
The authors have nothing to disclose.

Received: 13 June 2024 / Accepted: 20 November 2024
Published online: 05 December 2024

References

1. Chauveau F, Becker G, Boutin H. Have (R)-[11 C]PK11195 challengers fulfilled the promise? A scoping review of clinical TSPO PET studies. Eur J Nucl Med Mol Imaging. Springer Science and Business Media Deutschland GmbH; 2021. pp. 201–20.
2. Banati RB, Newcombe J, Gunn RN, Cagnin A, Turkheimer F, Heppner F et al. The peripheral benzodiazepine binding site in the brain in multiple sclerosis: Quantitative in vivo imaging of microglia as a measure of disease activity. Brain [Internet]. 2000;123:2321–37. https://doi.org/10.1093/brain/123.11.2321
3. Sucksdorff M, Matilainen M, Tuisku J, Polvinen E, Vuorimaa A, Rokka J et al. Brain TSPO-PET predicts later disease progression independent of relapses in multiple sclerosis. Brain [Internet]. 2020;143:3318–30. https://www.ncbi.nlm.nih.gov/pubmed/33006604
4. Rissanen E, Tuisku J, Vahlberg T, Sucksdorff M, Paavilainen T, Parkkola R et al. Microglial activation, white matter tract damage, and disability in MS. Neurol Neuroimmunol Neuroinflamm [Internet]. 2018;5:e443. https://www.ncbi.nlm.nih.gov/pubmed/29520366
5. Misin O, Matilainen M, Nylund M, Honkonen E, Rissanen E, Sucksdorff M et al. Innate Immune Cell–Related Pathology in the Thalamus Signals a Risk for Disability Progression in Multiple Sclerosis. Neurology - Neuroimmunology Neuroinflammation [Internet]. 2022;9:e1182. http://nn.neurology.org/content/9/4/e1182.abstract
6. Sucksdorff M, Tuisku J, Matilainen M, Vuorimaa A, Smith S, Keitilä J et al. Natalizumab treatment reduces microglial activation in the white matter of the MS brain. Neurol Neuroimmunol Neuroinflamm. 2019;6.
7. Lehto J, Sucksdorff M, Nylund M, Raitanen R, Matilainen M, Airas L. PET-measurable innate immune cell activation reduction in chronic active lesions in PPMS brain after rituximab treatment: a case report. J Neurol [Internet]. 2022 [cited 2023 Jan 24];1:1–4. https://link.springer.com/article/https://doi.org/10.1007/s00415-022-11539-4
8. Lehto J, Nylund M, Matilainen M, Sucksdorff M, Vuorimaa A, Rajander J et al. Longitudinal stability of progression-related microglial activity during teriflunomide treatment in patients with multiple sclerosis. Eur J Neurol [Internet]. 2023;n/a. https://doi.org/10.1111/ene.15834
9. Sucksdorff M, Rissanen E, Tuisku J, Nuutinen S, Paavilainen T, Rokka J, et al. Evaluation of the effect of fingolimod treatment on microglial activation using serial PET imaging in multiple sclerosis. J Nucl Med. 2017;58:1646–51.
10. Beaino W, Janssen B, Kooij G, van der Pol SMA, van Het Hof B, van Horssen J et al. Purinergic receptors P2Y12R and P2X7R: Potential targets for PET imaging of microglia phenotypes in multiple sclerosis. J Neuroinflammation [Internet]. 2017 [cited 2023 Feb 7];14:1–16. https://jneuroinflammation.biomedcentral.com/articles/https://doi.org/10.1186/s12974-017-1034-z
11. Giovannoni G, Popescu V, Wuerfel J, Hellwig K, Iacobeus E, Jensen MB et al. Smouldering multiple sclerosis: the 'real MS.'Ther. Adv Neurol Disord. 2022;15.
12. Nylund M, Sucksdorff M, Matilainen M, Polvinen E, Tuisku J, Airas L. Phenotyping of multiple sclerosis lesions according to innate immune cell activation using 18 kDa translocator protein-PET. Brain Commun. 2022;4.
13. Monif M, Burnstock G, Williams DA. Microglia: proliferation and activation driven by the P2X7 receptor. Int J Biochem Cell Biol [Internet]. 2010 [cited 2023 Jun 15];42:1753–6. https://pubmed.ncbi.nlm.nih.gov/20599520/
14. Bhattacharya A, Biber K. The microglial ATP-gated ion channel P2X7 as a CNS drug target. Glia [Internet]. 2016 [cited 2023 Jun 15];64:1772–87. https://pubmed.ncbi.nlm.nih.gov/27219534/
15. Clark AK, Staniland AA, Marchand F, Kaan TKY, McMahon SB, Malcangio M. P2X7-Dependent Release of Interleukin-1β and Nociception in the Spinal Cord following Lipopolysaccharide. The Journal of Neuroscience [Internet]. 2010 [cited 2023 Jun 15];30:573. /pmc/articles/PMC2880485/
16. Fantoni ER, Dal Ben D, Falzoni S, Di Virgilio F, Lovestone S, Gee A. Design, synthesis and evaluation in an LPS rodent model of neuroinflammation of a novel 18F-labelled PET tracer targeting P2X7. EJNMMI Res [Internet]. 2017 [cited 2023 Nov 24];7:1–12. https://link.springer.com/articles/https://doi.org/10.1186/s13550-017-0275-2
17. Territo PR, Meyer JA, Peters JS, Riley AA, McCarthy BP, Gao M et al. Characterization of 11 C-GSK1482160 for Targeting the P2X7 Receptor as a Biomarker for Neuroinflammation. J Nucl Med [Internet]. 2017 [cited 2023 Nov 24];58:458–65. https://pubmed.ncbi.nlm.nih.gov/27765863/
18. Beaino W, Janssen B, Kooijman E, Vos R, Schuit RC, O'Brien-Brown J et al. PET imaging of P2X7R in the experimental autoimmune encephalomyelitis model of multiple sclerosis using [11 C]SMW139. J Neuroinflammation [Internet]. 2020 [cited 2024 Feb 28];17:1–18. https://jneuroinflammation.biomedcentral.com/articles/https://doi.org/10.1186/s12974-020-01962-7
19. Burnstock G. P2X ion channel receptors and inflammation. Purinergic Signalling. 2016 12:1 [Internet]. 2016 [cited 2023 Jun 15];12:59–67. https://link.springer.com/article/10.1007/s11302-015-9493-0
20. Wilkinson SM, Barron ML, O'Brien-Brown J, Janssen B, Stokes L, Werry EL et al. Pharmacological Evaluation of Novel Bioisosteres of an Adamantanyl Benzamide P2X7 Receptor Antagonist. ACS Chem Neurosci [Internet]. 2017 [cited 2023 Jun 15];8:2374–80. https://pubs.acs.org/doi/full/10.1021/acschemneuro.7b00272
21. Janssen B, Vugts DJ, Wilkinson SM, Ory D, Chalon S, Hoozemans JJM et al. Identification of the allosteric P2X7 receptor antagonist [11 C]SMW139 as a PET tracer of microglial activation. Scientific Reports 2018 8:1 [Internet]. 2018 [cited 2023 Jun 15];8:1–10. https://www.nature.com/articles/s41598-018-24814-0
22. Akaike H. Information Theory and an Extension of Information the Maximum Theory Likelihood and an Principle Extension of the Maximum Likelihood Principle. Biogeochemistry [Internet]. 1998 [cited 2023 Jun 15];1998:199–213. https://link.springer.com/chapter/https://doi.org/10.1007/978-1-4612-1694-0_15
23. Hagens MHJ, Golla SSV, Janssen B, Vugts DJ, Beaino W, Windhorst AD, et al. The P2X7 receptor tracer [11 C]SMW139 as an in vivo marker of neuroinflammation in multiple sclerosis: a first-in man study. Eur J Nucl Med Mol Imaging. 2020;47:379–89.
24. Aarnio R, Alzghool OM, Wahlroos S, O'Brien-Brown J, Kassiou M, Solin O et al. Novel plasma protein binding analysis method for a PET tracer and its radiometabolites: A case study with [11 C]SMW139 to explain the high uptake of radiometabolites in mouse brain. J Pharm Biomed Anal. 2022;219.
25. Brumberg J, Aarnio R, Forsberg A, Marjamäki P, Kerstens V, Moein MM et al. Quantification of the purinergic P2X7 receptor with [11 C]SMW139 improves through correction for brain-penetrating radiometabolites. J Cereb Blood Flow Metab [Internet]. 2023 [cited 2023 Jun 16];43:258–68. https://pubmed.ncbi.nlm.nih.gov/36163685/
26. Sureau FC, Reader AJ, Comtat C, Leroy C, Ribeiro MJ, Buvat I et al. Impact of image-space resolution modeling for studies with the high-resolution research tomograph. J Nucl Med [Internet]. 2008 [cited 2024 Feb 13];49:1000–8. https://pubmed.ncbi.nlm.nih.gov/18511844/
27. Schmidt P, Gaser C, Arsic M, Buck D, Förschler A, Berthele A, et al. An automated tool for detection of FLAIR-hyperintense white-matter lesions in multiple sclerosis. NeuroImage. 2012;59:3774–83.
28. Kanellopoulos JM, Delarasse C. Pleiotropic Roles of P2X7 in the Central Nervous System. Front Cell Neurosci [Internet]. 2019 [cited 2024 Sep 11];13. https://pubmed.ncbi.nlm.nih.gov/31551714/
29. Nutma E, Stephenson JA, Gorter RP, de Bruin J, Boucherie DM, Donat CK et al. A quantitative neuropathological assessment of translocator protein expression in multiple sclerosis. Brain [Internet]. 2019;142:3440–55. https://www.ncbi.nlm.nih.gov/pubmed/31578541

30. Airas L, Rissanen E, Rinne JO. Imaging neuroinflammation in multiple sclerosis using TSPO-PET. Clin Transl Imaging. Springer-Verlag Italia s.r.l.; 2015. pp. 461–73.
31. Airas L, Yong VW. Microglia in multiple sclerosis - pathogenesis and imaging. Curr Opin Neurol [Internet]. 2022 [cited 2023 Jan 24];35:299–306. https://pubmed.ncbi.nlm.nih.gov/35674072/
32. Bodini B, Tonietto M, Airas L, Stankoff B. Positron emission tomography in multiple sclerosis - straight to the target. Nat Rev Neurol [Internet]. 2021; https://www.ncbi.nlm.nih.gov/pubmed/34545219
33. Frischer JM, Weigand SD, Guo Y, Kale N, Parisi JE, Pirko I et al. Clinical and pathological insights into the dynamic nature of the white matter multiple sclerosis plaque. Ann Neurol [Internet]. 2015 [cited 2024 Jan 5];78:710–21. https://pubmed.ncbi.nlm.nih.gov/26239536/
34. Kuhlmann T, Ludwin S, Prat A, Antel J, Brück W, Lassmann H. An updated histological classification system for multiple sclerosis lesions. Acta Neuropathol [Internet]. 2017 [cited 2023 Apr 6];133:13–24. https://pubmed.ncbi.nlm.nih.gov/27988845/
35. Laaksonen S, Saraste M, Nylund M, Hinz R, Snellman A, Rinne J et al. Sex-driven variability in TSPO-expressing microglia in MS patients and healthy individuals. Front Neurol [Internet]. 2024 [cited 2024 Feb 28];15:1352116. https://www.frontiersin.org/articles/https://doi.org/10.3389/fneur.2024.1352116/full
36. Schmidt S, Isaak A, Junker A. Spotlight on P2X7 receptor PET imaging: a bright target or a failing star? Int J Mol Sci. 2023;24(2):1374. https://doi.org/10.3390/ijms24021374.
37. Guneykaya D, Ivanov A, Hernandez DP, Haage V, Wojtas B, Meyer N et al. Transcriptional and Translational Differences of Microglia from Male and Female Brains. Cell Rep [Internet]. 2018 [cited 2024 Jun 5];24:2773–2783.e6. https://pubmed.ncbi.nlm.nih.gov/30184509/
38. Villa A, Gelosa P, Castiglioni L, Cimino M, Rizzi N, Pepe G et al. Sex-Specific Features of Microglia from Adult Mice. Cell Rep [Internet]. 2018 [cited 2024 Jun 5];23:3501–11. https://pubmed.ncbi.nlm.nih.gov/29924994/

Publisher's note

Supplement 1–7

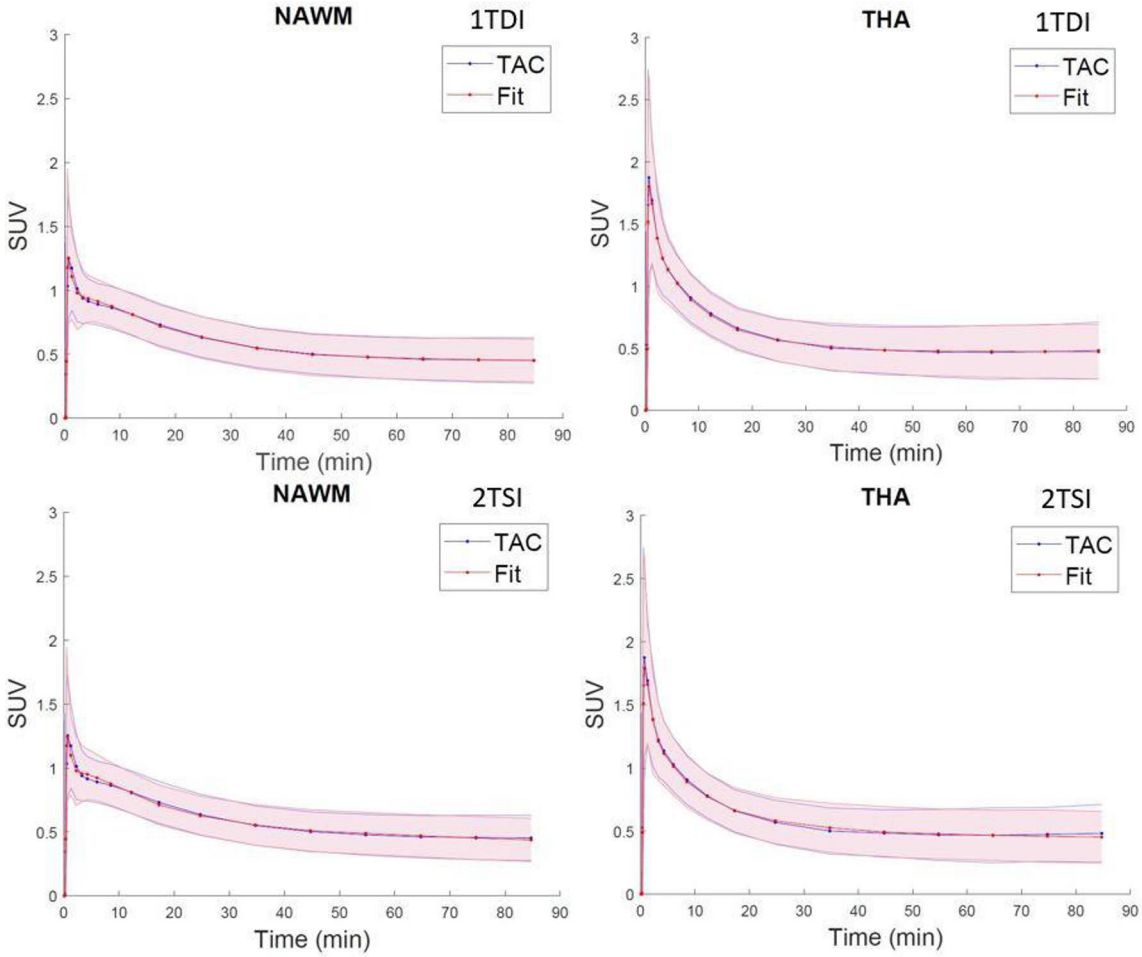

Supplement 1. Mean fits across all subjects with the dual-input one-compartment (1TDI; upper row) and single-input two-compartment (2TSI; lower row) models. NAWM = Normal appearing white matter. THA = Thalamus. SUV = Standardized uptake value. TAC = time activity curve

Supplement 2. 1TDI and 2TCM 90 min and 60 min AIC and log(mean residual) for all subjects (HC and MS)

	N	Min.	Max.	Mean	SD	CoV
Brain_1TDI_90_AIC	24	-62.21	111.25	-10.1680	49.24198	NA
Brain_1TDI_90_CoV	24	NA	NA	NA	NA	0.35136
NAWM_1TDI_90_AIC	24	-82.40	111.24	-9.1166	50.94148	NA
NAWM_1TDI_90_CoV	24	NA	NA	NA	NA	0.29970

Tha_1TDI_90_AIC	24	-67.22	111.68	-5.5173	49.38296	NA
Brain_1TDI_60_AIC	24	-53.72	101.13	-5.9888	43.46122	NA
Brain_1TDI_60_CoV	24	NA	NA	NA	NA	0.33677
NAWM_1TDI_60_AIC	24	-66.66	101.12	-3.1746	44.59499	NA
NAWM_1TDI_60_CoV	24	NA	NA	NA	NA	0.29527
Tha_1TDI_60_AIC	24	-51.47	101.50	.1169	42.68589	NA
Brain_1TDI_90_log_residual	24	-3.63	4.63	-1.1509	2.34486	NA
NAWM_1TDI_90_log_residual	24	-4.59	4.63	-1.1008	2.42578	NA
Tha_1TDI_90_log_residual	24	-3.87	4.65	− .9294	2.35157	NA
Brain_1TDI_60_log_residual	24	-3.82	4.78	-1.1660	2.41451	NA
NAWM_1TDI_60_log_residual	24	-4.54	4.78	-1.0097	2.47750	NA
Tha_1TDI_60_log_residual	24	-3.69	4.81	− .8268	2.37144	NA
Brain_2TCM_90_AIC	24	-66.21	107.25	-14.1680	49.24198	NA
Brain_2TCM_90_CoV	24	NA	NA	NA	NA	0.63014
NAWM_2TCM_90_AIC	24	-86.40	107.24	-13.1166	50.94148	NA
NAWM_2TCM_90_CoV	24	NA	NA	NA	NA	0.65529
Tha_2TCM_90_AIC	24	-71.22	107.68	-9.5173	49.38296	NA
Brain_2TCM_60_AIC	24	-58.72	96.13	-10.9888	43.46122	NA
Brain_2TCM_60_CoV	24	NA	NA	NA	NA	0.78752
NAWM_2TCM_60_AIC	24	-71.66	96.12	-8.1746	44.59499	NA
NAWM_2TCM_60_CoV	24	NA	NA	NA	NA	0.82852
Tha_2TCM_60_AIC	24	-56.47	96.50	-4.8831	42.68589	NA
Brain_2TCM_90_log_residual	24	-3.63	4.63	-1.1509	2.34486	NA
NAWM_2TCM_90_log_residual	24	-4.59	4.63	-1.1008	2.42578	NA
Tha_2TCM_90_log_residual	24	-3.87	4.65	− .9294	2.35157	NA
Brain_2TCM_60_log_residual	24	-3.82	4.78	-1.1660	2.41451	NA
NAWM_2TCM_60_log_residual	24	-4.54	4.78	-1.0097	2.47750	NA
Tha_2TCM_60_log_residual	24	-3.69	4.81	− .8268	2.37144	NA

NAWM = Normal appearing white matter, Tha = thalamus, AIC = Aikaike information criterion, CoV = Coefficient of variation, log_residual = logarithm of mean residual sum of squares.

Supplement 3. 1TDI AIC and CoV among all MS, PMS and RMS with 0–60 min and 0–40 min fits

	N	Min.	Max.	Mean	SD	CoV
Brain_1TDI_60_AIC_MS	15	-53.72	11.76	-22.8424	20.24445	NA
Brain_1TDI_60_CoV_MS	15	NA	NA	NA	NA	0.36462
NAWM_1TDI_60_AIC_MS	15	-66.66	32.43	-13.6393	24.95961	NA
NAWM_1TDI_60_CoV_MS	15	NA	NA	NA	NA	0.27110
Tha_1TDI_60_AIC_MS	15	-41.91	14.76	-14.2919	16.81169	NA
Tha_1TDI_60_CoV_MS	15	NA	NA	NA	NA	0.30766
Brain_1TDI_60_AIC_PMS	9	-53.72	11.76	-26.1549	21.94664	NA
NAWM_1TDI_60_AIC_PMS	9	-66.66	32.43	-14.7823	29.00347	NA
Tha_1TDI_60_AIC_PMS	9	-41.91	14.76	-19.4912	17.02978	NA
Brain_1TDI_60_AIC_RMS	6	-42.62	8.05	-17.8735	18.09749	NA
NAWM_1TDI_60_AIC_RMS	6	-27.15	24.30	-11.9248	19.81287	NA
Tha_1TDI_60_AIC_RMS	6	-26.90	8.14	-6.4929	14.34236	NA
Brain_1TDI_40_AIC_MS	15	-52.40	8.97	-22.8511	18.67182	NA
Brain_1TDI_40_CoV_MS	15	NA	NA	NA	NA	0.39615
NAWM_1TDI_40_AIC_MS	15	-61.03	27.37	-13.9037	22.65610	NA
NAWM_1TDI_40_CoV_MS	15	NA	NA	NA	NA	0.27089
Tha_1TDI_40_AIC_MS	15	-39.54	11.58	-15.1526	14.66424	NA
Tha_1TDI_40_CoV_MS	15	NA	NA	NA	NA	0.30801
Brain_1TDI_40_AIC_PMS	9	-52.40	8.97	-26.1649	20.43276	NA
NAWM_1TDI_40_AIC_PMS	9	-61.03	27.37	-14.9964	26.39051	NA
Tha_1TDI_40_AIC_PMS	9	-39.54	11.58	-20.1893	14.62004	NA
Brain_1TDI_40_AIC_RMS	6	-39.40	5.61	-17.8804	16.08640	NA
NAWM_1TDI_40_AIC_RMS	6	-25.45	20.25	-12.2646	17.81937	NA
Tha_1TDI_40_AIC_RMS	6	-25.07	2.85	-7.5976	12.08145	NA

NAWM = Normal appearing white matter, Tha = thalamus, AIC = Aikaike information criterion, CoV = Coefficient of variation

Supplement 4. 2TCM (0–90 min) HC vs. MS V_{T2T} comparison

		N	Mean	SD	Mean Difference	p
Brain V_{T2T}	MS	15	0.5785	0.3614	-0.1122	0.514

	HC	9	0.6906	0.4616		
NAWM V_{T2T}	MS	15	0.4942	0.2561	-0.2121	0.204
	HC	9	0.7064	0.5398		
Thalamus V_{T2T}	MS	15	1.0003	0.6117	-0.1991	0.535
	HC	9	1.1994	0.9414		
cGM V_{T2T}	MS	15	0.7613	0.5221	-0.0444	0.836
	HC	9	0.8056	0.4634		

cGM = cortical grey matter. NAWM = normal appearing white matter.

Supplement 5. 2TCM (0–90 min) RMS vs. PMS V_{T2T} comparison

	MS Type	N	Mean	SD	Mean Difference	p
NAWM V_{T2V}	RMS	6	0.5252	0.2479	0.0516	0.717
	PMS	9	0.4736	0.2742		
Thalamus V_{T2V}	RMS	6	1.3354	0.6528	0.5585	0.082
	PMS	9	0.7769	0.4981		
cGM V_{T2V}	RMS	6	1.0613	0.5804	0.5001	0.066
	PMS	9	0.5612	0.3925		
T1 lesional V_{T2V}	RMS	6	0.9161	0.6483	0.0756	0.810
	PMS	9	0.8405	0.5414		
T1 perilesional 3mm rim V_{T2V}	RMS	6	0.5483	0.2210	0.0315	0.837
	PMS	9	0.5167	0.3142		

cGM = cortical grey matter. NAWM = normal appearing white matter. RMS = Relapsing MS.

PMS = Progressive MS.

Supplement 6. Lesional, perilesional and NAWM [^{11}C]SMW139 V_{T2T} (2TCM 0–90 min)

Comparison	Mean	SD	p
T1 lesions - NAWM	0.3765	0.5470	**0.018**
T1 lesions - T1 3mm rim	0.3414	0.4656	**0.013**
T1 3mm rim - NAWM	0.0351	0.1293	0.311
T1 lesions PMS - NAWM PMS	0.3669	0.5286	0.071
T1 lesions PMS - T1 3mm rim PMS	0.3238	0.4641	0.070
T1 3mm rim PMS - NAWM PMS	0.0431	0.1378	0.376

T1 lesions RMS - NAWM RMS	0.3909	0.6247	0.186
T1 lesions RMS - T1 3mm rim RMS	0.3678	0.5109	0.138
T1 3mm rim RMS - NAWM RMS	0.0231	0.1270	0.675

T1 3mm rim = T1 perilesional 3 mm rim, NAWM = Normal appearing white matter

RMS = Relapsing MS. PMS = Progressive MS.

Supplement 7. Sex differences among all subjects

	Sex	N	Mean	SD	Mean Difference	p
Age	M	15	48.9267	12.2733	1.6933	0.739
	F	9	47.2333	11.2278		
Time from Dg	M	9	7.3422	8.6391	-7.0694	0.146
	F	6	14.4117	8.7451		
EDSS	M	9	3.8333	2.4109	− .58333	0.616
	F	6	4.4167	1.6558		
Brain volume (cm^3)	M	15	1204.7093	86.7725	191.8237	**< .001**
	F	9	1012.8856	103.1303		
T1 lesion voluime (cm^3)	M	9	19.5891	17.3728	6.8607	0.391
	F	6	12.7283	8.7613		
SMW V_{TDI} brain	M	15	0.1105	0.0342	0.0334	**0.015**
	F	9	0.0771	0.0208		
SMW V_{TDI} NAWM	M	15	0.1187	0.0243	0.0344	**0.007**
	F	9	0.0842	0.0325		
SMW V_{TDI} thalamus	M	15	0.1460	0.0618	0.0542	**0.025**
	F	9	0.0918	0.0344		

NAWM = Normal appearing white matter. EDSS = Expanded disability status scale

TURUN
YLIOPISTO
UNIVERSITY
OF TURKU

Painosalama, Turku, Finland 2025

ISBN 978-952-02-0223-1 (PRINT)
ISBN 978-952-02-0224-8 (PDF)
ISSN 0355-9483 (Print)
ISSN 2343-3213 (Online)